FATIGUE BEHAVIOR OF METALLIC ALLOYS OF DIFFERENT MICROSTRUCTURES

BY

MUHAMMED JAMIU ADINOYI

A Dissertation Presented to the
DEANSHIP OF GRADUATE STUDIES

KING FAHD UNIVERSITY OF PETROLEUM & MINERALS

DHAHRAN, SAUDI ARABIA

In Partial Fulfillment of the
Requirements for the Degree of

DOCTOR OF PHILOSOPHY

In

MECHANICAL ENGINEERING

DECEMBER 2017

KING FAHD UNIVERSITY OF PETROLEUM & MINERALS
DHAHRAN- 31261, SAUDI ARABIA

DEANSHIP OF GRADUATE STUDIES

This thesis, written by **MUHAMMED JAMIU ADINOYI** under the direction of his thesis advisor and approved by his thesis committee, has been presented and accepted by the Dean of Graduate Studies, in partial fulfillment of the requirements for the degree of **Doctor of Philosophy** in Mechanical Engineering.

Dr. Zuhair M. Gasem
Department Chairman

Dr. Salam A. Zummo
Dean of Graduate Studies

7/6/18
Date

Dr. Nesar Merah
(Advisor)

Dr. Jafar Albinmousa
(Co-Advisor)

Dr. Tahar Laoui
(Member)

Dr. Husain Jubran Al-Gahtani
(Member)

Dr. Zuhair M. Gasem
(Member)

DEDICATION

To

My Wife: Hajiya Avuh

and

My Children: Oyiza, Onize, Onazasi and Onoruoiza

ACKNOWLEDGMENTS

I give thanks to Allah upon whose favour I have achieved this and all I have achieved. Indeed, His favours upon me are countless and none of His favours can I ever deny.

I want to thank my committee members led by Prof. Nesar Merah. I wish to specially thank Prof. Nesar Merah for his quality advice and careful revision of the contents of this dissertation, bringing it to a level of being worthy of a PhD dissertation. I must not fail to mention his kindness and patience towards me. May Allah reward him in abundance.

I equally want to thank Dr. Jafar Albinmousa, my co-advisor. His relentless work spirit enabled me to have the experiments in this work done successfully. His knowledge of the subject of fatigue was a great asset to this work. My gratitude goes to other committee members; Prof. Tahar Laoui for his guidance on microstructure analysis, Prof. Hussein Al-Qahtani and Dr. Zuhair M. Gasem for their valuable inputs which raised the quality of this work.

I wish to express my appreciation to King Fahd University of Petroleum and Minerals for providing me the scholarship and the enabling environment for this work. I am thankful to the Department of Mechanical Engineering for providing the facility and support for my study and the research. I wish to acknowledge all the academic, administrative and technical staffs of the department with whom I have developed a cordial relationship. I thank ME technicians, particularly, Mr. Romeo Agua of the ME workshop and Mr. Lateef Hasimi of the ME Material Science Laboratory for their technical support. I would not forget to acknowledge King AbdulAziz Center for Science and Technology (KACST) for funding the project (KASCT 230-34) under which this work was carried out.

I want to appreciate my family especially my wife, Hajia Sidikat Lawal, and my children: Na'imatullah Oyiza, Tasneem Onize, Nadhrah Onozasi and AbdulHakeem Onoruoiza, for their unalloyed support, endurance, understanding and prayers. You are my backbone. I would not forget the support of my brothers, sisters and my extended family. My special thanks to my brothers Dr. AbdulKareem and Engr. Momohjimoh Adinoyi and their families.

My thanks go to my departmental colleagues, friends back home and members of the Nigeria community at KFUPM and environs for their comradeship. My thanks to Dr. Muhammed Onimisi, Dr. Hamza Salami and Dr. Zakariyyah Jamiu and their families, and Engr. Ibrahim Momohjimoh.

May Allah reward everyone who in one way or another has helped to make this work successful and to be a worthwhile experience.

TABLE OF CONTENTS

LIST OF TABLES

LIST OF FIGURES

LIST OF NOMENCLATURES

b	Axial fatigue strength exponent
b_s	Shear fatigue strength exponent
c	Axial fatigue ductility exponent
$\mathrm{c_s}$	Shear fatigue ductility exponent
d	Diameter of solid specimen
d_i	Inner diameter of tubular specimen
d_o	Outer diameter of tubular specimen
E	Elastic modulus
Eq	Equation
eqv	Equivalent
Exp	Experimental
Fig	Figure
Freq	Frequency
G	Shear modulus
K	Monotonic tensile strength coefficient
K'	Axial fatigue strength coefficient
K_s	Monotonic Shear strength coefficient
K'_s	Shear fatigue strength coefficient
mm	Millimeter
MPa	Mega Pascal
n	Monotonic tensile strain hardening exponent

n'	Axial fatigue strain hardening exponent
N_f	Fatigue life
n_s	Monotonic shear strain hardening exponent
n'_s	Shear fatigue strain hardening exponent
N_t	Transition fatigue life
Spec	Specimen
γ_a	Shear strain amplitude
γ_e	Elastic shear strain amplitude
γ_f'	Shear fatigue ductility coefficient
γ_p	Plastic shear strain
ε_a	Axial strain amplitude
ε_e	Axial elastic strain amplitude
ε_f'	Axial fatigue ductility coefficient
ε_p	Axial plastic strain amplitude
θ	Phase angle
σ_a	Axial stress amplitude
σ_f'	Axial fatigue strength coefficient
σ_m	Axial mean stress
σ_{max}	Maximum axial stress
σ_{min}	Minimum axial stress
τ_a	Shear stress amplitude
τ_f'	Shear fatigue strength coefficient
τ_m	Shear mean stress

τ_{max}	Maximum shear stress
τ_{min}	Minimum shear stress

ABSTRACT

Full Name : Muhammed Jamiu Adinoyi

Thesis Title : Fatigue Behavior of Metallic Alloys of Different Microstructures

Major Field : Mechanical Engineering

Date of Degree : December 2017.

This work investigates the monotonic and fatigue behavior of three important engineering alloys, namely, AW2099-T83 aluminum-lithium alloy, ZK60A magnesium alloy and AISI 410 stainless steel. These alloys were selected to meet a combination of properties frequently demanded of metallic alloys. These are low weight, high strength-to-weight ratio and corrosion resistance. The study began with the characterization of the microstructures of the alloys. It was found that grain sizes and distributions varied with orientations and locations in AW2099-T83 and ZK60A alloys. However, they remained the same in AISI 410 stainless steel, regardless of orientation and location of metallographic analysis. These results were used to explain some of the behaviors of the alloys under monotonic and fatigue loading conditions.

Monotonic tensile and torsional tests were performed on specimens machined parallel to the extrusion direction. The descending order of the strength of the alloys under tensile and torsion loadings was: AISI 410, AW2099-T83 and ZK60A. The largest deformation under static loading was shown by AISI 410, while AW2099-T83 showed minimal plasticity. ZK60A alloy exhibited the largest post-yield strain work hardening.

The mechanical properties obtained from these tests were used in the analysis of the fatigue behavior of the alloys.

A range of strain amplitudes were selected for fatigue testing under cyclic axial, cyclic torsion and multiaxial proportional and nonproportional loading paths. Smooth solid specimens were used for cyclic axial loading while tubular specimens were utilized for cyclic torsion and multiaxial testing. Fatigue behavior was characterized in all the loading paths by hysteresis loops, peak stress, mean stress, stress amplitude and fatigue life.

It was found that the hysteresis loops of the alloys were symmetrical with respect to shape, regardless of loading paths and applied strain amplitudes. Plastic strain was present at all applied strain amplitudes for ZK60A and AISI 410 alloys, but was only observed for AW2099-T83 alloy at cyclic strain amplitude close to the value of the yield strain in monotonic behavior. Cyclic stress level was dependent on the applied strain amplitude and relative to the monotonic strength of the alloys. Cyclic strain hardening in AW2099-T83 alloy was observed in the early fatigue cycles at high strain amplitudes, but at later cycles in low and intermediate strain amplitudes. Mean stress evolution in AW2099-T83 alloy was dependent on both the applied strain amplitudes and the number of cycles. Cyclic hardening was found to be insignificant in ZK60A alloy. Compressive mean stress was observed in ZK60A alloy regardless of applied strain amplitude and the number of cycles. AISI 410 alloy showed cyclic softening irrespective of strain amplitude and loading path, and its mean stress decreased continuously with the number of fatigue cycles.

Fatigue parameters, for the three alloys in axial and torsional loading modes, were found by performing curve fittings. The uniaxial fatigue life of the alloys was correlated with Coffin-Manson equation. Good correlations were generally achieved. However, the axial fatigue life data of AW2099-T83 alloy correlated better with Basquin equation due to the absence of plastic strain in the cyclic axial tests.

Under biaxial loading path, it was found that hysteresis loop from uniaxial tests were preserved under nonproportional loading for AW2099-T83 alloy at similar strain amplitude. No difference was observed in the hysteresis loop for ZK60A alloy in the entire loading path for the same applied strain amplitude. Significant nonproportional cyclic hardening was observed for AISI 410 alloy. This was identifiable by the rounding of the tip of the hysteresis loop in nonproportional loading.

Von Misses equivalent strain method was used to develop strain-life curves for the three alloys where it was found that cyclic torsional loading was most destructive for AW2099-T83 alloy. While cyclic axial loading path was most damaging for ZK60A alloy, multiaxial loading paths were most destructive to AISI 410 alloy. In addition, Fatemi-Socie (FS) and Smith-Watson-Topper (SWT) critical plane criteria were used to predict fatigue life under all the loading paths for the three alloys. The FS yielded better prediction than SWT for the three alloys within a factor-of-two scatter band.

The crack profile in cyclic torsion for AW2099-T83 alloy was found to be dependent on the applied strain amplitude. Branching crack was observed at low strain amplitudes, but straight crack resulted at high strain amplitudes. In Multiaxial fatigue, the crack in ZK60A and AISI 410 alloys grew normal to specimen axis. However, in AW2099-T83 alloy, crack shifted from transverse to longitudinal planes. The failure mode of the fatigue specimens in cyclic axial for AW2099-T83 alloy was found to be dependent on applied strain amplitudes while the ZK60A and AISI 410 alloys fractured in consistent manner regardless of applied strain amplitude.

To summarize, the difference in the stress response of the three alloys can be explained by the different microstructures and dislocation behavior of the alloys. The microstructure of AW2099-T83 alloy was strengthened by aging precipitates that interacted with dislocations causing cyclic hardening. However, when the precipitates were sheared due to high stress, their resistance to dislocation movement was weakened and cyclic softening resulted. The ZK60A alloy hardened due to fewer slip planes present in its microstructure and due to twining mode of dislocation. With increase in the number of cycles, dislocation was increased but there was insufficient plane for dislocation mobility to occur. The overall softening observed in AISI 410 alloy was because of its tempered martensite which did not restrict dislocation mobility. In addition, cycle-dependent and strain-dependent fatigue behavior as were seen in AW2099-T83 and ZK60A alloys could be linked to their microstructures both of which exhibit strong texture in their grain structures due to processing. However, such behavior was not seen in AISI 410 alloy which exhibited the same grain structures and sizes in all the orientations.

ملخص الرسالة

الاسم بالكامل: ادينوي محمد جامو

عنوان الرسالة: سلوكيات الكلال لسبائك معدنية من بنى مجهرية مختلفة

المجال الرئيسي: الهندسة الميكانيكية

تاريخ الدرجة : ديسمبر ، 2017.

هذا العمل يحقق الرتابة وسلوك الكلال لثلاثة سبائك هندسية مهمة ، وهي سبيكة الألومنيوم - ليثيوم AW2099-T83 ، سبائك المغنيسيوم ZK60A والفولاذ المقاوم للصدأ AISI 410. وقد تم اختيار هذه السبائك لتحقيق مزيج من الخصائص المطلوبة كثيرا في السبائك المعدنية. هذه السبائك منخفضة الوزن و لديها نسبة عالية من المتانة بالنسبة إلى الوزن ومقاومة للتآكل. بدأت الدراسة بتوصيفات البنية المجهرية للسبائك. وقد وجد أن حجم وتوزيع الحبيبات إختلفت بإختلاف الاتجاهات والمواقع في سبائك AW2099-T83 و ZK60A. ومع ذلك توجد نفس الخصائص في الفولاذ المقاوم للصدأ AISI 410 ، بغض النظر عن إتجاه وموقع تحليل الفحص المعدني. تم استخدام هذه النتائج لشرح سلوك بعض السبائك تحت ظروف التحميل الرتيب والكلال.

تم إجراء اختبارات الشد والالتواء أحادي الطور على عينات تم تشكيلها بالتوازي مع اتجاه البثق. حيث وجد أن الترتيب التنازلي لمتانة السبائك تحت الشد والالتواء: AISI 410 و AW2099-T83 و ZK60A. حدث أكبر تشوه تحت تحميل ثابت لسبيكة AISI 410 ، بينما أظهرت سبيكة AW2099-T83 الحد الأدنى من اللدونة. أظهرت سبيكة ZK60A أكبر تحمل post-yield strain. تم استخدام الخصائص الميكانيكية التي تم الحصول عليها من هذه الاختبارات في تحليل سلوك التعب من السبائك.

تم اختيار مجموعة من مدي الإجهاد لاختبار الكلال تحت محور دوري والتواء دوري و متعدد المحاور ومسارات تحميل متناسبة وغير متناسبة. تم استخدام عينات صلبة ناعمة للتحميل المحوري الدورى بينما تم استخدام العينات الأنبوبية للالتواء الدوري والاختبارات متعددة المحاور. تم وصف سلوك الكلال في جميع مسارات التحميل من خلال حلقات hysteresis ، أعلي إجهاد و الإجهاد المتوسط و اتساع التوتر وحياة التعب.

وقد وجد أن حلقات التلاشي من السبائك كانت متماثلة فيما يتعلق بالشكل ، بغض النظر عن مسارات التحميل وسعة الإجهاد. كان الانفعال اللدن موجود في جميع سعات الانفعال المطبقة على سبائك ZK60A و AISI 410 ، ولكن لوحظ فقط في سبيكة AW2099-T83 عند سعة الانفعال الدورية انه قريب من قيمة الانفعال الناتج فيmonotonic behavior . مستوى الإجهاد الدوري يعتمد على سعة الانفعال المبذول ومتناسب مع متانة monotonic للسبائك. وقد لوحظ انفعال إجهاد دوري في سبيكة AW2099-T83 في دورات الكلال الأولى بسعات عالية من الانفعال ، ولكن لوحظ في الدورات المتأخرة أنه في السعة المنخفضة والمتوسطة السعة. يعتمد متوسط تطور الاجهاد في سبيكة AW2099-T83 على سعات الانفعال المطبقة وعدد الدورات. وجد ان التصلب الدوري غير مهم في سبيكة ZK60A. لوحظ ضغط اجهاد متوسط في سبيكة ZK60A بغض النظر عن سعات الانفعال المطبقة وعدد الدورات. أظهرت سبيكة AISI 410 تليين دوري بغض النظر عن سعة الانفعال ومسار التحميل ، وانخفض مستمر لمتوسط الإجهاد مع عدد دورات الكلال.

تم العثور على معاملات الكلال بالنسبة للسبائك الثلاثة في أوضاع التحميل المحورية والالتوائية عن طريق أداء تناسق المنحنى. يرتبط عمر الكلال أحادي المحور للسبائك بعلاقة مترابطة مع معادلة Coffin-Manson. تم تحقيق علاقة مترابطة جيدة مع المعادلة. مع ذلك ، ترتبط معلومات عمر الكلال المحوري لسبيكة AW2099-T83 بشكل أفضل مع معادلة Basquin بسبب عدم وجود انفعال لدن في الاختبارات المحورية الدورية.

تحت مسار التحميل ذو المحاور الثنائية ، تم العثور على أن حلقة hysteresis من اختبارات أحادية المحور تم الحفاظ عليها تحت تحميل غير نسبي لسبيكة AW2099-T83 عند سعة انفعال مماثلة. لم يلاحظ أي اختلاف في حلقة hysteresis لسبيكة ZK60A في كل مسار التحميل لنفس سعة السلالة المطبقة. وقد لوحظت صلابة حلقية غير متناسبة كبيرة لسبيكة AISI 410. تم التعرف على هذا من خلال تقريب طرف حلقة hysteresis في التحميل غير النسبي.

تم استخدام طريقة Von Misses للانفعال المكافىء لتطوير منحنيات عمر الانفعال للسبائك الثلاثة حيث وجد ان التحميل الالتوائي الدوري هو الأكثر تدميرا لسبيكة AW2099-T83. بينما كان مسار التحميل المحوري الدوري أكثر ضررًا بالنسبة لسبيكة ZK60A ، كانت مسارات التحميل متعددة المحاور أكثر تدميراً لسبيكة AISI 410. بالإضافة

إلى ذلك، تم استخدام معايير الطائرة الحرجة Fatemi-Socie (FS)وSmith-Watson-Topper (SWT) للتنبؤ بحياة الكلال تحت جميع مسارات التحميل للسبائك الثلاثة. نتجت FS تنبؤات أفضل من SWT للسبائك الثلاثة ضمن نطاق عامل مبعثر ثنائي.

ولقد وجد أن صورة الشرخ في الالتواء الدوري لسبيكة AW2099-T83 تعتمد على سعة الانفعال المطبقة. لوحظ وجود الشروخ المتفرعة في الاتساع المنخفض للانفعال، ولكن الشروخ المستقيمة نتجت عن سعات الإنفعال العالية. في الكلال متعدد المحاور، تولد الشرخ في سبائك ZK60Aو AISI 410 عمودي علي محور العينة. ومع ذلك في سبيكة AW2099-T83، تحول الشرخ من المستويات المستعرضة إلى الطولية. وجد أن وضع الفشل لعينات الكلال في الاختبارات المحورية الدورية لسبيكة AW2099-T83 يعتمد على سعات الانفعال المطبقة، بينما يتم تكسير سبائك ZK60Aو AISI 410 بطريقة متناسقة بغض النظر عن سعة الانفعال المطبقة.

للتلخيص، يمكن تفسير الاختلاف في استجابة الإجهاد للسبائك الثلاثة من خلال الهياكل المجهرية المختلفة وسلوك التفكك للسبائك. تم تقوية البنية المجهرية لسبائك AW2099-T83 بواسطة رواسب قديمة تتفاعل مع التفكك مسببةً تصلبًا دوريًا. ومع ذلك، عندما تم فصل الرواسب بسبب الإجهاد العالي، فقد ضعفت مقاومتها لحركة التفكك وتسبب في تليين دوري. سبيكة ZK60A قوية بسبب انخفاض عدد أسطح الانزلاق في البنية المجهرية ونمط التوأمة في الخلع. مع زيادة عدد الدورات، زاد الخفض ولكن لم يكن هناك مستوى كاف لحركة التفكك. لوحظ تزييت كامل في سبائك AISI 410 بسبب خوائطه المخففة التي لم تحد من حركية التفكك. بالإضافة إلى ذلك، يمكن ربط كلا من الكلال المرتبط بالانفعال و المرتبط بالدورة، استنادا إلى سبائك AW2099-T83 و ZK60A، بهياكلها المجهرية و الذي يظهر أنسجة قوية في هياكل الحبوب بسبب المعالجة. ومع ذلك، لم يلاحظ مثل هذا السلوك في سبائك AISI 410 التي حافظت على نفس هياكل وأحجام الحبوب في جميع الاتجاهات.

CHAPTER 1

INTRODUCTION

1.1 Fatigue of Metallic Materials

Fatigue is a cumulative damage process leading to failure of structures and engineering components due to cyclic or repeated loading. Fatigue involves a mechanism in which stress-strain history change periodically. Hence, the forward stress-strain event can be different from reversed event in a number of way. Such a cyclic effect on the stress-strain behavior of material was first observed by Bauschinger in 1886. Bauschinger found that the yield strength of material is reduced in a reverse direction after the initial forward loading. This phenomenon is known as Bauschinger effect. The mechanism of Bauschinger effect is due to the change in the dislocation substructure resulting from the microscopic stress distribution of the material. The alternate formation and dissolution of dislocation walls or cells or subgrain boundaries in the structure of material due to forward-reverse loading are the contributing factor to Bauschinger effect. This interaction usually is dependent on the type of precipitates or subgrain in the microstructure. Precipitates in age-hardened alloys can either be coherent or sharable whereby they can be cut through by stress during loading or incoherent, those which resist penetration [1].

One common characteristic of fatigue is that the load causing failure is lower than the yield or ultimate strength of the material. This is why fatigue was not fully understood in early work investigating material failure process, because it was not initially believed that load far below the yield or ultimate strength of material could cause its failure. Historical background on the early work to understanding fatigue has always been linked to Wöhler who performed several fatigue tests for tension, compression and bending loads [1,2]. The popularized stress-life (S-N) curve owed its origin to Wöhler. Majority of engineering failure is due to fatigue and it is reported to account for 90% of these failures [3]. Real life cases of fatigue failures of engineering components and structures, and numerous researches on fatigue have been published [4–6].

1.2 Fatigue Process

The fatigue damage process occurs in three phases: crack initiation, crack propagation and fracture. The crack initiation phase is the beginning of the fatigue damage where cracks begin to form or nucleate from points of imperfection or discontinuities such as notches, inclusion and scratches. These points act as stress concentration points and form the weakest link from where crack potentially grows. Prior to the nucleation of cracks, sub-structural and microstructural changes occur, which appear as fine slip (dislocation due to shear deformation) markings on the surface of structure [1,2,7]. Slip lines multiply as cycling continues and they are consistently concentrated at particular bands where fatigue cracks eventually initiate. This region of accumulated slip where fatigue crack starts is referred to as persistent slip band (PSB). The persistent slip band can be viewed as a kind of intrusion on the surface of cycled specimen due to the relative movement between colonies of slip lines.

The formation of crack is followed by crack propagation wherein the nucleated cracks coalesce and progressively increase in size, crossing several grain boundaries. Crack growth is both a micro and macro process whose length scale can be used to define fatigue failure or remaining life of component. When crack growth is within a small length usually in the dimension of a few grains, such crack is termed stage I fatigue crack growth. Stage II crack results when crack has crossed several grain boundaries due to increase in load intensity or long range cycling. Material slip characteristics, stress level and microstructural dimension are factors that influence the microscopic mode of fatigue crack growth [1].

Fracture (phase III) occurs when the crack has grown to a critical size or become unstable that the remaining area of the loading plane is no longer capable of sustaining load. Thus, the material or component disintegrates or falls into pieces. These three phases can often been distinguished in the fractured surface of component which failed by fatigue as illustrated in Fig. 1.

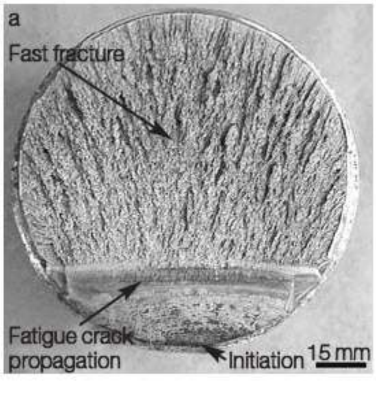

Figure 1: A typical fatigue fracture surface [8].

The proportion of each phase is a function of the stress level, microstructure, material properties, environment, etc. A substantial portion of the life cycle may be spent in any of the three phases. Low-level stress or strain usually causes a significant portion of the life to be expended on crack formation, while crack propagation dominates the life when the cycling load is high [2].

1.3 Fatigue Life

The number of load cycles a component withstands before it eventually fails is a measure of its fatigue life. However, the definition of fatigue failure has a technical concept. Fatigue failure could be the beginning of crack, the growth of crack to a certain length scale, the decrease in load to a predetermined percentage or total fracture. The last criterion is usually never applied in real life application. Therefore, fatigue life is defined based on any of those constraints aforementioned and it ranges from few hundred cycles to several hundred or million cycles. Low-cycle fatigue (LCF) is characterized by high-level stress or strain, which means that the fatigue life will be in several tens to few hundreds of cycles. Several thousands to million cycles resulting from low-cyclic load typify high-cycle fatigue (HCF). The other distinction for the classification of fatigue life is the amount of plastic deformation prior to failure. In HCF, there is minimal or total absence of plastic deformation. The LCF is, however, a plastic deformation-controlled process with few numbers of cycles prior to failure. Basquin proposed the relationship between fatigue life and cycling stress in a component that is designed for high cycle fatigue.

$$S_a or\ \sigma_a = A\left(N_f\right)^B \ldots\ldots\ldots\ldots\ldots\ldots (1.1a)$$

Where S_a or σ_a is the stress amplitude, N_f is the life for a particular stress amplitude and A and B are constants obtained when the data is fitted to the equation on a log-log curve. Alternatively,

$$\sigma_a = \sigma_f'\left(2N_f\right)^b \text{.......................(1.1b)}$$

Where σ_f' is the fatigue strength coefficient and b is the fatigue strength exponent. σ_f' is usually taken to be equal to the true fracture stress of the material in tensile test and $b = B$. For some materials, like steel alloy, the fatigue curve shows a horizontal asymptote meaning that below certain stress level, the component will go for infinite number of cycles without failure. The stress at which this occurs is called the fatigue limit or endurance limit of the material. For others such as the aluminum alloy, the fatigue curve is a continuous one with no clear point of discontinuity. The fatigue strength for such materials is often defined at 10^6 or 10^7cycles. The fatigue strength of a material is the stress for a specified number of cycles.

On the other hand, Coffin and Manson have proposed a strain based approach for low-cycle fatigue because of the involvement of high plastic deformation [1,2]. The Coffin-Manson relation is expressed in Eq. (1.2). Where ε is the applied strain amplitude, ε_f' is the fatigue ductility coefficient, c is the fatigue ductility exponent and N_f is the fatigue life.

$$\varepsilon = \varepsilon_f'\left(2N_f\right)^c \text{................(1.2)}$$

Fatigue life is influenced by loading condition, microstructure, surface finish, environment environmental factors such as chemical, heat, temperature, pH level etc.). Fatigue behavior is, in fact, one material behavior that is highly sensitive to a wide range of factors. The design for fatigue is therefore a careful process taking into consideration as many factors as possible.

1.4 Uniaxial and Multiaxial Fatigue Loading

A cyclic load acting in only one direction or axis is referred to as a uniaxial fatigue, as illustrated in Fig. 2(a). Such single load can be either axial, bending or torsion. In a constant amplitude uniaxial fatigue situation, the loading axis remains fixed throughout the load-time history. However, real life cases have shown that two or more repeating stresses or strains can act simultaneously on a component independent of one another. This is referred to as multiaxial fatigue (Fig. 2(b)). For example, a rotating shaft is concurrently under cyclic torsional and bending stresses. A biaxial state of stress or strain is referred to here as multiaxial fatigue. Biaxial or multiaxial loading can be either proportional or nonproportional, as illustrated in Fig. 3. In the former case, the principal axis remains either fixed or changes with respect to the loading axis. In a proportional biaxial loading of cyclic torsion and tension-compression loading, both loading modes reach their maximum and minimum values at the same time. This is also known as in-phase loading. A nonproportional loading occurs when the principal load axes change orientation with time and load magnitude. When one of the loads reaches either minimum or maximum value before the other, it is referred to as nonproportional or out-of-phase loading. The amount of lag or lead between the two loads is the phase angle ϕ, implying that for a proportional loading, the phase angle between the cycling loads is zero. Phase angle difference in nonproportional loading can vary between -90° and 90°. Nonproportional loading often imposes additional effect that is not usually observed in proportional loading.

The additional hardening of material leading to higher damage under nonproportional load have been observed [9,10]. The complexity in multiaxial fatigue demands a thorough analysis and an investigation of its damage mechanism.

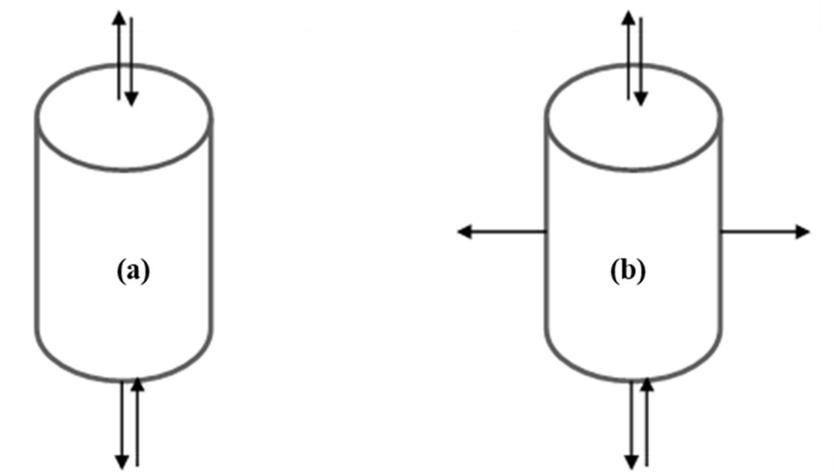

Figure 2: Schematic of a body under fatigue load.

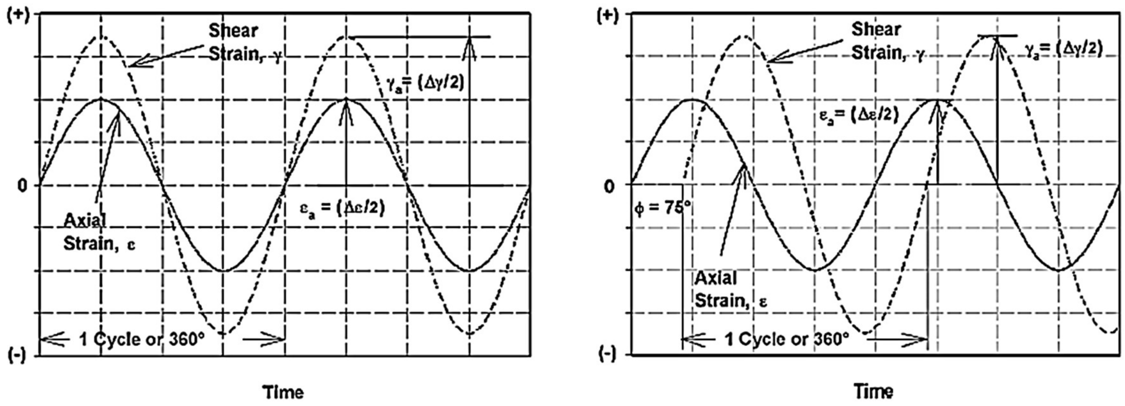

Proportional waveform **Nonproportional waveform**

Figure 3: Schematic of axial and shear strain waveforms for proportional and nonproportional Axial-torsional fatigue test [11].

1.5 Strain-Controlled Fatigue Test

A strain-controlled fatigue experiment is that in which a specimen is loaded cyclically in a predetermined strain value until the specimen fails. As mentioned in the previous section, the definition of failure in fatigue has a technical concept because the criteria for failure vary. Strain-controlled approach to fatigue test can better characterize fatigue especially in low cycle fatigue where significant plastic deformation can be present. Although well-suited to notch members, strain-controlled fatigue experiments are becoming popular even though the procedure and equipment are more complex and expensive than the traditional stress- or load-controlled fatigue test [2]. Besides, strain can be measured directly unlike stress, which depends on other physical parameters. Strain-controlled fatigue is appealing in low-cycle fatigue due to its capability in predicting fatigue crack initiation and early crack growth [1].

1.6 Analysis of Fatigue Experimental Data

A detailed analysis of the states of strains and stresses is required for full description of material fatigue characteristics. Strain limits-maximum and minimum, mean strain, strain amplitudes are necessary parameters to characterize the fatigue characteristics of components. The applied strain in a strain-controlled test generates forces and the number of cycles to failure as the most important experimental data. Forces are used to determine various stresses, while the combination of applied strain, resultant stresses and fatigue life are utilized to find a number of fatigue parameters and material fatigue constants. In analyzing the data for strain-controlled fatigue, a hysteresis loop, as shown in Fig. 4, at half-life cycle is considered. A hysteresis loop is the energy per unit volume during the fatigue cycle.

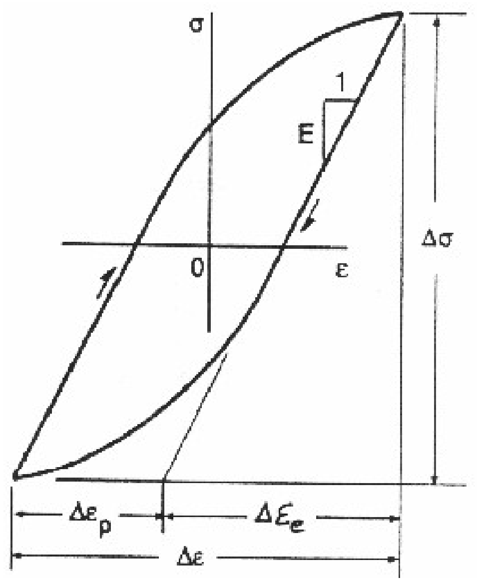

Figure 4: Typical fatigue test hysteresis loop.

Associated strain-controlled fatigue test terms are hereby defined, followed by procedural analysis of strain, stress and fatigue life parameters.

- Maximum strain, (ε_{max}): This is the maximum nominal strain attained during the test cycle.
- Minimum strain (ε_{min}): The minimum strain reached during cycling. If this strain is numerically equal and opposite in sign to the maximum strain, the loading condition is defined to be completely reversed.
- Strain range, $(\Delta\varepsilon)$: It is the difference between the maximum and minimum strains.
- Strain amplitude, $\left(\frac{\Delta\varepsilon}{2} or\ \varepsilon_a\right)$: It is one-half the strain range. It is also referred to as the alternating strain.

- Mean strain, (ε_m): It is the arithmetic average of the maximum and minimum strains. For a completely reversed loading, the mean strain is zero.
- Strain ratio (R): It is the ratio of minimum stress to maximum strain. R is -1 for completely reversed strain.

1.6.1 Cyclic Axial Test

The data analysis is usually performed following the procedure of ASTM E606 [12]. In a tension-compression test, a solid specimen is commonly employed. Hence, the stress amplitude, $\frac{\Delta\sigma}{2}$, is expressed as:

$$\frac{\Delta\sigma}{2} = \frac{P_a}{A} \ldots\ldots\ldots\ldots\ldots (1.3)$$

Where P_a is the load amplitude and A is the area of the gage section of the specimen. For a circular gage section with diameter *d*,

$$A = \frac{\pi d^2}{4} \ldots\ldots\ldots\ldots\ldots (1.4)$$

The strain amplitude is made up of the elastic and plastic strains. The relation between these strains is given as

$$\frac{\Delta\varepsilon}{2} = \varepsilon_a = \varepsilon_e + \varepsilon_p \ldots\ldots\ldots\ldots (1.5)$$

Where $\frac{\Delta\varepsilon}{2}\, or\ \varepsilon_a$ is the total strain amplitude, ε_e is the elastic strain and ε_p is the plastic strain. The elastic portion can be derived from the stress amplitude and the Young modulus, *E*, of the material,

$$\varepsilon_e = \frac{\Delta\sigma}{E} \ldots\ldots\ldots\ldots\ldots (1.6)$$

Plastic strain can be measured from a hysteresis loop at the point where the loop crosses the strain axis, i.e., the strain at which the stress is zero. But more often, from the following derivation,

$$\varepsilon_a = \frac{\Delta\varepsilon}{2} = \frac{\Delta\sigma}{2E} + \varepsilon_p \text{.............. (1.7a)}$$

From which,

$$\varepsilon_p = \varepsilon_a - \frac{\Delta\sigma}{2E} \text{.............. (1.7b)}$$

A cyclic stress-plastic strain relationship for most metallic alloys often follows Eq. (1.8).

$$\sigma_a = K'\left(\varepsilon_p\right)^{n'} \text{.............. (1.8)}$$

Where K' and n' are the fatigue strength coefficient and exponent, respectively, and are material fatigue properties. These can be found by fitting experimental plastic strain and the stress amplitude data to a curve on a log-log scale. In such a linearized curve, n' is the slope, while K' is the intercept on the stress axis.

From Eq. (1.8), the plastic strain amplitude can be expressed as given by Eq. (1.9):

$$\varepsilon_p = \left(\frac{\sigma_a}{K'}\right)^{\frac{1}{n'}} \quad or \quad \frac{\Delta\varepsilon_p}{2} = \left(\frac{\Delta\sigma}{2K'}\right)^{\frac{1}{n'}} \text{......... (1.9)}$$

Substituting Eq. (1.9) in (1.7a) gives Eq. (1.10). This equation represents the cyclic stress-strain curve of a material that has undergone fatigue testing.

$$\varepsilon_a = \varepsilon_e + \varepsilon_p = \frac{\sigma_a}{E} + \left(\frac{\sigma_a}{K'}\right)^{\frac{1}{n'}} \text{ or } \frac{\Delta\varepsilon}{2} = \frac{\Delta\sigma}{2E} + \left(\frac{\Delta\sigma}{2K'}\right)^{\frac{1}{n'}} \text{... (1.10)}$$

The number of cycle to failure, or fatigue life, can be related to the stress, elastic strain and plastic strain through a number of equations. The stress amplitude, $\sigma_{a,}$ is related to the fatigue life, N_f, in the power equation, Eq. (1.1b), previously given in section 1.3. The equation is rewritten here:

$$\sigma_a = \frac{\Delta\sigma}{2} = \sigma_f'\left(2N_f\right)^b \ldots\ldots\ldots\ldots (1.1b)$$

The plot of σ_a versus $2N_f$, the number of reversals to failure, on a log-log plot often result to a straight-line curve whose slope represents b and the intercept on the stress axis is σ_f'. Plotting the elastic strain amplitude, ε_e, and the number of reversal to failure, $2N_f$, on a log-log plot usually follows the curve represented by Eq. (1.11)

$$\varepsilon_e = \frac{\sigma_f'}{E}\left(2N_f\right)^b \ldots\ldots\ldots\ldots (1.11)$$

Where $\frac{\sigma_f'}{E}$ *and* b are the intercept and slope, respectively.

Similarly, plotting the plastic strain amplitude, ε_p, against $2N_f$ follow a power curve represented by Eq. (1.12).

$$\varepsilon_p = \varepsilon_f'\left(2N_f\right)^c \ldots\ldots\ldots\ldots (1.12)$$

Where ε_f' is the fatigue strain ductility coefficient and c is the fatigue ductility exponent.

The combination of Eq. (1.11) and (1.12) gives Eq. (1.13), the so-called Coffin-Manson equation with which the strain-life correlation for most metals and alloys can be represented. Typical strain life curve for metallic alloys is shown in Fig. 5.

$$\varepsilon_a = \frac{\sigma_f'}{E}\left(2N_f\right)^b + \varepsilon_f'\left(2N_f\right)^c \ldots\ldots\ldots\ldots (1.13)$$

The parameters are defined as for Eq. (1.1) and (1.2) in section 1.3.

A transition life, N_t, the fatigue life at which the elastic and plastic strain amplitudes are equal, can be estimated from Eq. (1.14):

$$N_t = 0.5\left(\frac{\sigma_f'}{\varepsilon_f' E}\right)^{\frac{1}{(c-b)}} \ldots\ldots\ldots\ldots\ldots\ldots (1.14)$$

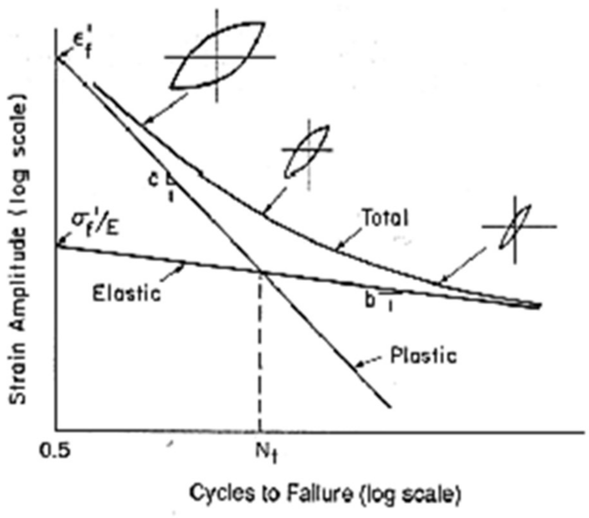

Figure 5: A typical strain-life curve [13].

1.6.2 Cyclic Torsion Test

Similar derivations can be made for cyclic torsion taking into account the specimen geometry and the axis of loading.

For a torsional fatigue test, a tubular specimen with outer diameter, d_o, and inner diameter, d_i, is used. Thus, the shear stress amplitude τ_a on the ring cross section (thickness) due to torque moment (forth-and-back twisting) is given by:

$$\tau_a = \frac{T_a d_o}{2J} \;\ldots\ldots\ldots\ldots\ldots\ldots\ldots \;(1.15a)$$

$$J = \frac{\pi\left(d_o{}^4 - d_i{}^4\right)}{32} \ldots\ldots\ldots\ldots\ldots....(1.15b)$$

T_a is the torque amplitude and J is the polar moment of inertia.

Therefore, the shear stress over the thickness of a tubular specimen is:

$$\tau_a = \frac{16 T_a d_o}{\pi\left(d_o{}^4 - d_i{}^4\right)} \;\ldots\ldots\ldots\ldots\ldots \;(1.16)$$

Likewise, the shear strain amplitude is the sum of elastic and plastic components as expressed by Eq. (1.17).

$$\gamma_a = \gamma_e + \gamma_p \text{.............. (1.17)}$$

Where γ_a is the total shear strain amplitude, γ_e is the elastic strain and γ_p is the plastic strain. Similarly, the elastic component can be derived from the shear stress amplitude and the Shear modulus, G, of the material,

$$\gamma_e = \frac{\tau_a}{G} = \frac{\Delta\tau}{2G} \text{ .... (1.18)}$$

Corollary,

$$\gamma_a = \frac{\tau_a}{G} + \gamma_p \quad \text{................ (1.19a)}$$

$$\gamma_p = \gamma_a - \frac{\tau_a}{G} \quad \text{............... (1.19b)}$$

Hence, a cyclic shear stress-plastic strain relationship can be written,

$$\tau_a = \ K_s{}'(\gamma_p)^{n_s{}'} \text{ .... (1.20a)}$$

Where $K_s{}'$ and $n_s{}'$ are the shear fatigue strength coefficient and exponent, respectively. $K_s{}'$ and $n_s{}'$ are found from the fitted data of plastic strain and the shear stress to a linearized power curve on a log-log scale.

Therefore,

$$\gamma_p = \left(\frac{\tau_a}{K_s{}'}\right)^{\frac{1}{n_s{}'}} \text{ .... (1.20b)}$$

Substituting Eq. (1.20b) into Eq. (1.19a) gives Eq. (1.21), which represents the cyclic shear stress-strain curve of the material.

$$\gamma_a = \frac{\tau_a}{G} + \left(\frac{\tau_a}{K'}\right)^{\frac{1}{n'}} \text{ .... (1.21)}$$

Similar relationships between shear fatigue life, shear stress and the strain components can be derived as are for the cyclic axial. The relationship between the shear stress amplitude, τ_a, and fatigue life, N_f, is obtained by substituting the cyclic axial terms in Eq. (1.11) with the appropriate cyclic shear terms.

Therefore,

$$\tau_a = \tau_f'\left(2N_f\right)^{b_s} \text{..............} \ (1.22)$$

Where τ_f' is the shear fatigue strength coefficient and b_s is the shear fatigue strength exponent. A log-log plot of τ_a versus $2N_f$ results in a straight-line curve whose slope is b_s and the intercept on the stress axis is the shear fatigue strength coefficient, τ_f'.

The elastic strain amplitude, γ_e and $2N_f$, when plotted on a log-log scale can be fitted to a line represented by Eq. (1.23a). Similar power relationship exists between plastic strain amplitude, $\gamma_{p,}$ and $2N_f$ denoted by Eq. (1.23b).

$$\gamma_e = \frac{\tau_f'}{G}\left(2N_f\right)^{b_s} \text{..............} \ (1.23a)$$

$$\gamma_p = \gamma_f'\left(2N_f\right)^{c_s} \text{..............} \ (1.23b)$$

Where $\frac{\tau_f'}{G}$ *and* γ_f' are the intercepts on the respective curve and b_s and c_s are corresponding slope. Thus, τ_f' and γ_f' are the shear fatigue strength and ductility coefficient, where b_s and c_s are shear fatigue strength exponent and shear ductility exponent, respectively.

Hence, an analogous of Coffin-Manson equation, Eq. (1.24), for shear strain-life relation can be obtained from Eq. (23a) and (23b).

$$\gamma_a = \frac{\tau_f'}{G}\left(2N_f\right)^{b_s} + \gamma_f'\left(2N_f\right)^{c_s} \quad \text{……………. (1.24)}$$

Similarly, the transition shear fatigue life is:

$$N_t = 0.5\left(\frac{\tau_f'}{\gamma_f' G}\right)^{\frac{1}{(c_s - b_s)}} \quad \text{………..……….(1.25)}$$

1.7 Multiaxial Fatigue Analysis

Unlike uniaxial fatigue where the Coffin-Manson curve has become a standard curve to correlate strain and life, such an established curve does not exist for multiaxial fatigue. In a biaxial fatigue, an axial mode as well as shear mode responses is obtained. The empirical derivation for stresses and strains follow the procedures already presented under section 1.6. However, to develop a correlation between strain or stress and fatigue life, a more involving analysis is required. The magnitudes and directions of the principal stress or strain (normal and shear) need to be properly evaluated and ascertained. Identification of planes on which these principal or maximum values exist may equally be important. Although few planes experience these maximum values, a substantial percentage of the principal stress is experienced by planes oriented ±13° from the loading plane [2]. Then, the principal values is considered as a damage model which can be related to fatigue life in a relation that is based on classical theory or the trend of experimental data. Methods for multiaxial fatigue analysis include stress-based, strain-based, energy and critical plane criteria. Because this study is focused on strain-controlled fatigue, the strain-based approach and critical plane criteria are discussed.

1.7.1 Strain-Based Approach

The strain-based approach is a criterion based on equivalent strain. The method evaluates single strain amplitude that represents all the strains in the component. This single strain is applied as the strain amplitude in the strain-life equation, e.g., Eq. (1.13) or (1.24).

The frequently used equivalent strain methods and their mathematical representations are:

i. The maximum principal strain theory:

$$\varepsilon_{eqv} = \varepsilon_{a1} = \frac{\sigma_f'}{E}\left(2N_f\right)^b + \varepsilon_f'\left(2N_f\right)^c \ldots\ldots\ldots\ldots\ (1.26)$$

ii. Maximum shear strain theory:

$$\varepsilon_{eqv} = \frac{\varepsilon_{a1}-\varepsilon_{a3}}{1+v} = \frac{\sigma_f'}{E}\left(2N_f\right)^b + \varepsilon_f'\left(2N_f\right)^c \ldots\ldots\ (1.27)$$

For each of the methods above, ε_{eqv} is the equivalent strain amplitude while $\varepsilon_{a1}, \varepsilon_{a2}$ *and* ε_{a3} are principal strain amplitudes with $\varepsilon_{a1} > \varepsilon_{a2} > \varepsilon_{a3.}$ The equivalent strain approaches are suitable for proportional loading. They are rarely used for non-proportional loading, as they cannot take into account the extra hardening resulting from this type of loading path.

1.7.2 Critical Plane Methods

The critical plane approaches make use of the experimental observation that cracks often initiate from a preferred plane of loading. The plane where damage begins is either a maximum shear plane or normal plane depending on the material type and loading condition. Thus, fatigue analysis approaches are developed which incorporate this plane and the damage parameter into a model. Several of these models can predict fatigue life and cracking plane-the critical plane- to a reasonable estimation. Some customary critical plane criteria are the Brown-Miller model [14], the Fatemi-Socie (FS) model [15], Smith-Watson-Topper (SWT) criterion [16,17] and Liu model [18,19]. Critical plane approach attempts to give a physical meaning to fatigue damage. It identifies a plane in which stress, strain and cracking parameters are critical (largest). As such, the models are developed based on stress, strain and energy on a particular loading plane. The parameter upon which a model is based influences its ability to make successful life prediction for a particular failure mode. For instance, Brown and Miller's model [14] can hardly account for additional hardening because the damaging parameters are all strains, whereas additional hardening is a stress phenomenon. Meanwhile, the normal stress in the F-S model incorporates the effect of additional hardening [15]. In most fatigue problem involving multiaxiality, the critical plane criteria are widely used because they have shown significant success in addressing multiaxial fatigue problems. The Fatemi-Socie (FS) and the Smith-Watson-Topper criteria (SWT) are two of the several fatigue criteria that have been commonly employed due to their relative success in predicting fatigue life and cracking behavior of alloys to a reasonable estimation [16,18,20–24]. These two criteria are discussed below.

i. Fatemi-Socie (FS) Criterion

The Fatemi-Socie, or FS, model identifies the maximum shear plane as the critical plane. The maximum shear strain amplitude and maximum normal stress on this plane are the damaging parameters in the fatigue process. The Fatemi-Socie criterion is expressed as :

$$\frac{\Delta\gamma_{max}}{2}\left(1+k\frac{\sigma_{n,max}}{S_y}\right)=C \ldots\ldots\ldots\ldots\ldots\ldots\ldots\ldots\ldots\ldots (1.28a)$$

Where $\frac{\Delta\gamma_{max}}{2}$ is the maximum strain amplitude, $\sigma_{n,max}$ is the maximum normal stress. S_y is the material yield stress and k is a material constant which is found by fitting fatigue test data from a uniaxial fatigue test to data from simple torsion fatigue test. In the absence of any test data, $k \approx 1$ [2]. The ratio $\frac{\sigma_{n,max}}{S_y}$ maintains the dimensionless feature of strain. Eq. (1.27a) can be written in terms of shear strain-life properties from fully reversed torsional test [2]:

$$\frac{\Delta\gamma_{max}}{2}\left(1 + k\frac{\sigma_{n,max}}{S_y}\right) = \frac{\tau_f'}{G}\left(2N_f\right)^{b_s} + \gamma_f'\left(2N_f\right)^{c_s} \quad \ldots\ldots\ldots\ldots (1.28b)$$

ii. Smith-Watson-Topper Criterion

The basis for evaluating multiaxial fatigue by the Smith-Watson-Topper (SWT) model damage is a product of maximum normal strain range and the accompanying principal normal stress on same plane. The Smith-Watson-Topper model is given as:

$$\frac{\Delta\varepsilon_1}{2}\sigma_{n,max} = \frac{{\sigma_f}'^2}{E}\left(2N_f\right)^{2b} + {\varepsilon_f}'{\sigma_f}'\left(2N_f\right)^{b+c} \quad \ldots\ldots\ldots\ldots\ldots\ldots (1.29)$$

Where $\frac{\Delta\varepsilon_1}{2}$ is the maximum normal strain range, while $\sigma_{n,max}$ is the maximum normal stress on the maximum strain range plane. ${\varepsilon_f}', {\sigma_f}', b, c \; and \; E$ are fatigue ductility coefficient, fatigue strength coefficient, fatigue strength exponent, fatigue ductility exponent and Young modulus, respectively. These materials constants are evaluated from uniaxial fatigue tests data of the materials being considered.

1.8 Outline of Dissertation

A general background on fatigue has been presented in chapter one. This is necessary to provide the fundamental understanding prerequisite for in-depth discussion and analysis of fatigue behavior. A survey of literature in the subject of fatigue is carried out in chapter two. The literature survey starts with a review of plastic deformation characteristics in metallic alloys. A general review on fatigue of alloys then follows. In the concluding part of the review, a tabular summary is presented of the state of research for the alloys of interest. The objectives and scope of this research work is also defined in the same chapter. Chapter three constitutes material description and the detailed experimental procedure. Equipment and fixtures for testing are stated and the designs of experiments are given. Test specimen preparation details are presented. Thereafter, in chapter four, the experimental results are analyzed and discussed along with the suitability of the application of existing models. Results are presented in tables and analysis illustrated with suitable curves. The final chapter, chapter five, contains the summary and conclusions drawn from the work and recommendation for future work.

CHAPTER 2

LITERATURE REVIEW

2.1 Introduction

A brief background on plastic deformation behavior is presented. It is followed by a general review of the literature on fatigue of metallic alloys; focusing on fatigue behavior of alloys of aluminum, steel and magnesium. The numerous variables that affect fatigue process are highlighted. Relevant criteria or approaches for solving multiaxial fatigue problems are reviewed. Current research data for the three materials of interest are assessed.

2.2 Plastic Deformation in Metallic Alloys

Because the fatigue process in metallic alloys involves inelastic deformation, which depends on the material crystallography, a brief review on the crystal system and their deformation mode is appropriate.

Plastic deformation is an irreversible deformation in metallic alloys. It occurs in crystalline solid materials due to slip and twinning. The former is the major form of deformation in metals and alloys. Twinning occurs for material with few deformation planes. Both deformation mechanisms are function of crystallographic structure of a material. Dislocation happens in a preferred orientation and direction in a crystal. Planes with high atomic density constitute the slip plane, while slip direction is the crystallographic direction that is closely packed with atoms [3] . The slip plane and slip direction constitute the slip system, which differs from one crystal system to another. Crystal structures that are prevalent in metallic alloys and have widely been studied are the cubic and hexagonal structures. These include the face-centered cubic (FCC), body-centered cubic (BCC) and the hexagonal close-packed (HCP), as shown in Fig. 6. For FCC, the slip systems are 12, while BCC have as much as 48. The HCP has the fewest slip system with only three independent slip systems available and mainly restrained to the basal plane [3]. Deformation in this type of material requires the activation of more slip systems or twinning. This is why twinning mechanism is prevalent in HCP.

The foregoing theories concerning crystallographic and deformation have been found to be mostly validated in single crystal metal. For polycrystalline metallic alloys, material microstructure becomes the most plausible parameter that influences the fatigue behavior of alloys. The microstructural feature of any metallic alloy arises from the processing route which include deformation process and heat treatment history. Casting and forging are two primarily route to deforming a metal or alloy to a required shape. These two processes, especially forging, have the potential to bequeath a variety of microstructure to alloys. Forging processes include compression, extrusion and rolling. Subsequent heat treatment alters the microstructure through regeneration of new structure by recrystallization or precipitation. The heat treatment chosen for a particular alloy depends on the alloy composition.

For most aluminum alloys, precipitation heat treatment is commonly deployed. This heat treatment process lead to a material with considerable strength and ductility, both of which depend on temperature and time. Tempering is a major heat treatment process for many magnesium and steel. Magnesium alloys are usually hot-worked. While the vast majority of magnesium components are formed by die-casting, high performance magnesium for structural applications are developed through extruded profiles, rolled sheets and forging [25]. These forming processes bequeath a microstructure with mechanical properties which usually manifest in the form of high strength and ductility.

Alloys of different base metals with different microstructural feature can have comparable strength and/or ductility. Many Such alloys have been studied in monotonic tension. However, several important engineering alloys have still not been studied in fatigue, or the available data with respect to fatigue does not commensurate with its application in area where fatigue is prevalent. Alloys like aluminum-lithium, magnesium-zinc-zirconium system and some kinds of stainless steel have not been extensively investigated in spite of their technological importance. Aluminum-lithium alloys, which also has considerable amount of copper and magnesium, have extensive application in the aerospace industry because of their high-strength-to-weight ratio [26–28]. Magnesium alloyed with zinc and zirconium has a weakened texture which enhances plastic deformation and improves its strength-to-weight ratio [25,29]. Stainless steel has been typically known to have good corrosion resistance due to considerable presence of chromium.

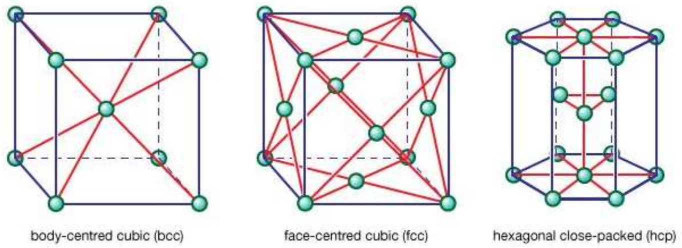

Figure 6: Common metallic alloy crystallography [30].

2.3 Fatigue Behavior of Metallic Alloys

Metallic alloys differ widely in their response to fatigue. A variety of factors, ranging from surface characteristics [31,32], microstructure [33–37], processing [38–40], environment [41], stress-strain level [32] to loading mode and path [42,43], affect the performance of components under fatigue processes. Under multiaxial fatigue, behavior differs considerably from the uniaxial characteristics because the stress state in both differs.

Material structure is an outcome of material processing. The material processing route adopted for a particular alloy may or may not influence its fatigue behavior significantly [38,39]. The dependence of fatigue behavior with respect to processing and material directions in magnesium alloys have been reported [44,45]. A review of the fatigue behavior of wrought magnesium in the form of extrusion, rolled sheet and rolled plate did not show any difference in fatigue behavior [46]. The limited slip system of the Mg alloy, a hexagonal closed-packed (HCP), is attributed to the similarity in behavior.

The vulnerability of large elongated grains to early cracking has been reported by Xiong et al [47] for AZ31B. Twin deformations were observed to be highly concentrated in this grain structure. The small, short grains contain almost no deformation twin. The authors noted that grains orientations are fixed for large grains. As such, during nonproportional loading in which loading axis rotates with time, the possibility of alignment of loading axis and grain orientation is high, thereby increasing the chances of activating more slips. It has been observed that twining contribution to fatigue failure would only occur in a particular plane in AZ31 [48].

De-Feng et al. [49] reported that large and elongated structural particles that are parallel to loading axis in A365 cast aluminum are more susceptible to fatigue cracking. The presence of oxide films and pores due to casting, and silicon inclusion accelerate crack growth in the alloy, especially at the surface. Multiple cracking happened in the nonproportional loading as against the parallel ones in uniaxial loading. The shortest fatigue life was in the out-of-phase 90° loading path due to the rotation of the principal axis [49].

Le et al [50] observed that an Al-Si alloy microstructure with casting porosity has greater detrimental effect on both uniaxial and proportional multiaxial fatigue than is for pure torsional loading. The authors reported that crack initiation mechanism in the loading cases were different. While cracks initiated from pores in the uniaxial and multiaxial cases, the crack in torsional loading began from planes with no evidence of porosity. Effects of microstructural heterogeneity for different types of aluminum alloys have been reported by Deng at al [51] and Huter et al [52].

Besides microstructure, less-controllable but inherent material phenomenon can influence the fatigue behavior of alloys. One such factor is dynamic strain aging (DSA). DSA is a concept of increased flow stress owing to mobile solid atoms repeatedly locking moving dislocation [53]. Stress increases because the dislocations attempts to break loose from the locking by the solute atom or precipitates [54]. It can be implied from published research work that DSA is both strain and temperature dependent concept [53–60].

Dynamic strain aging and its effect on the cyclic behavior of several steel alloys have been extensively reported [54,55,60–64]. Chen et al [61] observed serration-type features in the LCF behaviors of pre-hardening Hadfield steel. It was attributed to an interaction between dislocations and between dislocations induced deformation twins. Isotropic hardening during low cycle fatigue test of A48-type steel was due to the interaction between solute atoms and dislocation [63]. Srinivas et al [60] concluded that decrease in fatigue life observed at comparable low strain amplitude for LCF study of 9Cr-1Mo steel at 300°C was due to DSA effect.

The loading mode in fatigue has substantial influence on the fatigue damage. Four loading modes are frequently considered in multiaxial fatigue: pure axial fatigue loading (tensile-compression), pure torsional cycling, proportional (in-phase loading) and nonproportional (out-of-phase) loading paths. Loading path effects have been the subject of many research works [9,23,65,66]. Nonproportional loading path is extensively reported to be more damaging than the proportional loading mode in a multiaxial fatigue. This effect frequently result to low fatigue life [10,18,20,23,47]. The more damaging tendency of out-of-phase loading is attributed to the activation of more slip planes which causes additional hardening, greater twinning effects and increase in strain energy [18,47]. Shorter fatigue life due to nonproportional loading have also been reported by Shamsaei et al [23] for titanium alloy.

Anes et al. [18] studied the multiaxial fatigue lives of $42CrMo_4$ and AZ31, a BCC and an HCP alloys, respectively in a stress-controlled fatigue experiment. They observed that both alloys have lowest fatigue lives under nonproportional loading at the same equivalent stress, while having their maximum life in pure shear cycling. In between, the proportional loading was less damaging than the pure axial-compression loading for the $42CrMo_4$. However, in the Mg alloy AZ31, both loading paths produced almost the same fatigue life.

The twinning effect in the Mg alloy was attributed to its fatigue mechanism.

A study carried out by Facherie et al [20] on AISI 316L shows that pure torsional fatigue endured more cycles than uniaxial fatigue for the same equivalent strain amplitude. Irregular crack surface present in torsional cycling gave rise to mechanical interlocking causing high friction to slow down crack growth rate in the torsional fatigue test. The nonproportional loading caused reduction in fatigue life by tenfold due to material hardening.

Contrasting results on the effect of nonproportionality was reported by Jahed and Albinmousa [16]. The authors reported that additional hardening due to nonproportional loading observed in multiaxial fatigue study of AZ31B did not show any significant effect on the fatigue life. They suggested that the different mechanism of deformation in magnesium alloys might be responsible for the absence of any detrimental effect on the observed fatigue life in spite of nonproportionality hardening.

The multiaxial fatigue behavior of alloys can also depend on alloy type, loading mode as well as strain level. Cyclic stress-strain history, otherwise known as hysteresis loop, is a common feature in strain-controlled fatigue. Hysteresis loop is a measure of plastic deformation or an indication of the extent of residual cyclic strain or accumulated plasticity. For magnesium and other hexagonal closed pack (HCP) alloys, the hysteresis loop shape can change from being symmetric to asymmetric depending on the strain level [46,47,67]. It was observed the hysteresis loop generated from a fatigue experiment on magnesium alloys changed from symmetric to asymmetric when the strain level was above a certain amplitude in both axial-compression, proportional and nonproportional multiaxial loadings [46,47,67]. However, for cyclic torsion loading, the compression fatigue cycling is asymmetric and independent of strain level. Asymmetric behavior was linked to twinning while the symmetric loop was attributed to de-twinning effect [47,67]. The point at which asymmetry sets in also depends on the phase angle between the axial and torsional phase in the multiaxial cycling [47].

Many theories developed for material behavior in the monotonic regime under static loading have been extended to solve multiaxial fatigue problems. These include the Tresca, Von Mises and Rankine theories. The weakness and strength of these theories are summarized by Fatemi and Socie [15]. This includes their inability to handle nonproportional loading. The absence of established curve fit, like the Coffin-Manson, for correlating fatigue life with applied strain has led to several models being proposed to predict the fatigue life of components. Fatigue criteria are fatigue equations developed from trend of fatigue data or physical observation of fatigue characteristic of materials in order to model the constitutive behavior of materials. Some of these models were already reviewed under sections 1.7.

Several fatigue criteria have been compared and tested for different alloys and the results show that the level of applicability of each model to an alloy varies [68,69]. Fifteen known fatigue criteria were used by Lei et al [69] on two hundred and twenty-five fatigue data for 304L stainless steel. Most of them correlate experimental data well with the prediction in uniaxial situation, but fail when applied for multiaxial fatigue life prediction.

Jahed and Albinmousa [46] shows that a two-parameter energy model is capable of good correlation for experimental fatigue data from wrought magnesium alloys regardless of loading conditions and processing method. This conclusion was reached from analyzing 354 different fatigue tests data for different magnesium alloys.

The investigation of three fatigue criteria, namely, Smith-Watson-Topper (SWT), Fatemi-Socie (FS) and Jiang models on AISI 316L by Facheris et al. [20] gave an acceptable level of prediction by SWT and FS for the proportional loading and axial tension-compression loading. The Jiang model made the best correlation between the experimental data and prediction for all loading path investigated because of its ability to take into account all stresses and strains contributions.

Farahani's energy-critical plane fatigue model [65] considers the summation of the normal energy range and the shear energy strain range calculated from the critical plane on which Mohr's circle of stresses and strains are the largest. The model gave a good correlation for multiaxial data from several materials both in the high cycle life (HCF) and in low cycle fatigue (LCF) because of its ability to take into account mean stress effect and strain-dependent hardening.

Even with relative success of some fatigue criteria to produce good correlation between experimental data with prediction for several materials and loading conditions, yet no single model or parameter is successful in all loading conditions and materials. Hence, modifications in existing models are performed in order to make reasonable prediction for fatigue life of alloys, especially under nonproportional loading.

A modified SWT model was applied by Xiong et al [47] to predicts the fatigue life of AZ316A. The proposed modified model is presented in the form:

$$FP = 2b\Delta\varepsilon\langle\sigma_{max}\rangle + \frac{1-b}{2}\Delta\tau\Delta\gamma \ldots\ldots\ldots\ldots\ldots\ldots\ldots\ldots\text{(2.1)}$$

FP is fatigue (damage) parameter; σ and τ are normal and shear stresses on a material plane; ε and γ are the corresponding normal and shear strains; Δ represents the ranges of these parameters and b is a material-related constant ranging between 0 and 1.0. When the value of b is unity, FP reverts to the original SWT parameter. The Mac-Cauley bracket ‹› is used such that the damage parameter remains positive. The term within it is defined as follows: $\langle x\rangle = 0.5(x + |x|)$. The author observed that the ability of the model to predict cracking behavior is dependent on the choice of value for *b.*

A multiaxial damage parameter proposed by Sun-Shang-Bao [70] showed a good correlation for multiaxial fatigue behavior of several alloys. The damage parameter which itself is a modification of SWT parameter is given as:

$$\frac{\Delta\varepsilon_{eq}^{*}}{2} = \left(\varepsilon_{n}^{*2} + \frac{v_{eff}(2-v_{eff})}{(1+v_{eff})^{2}}\left(\frac{\Delta\gamma_{max}}{2}\right)^{2}\right)^{1/2} \ldots\ldots\ldots\ldots\ldots\ldots\text{(2.2)}$$

Where $\Delta\varepsilon_{eq}^{*}$ and ε_{n}^{*} are the equivalent normal strain range and normal strain excursion in the maximum shear plane. v_{eff} is the effective Poisson's ratio. The combination of the normal and shear strain as a damage parameter is derived from the increment observed in these parameters due to additional hardening during nonproportional loading.

Li et al [42] proposed a modified form of the Sun-Shang-Bao's model [70] in order to improve its life prediction capability for nonproportional loading. The author noted that the normal strain excursion ε_{n}^{*} in the earlier model could not account for the additional cyclic hardening. Hence, they proposed a model in which a stress term was introduced to achieve the form given below:

$$\frac{\Delta\varepsilon_{eq}^{cr}}{2} = \sqrt{\frac{3-v_{eff}}{4(1+v_{eff})}\left(\frac{\Delta\gamma_{max}}{2}\right)^2 + \frac{\sigma_{n,max}}{\sigma_{n,a}^{pro}}\left(\frac{\Delta\varepsilon_n}{2}\right)^2} = \frac{\sigma_f'}{E}\left(2N_f\right)^b + \varepsilon_f'\left(2N_f\right)^c \text{ ...(2.3)}$$

Where $\varepsilon_f', \sigma_f', b, c\ and\ E$ are same as defined for Eq. 1.1a and 1.2. v_{eff} is the effective Poisson ratio, $\Delta\varepsilon_{eq}^{cr}$ is strain range on the critical plane, $\sigma_{n,a}^{pro}$ is the in-phase normal stress amplitude. The authors [42] tested the model on sixteen experimental data. It was reported that reliable fatigue life prediction was achieved for both proportional and nonproportional loadings.

Anes et al. [71] proposes a stress scale factor (ssf) whose value is constant for proportional loading but varies with stress amplitude and loading path in nonproportional loading. The proposed factor led to the formulation of a new equivalent shear stress, which accounts for the changing ratio of stress under this condition. The new equivalent shear stress, τ_{eqv}, is defined as:

$$\tau_{eqv} = \max(\tau_a + ssf(\lambda, \sigma_a).\sigma_a) \text{..................(2.4)}$$

Where $\tau_{eqv}, \tau_a, \lambda,\ and\ \sigma_a$ are the equivalent shear stress, shear stress amplitude, stress ratio and normal stress amplitude, respectively. The new equivalent stress as damage parameter was satisfactorily applicable to both proportional and nonproportional loading.

In spite of their prediction capability, many critical plane models contain material constants that needed to be evaluated by experiments other than the multiaxial fatigue. For instance, FS model [15] requires a uniaxial experiment to determine shear yield. Multiaxial life prediction based on uniaxial fatigue properties obtained from tensile testing data have been demonstrated by Shamsei and McKelvey [22] using three different prediction methods, namely, Muralidharan–Manson, Bäumel–Seeger, and Roessle–Fatemi.

Life prediction tools based on models or theoretical approach other than critical plane have also been assessed elsewhere [72,73]. Finite element analysis has proved to be a useful tool for fatigue analysis in complementing experimental fatigue [21,42,68,74–77]. Muhammed Pour et al. [21] carried out fatigue life prediction for riveted aluminum joint using finite element modeling. The result compared well with the life prediction obtained for same components based on FS and SWT models.

Reliable fatigue life prediction criteria for materials and components would depend on the homogeneous and consistency of the multiaxial fatigue data used and fatigue data must reflect the service performance of the material [78].

Few works have related crystallographic structure of materials to multiaxial fatigue behavior because of the involving analysis required and expensive experimental set up. A study to relate material crystallography to reduction in fatigue lives was carried out by Itoh and Sakane [9] and Itoh and Yang [43] wherein they proposed a nonproportional factor to reflect the severity of nonproportional loading and the material influence on the degree of life reduction due to nonproportional loading. The material fatigue parameter proposed is:

$$\alpha^* = \begin{cases} 0.8\alpha + 0.1, \ for\ FCC \\ 2(0.8\alpha + 0.1), \ for\ BCC \end{cases} \quad \text{.............(2.5)}$$

Fatigue constants so obtained were implemented on several FCC and BCC alloys and the result returned a fair correlation between experimental fatigue data and calculated life. Additional hardening was noted to have a close relation to the reduction in life in the tested materials. They attributed this to the materials deformation characteristic that is dependent upon material crystallography. Sakane et al [79] reported that substructural damage during fatigue can be directly related to microstructure. They observed that dislocation cells, dislocation bundles, twins and stacking faults are involved in the damage process.

Several crack growth paths can be encountered in fatigue. The method of crack growth in many materials depends on the loading mode and the material. For tensile loading, the cracks are usually deeper, growing perpendicular to the axis of loading. On the other hand, a shallow crack growing along the axis of loading is found most in shear loading [15]. Cracks usually initiate from discontinuities and inclusions such as those in welded product [80,81] . Using models to predict cracking behavior is much more difficult than to predict fatigue life. A model can reasonably predict a crack mode if its damaging parameters is of same type as the material cracking behavior. Fatigue life developed with shear parameters would correctly predict only shear cracking [47].

Gao et al [24] observed that FS and Jiang model were unsatisfactory in the prediction of crack plane for pressure vessel steel 16MnR, which cracked in tensile mode. They observed shear cracking under torsional load while the cracking was tensile in nature in a tension-compression loading. The 90° out of phase showed a cracking similar to the uniaxial tensile loading mode.

Anes et al. [18] showed that different loading paths resulted in almost same cracking behavior and surface topography for a FCC and HCP alloys. The topography in each cracked contained a fatigue zone and fracture zone. The change in topography was the result of different fatigue mechanism.

Mikheevskiy et al [82] modelled the fatigue crack growth in fatigue process as blunt notch with tip radius ρ^*. The results of simulation show that the formulation can estimate fatigue crack growth in both constant and variable amplitude loading.

The foregoing review has revealed the complex subject of both uniaxial and multiaxial fatigue and the difficulty in predicting life and crack behaviour of material. While models are widely used as life predicting criteria, it is also readily obvious that the fatigue behaviour is strongly dependent on material crystallography and microstructure. It appears, however, that much attention was devoted to life prediction without providing a material-based explanation for fatigue behaviour. Therefore, work is required to arrive at an explanation of fatigue behaviour of materials with respect to microstructure. To the best of our knowledge, no work has investigated the torsional, axial and multiaxial fatigue behaviour of three different alloys of important engineering materials such as stainless steel, aluminium alloy and magnesium alloy.

More so, while fatigue behavior of several aluminium, steel and magnesium alloys have been studied widely and their data readily available, fatigue data for several others important alloys of engineering significance such as aluminum –lithium, stainless steel and magnesium-zirconium-zinc alloys are scarce. Hence, the need to qualify and quantify their fatigue behavior and fatigue related constants is necessary. Three important engineering alloys whose fatigue data are largely unavailable are AW2099-T83 Aluminum-Lithium, ZK60A magnesium alloy and AISI 410 stainless steel. Aluminium-lithium, in particular, is an established alloy in the aerospace industry because of its high specific strength [83–86].

The specific weight characteristic of aluminum-lithium is due to addition of lithium (Li). An addition of one-percent Li to Al decreases the latter weight by 3% while increasing the modulus of elasticity by 6% [87,88]. Li et al. [89] observed that the simultaneous addition of Li above 1% and copper (Cu) up to 3.66% in Al-Cu-Li alloy can greatly improve its strength.

In spite of its high specific strength, historical development shows that there were challenges in the properties of Al-Li which limited its usage at early stage of development [83,90]. Consequently, Al-Li alloy has undergone several developmental stages resulting in different forms and generations of the alloy. The development of the first generation of the alloy started in 1920, but it was not until the 1950's that it was first put into use in the form of Al-Li 2020. The second generation which includes Al-Li 2020, 2090, 2091, 8090 and 8091 alloys spanned over three decades [26,83,85,88]. Up to the mid 90's when the second generation is thought to have reached maturity, challenges such as prohibitive cost, poor fatigue performance, low fracture toughness, poor corrosion resistance and high anisotropic behavior were encountered [83,85,90,91]. These drawbacks limited the application of Al-Li alloy in the aircraft industry. However, with further research and development, a third generation of the alloy with better corrosion resistance, fatigue crack growth performance, better mechanical strength and toughness has been introduced [85,90,92].

The key feature of the third generation is that it contains less than 2% Lithium (Li); the earlier generation has Li content up to 2.7%. It was projected that the new generation of Al-Li alloy may find application in numerous body parts of airplanes such as the fuselage skin, wing, doors, windows, etc. [85,88].

The aerospace industry is such an engineering field where combinations of high strength but low weight materials are required. Any alloy that demonstrates high strength to weight ratio is thus sought after. The transportation industry in general requires these types of alloys for low fuel consumption and high efficiency. For this reason, light weight metals such as aluminum and magnesium alloys are now forming the significant parts of ground vehicles, like the wheel, axle and engine blocks [67,81].

Steel is traditionally known for its high strength. AISI 410 steel has good corrosion resistance and is used in the construction of plastic molds, screws for extruder, valves, shafts, bearings and blades in compressors and turbines [93–95]. Ships and oil rigs and exploration platforms are built with various steel alloys [4]. Pressure vessels, fuel and gas tanks, wind tunnel compressor blades and wheels, aircraft landing gears, horizontal stabilizers are major components built with steel alloys [4]. These components experience one type of fatigue load or the other. Major failures that have occurred in them are linked to fatigue [4].

A survey of fatigue data for Aluminum-lithium, ZK60A and AISI 410 alloys in published literature shows that not much is available in the field of fatigue, as can be seen in Table 1. Therefore, available fatigue information for these alloys does not commensurate their applications in engineering structures where fatigue is significant. As such, the fatigue design and characterization of these materials are important. Fatigue properties such as load-dependent life cycles, crack behavior, stress or/and strain response and material constants as will be required for use in certain fatigue models and engineering design are therefore necessary for these materials. Therefore, these define the objectives of the present work.

Table 1: Summary of fatigue data for AW2099-T83, ZK60A and AISI 410 alloys.

			Properties determined			
Material	**Material Form**	**Microstructure**	**Fatigue test**	**Fatigue constant**	**Fatigue life**	**Reference**
AW2099-T83	Extrusion and ISP	Grain structure	None	None	None	[96–98]
AW2099-T83	Extrusion	Grain structure	Fatigue crack growth study	None	None	[99]
ZK60A	Extrusion	Grain structure	Uniaxial LCF	None	Yes	[100]
ZK60A	Extrusion	Theoretical grain structure	Theoretical fatigue study	Twinning-detwinning	None	[101]
AISI 410	NA	None	Biaxial	None	Yes	[43]

2.4 Objective and Scope

The main objectives of this work are outlined as follows.

1. Conduct a microstructural characterization for AW2099-T83 aluminum-lithium alloy, ZK60A magnesium alloy and AISI 410 stainless steel alloy.
2. Conduct tensile and torsional monotonic tests for three different metallic alloys to determine mechanical properties that are required in fatigue behavior analysis.
3. Conduct uniaxial and multiaxial fatigue experiments under different loading paths on AW2099-T83 aluminum-lithium alloy, ZK60A magnesium alloy and AISI 410 stainless steel alloy.
4. Study strain variation effect on each alloy and analyze their responses under axial, torsional and multiaxial proportional and non-proportional loading paths.
5. Investigate crack profile for each of the alloys in torsion and multiaxial fatigue.
6. Provide an analysis for the damage mechanism in each of the representative alloys through qualitative examination of the damaged surface using SEM.
7. Test existing fatigue models on experimental data in order to evaluate which model is best suited for a particular microstructure.

This set of objectives will be achieved through careful planned experimental program and results analysis.

CHAPTER 3

MATERIALS AND EXPERIMENTAL DETAILS

3.1 Materials

The three metallic alloys investigated in this work are AW2099-T83 aluminum-lithium alloy, ZK60A magnesium alloy and AISI 410 stainless steel. Table 2 gives the information about the dimensions and the shape of the as-received materials. The aluminum-lithium was acquired from Smiths Metal Centres Ltd, UK, while the Magnesium alloy was acquired from Russia and the stainless steel was purchased from advanced precision system, Dammam, Saudi Arabia. The chemical compositions of the alloys are shown in Table 3. The composition for AW2099-T83 and AISI 410 are obtained from the mill certificates provided by suppliers while that of ZK60A is as per ref [91]. Subsequent reference to the alloys will be by their codes; AW2099-T83 for the Aluminum-Lithium, ZK60A for Magnesium alloy and AISI 410 for the stainless steel.

3.2 Characterization of Microstructure

Specimens of sizes about 6 mm by 6 mm for metallographic analysis were cut with abrasive saw from specific locations in the transverse direction (T's) and the extrusion direction (E's) of the billets and rod as shown in Fig. 7. All samples were securely mounted on plastic holders using hot mounting process for AW2099-T83 and AISI 410, while ZK60A was cold mounted. Each of the samples was polished in succession with 240, 320, 400 and 600 grit size abrasive papers. AW2099-T83 was given final polishing with diamond paste of 9, 6, 3 and 1-micron sizes to obtain mirror-like surfaces. To achieve the same surface finish for ZK60A and AISI 410, alumina powder of 5 and 3 microns were used. AW2099-T83 specimens were etched in a solution of 10 g sodium hydroxide in 100 ml of water by immersion for 40 seconds. AISI 410 samples were etched by swabbing for 40 seconds with a solution containing 5 ml of HCl acid and 1 g of picric acid in 100 ml of ethanol. ZK60A was etched in a solution made from 5g of picric acid, 5 ml of acetic acid, 10 ml of water and 100 ml of ethanol. Etched samples were observed with Meiji optical microscope equipped with Image 3 camera. The metallography and all subsequent mechanical testing are conducted on as-received condition.

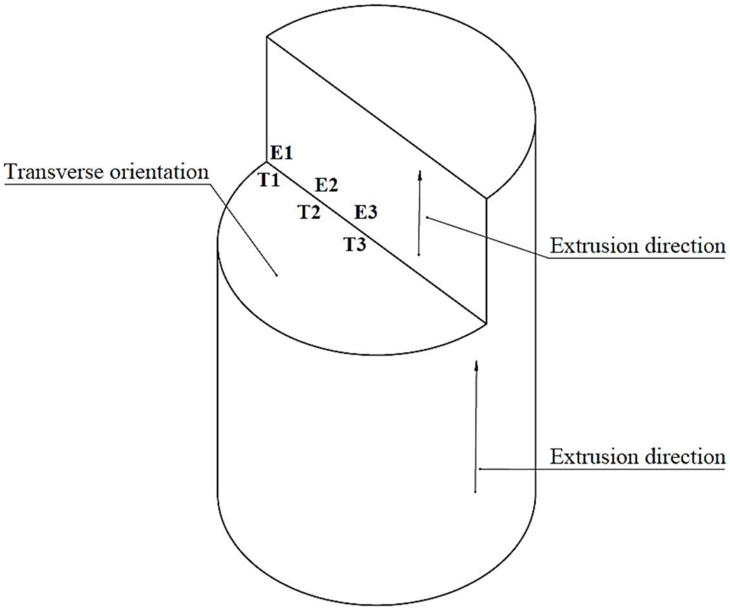

Figure 7: Locations of sample for metallographic analysis.

Table 2: Alloys dimension and geometry.

Materials	Geometry	Diameter (mm)	Length (mm)	No of pieces
AW2099-T83	Extruded billet	150	1000	1
ZK60A	Extruded billet	150	1000	2
AISI 410	Extruded rod	25.4	1000	24

Table 3: Alloys Chemical Compositions.

Alloys	Elements (%wt)													
	Cr	**Al**	**C**	**Cu**	**Fe**	**P**	**Li**	**Mg**	**Mn**	**Si**	**S**	**Ti**	**Zn**	**Zr**
AW2099-T83		94		2.7	0.02	-	1.8	0.29	0.3	0.02		0.03	0.7	0.1
ZK60A								95					4.5	0.5
AISI 410	12.1		0.11	-	86.7	0.018	-	-	0.7	0.33	0.002			

3.3 Monotonic Tests

3.3.1 Tensile Testing

Tensile tests were conducted on the three alloys using Instron 5569 tensile test machine (Fig. 8). Test specimens were machined parallel to the extrusion direction according ASTM E8-08 Standard [102], resulting in a gauge length of 25.0 mm and a gauge diameter of 6.0 mm (Fig. 9). Tests were conducted following the same standard [102] with a crosshead speed of 2 mm/min. Extensometer with 12.5 mm gauge was used to measure strains up 1% after which it was removed and the piston displacement was considered for the rest of test. Resultant force and strain data, which are automatically recorded in the computer during the test, are analyzed to determine the tensile properties of the alloys. A minimum of five specimens were tested for each alloy type.

Figure 8: Instron Tensile Testing Machine.

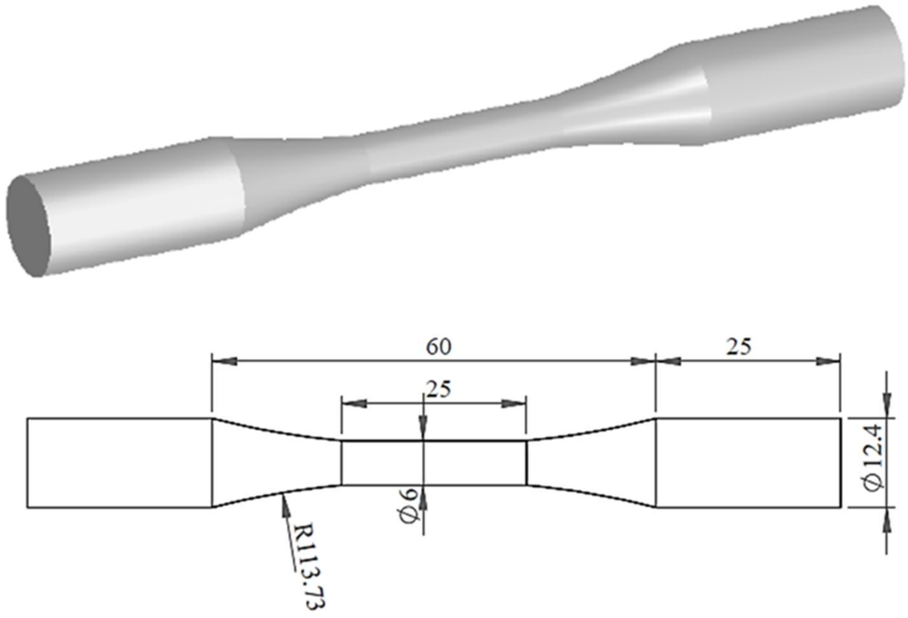

Figure 9: Tensile test specimen (All dimensions in mm).

3.3.2 Shear (Torsion) Testing

Smooth tubular specimens (Fig. 10) machined parallel to the extrusion direction were used for monotonic torsion test as per Albinmousa [103]. The inner and outer surface of the test specimens were polished and honed to achieve an average roughness of 0.16 micron. The torsion tests were performed at the rate of 0.2 deg./sec on 50-KN capacity MTS 810 universal testing machine (Fig. 11). During the tests, the axial force was maintained at zero to ensure that test specimens were not axially loaded. One to two specimens each were tested in torsion for each of the alloy.

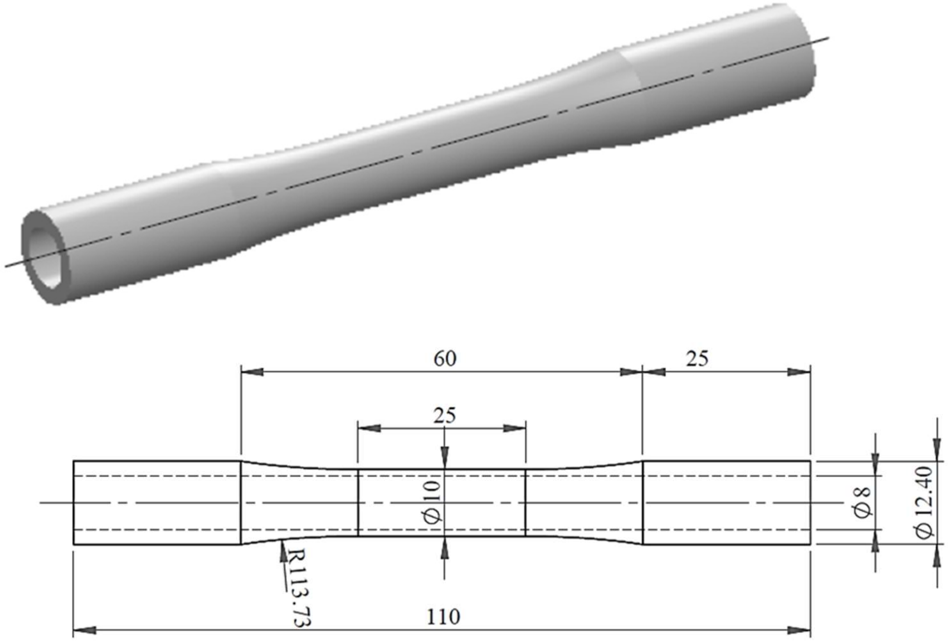

Figure 10: Tubular specimen for cyclic torsion and multiaxial fatigue tests (All dimensions in mm).

Figure 11: MTS 810 universal testing machine.

3.4 Uniaxial Fatigue Tests

3.4.1 Cyclic Axial Test

Strain-controlled tension-compression tests were conducted as per ASTM E606-12 Standard [12] on solid specimens (Fig. 12) of the three alloys on an Instron servo-hydraulic test frame with a load capacity of 100 KN at Westmoreland Testing facilities in the United Kingdom. The solid specimens were prepared on a CNC machine with aerospace certified coolant. Gauge sections were machined in one pass for a uniform profile. This was followed by three-stage polishing with aluminum oxide abrasive belts of grades P240 (59 μm), P400 (39 μm) and P800 (22 μm), respectively. During polishing, the specimen rotates at about 3-4 rpm while belt running speed was about 50-70 mm/min and forward speed was 12-16 mm/min. AW2099-T83 and ZK60A were machined with smooth grip, while AISI 410 was threaded because of its higher stiffness. Alignment cells were used on test fixture to minimize off-axis load and incidence of buckling. The extensometer used has a gauge length of 11 mm. Table 4 represents the test matrix for the applied strain amplitudes for the three alloys. All strain amplitudes were duplicated. The command waveform for all cyclic tests is sinusoidal. All tests were conducted at a frequency of 1 Hz. A total of forty tests was conducted. Completely reversed strain amplitudes (strain ratio, R= -1) were used in all the cyclic tests (axial, shear and multiaxial).

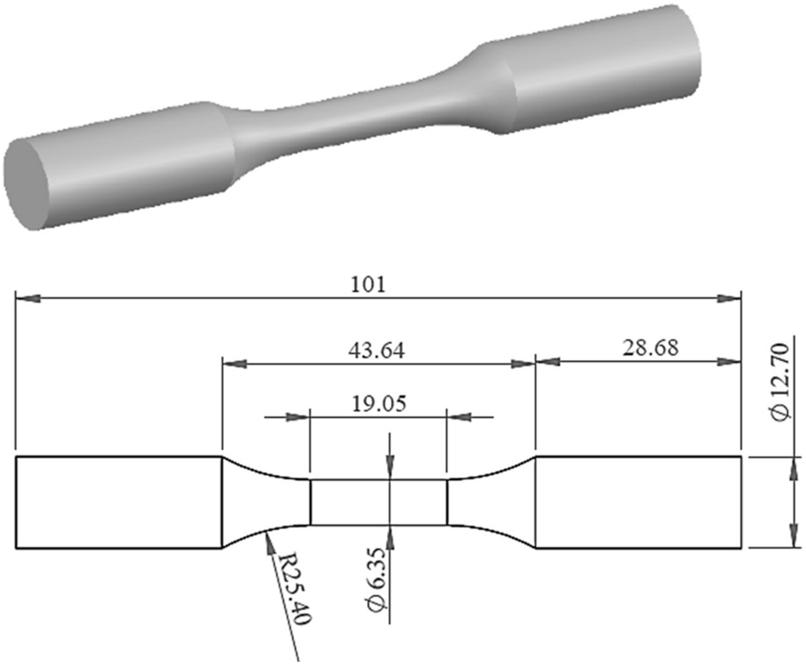

Figure 12: Cyclic axial test specimen (All dimensions in mm).

Table 4: Test matrix for cyclic axial test.

Materials	**Strain amplitude $\frac{\Delta\varepsilon}{2}$ (%)**							
AW2099-T83	0.3	0.4	0.5	0.6	0.7	-	-	-
ZK60A	0.28	0.3	0.35	0.4	0.5	0.6	0.7	0.8
AISI 410	0.3	0.4	0.5	0.6	0.7	0.8	0.9	-

3.4.2 Cyclic Torsion Test

Strain-controlled torsional fatigue tests were performed on the three alloys using the tubular specimen in Fig. 10, according to ASTM E2207-08 [11] guideline for multiaxial fatigue testing with modification to fit cyclic torsion test. Tubular specimens are utilized for torsional tests to enable uniform distribution of stress across its thickness.

The preparation of the specimens was already discussed in section 3.3.2. Using the ASTM E2207-08 standard for cyclic torsion test, the cyclic axial mode of the machine is switched to zero load. The test was carried out on an Instron 8874 fatigue-testing frame (Fig. 13(a)) with a torque capacity of ±100 Nm. A total of twenty-nine tests were conducted. Frequencies were varied to reduce testing time especially at low strain amplitudes. The applied shear strain amplitudes and frequencies are presented in Table 5. All tests were conducted at a strain ratio of -1.0. One to three tests were performed for each strain level and tests were stopped when the torque dropped to 50% of its maximum-recorded value during cycling.

Table 5: Test matrix for cyclic torsion test.

AW2099-T83		**ZK60A**		**AISI 410**	
Strain amplitude $\frac{\Delta\gamma}{2}$ (%)	**Freq. (Hz)**	**Strain amplitude $\frac{\Delta\gamma}{2}$ (%)**	**Freq. (Hz)**	**Strain amplitude $\frac{\Delta\gamma}{2}$ (%)**	**Freq. (Hz)**
0.5	0.35	0.4	0.5	0.5	0.4
0.6	0.3	0.6	0.4	0.7	0.3
0.7	0.25	0.8	0.3	1.5	0.1
0.75	0.2	1.0	0.3	-	-
1	0.1	1.3	0.2	-	-
1.5	0.06	1.5	0.1	-	-

3.5 Multiaxial Fatigue Tests

Multiaxial fatigue tests were conducted on the three alloys according to ASTM 2207-E08 [11] using similar tubular specimen shown in Fig. 10, on Instron 8874 biaxial fatigue machine (Fig. 13(a)). Biaxial extensometer, in Fig. 13(b), capable of measuring both axial and torsional strains was used to record strain data. Applied strain amplitudes were achieved by selecting a constant strain amplitude which is normalized by the yield strain of each alloy in monotonic tensile and torsional tests according to Eq. 3.1.

$$\varepsilon = \frac{\varepsilon_x}{\varepsilon_{ys}} \ldots\ldots\ldots\ldots\ldots\ldots\ldots\ldots\ldots (3.1a)$$

$$\gamma = \frac{\gamma_x}{\gamma_{ys}} \ldots\ldots\ldots\ldots\ldots\ldots\ldots\ldots\ldots (3.1b)$$

Where ε and γ are the normalized applied axial and shear strain amplitudes, ε_x and γ_x are any selected strain level, and ε_{ys} and γ_{ys} are the corresponding strains at yield point in monotonic tests. This normalization is done on the account that the materials have different yield strengths. The investigated biaxial strain amplitudes are illustrated in Table 6 for both proportional (0° in-phase) and non-proportional (90° out-of-phase) loadings. A total of sixteen tests were conducted under multiaxial fatigue.

Table 6: Test matrix for multiaxial fatigue test.

Alloys	**AW2099-T83**		**ZK60A**				**AISI 410**	
Phase angle	0°	90°	0°	90°	0°	90°	0°	90°
Axial strain amplitude (%)	0.53	0.53	0.32,	0.32,	0.43	0.43	0.30	0.30
Shear strain amplitude (%)	0.66	0.66	0.40	0.40	0.40	0.40	0.42	0.42
Axial strain amplitude (%)	0.53	0.53	0.32,	0.32,	0.43	0.43	0.30	0.30
Shear strain amplitude (%)	0.76	0.76	0.46	0.46	0.46	0.46	0.48	0.48

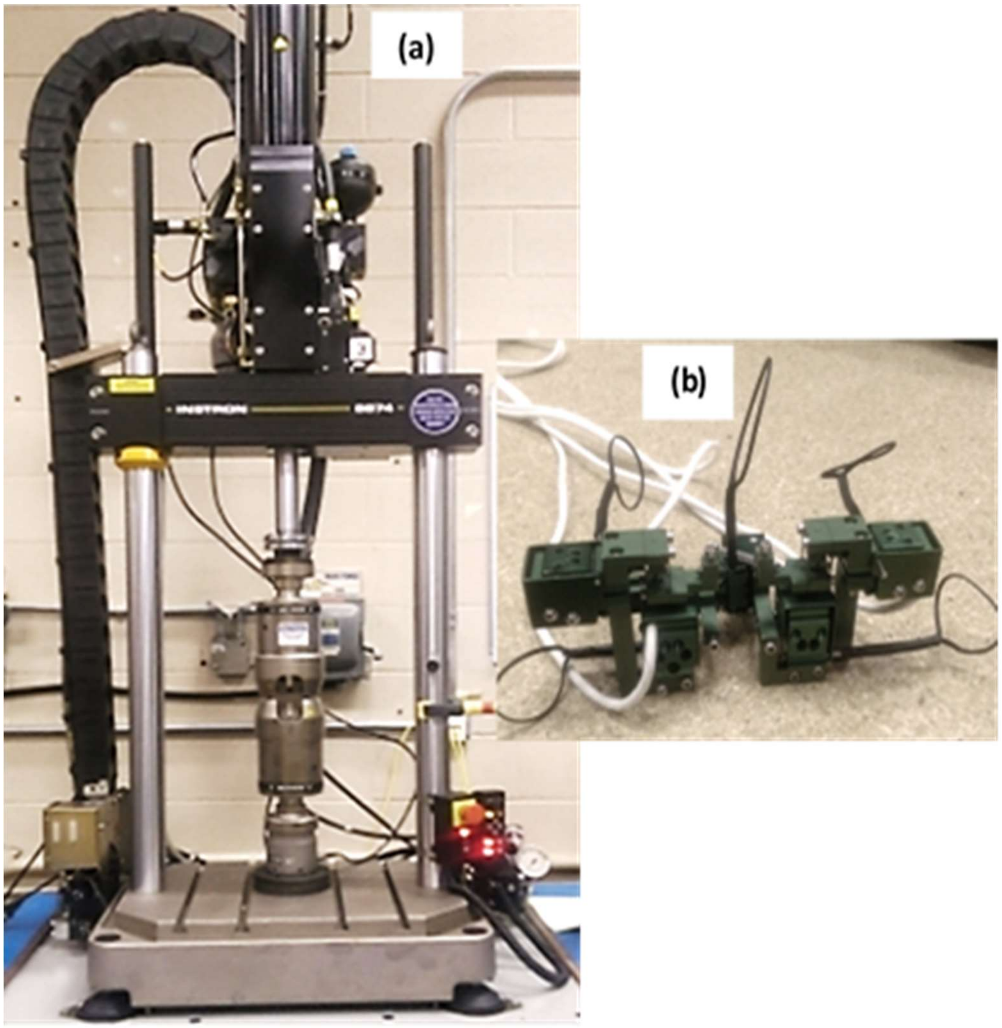

Figure 13: Biaxial testing facilities: (a) Instron 8874 Biaxial fatigue machine, (b) Biaxial extensometer.

CHAPTER 4

RESULTS AND DISCUSSION

4.1 Introduction

The results obtained from the series of tests described in the preceding chapter are presented and discussed in this chapter. Characterization of microstructure, which entails grain structure and grain size, is presented first. Both tensile and torsional mechanical properties, which include ultimate tensile strength, yield strength, elastic modulus, shear modulus and plastic flow coefficients, etc., are given. In the result for fatigue, fatigue life and various stress responses, which include peak stresses and mean stresses from the different fatigue tests are presented and discussed. Finally, fatigue tested specimens with fractured surfaces and cracking are presented and explained. The approach to presentation of results is by discussing specific observations from each test for each alloy. Then a final remark that is generally comparative is given.

4.2 Characterization of Microstructure

Microstructure is an outcome of material processing that includes deformation and heat treatment process for metallic alloys. Besides composition of alloys, microstructure has the most significant influence on alloys behavior; it determines the properties of alloys. The microstructures of the three alloys in the orientations shown in Fig. 7 are presented and discussed in this section.

4.2.1 AW2099-T83 Alloy

Figure 14(a) represents the optical metallographs of the microstructure of AW2099-T83 in the different orientations and locations. The microstructure at T1 location in the transverse orientation is composed of small grains of about 10 µm and large grains of about 40 µm. Grains at locations T2 and T3 are almost equiaxial and smaller than those near the edge of the extrusion. Thus, grain size becomes smaller in the direction towards the center in the transverse orientation. Grain structures similar to T1 were reported by Jata and Starke [104]. The large grains are unrecrystallized grains, while the smaller grains are recrystallized grains following solution heat treatment [96,104]. Unrecrystallized grains were reported for similar materials and were attributed to dynamic recovery and the presence of Al_3Zr [98,99]. It has been reported that a recrystallized grain is undesirable for this type of alloy as it degrades its mechanical property, particularly the resistance to fatigue crack growth [99,104].

The grains along the extrusion direction are unrecrystallized and elongated in the direction of extrusion. This is mainly due to the strain imposed by the extrusion die on the side of the billet. Similar grain structure is reported by Lin et al [97] for similar material. Nonetheless, elongated grain is the primary grain in aluminum alloys following hot working owing to their high stacking fault energy [98]. Sub-grains become more noticeable in the region towards the center along the extrusion direction. Variation in grain structure and size in different orientations have been reported by a number of researchers for similar material [96–98,105]. Homogenization heat treatment and aging process can significantly influence the microstructure and, by extension, the mechanical behavior of AW2099-T83 alloys [97,106,107]. Average grain sizes measured for AW2099-T83, using linear intercept method, are given in Table 7.

4.2.2 AISI 410 Alloy

Figure 14(b) shows the optical metallographs of the microstructure of AISI 410 stainless steel alloy. It is worth mentioning here that samples for metallography of AISI 410 were taken from the edges (T1, E1) and centers (T3, E3) of the rod on account of the smaller diameter compared to AW2099-T83 and ZK60A. The microstructure is a tempered martensite structure, as it is common with quenched steels. Martensitic structure is known to give high strength to steel. The structure compares to a hardened and tempered AISI 410 steel reported by Krishna and Bandyopadhyay [95]. No significant difference is observed both in the structure and grain sizes of the steel in both orientations. A grain size of about 5 μm, recorded in Table 7, was obtained by linear intercept method. The darker areas are regions of retained austenite which did not transform to martensite during the diffusionless transformation process. Heat treatments and electrochemical processes can be used to achieve different dimensions of martensitic structure for the alloy [93,108].

4.2.3 ZK60A Alloy

Microstructures for ZK60A are presented in Fig. 14(c) for similar orientation as for AW2099-T83. The variations in structure and grain sizes are obvious both in orientations and in locations, especially in the extrusion direction. The structures in the transverse orientation appear coarse and are mostly equiaxed. Similar observations were reported for ZK60A by Xiong et al [109]. There is the presence of twin structures in the transverse orientation. The grain in the extrusion direction close to the surface, i.e. E1, is a combination of large and small grains and with some twin structure. However, towards the core, at E2, some of the grains are elongated in extrusion direction. No twinning is observed in this location. Grain sizes measured using linear intercept are presented in Table 7.

The results of microstructure presented here will be applied to explaining the cyclic behavior of the alloy in terms of stress evolution and hysteresis loops. The fracture mechanism and cracking behavior of the alloys will also be explained from the alloy microstructure.

Table 7: Average grain size for the three alloys.

Average grain sizes (µm)						
Location	**T1**	**T2**	**T3**	**E1**	**E2**	**E3**
AW2099-T83	40 ± 1.68	8.4 ± 1.47	6.6 ± 1.53	12.6 ± 2.09	7.24 ± 1.83	7.74 ± 1.55
AISI 410	5± 1.5					
ZK60A	18 ± 1.4	24 ± 1.35	45 ± 2.5	10.7-13.8 ± 2	46-180 ± 10	

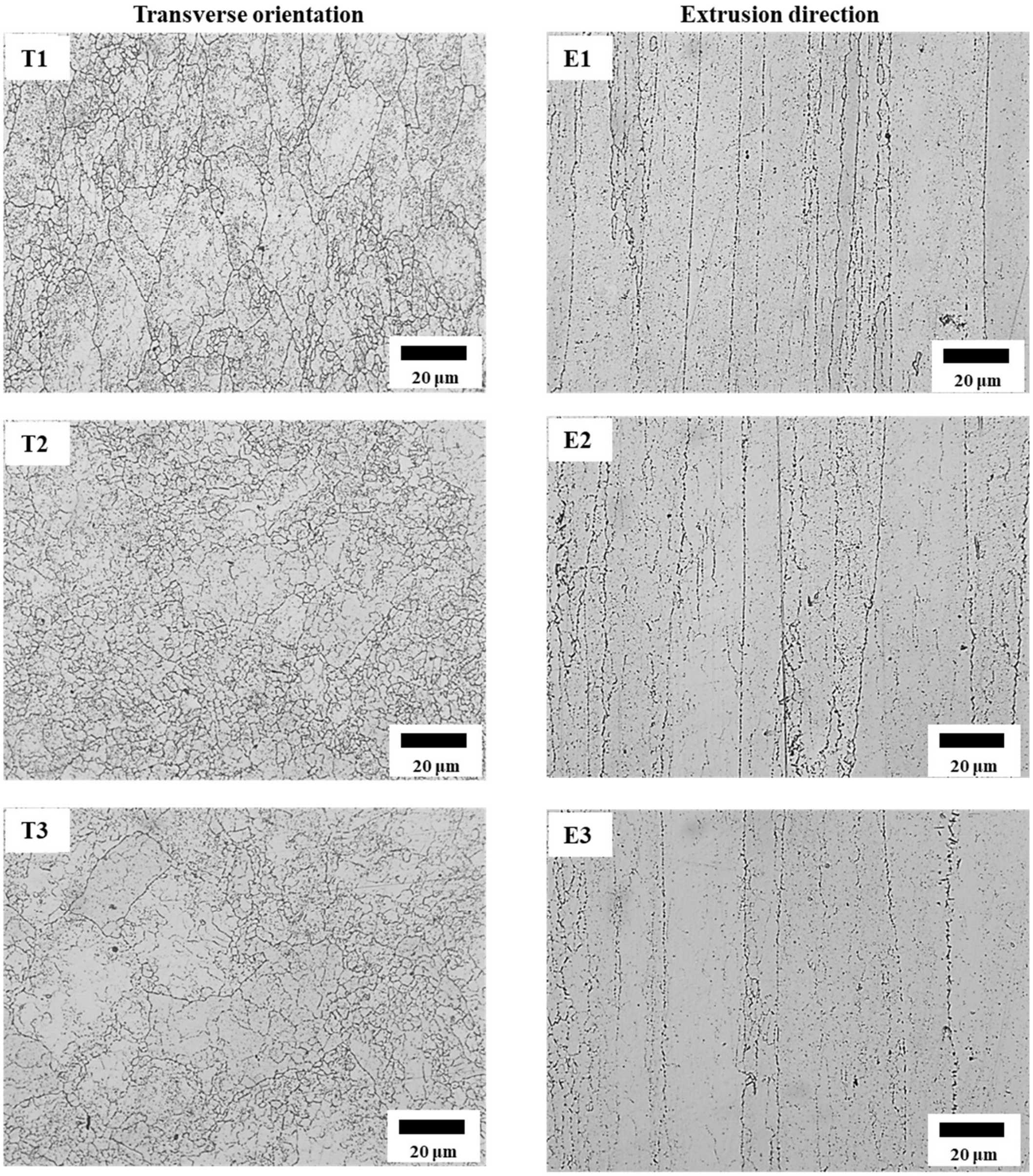
Transverse orientation
Extrusion direction
T1
20 µm
E1
20 µm
T2
20 µm
E2
20 µm
T3
20 µm
E3
20 µm

(a)

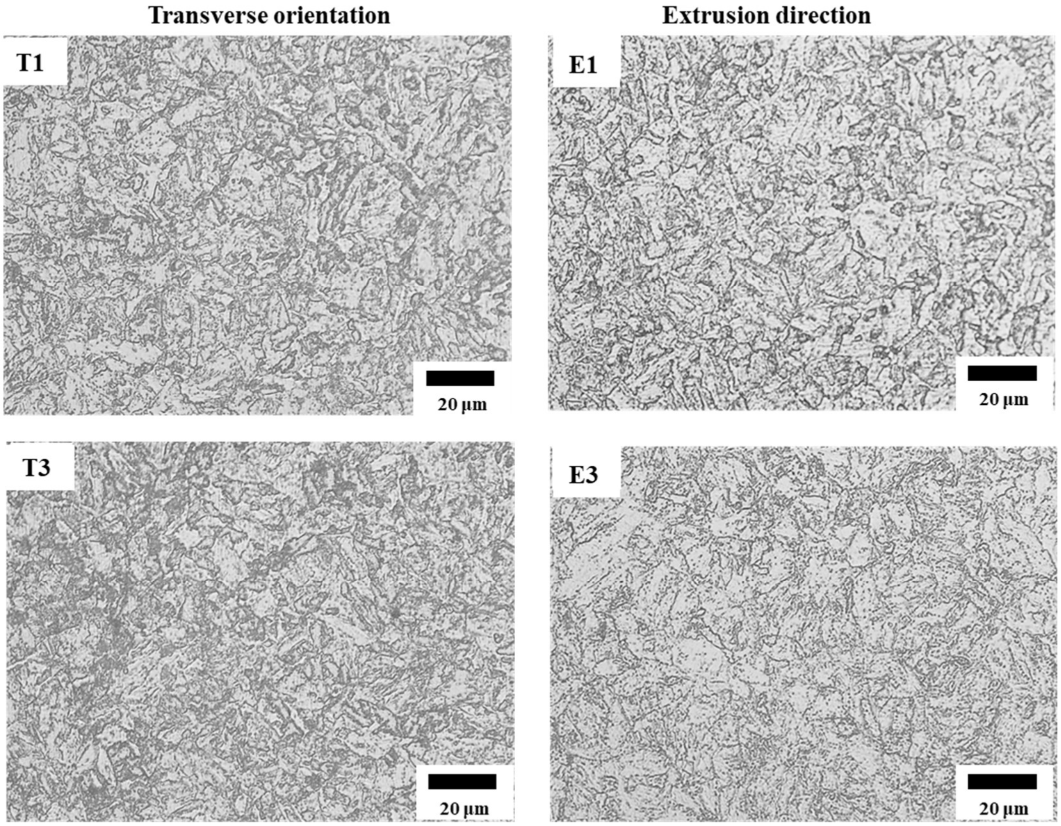
Transverse orientation
Extrusion direction
T1
20 μm
E1
20 μm
T3
20 μm
E3
20 μm

(b)

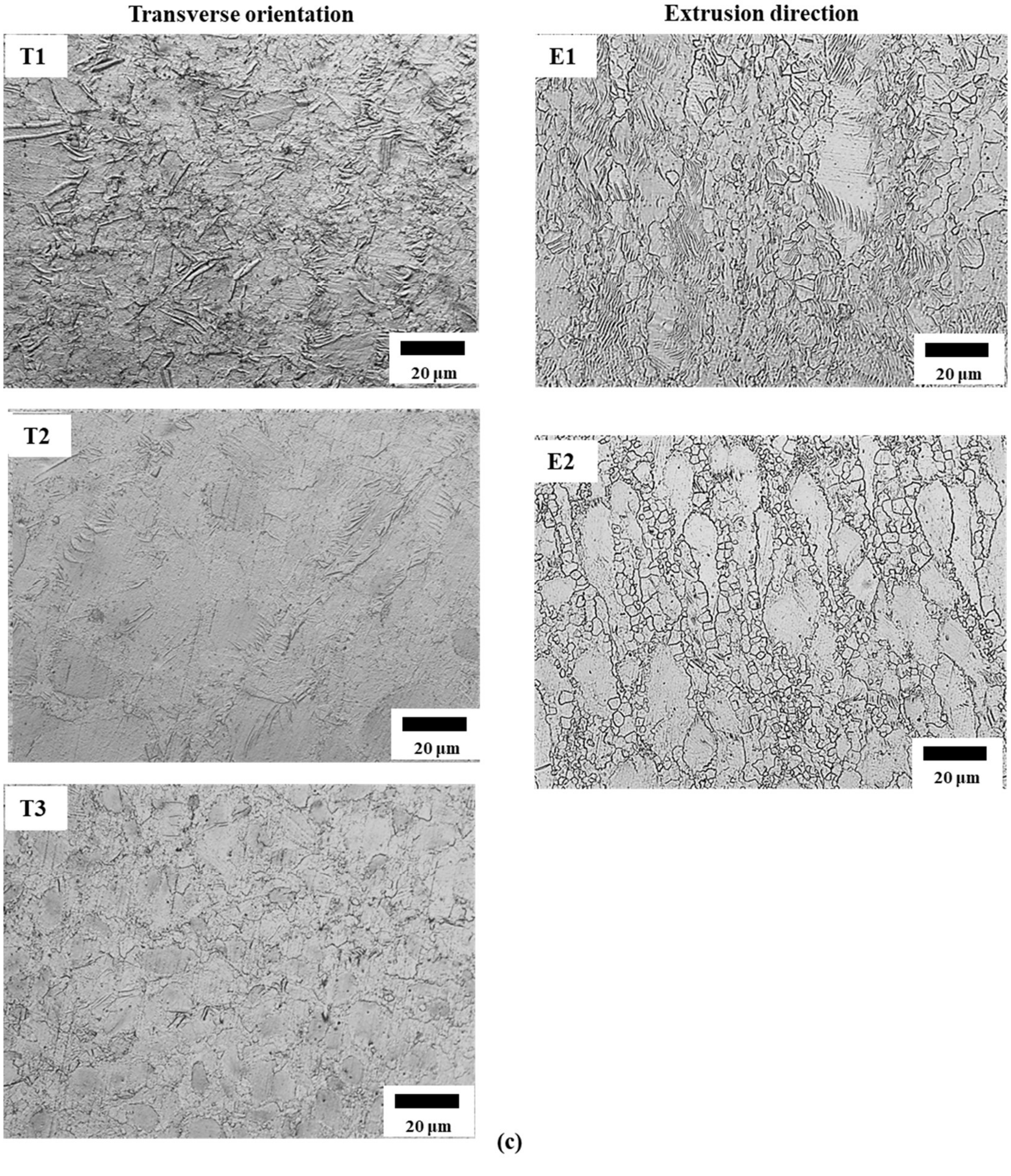

Figure 14: Optical metallographs for the three alloys: (a) AW2099-T83, (b) AISI 410 and (c) ZK60A.

4.3 Monotonic Tests Results

Tensile and torsional quasi-static mechanical tests were conducted for the three alloys. These tests are used to obtain the static mechanical properties of the alloys. The properties evaluated which are given in this section include ultimate strength, 0.2% yield strength, elastic modulus, shear modulus, fracture stress, percentage elongation, plastic flow coefficient and exponents.

4.3.1 Tensile Properties of AW2099-T83, ZK60A and AISI 410 Alloys

The characteristic engineering stress-strain curves for the three alloys are presented in Fig. 15. The AW2099-T83 (Fig. 15(a)) exhibits a deformation behavior nearly similar to elastic, perfectly plastic material. The curve consists of an elastic and plastic portion with very little amount of post yielding strain work hardening. The average yield and ultimate strengths for the alloy are found to be 549 and 577 MPa, respectively. The stress-strain ($\sigma - \varepsilon$) data from the plastic portion of the curve were fitted to a log-log line represented by Eq. (4.1) to determine the strain-hardening coefficient, *K,* and exponent, *n,* illustrated in Table 8.

$$\sigma = K\varepsilon^{n} \quad \text{.................. (4.1)}$$

Where σ is the static stress and ε is the plastic strain. The tensile property obtained from testing of three specimens of the present alloy is given in Table 8 along with the standard deviations. The presented tensile mechanical property is comparable with those reported in literature for a similar material [98,110]. However, it is higher than several other types of Al-Li alloy reported in the literature [88,90,92,111,112]. It has been shown that increase in the Cu and Li contents of the alloy promotes the formation of strengthening precipitates such as T1(Al_2CuLi) and θ'(Al_2Cu) which increase the alloy's strength [92,113]. Aging condition, homogenization heat treatment, orientation of testing and precipitate phase are factors which influence the alloy tensile property [87,96–98,110]. It is worth mentioning that in spite of the high number of researches on the tensile property of the alloy, the characteristic stress-strain curve is rarely reported.

The representative engineering strain-stress curve for ZK60A magnesium alloy is shown in Fig. 15(b). The characteristic curve illustrates that the material exhibits post-yield hardening and necking. An ultimate stress of 284 MPa is achieved while the yield stress is 221 MPa. The mechanical property, presented in Table 8, is comparable to the one reported by Feng et al [113] and Xiong et al [109] for similar material, while being slightly higher than the values reported by Paramsothy et al [114]. The variation observed in mechanical properties of similar alloys can be attributed to factors including processing methodology, heat treatment and test condition. The work hardening characteristic (K and n) was similarly determined with Eq. (4.1). The inelastic deformation behavior of magnesium alloys in tension is linked to microyielding and macroyielding processes [109,115]. The former process is most likely due to the action of basal slip in favorably oriented grain, while the latter process is an interaction of basal slip and prismatic slip [115]. Xiong et al [109] explained that microyielding process is responsible for the initial high rate of hardening observed, while the decrease in hardening rate that accompanied failure is due to macroyielding process.

Typical AISI 410 engineering stress-strain curve is presented in Fig. 15(c). The curve possesses both elastic and plastic regions with the alloy achieving an average ultimate stress of 591 MPa and yield strength of 489 MPa, as shown in Table 8. The tensile strength is in close agreement with the value reported for same alloy by Hejripour and Aidun [94]. Similar approach, as was for AW2099-T83, was applied to finding the strain-hardening coefficient, *K*, and exponent, *n*. Low strain work hardening exponent is recorded for the alloy because its stress does not increase significantly after yielding. In addition, the curve rapidly drops after the alloy achieved the maximum stress signifying poor resistance to plastic deformation and moderate necking. Consequently, the inelastic behavior makes a weak fitting for Eq. (4.1).

Figure 15(d) compares the engineering stress-strain curves for the three alloys. While AW2099-T83 and AISI 410 possess nearly the same level of ultimate strengths of about 600 MPa, their fracture strains are quite different, with AISI 410 having a higher fracture strain of about 21% which is thrice the fracture strain of 7% for AW2099-T83. ZK60A exhibits the lowest strength of 284 MPa, which is less than half the strengths of AW2099-T83 and AISI 410. However, the alloy has the highest strain work hardening capacity compared with AW2099-T83 and AISI 410 alloys.

The alloys monotonic tensile behavior can be related to both their microstructures which stem from the heat treatment, and their crystallographic structure. Aluminum-lithium alloy is typically strengthened by precipitation heat treatment which introduces fine particles of precipitates. Crystal lattice structures around this precipitates are usually distorted causing lattice strain in particle-matrix interface [3]. The distortion and precipitate particles act as barrier to plastic deformation with a resultant effect of a strong and hard alloy. Therefore, the high strength, but low ductility, characteristic of AW2099-T83 alloy can be attributed to its microstructure.

AISI 410 exhibits tempered martensite microstructure with grain size of about 5 μm, as previously shown in Fig. 14(b). Tempered martensite is a ferrite-cementite phase with enhanced ductility and toughness arising from the ferrite. The cementite phase acts as reinforcement for the ferrite matrix accounting for the relatively high strength [3]. Also, the small size of the microstructure means that many grain boundaries are present within a small unit volume. These boundaries act as barriers to dislocation motion making it difficult for dislocation to be transmitted during plastic deformation, thereby giving the alloy its relatively high strength.

ZK60A alloy possesses fewer slip planes making it possible for dislocations to pile up easily and giving rise to high strain work hardening characteristic. While necking was observed in both AISI 410 and ZK60A alloys, as illustrated in Fig. 16, no necking was observed in AW2099-T83, signifying a semi-brittle behavior.

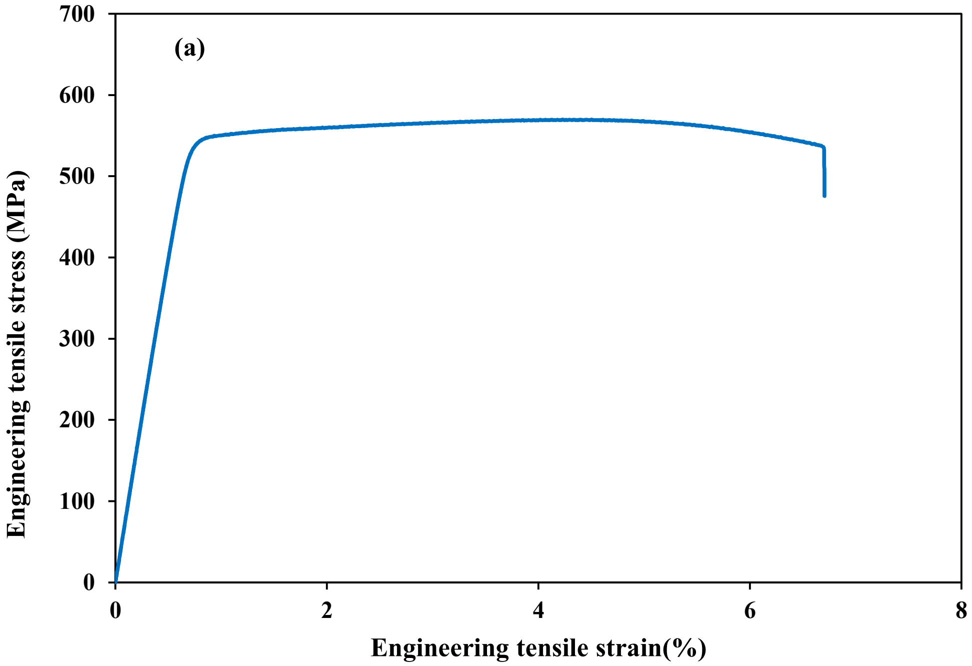

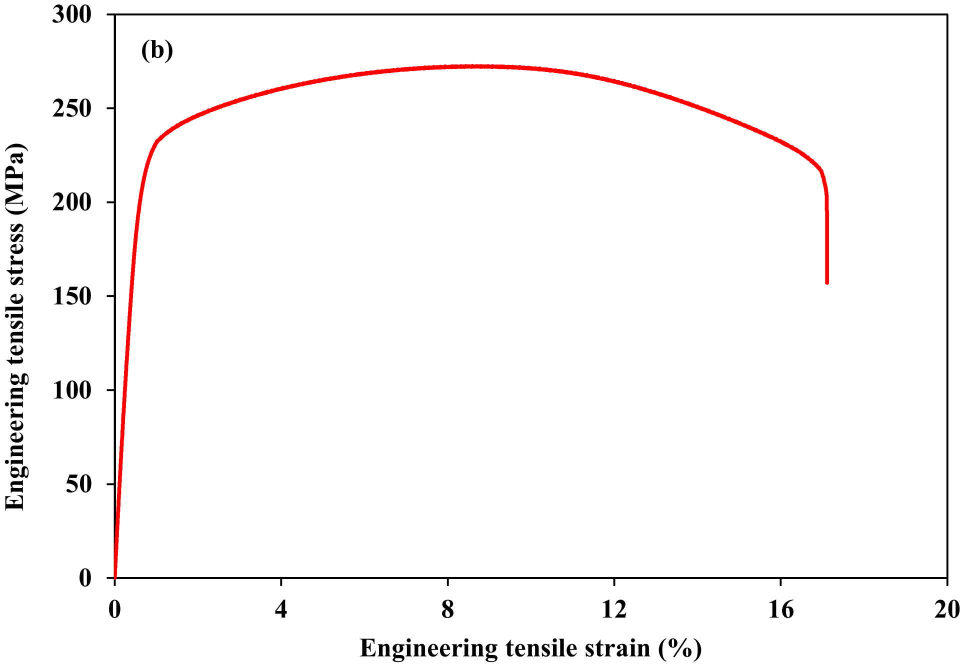

(b)
300
250
200
150
100
50
0
0
4
8
12
16
20
Engineering tensile strain (%)
Engineering tensile stress (MPa)

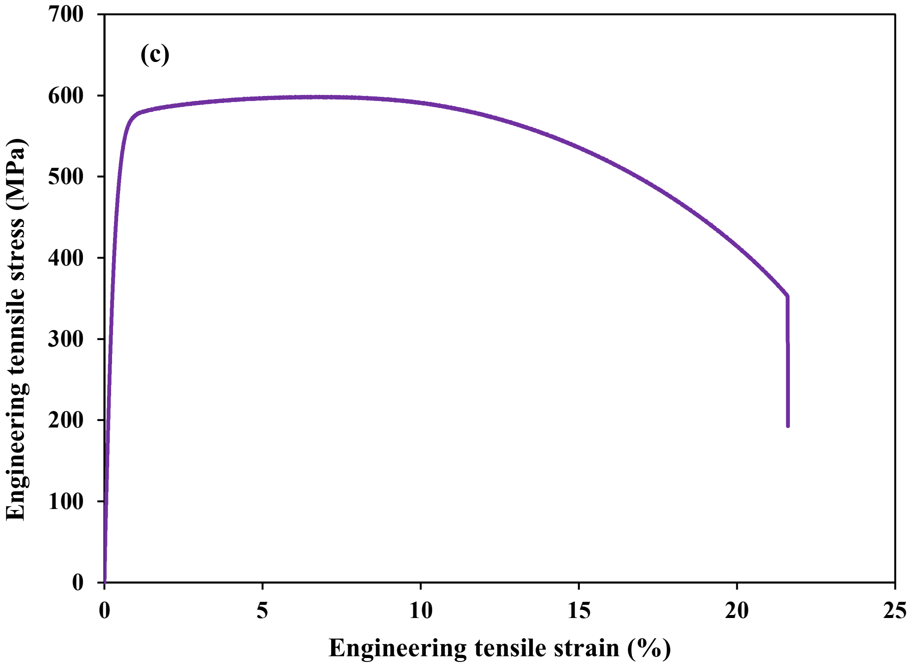

(c)
700
600
500
400
300
200
100
0
0
5
10
15
20
25
Engineering tensile strain (%)
Engineering tennsile stress (MPa)

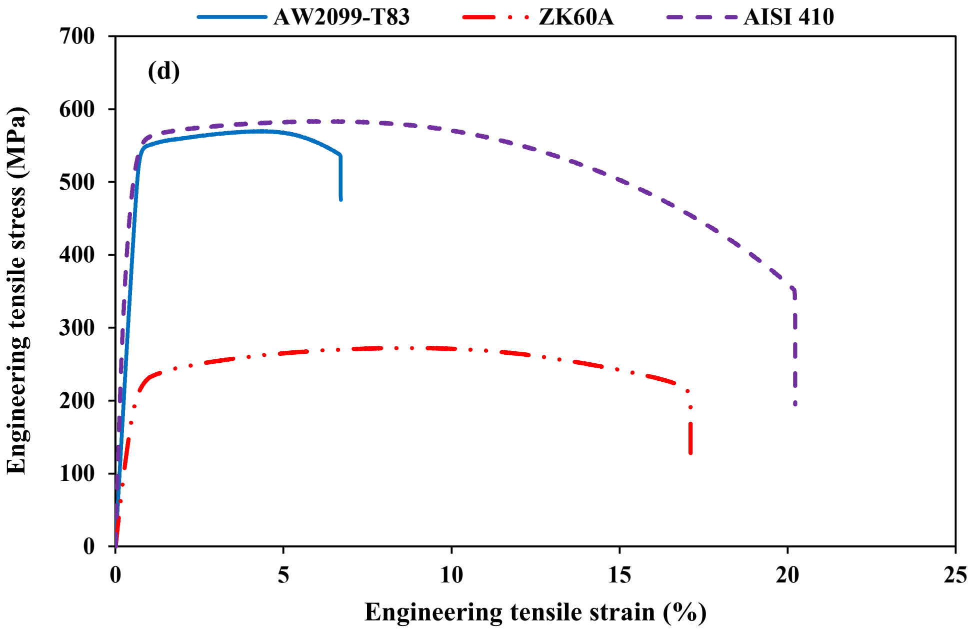

Figure 15: Stress strain curves for (a) AW2099-T83, (b) AISI 410, (c) ZK60A, and (d) the three alloys.

Table 8: Monotonic tensile property for the three alloys.

Engineering Tensile Property	**AW2099-T83**	**ZK60A**	**AISI 410**
Tensile strength (MPa), U_{ts}	567 ± 10.11	284 ± 9.9	591 ± 10
0.2% Yield stress (MPa)	549 ± 9.26	221 ± 9.15	489 ± 23.8
Elastic Modulus (GPa), E	80 ± 0.84	44 ± 0.59	208 ± 0.21
Strain hardening coefficient, K (MPa)	680 ± 15.76	411 ± 17	551 ± 13.93
Strain hardening exponent, n	0.0437 ± 0.01	0.1165 ±0.01	0.05 ± 0.02
Reduction in area (%)	8.0 ± 0.02	38 ± 0.015	61. ± 0.01
Elongation (%)	2.5 ± 0.22	7.0 ± 1.4	3.6 ± 0.3
Fracture stress (MPa)	530 ± 4.95	217 ± 5.95	340. ± 7.04
Fracture strain (%)	6.58 ± 0.7	18 ± 1.14	21 ± 0.98

4.3.2 Fracture Modes under Tensile Loading

SEM micrographs of the fractured surfaces and photographic images for failed specimens for the three alloys are shown in Fig. 16. AW2099-T83 specimen failed in the plane of maximum shear; that is, 45° to the specimen axis. There was no obvious reduction in the cross sectional area, indicating that little or no necking was present. This is in agreement with the 8% reduction area as recorded in Table 8. The macroscopically brittle fracture of AW2099-T83 is attributable to the presence of shearable precipitates which lead to inhomogeneous slip distribution and causing loss of ductility due to particles hardening [92]. Fractured surfaces of the specimens were bright and shiny. These are indicative of a semi-brittle mode of failure. AISI 410 failed on the plane perpendicular to the specimen axis. This is the plane of maximum normal stress for the tensile loading. There is gross reduction in cross section area. The percentage reduction in area is 61% as presented in Table 8 for tensile mechanical properties. Fractured surface was dull with the edge of fracture thinly serrated, which is a characteristic of ductile alloys. For ZK60A, the fracture also occurred on a plane perpendicular to the loading axis. The reduction in area was 38 % (Table 8). The edge was sawed as was observed for AISI 410, but the gaps of the serrations are larger and their dimension higher. Therefore, ZK60A can be classified as moderately ductile.

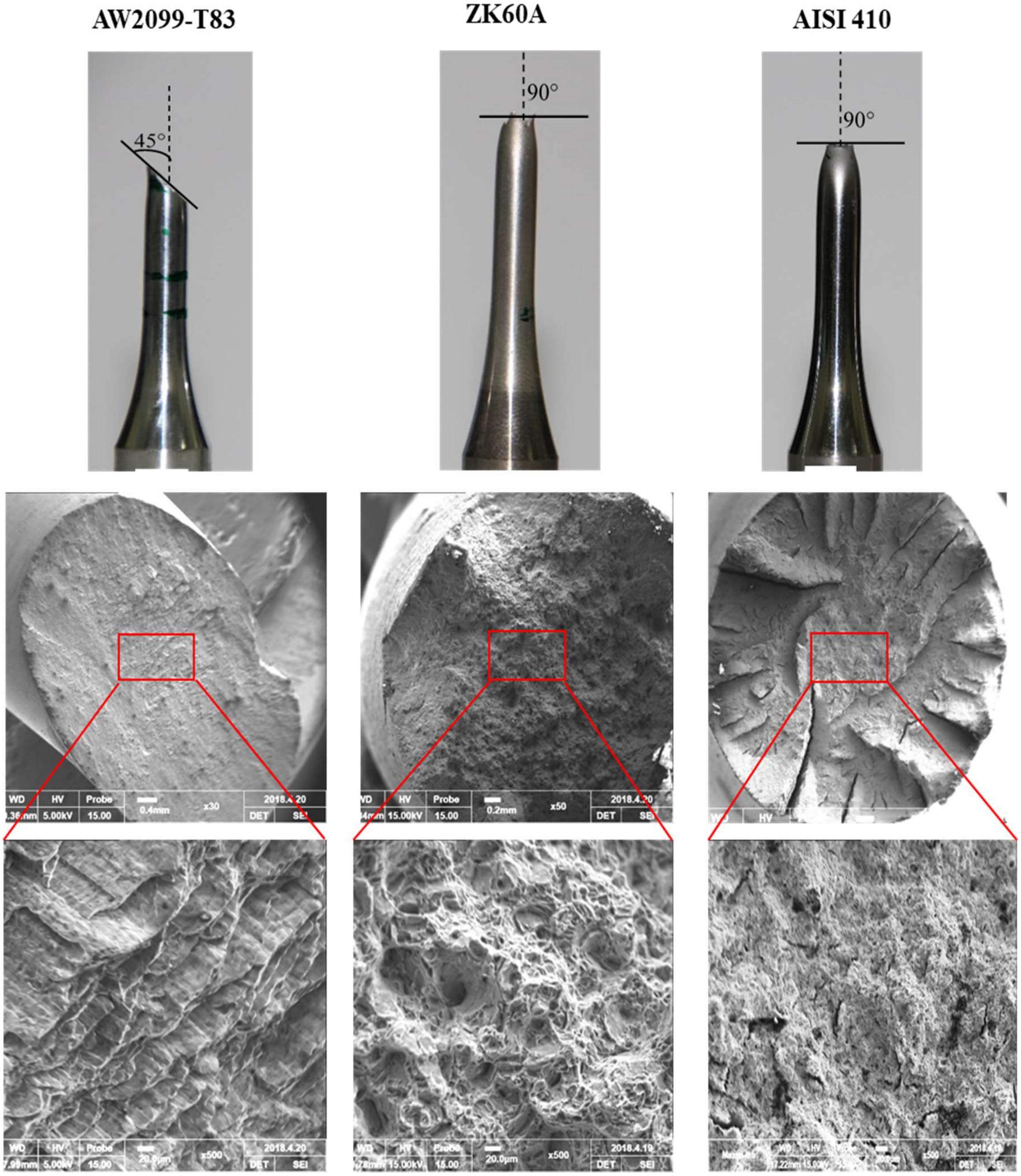

Figure 16: Fractured tensile specimens for the three alloys.

4.3.3 Torsional Behavior of AW2099-T83, ZK60A and AISI 410 Alloys

Figure 17(a) illustrates the monotonic torsional behaviour of AW2099-T83 alloy. The curve comprises an elastic and a plastic region with a fairly, steep rise in stress after yielding. The maximum stress attained is 296 MPa at a fracture shear strain of 0.25 rad. The mean shear yield strength is 229 MPa. Hardening behaviour was determined from true shear stress-strain by employing Eq. (4.2). Where $\boldsymbol{K_s}$ and $\boldsymbol{n_s}$ are the shear strength coefficient and exponent, respectively. The average mechanical properties obtained under torsional loading for AW20899-T83 alloy are presented in Table 9.

$$\boldsymbol{\tau = K_s \gamma^{n_s}} \quad \ldots\ldots\ldots\ldots (4.2)$$

The monotonic shear stress-strain curve for ZK60A alloy, shown in Fig. 17(b), possesses a linear portion and steeply rising plastic region reaching an average maximum stress of 182 MPa (Table 9). As mentioned earlier for tensile results analysis, such a sharp rise in stress in the plastic region is an indication of higher strain work hardening.

The representative engineering shear stress-strain curve for AISI 410 alloy is shown in Fig. 17(c). It consists of a plastic region that is almost flat, signifying a low hardening behavior. As can be seen from Table 9, the material attained an ultimate shear strength of approximately 473 MPa and fracture strain of 0.1742 rad.

The typical engineering stress-strain curves for the three alloys are compared in Fig. 17(d), revealing that AISI 410 exhibits the highest torsional strength followed by AW2099-T83, while ZK60A shows the least monotonic torsional strength. In terms of ductility, the shear fracture strain of AW2099-T83 is on the average 25% higher than the shear strengths of

AISI 410 and ZK60A. It can be seen that all the alloys exhibit higher hardening under monotonic torsion than under monotonic tensile post-yielding.

In summary, the physical characteristic of the curves and the mechanical properties in torsion differ from those of the monotonic tensile since the loading axes are different. The variation in microstructure for AW2099-T83 and ZK60A in Fig. 14 may as well have influenced the behaviour of these materials under torsional loading.

The mechanical properties determined are useful in the analysis of torsional fatigue behavior in subsequent sections. The choice of strain amplitudes to be applied for torsional fatigue and multiaxial fatigue testing will be selected based on these results.

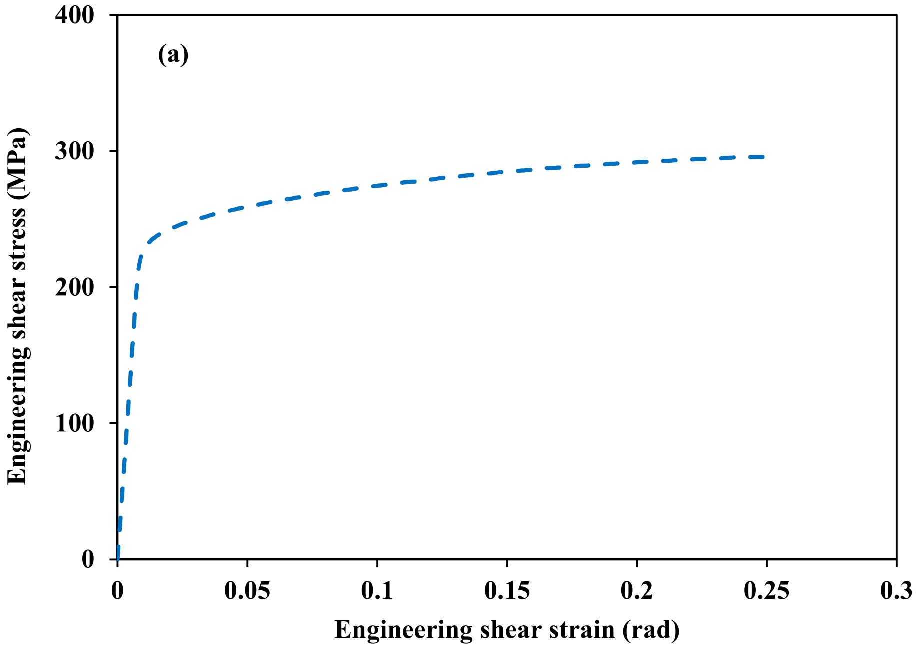

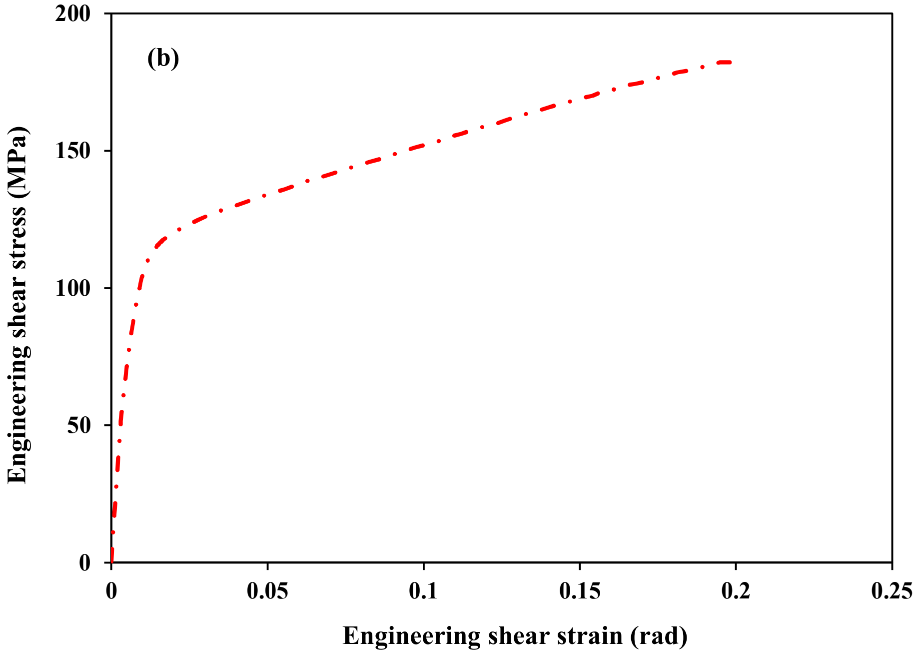
(b)
Engineering shear stress (MPa)
Engineering shear strain (rad)
0
50
100
150
200
0
0.05
0.1
0.15
0.2
0.25

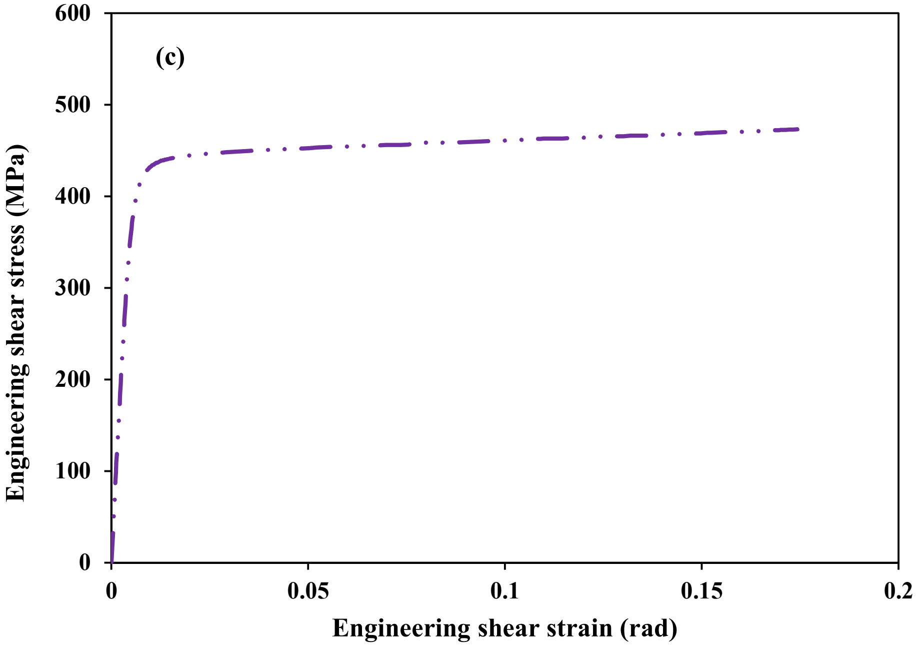
(c)
Engineering shear stress (MPa)
Engineering shear strain (rad)
0
100
200
300
400
500
600
0
0.05
0.1
0.15
0.2

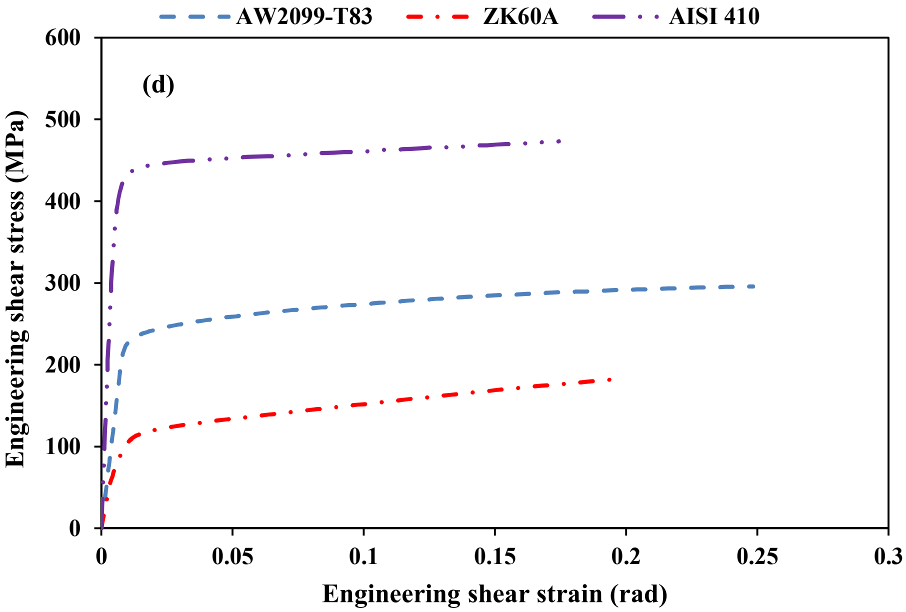

Figure 17: Torsional stress-strain curves for: (a) AW2099-T83, (b) ZK60A, (c) AISI 410 and (d) the three alloys.

Table 9: Torsional mechanical properties for the three alloys.

Engineering Torsional Property	AW2099-T83	ZK60A	AISI 410
Shear strength, τ_{us} (MPa)	296	182	473
0.2% Shear yield τ_{ys} (MPa)	229	89	402
Shear Modulus, G (GPa)	27	17	79
Fracture stress, τ_f (MPa)	295	182	473.
Fracture strain, τ_f (rad)	0.2483	0.1931	0.1742
Strain hardening coefficient, K_s	447	236	499
Strain hardening exponent, n_s	0.1557	0.18	0.0323

4.4 Analysis of Fatigue Results.

The results from the fatigue testing are presented and discussed in this section. Four loading paths, which include tensile, torsional, multiaxial proportional and non-proportional loadings, have been investigated for each of the alloys. Fatigue life, cyclic strain components and stress responses from each of the alloys are presented and analyzed.

4.4.1 Axial Fatigue Behavior

i. Cyclic Axial Stress-Strain Curve

Tension-compression fatigue results and experimentally determined material fatigue parameters for the three alloys are given in Tables 10-12. The results from the tables are used to find fatigue parameters and strain-fatigue life curves which are discussed later in this section. The fatigue life and cyclic axial forces were recorded by the computer system integrated to the testing fixture. The axial stress amplitudes have been calculated using Eq. (1.3) and (1.4), while the elastic and plastic components of the applied strain are obtained from Eq. (1.6) and (1.7). By fitting the plastic strain data and axial stress amplitude of individual alloys to a line represented by Eq. (1.8), curves in Fig. 18 are generated to find the fatigue strength coefficient, K', and fatigue exponent, n', given in Table 13. The fitting curve for ZK60A is done for plastic strain greater than 0.0005 in order to improve fitting accuracy. The coefficient K', and exponent n' so determined are used to construct the cyclic stress-strain (CSS) curves of the alloys in Fig. 19. The CSS curve represents the uniaxial deformation of material subjected to cyclic load. The Ramberg-Osgood fits are also illustrated in Fig. 19. These curves smoothly deviate from linearity to plastic region regardless of the monotonic tensile curves in Fig. 15. This is the typical characteristic of cyclic stress-strain curves and as such, they can be described by the Ramberg-Osgood equation, Eq. (1.10). The lack of absolute fit of some of the fatigue data at low strain, especially for ZK60A, is due to the very small plastic strain deformation at such applied strain amplitude. It is worth noting that there is no CSS curve for AW20999-T83 because of the absence of K' and n' for the range of plastic strain amplitudes investigated for the alloy.

Table 10: Axial fatigue results and experimental parameters for AW2099-T83 alloy.

Spec. ID	d (mm)	ε_a (%)	σ_{max} (MPa)	σ_{min} (MPa)	σ_a (MPa)	σ_m (MPa)	ε_e (%)	ε_p (%)	N_f (Cycle)
63448C	6.37	0.3	249.63	-223.12	236.38	13.26	0.3	0	100000 (stopped)
63449C	6.37	0.3	281.78	-206.33	244.06	37.73	0.3	0	156375
63446C	6.36	0.4	344.75	-309.97	327.36	18.39	0.4	0	23066
63447C	6.37	0.4	320.03	-313.24	316.64	3.39	0.4	0	37215
63444C	6.36	0.5	404.14	-394.06	399.1	5.04	0.5	0	8925
63445C	6.36	0.5	404.92	-398.82	401.87	3.05	0.5	0	6875
63450C	6.36	0.6	493.4	-453.25	473.33	20.08	0.6	0	1816
63452C	6.36	0.6	469.36	-473.54	471.45	-2.09	0.6	0	2966
63451C	6.37	0.7	520.21	-506.73	513.47	6.74	0.6	0.1	785
63453C	6.36	0.7	519.37	-505.12	512.25	7.13	0.6	0.1	929

Table 11: Axial fatigue results and experimental parameters for ZK60A alloy.

Spec. ID	d (mm)	ε_a (%)	σ_{max} (MPa)	σ_{min} (MPa)	σ_a (MPa)	σ_m (MPa)	ε_e (%)	ε_p (%)	N_f (Cycle)
63457C	6.36	0.28	109.66	-118.09	113.38	-3.72	0.26	0.02	107936
63467C	6.36	0.28	111.72	-115.05	113.39	-1.67	0.26	0.02	301827
63462C	6.36	0.3	112.73	-118.75	115.74	-3.01	0.26	0.04	52923
63465C	6.36	0.3	115.61	-122.08	118.85	-3.24	0.27	0.03	112187
83564C	6.36	0.35	132	-133	132.5	-0.5	0.3	0.05	183063
86255C	6.37	0.35	145	-155	150	-5	0.34	0.01	72578
63461C	6.36	0.4	129.04	-134.36	131.7	-2.66	0.3	0.1	6311
63464C	6.36	0.4	130.4	-139.12	134.76	-4.36	0.3	0.1	5953
63459C	6.36	0.5	140.4	-151.88	146.14	-5.74	0.33	0.18	3431
63463C	6.35	0.5	134.99	-136.16	135.58	-0.58	0.31	0.19	3372
63458C	6.36	0.6	148.09	-159.72	153.91	-5.82	0.35	0.25	1990
63460C	6.36	0.6	149.21	-161.43	155.32	-6.11	0.35	0.25	1876
63456C	6.37	0.7	153.44	-166	159.72	-6.28	0.36	0.34	1059
83562C	6.37	0.8	165	-164	164.5	0.5	0.37	0.43	1074
83563C	6.37	0.8	163	-181	167	-4	0.38	0.42	1263

Table 12: Axial fatigue results and experimental parameters for AISI 410 alloy.

Spec. ID	d (mm)	ε_a (%)	σ_{max} (MPa)	σ_{min} (MPa)	σ_a (MPa)	σ_m (MPa)	ε_e (%)	ε_p (%)	N_f (Cycle)
70075C	6.36	0.3	398.69	-354.77	376.73	21.96	0.18	0.12	23570
70077C	6.34	0.3	410.41	-380.89	395.65	14.76	0.19	0.11	25865
70072C	6.35	0.4	413.05	-403.86	408.46	4.6	0.2	0.2	8435
70074C	6.33	0.4	410.36	-396.46	403.41	6.95	0.19	0.21	9131
70079C	6.35	0.5	415.8	-418.69	416.75	-0.94	0.2	0.3	4567
70082C	6.35	0.5	420.01	-421.9	420.96	-0.94	0.2	0.3	4207
70080C	6.36	0.6	437.22	-438.2	437.71	-0.49	0.21	0.39	2273
83565C	6.35	0.6	455	-457	456	-1	0.22	0.38	2821
70081C	6.33	0.7	449.63	-456.02	452.83	-3.19	0.22	0.48	993
86254C	6.25	0.7	458	-468	463	-5	0.22	0.48	1339
70076C	6.26	0.8	466.04	-467.46	466.75	-0.71	0.22	0.58	930
70078C	6.34	0.8	460.49	-477.16	468.83	-8.34	0.23	0.57	675
70073C	6.36	0.9	473.58	-479.88	476.73	-3.15	0.23	0.67	481

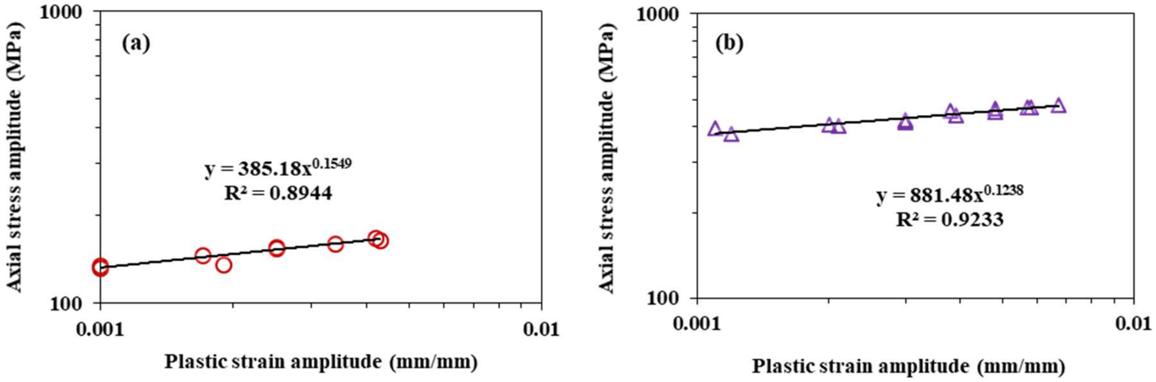

Figure 18: Regression curves to estimate axial strength coefficient K' and exponent, n' for: (a) ZK60A (b) AISI 410.

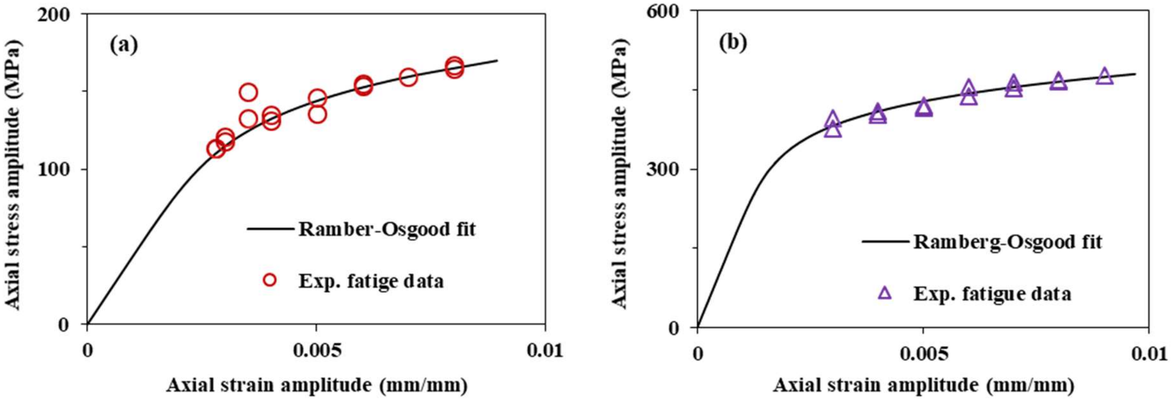

Figure 19: Cyclic axial stress-strain curve for: (a) ZK60A (b) AISI 410.

ii. Hysteresis Loops Evolution

A hysteresis loop is a closed cyclic stress-strain curve. It represents the energy-stored per unit volume during a fatigue cycle. Representative loops for the second and half-life cycles for all the strain amplitudes considered in section 3.4 are presented in Figs. 20-22 for AW2099-T83, Zk60A and AISI 410 alloys. The second loop is considered because it is the first complete loop, while half-life loop is the representation of the stable stress-strain behavior of a material under cyclic loading. It can be seen from the illustrations that the three materials exhibit different trends of cyclic axial behavior.

As evident from Fig. 20, AW2099-T83 alloy does not show any plastic strain for the applied strain amplitudes less than 0.6%. The deformation here is elastic; signifying that the total strain was recovered in each cycle. Therefore, the tensile cycle and the compression cycle follow the same path, which explains the absence of hysteresis loop for applied strain amplitudes less than 0.6%. Although at applied strain amplitude of 0.6%, plastic deformation of about 0.01-0.02% was recorded, yet it is quantitatively negligible. As such, appreciable plastic strain, measuring about 0.06-0.07%, occurs at the applied strain amplitude of 0.7%. There is a little increase in plastic strain as the number of cycle increases from the second to half-life cycle. Peak stresses (stresses at the tips of the hysteresis loop) rise with increase in applied strain amplitude. The shape of the hysteresis loop is symmetrical which is attributable to slip deformation mode.

In general, an alloy exhibits low cyclic plastic deformation due to its high strength or when under low applied strain amplitude that cannot activate plastic deformation [16,44,116]. The strengthening mechanism of the alloy, as mentioned previously in section 4.2, creates many precipitates that inhibit plastic deformation. The monotonic strength of a metal is also a factor that influences the width of hysteresis loop. A high strength alloy resists an imposed strain elastically resulting to a slim hysteresis loop [117].

The hysteresis loop evolution for ZK60A is illustrated in Fig. 21. Unlike AW2099-T83, the alloy exhibits plastic deformation at all levels of applied strain. The second and half-life cycles almost superimpose on each other indicating that there is no plastic strain increment with increase in the number of cycles. Most of the hysteresis loops obtained at low strain amplitudes are symmetrical. However, the second cycle hysteresis loop shows a little concavity for strain amplitudes higher than 0.5%. This may be an indication of twinning effect. Twinning is common with magnesium alloys in the first few cycles at strain amplitudes above 0.3% which usually causes the hysteresis loop to be asymmetrical or sigmoidal in shape [16,47,103,115,118,119]. Asymmetric hysteresis loop for ZK60 have been reported by Xiong et al. [109,120] and Yu et al. [121] at strain amplitude above 0.4% which they attributed to twinning effect. Wu et al [100] has reported an asymmetric hysteresis loop for ZK60A at strain amplitude higher than 1.0%. No pronounced asymmetry was observed by Vasilev et al [122] for similar material. However, a little concavity on the hysteresis loop was attributed to twinning effect by the authors. ZK60A in the current study shows no clear asymmetry except for a little irregularity at strain amplitude above 0.5% which is in agreement with the work of Vasilev et al [122]. It can be inferred that twinning deformation occurs but it was not extensive to reflect in the hysteresis loop. The difference in microstructure due to processing route can be a reason for the observed differences in hysteresis loops.

Figure 22 illustrates the hysteresis loop evolution for AISI 410 stainless steel alloy. Likewise, plastic strain is present at all applied strain amplitudes. However, the hysteresis loops for AISI 410 are wider at same applied strain amplitudes, compared to ZK60A and AW2099-T83. The half-life cycle hysteresis loops are larger than the second cycles indicating that plastic deformation increases with the number of cycles. This implies fatigue damage accumulates with cycling. The shape of the hysteresis loops are also symmetrical meaning that the predominant deformation mode is by slip mechanism. Similar low cycle fatigue behavior of several types of steels including stainless steel, low alloy steel and carbon steel has been published by a number of researchers [61,63,123–130]. The stabilized cycles hysteresis loops are comparable to the one observed in the current investigation, where wide hysteresis loops which are indicative of large plastic strain deformation are the common observations. Furthermore, serration-like features are present in the final phase of the compression cycle in the hysteresis loop of AISI 410 at applied strain amplitude above 0.7%. Similar observations have been reported for several steels [55,60–64].

The trend in the hysteresis loop evolution for the three alloys can be summarized as follows. Observably, the peak stress depends on the applied strain amplitude and tensile strength (or yield strength) of the alloy. With higher applied strain amplitude, the evolved stress increases. In addition, the higher the tensile strength of the alloy, the higher the peak stress. As an example, the stress evolution at 0.5% applied strain is highest in AISI 410, followed by that of AW2099-T83 and then that of ZK60A.

Besides the monotonic strength, the ductility of an alloy is another factor that influences the hysteresis loop evolution. Both AISI 410 and ZK60A exhibit plastic strain at all levels of applied strain, with the former showing higher deformation at equal applied strain amplitude. Of the three alloys, AISI 410 has the highest fracture strain of 21% in uniaxial tension, as is reported in section 4.3. Hence, the highest plastic deformation at the same strain amplitude for the three alloys. The resistance of AW2099-T83 to plastic deformation can be attributed to its low ductility coupled with its high strength. Thus, the uniaxial strength and ductility of the alloys influence their fatigue deformation behavior.

The measurable surface area in hysteresis loop is useful for plastic energy-based characterization of fatigue behavior of alloys. Therefore, the inference that can be drawn is that it would be possible to correlate fatigue life with energy parameters for ZK60A and AISI 410 alloys at all strain amplitudes, while AW2099-T83 alloy will only be amenable to energy-based approach at applied strain amplitude 0.7% or higher.

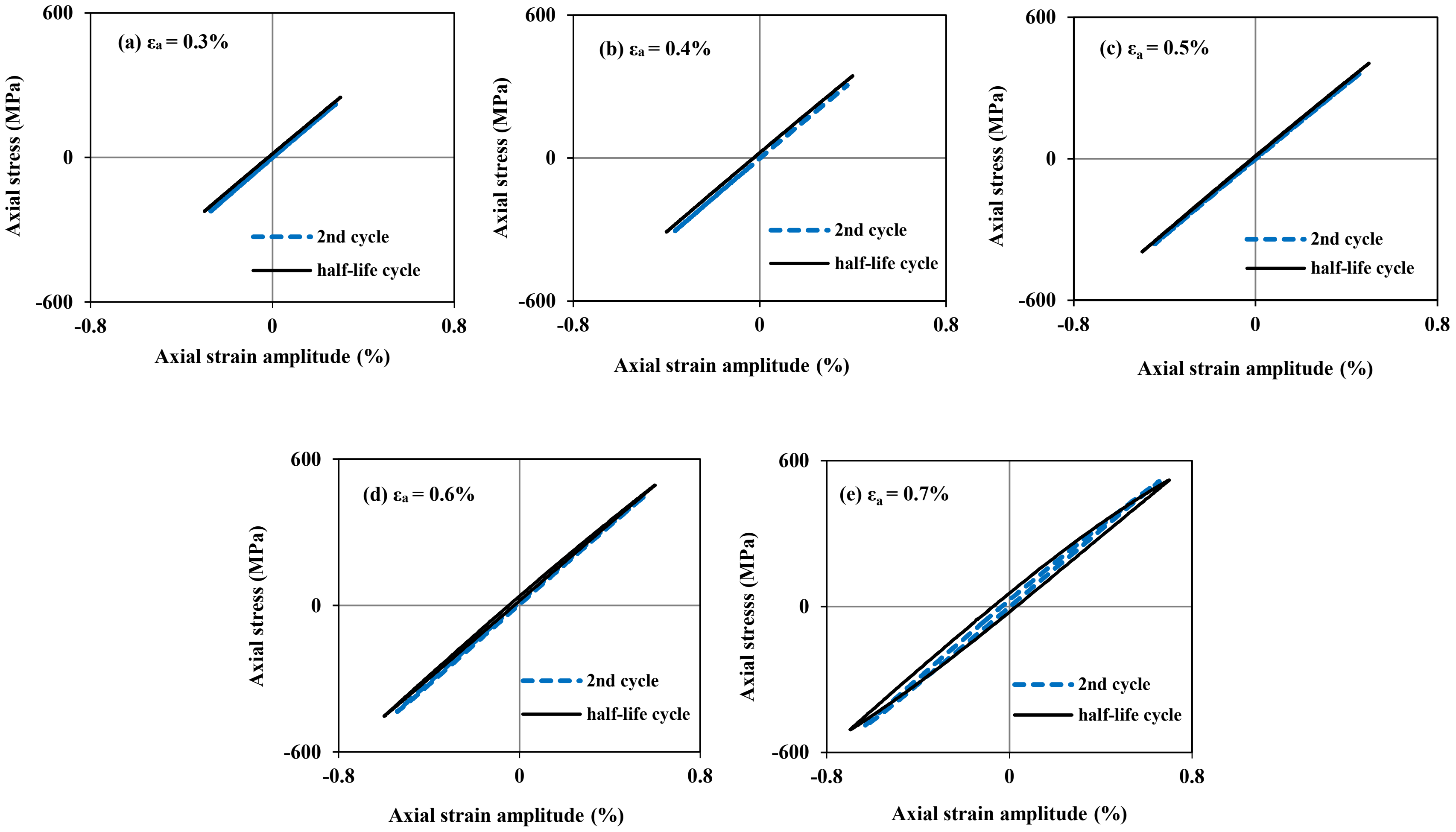

Figure 20: Hysteresis loop evolution for AW2099-T83 Al-Li alloy for all the axial strain amplitudes studied.

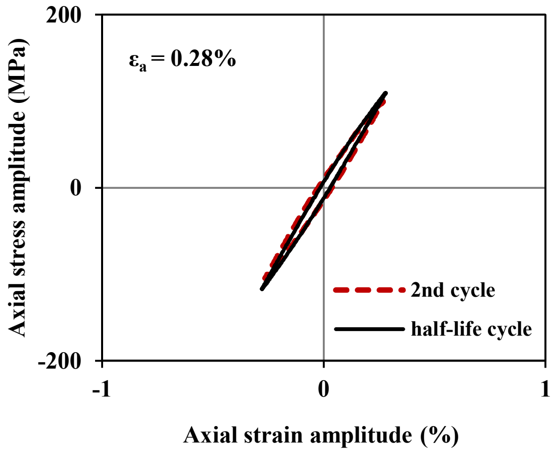
$\varepsilon_a = 0.28\%$
200
0
-200
-1
0
1
Axial stress amplitude (MPa)
Axial strain amplitude (%)
2nd cycle
half-life cycle

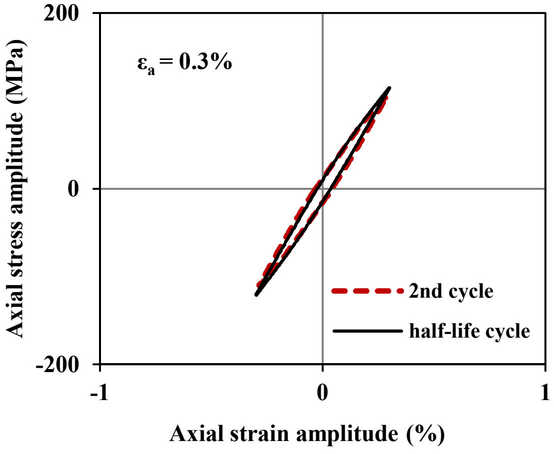
$\varepsilon_a = 0.3\%$
200
0
-200
-1
0
1
Axial stress amplitude (MPa)
Axial strain amplitude (%)
2nd cycle
half-life cycle

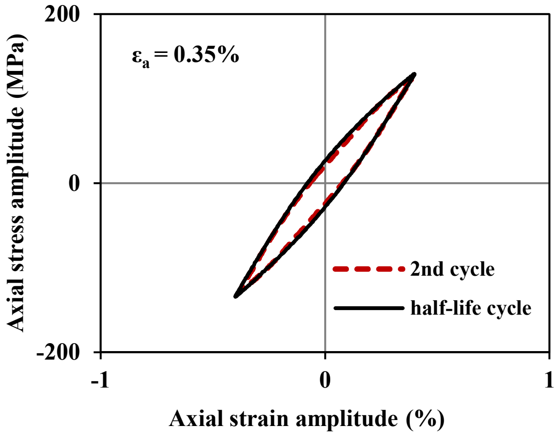
$\varepsilon_a = 0.35\%$
200
0
-200
-1
0
1
Axial stress amplitude (MPa)
Axial strain amplitude (%)
2nd cycle
half-life cycle

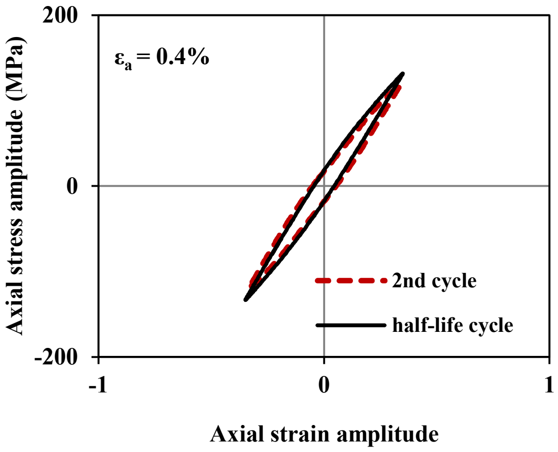
$\varepsilon_a = 0.4\%$
200
0
-200
-1
0
1
Axial stress amplitude (MPa)
Axial strain amplitude
2nd cycle
half-life cycle

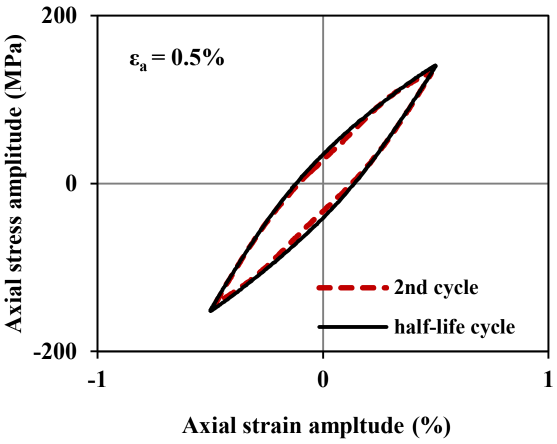
$\varepsilon_a = 0.5\%$
200
0
-200
-1
0
1
Axial stress amplitude (MPa)
Axial strain ampltude (%)
2nd cycle
half-life cycle

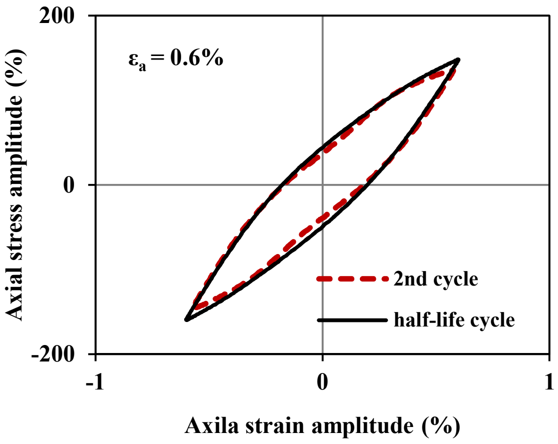
$\varepsilon_a = 0.6\%$
200
0
-200
-1
0
1
Axial stress amplitude (%)
Axila strain amplitude (%)
2nd cycle
half-life cycle

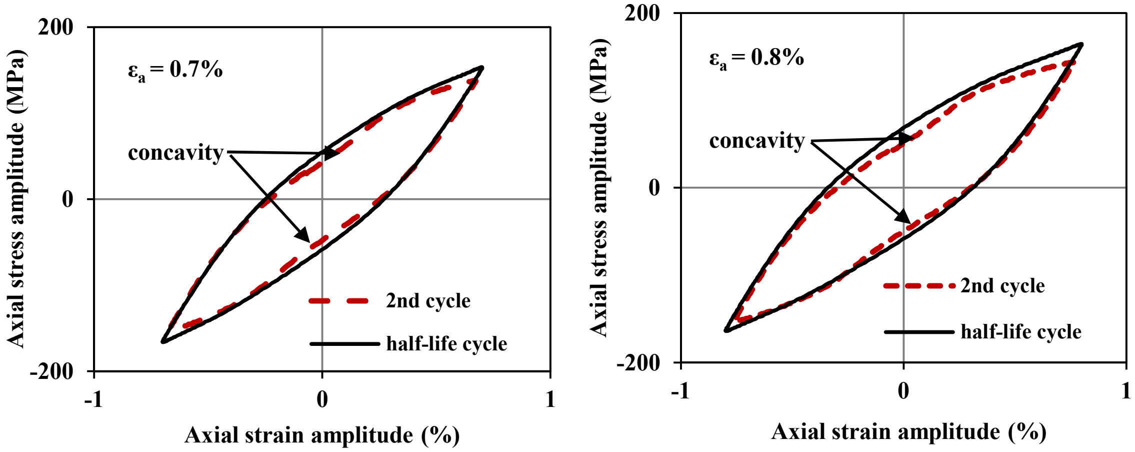

Figure 21: Hysteresis loop evolution for ZK60A Mg alloy for all the axial strain amplitudes studied.

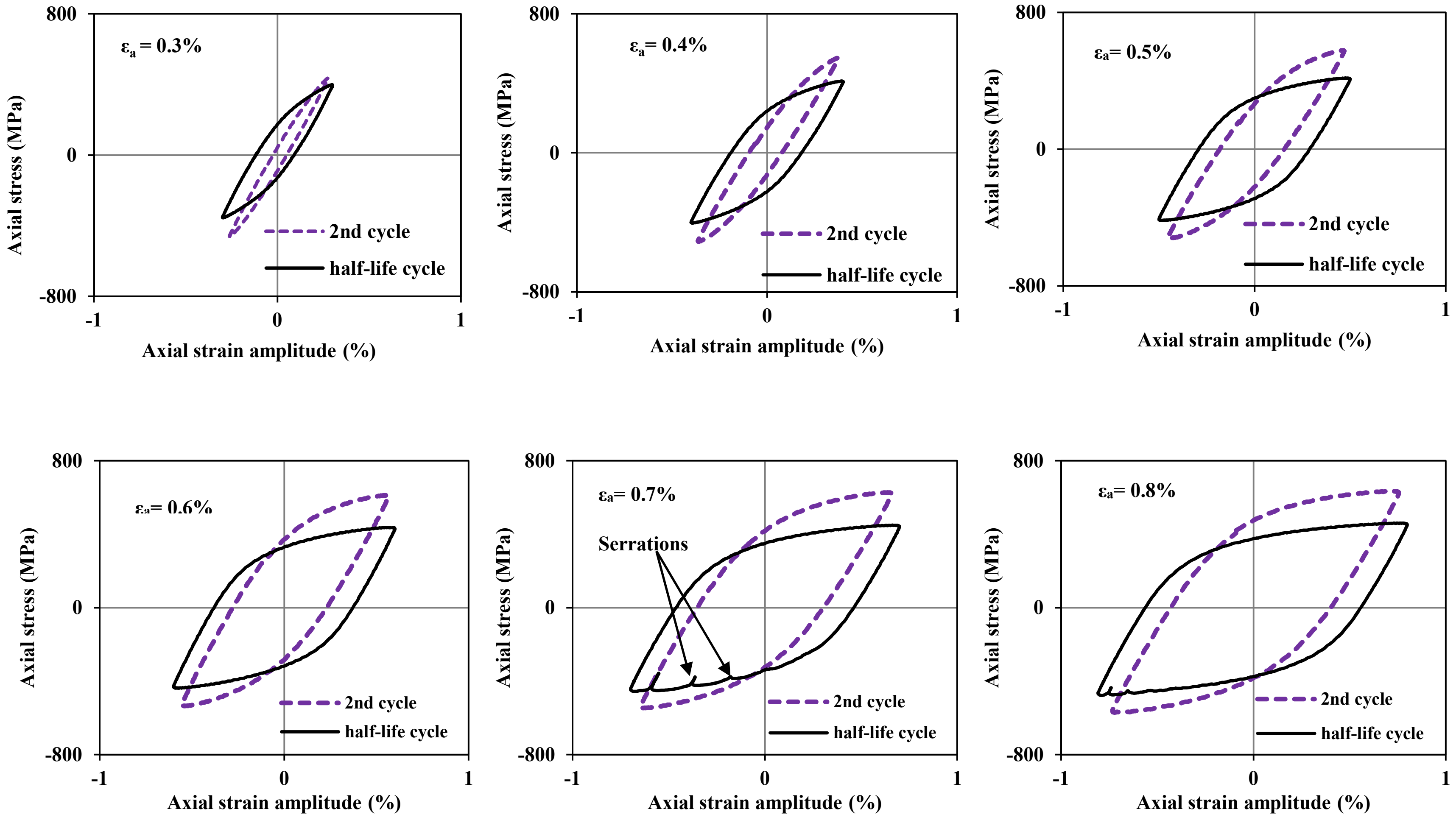
ε_a = 0.3%
ε_a= 0.4%
ε_a= 0.5%
ε_a= 0.6%
ε_a= 0.7%
Serrations
ε_a= 0.8%
2nd cycle
half-life cycle
Axial stress (MPa)
Axial strain amplitude (%)
800
0
-800
-1
0
1

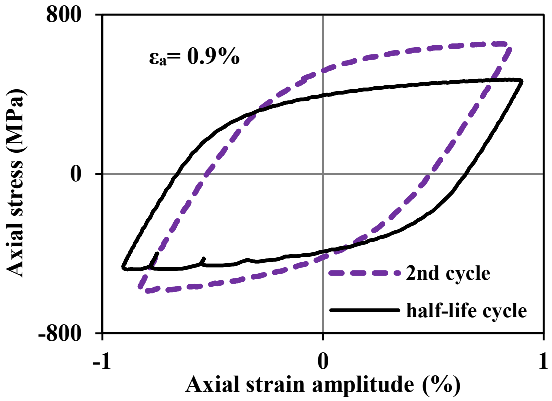

Figure 22: Hysteresis loop evolution for AISI 410 stainless steel for all the axial strain amplitudes studied.

iii. Cyclic Stress Response

The cyclic stress response is for the description of the stress evolution with the number of cycles during fatigue loading cycles. Any transient behavior such as cyclic hardening and softening can be observed and explained from the cyclic stress behavior of an alloy. The cyclic stress response is presented in Fig. 23 for the three alloys. Both maximum and minimum stresses are plotted against the number of cycles on a semi-log scale.

As can be seen from Fig. 23(a), AW2099-T83 alloy shows slight increment in cyclic stress with the number of cycles for different applied strain amplitude. The point at which stress increases with respect to cycle is different for each applied strain amplitude. Therefore, an analysis of the cyclic stress trend is necessary at each applied strain amplitude.

At the applied strain amplitude of 0.7%, maximum stress slightly increases until the 5th cycle followed by stress stabilization. On the other hand, the minimum stress rises slightly until the 30th cycle before the stress begins to drop until failure. Hence, the overall cyclic stress curve behavior is that of initial cyclic hardening, followed by cyclic softening until failure. The stress increment during hardening is about 30 MPa. Similarly, at 0.6% applied strain amplitude, initial cyclic hardening, which causes a cyclic stress rise of about 40 MPa in the alloy, is observed. Then, cyclic stabilization is seen after the 100th cycles. After few cycles of stress stabilization, the alloy cyclically softened to failure. This trend of initial cyclic hardening to be followed by cyclic softening is in contrast with cyclic stress behavior at strain amplitude with no quantifiable plastic strain.

At applied strain amplitude of 0.3 %, stress increment measuring about 1-12 MPa in cyclic hardening was observed until failure. This range in cyclic stress variation indicates a highly fluctuating cyclic stress with the number of cycles. However, for the applied strain amplitude of 0.4 %, the stress remained constant until the 1000th cycle where cyclic hardening begins resulting in stress increment of 39 MPa at failure. For 0.5 % applied strain amplitude, cyclic hardening is also observed as the stress increases by about 25 MPa from the tenth cycle to the 8000th cycle before the specimen failed.

These varied trends across the applied strain level suggest that the cyclic stress response of AW2099-T83 in axial fatigue depends on the applied strain amplitudes and the number of cycles. For high strain amplitude, or in the actual low cycle fatigue, cyclic hardening is observed, followed by stabilization and then cyclic softening. On the other hand, at low and medium strain amplitudes, the material would cyclically harden until failure.

The presence of cyclic hardening at low strain amplitude for AW2099-T83 may be explained by the change in the dislocation density of the material due to slip deformation. When an alloy is cyclically strained, slips happen and dislocation gradually builds up. The rise in dislocation density however restricts dislocation mobility [2]. The restriction manifests in the form of increment in stress or cyclic hardening. Cyclic hardening can be due to dislocation-dislocation interaction or dislocation pile-up [1]. Srivatsan and Coyne [91] have reported that Al-Li-Cu alloys generally softened to failure under laboratory condition, in dry air, distilled water and vacuum over plastic strain amplitudes ranging between 0.02% and 1.8%. The authors [91] explained that once precipitates are cut, particles offer less resistance to dislocation movement in the active slip plane and local work hardening capacity are reduced resulting to cyclic softening. Little amount of hardening in first few cycles in dry air and distilled water was reported which was attributed to the increase in dislocation.

Figure 23(b) displays the cyclic stress curve for ZK60A magnesium alloy. It can be seen that the alloy cyclically hardened, even though slightly, throughout its cyclic life, regardless of applied strain amplitude. The amount of cyclic hardening is also negligible compared to that of AW2099-T83. The highest stress increment due cyclic hardening is about 10 MPa. Marginal cyclic hardening for ZK60 have been reported by Yu et al [121]. Low strength, soft metals are known to harden due to low dislocation density when subjected to loading [2]. In addition, the absence of sufficient independent slip planes for HCP alloys generally causes dislocation immobility, which impedes its movement, thereby causing the alloy to harden. The rate of hardening, from the slope of the curves, is dependent on the applied strain amplitude; with higher strain amplitude showing greater rate of hardening. Cyclic hardening of magnesium alloys in axial cyclic tests has been reported extensively and it is commonly attributed to twinning-detwinning mechanism as reviewed in chapter two [48,67,100,115,118–120,131]. The majority of the cited works also observed that cyclic hardening is strain dependent, being higher at high strain amplitudes. Wu et al [100] reported that the phenomenon of cyclic hardening in Mg alloys is due to a twinning-detwinning process and is typical of hexagonal close-packed alloys.

Figure 23(c) illustrates cyclic stress behavior with the number of cycles for AISI 410 alloy. The alloy cyclically softens to failure at all applied strain amplitudes. An initial increase in cyclic stress with the number of cycle for the first ten cycles can be observed. It is obvious from Fig. 23(c) that the softening behavior is independent of applied strain amplitudes, as the cyclic stress curves at all applied strain amplitudes converge to a single path. It can be deduced that the failure stress at each strain amplitude is approximately 400 MPa.

Softening behavior is anticipated for high strength, hard alloys [2]. Martensitic steels exhibit softening behavior when subjected to low cycle fatigue [123,125,128]. Ductile alloys and initially hard alloys soften when subjected to cyclic loading because of the rearrangement of dislocations, which offer less or no resistance to dislocation mobility.

The trend in cyclic stress response can also be assessed by plotting cyclic stress against fatigue life ratio. Fatigue life ratio is the fraction of fatigue life at a given time for a given strain amplitude. Such curves are given in Fig. 24 for the three alloys investigated.

From Fig. 24(a), for applied strain amplitudes in the range 0.3% to 0.5%, AW2099-T83 hardens for less than 10% of the lives then it maintains a fairly stable behavior, followed by softening before fracture. The proportion of fatigue life for which a stable cyclic stress is sustained decreases with strain amplitude. Softening begins at 70% of fatigue life for the 0.5% strain amplitude, at about 88% for 0.4% and almost no softening for 0.3%. However, at strain amplitudes in the range of 0.6% to 0.7%, the hardening behavior transits directly to softening behavior at much lower percentage of about 20% of fatigue life. Initial cyclic hardening for low a fraction of fatigue life at high strain amplitude have been reported for Aluminum alloy 6082-T6 by Borrego et al [132].

Figure 24(b) shows cyclic stress variation with fatigue life ratio for ZK60A. The alloy displays an initial increase in stress which reaches a maximum at about 10% of total fatigue life. It then maintains a steady, low cyclic hardening rate for the rest of the fatigue lives before fracture. Stress responses at applied strain amplitude of 0.28% and 0.35% are almost similar indicating that the fatigue life obtained at these strain amplitudes is of nearly same cycles, as can be seen from Table 11.

In Fig. 24(c), the cyclic stress response with fatigue life ratio is shown for AISI 410 stainless steel. A rapid decrease in stress is observed initially; followed by a steady decreasing stress and a final rapid softening which culminates in failure. Similar observation is reported by Branco et al [123] for high strength martensitic steel and by Mazánová et al [133] for 316L stainless steel.

To summarize, stress evolution depends on microstructure and dislocation behavior. The difference in the stress response of the three alloys can therefore be explained by the different microstructure and dislocation behavior. The microstructure of AW2099-T83 is strengthened by aging precipitates as have been reported in a number of published works [96,97,106,107]. Such precipitates can interact with dislocations causing hardening at one point. However, when they are sheared due to high stress, their resistance to dislocation movement is weakened and cyclic softening results [91]. The tendency for HCP alloys to harden is generally known to be due to fewer slip planes present in their crystals and the twin-dominant mode of dislocation [109]. With increase in number of cycles, dislocation is increased but there are insufficient planes for dislocation mobility to occur. Cycle-dependent and strain-dependent stress response as seen in AW2099-T83 and ZK60A can be linked to their microstructures, both of which exhibit strong texture with respect to extrusion orientation. Such behavior is not seen in AISI 410 which exhibits the same grain structure and size in all orientations.

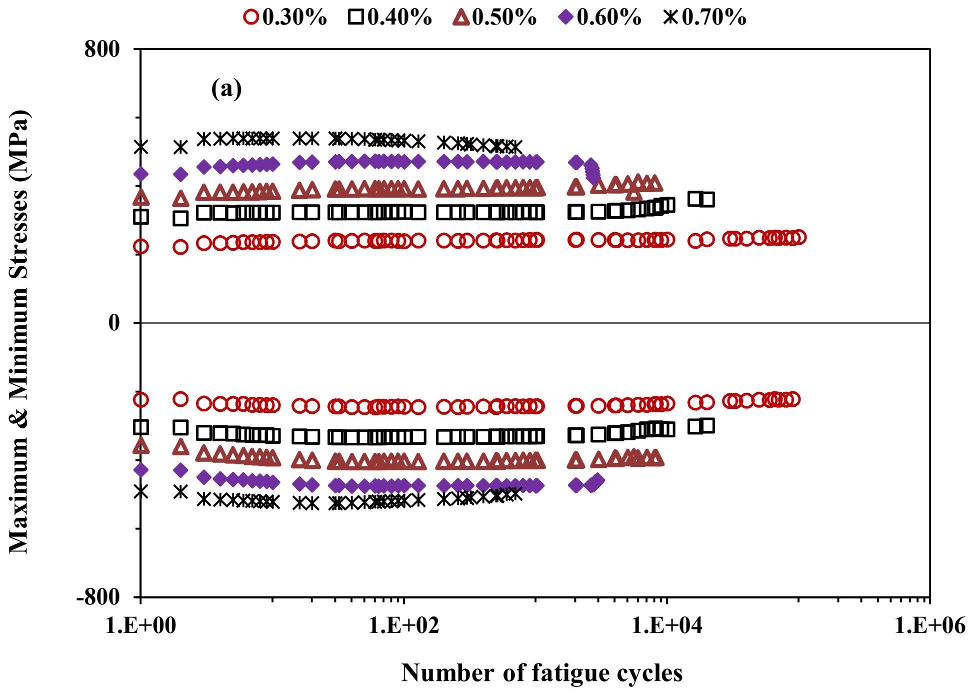
○0.30% □0.40% △0.50% ◆0.60% ✕0.70%
(a)
800
0
-800
Maximum & Minimum Stresses (MPa)
1.E+00
1.E+02
1.E+04
1.E+06
Number of fatigue cycles

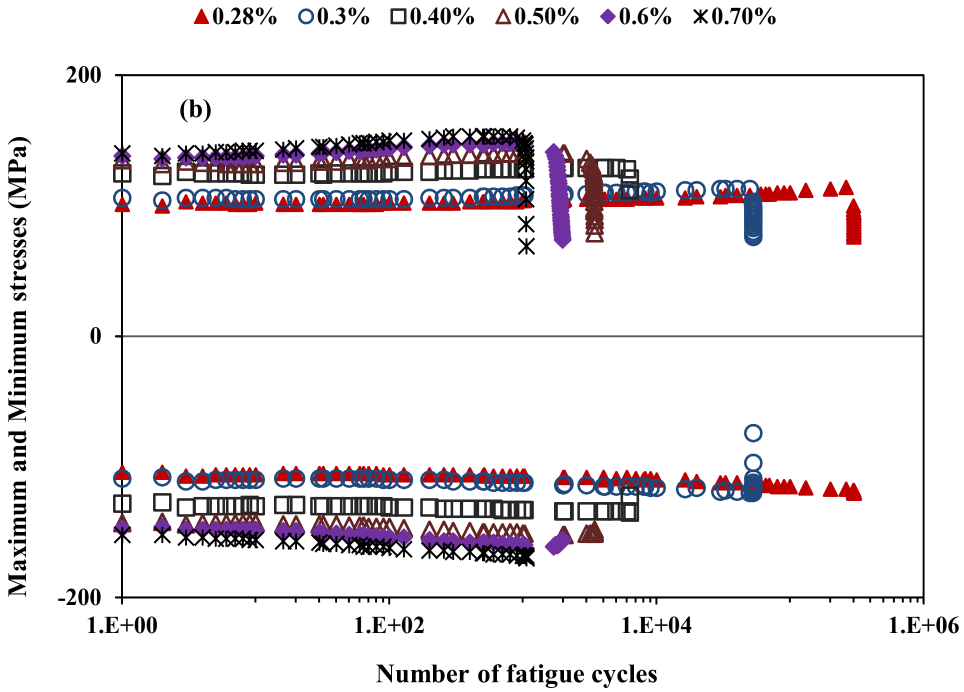
▲0.28% ○0.3% □0.40% △0.50% ◆0.6% ✕0.70%
(b)
200
0
-200
Maximum and Minimum stresses (MPa)
1.E+00
1.E+02
1.E+04
1.E+06
Number of fatigue cycles

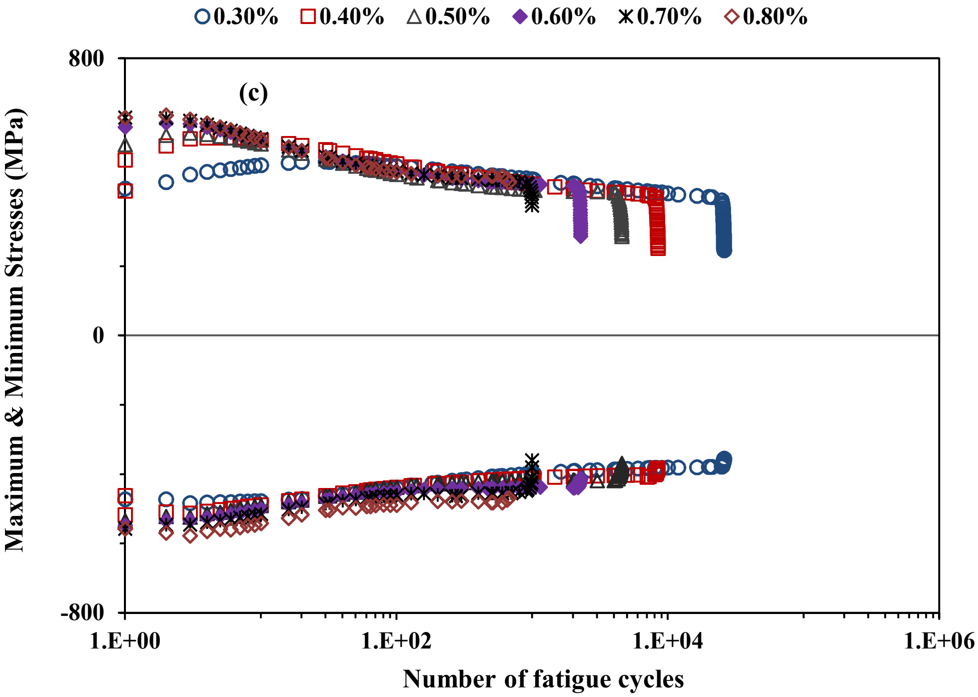

Figure 23: Cyclic stress curves for the three alloys: (a)AW2099-T83, (b) ZK60A and (c) AISI 410.

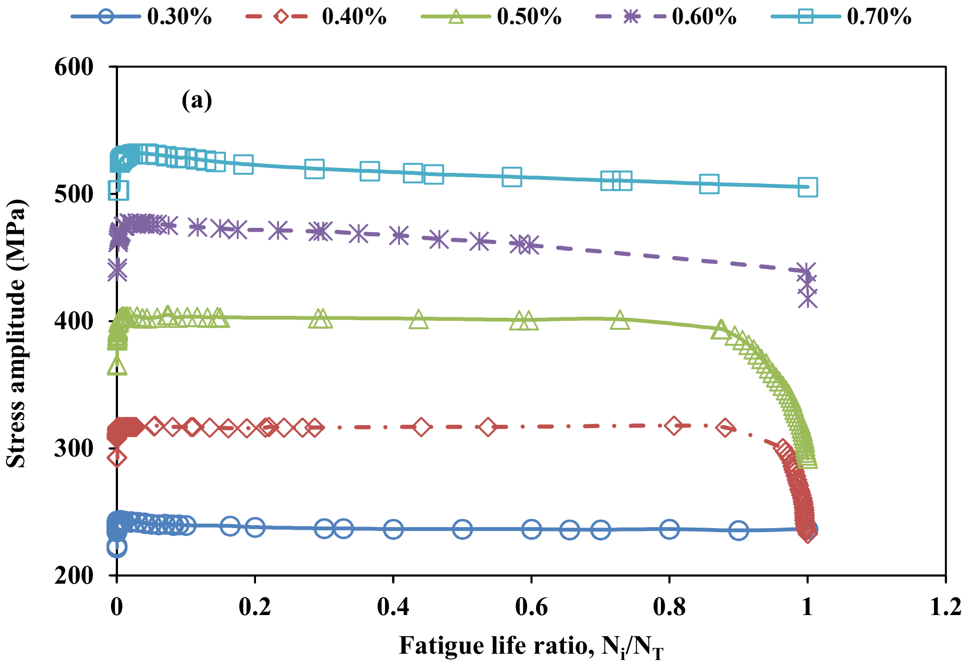

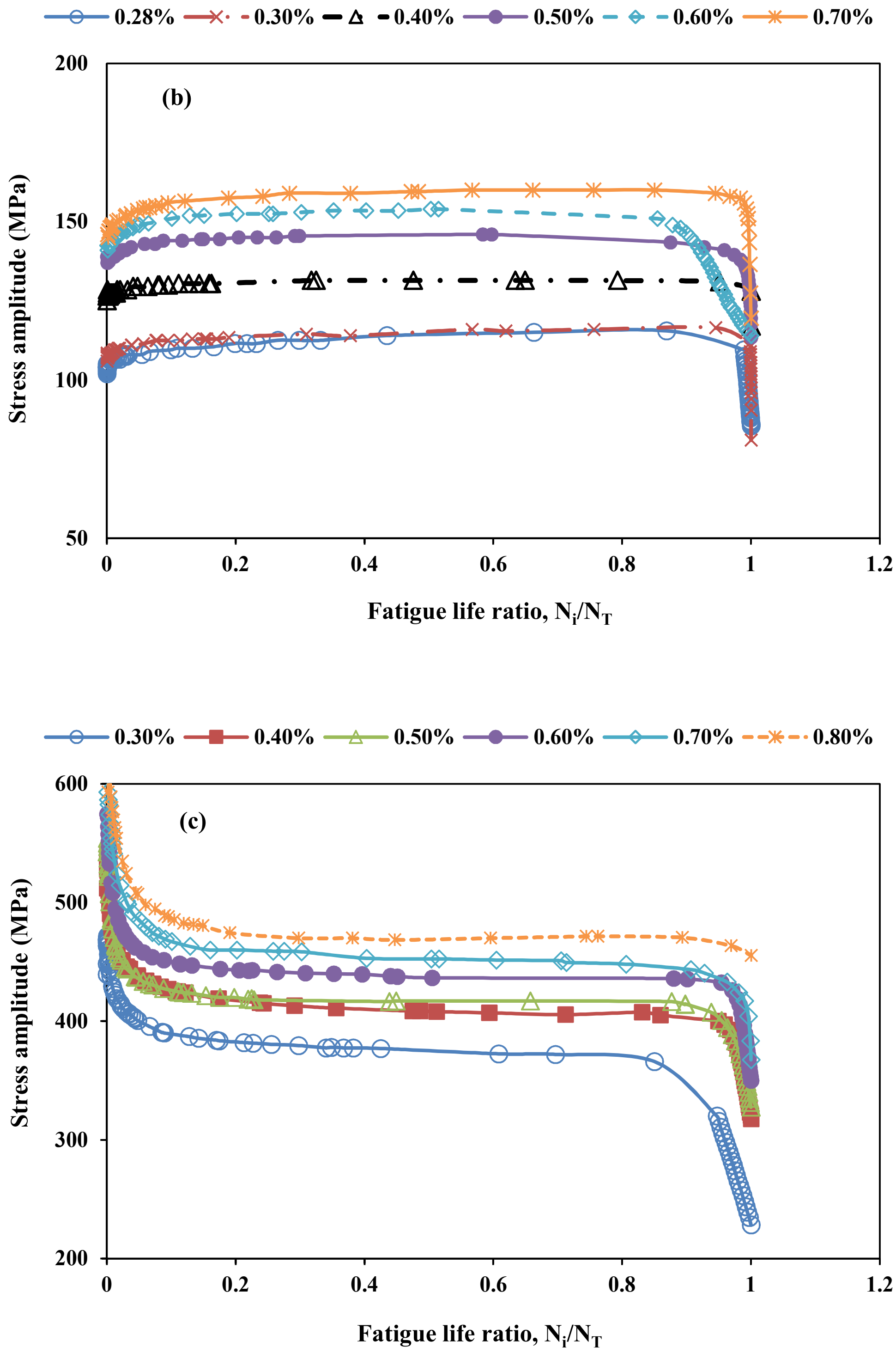

Figure 24: Cyclic stress amplitude vs. fatigue life ratio for the three alloys: (a) AW2099-T83, (b) ZK60A and (c) AISI 410.

iv. Axial Mean Stress Evolution

Figure 25(a) displays the mean stress evolution with the number of cycles for AW2099-T83. The alloy shows negative mean stress at applied strain amplitudes of 0.3% to 0.5%. This trend continued until the 3000^{th} cycle before the mean stress rises to become tensile. However, for 0.6% applied strain amplitude at which the fatigue life was less than a thousand cycle, the mean stress remained negative until failure. Applied strain amplitude of 0.7% produces tensile mean stress for the entire fatigue life. It can be deduced from Fig. 25(a) that there is a tendency for the mean stress to rise abruptly at lower applied strain amplitude with higher number of cycles. Thus, the pattern of the mean stress evolution depends on both the strain level and the number of cycles, which can be summarized as follows: at applied strain amplitudes less than 0.6%, the mean stress is compressive and can become tensile if the fatigue life exceeds three thousand cycles. However, as the cycling strain amplitude approaches the monotonic yield strain of the alloy, the mean stress becomes positive.

The mean stress versus the number of cycles, as shown in Fig. 25(b) for ZK60A is entirely compressive regardless of applied strain amplitude and the number of cycles. Increase in the applied strain level does not change the trend in the mean stress with the number of cycles. The largest compressive mean stress observed is less than -10 MPa. Yu et al. [121] have reported higher tensile mean stress evolution for ZK60. Xiong and Jiang [120] have shown that mean stress evolution for ZK60 fluctuates between compressive and tensile mode depending on the applied strain amplitude.

The mean stress evolution for AISI 410 stainless steel is generally tensile for the entire duration of the fatigue life, as indicated in Fig. 25(c). However, there is a possibility for the mean stress to become compressive with increasing numbers of cycles. As can be seen from Fig. 25(c), at low applied strain amplitude of 0.3% and 0.4%, the mean stress initially starts at a negative value before becoming positive for most of the remaining life.

In summary, mean stress development indicates the asymmetry of evolved cyclic stress. Negative mean stress shows that the compressive stress is higher, while positive mean stress signifies that the tensile stress response is larger. It is clear from the illustrations in Fig. 25 that mean stress evolution for the three alloys varies. This is because of the different crystallography, microstructure and strengthening mechanism. Negative mean stress can indicate softening for high strength metals. Therefore, the negative means stress for AW2099-T83 and AISI 410 alloys can be attributed to their high strength and hardness. The evolution of tensile mean stress with fatigue cycle for AW2099-T83 may suggest that at longer cycle, the density of dislocation has increased resulting in dislocations-dislocation interaction. This interaction will result in cyclic hardening, translating to positive mean stress. However, for ZK60A, negative mean stress can be linked to twinning effect which is the predominant deformation mode for HCP alloys. Hence, the evolution of negative mean stress for ZK60A alloy signifies that a higher negative stress response evolved due to twinning mechanism [121]. Compressive mean stress is believed to have little or no effect on the specimen life while tensile mean stress contributes to lower the life of components [119].

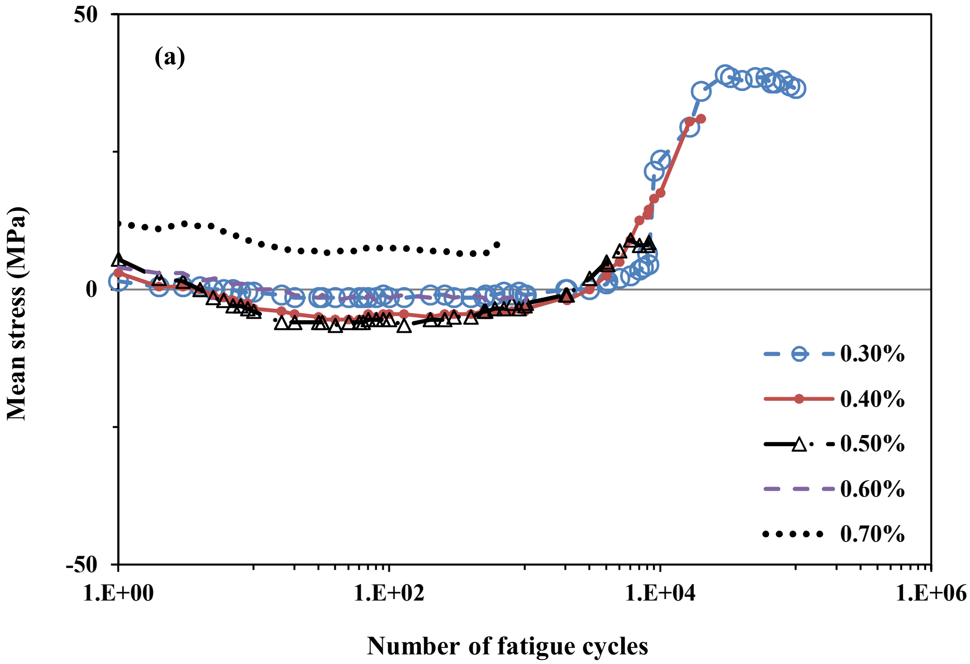
(a)
Mean stress (MPa)
50
0
-50
1.E+00
1.E+02
1.E+04
1.E+06
Number of fatigue cycles
0.30%
0.40%
0.50%
0.60%
0.70%

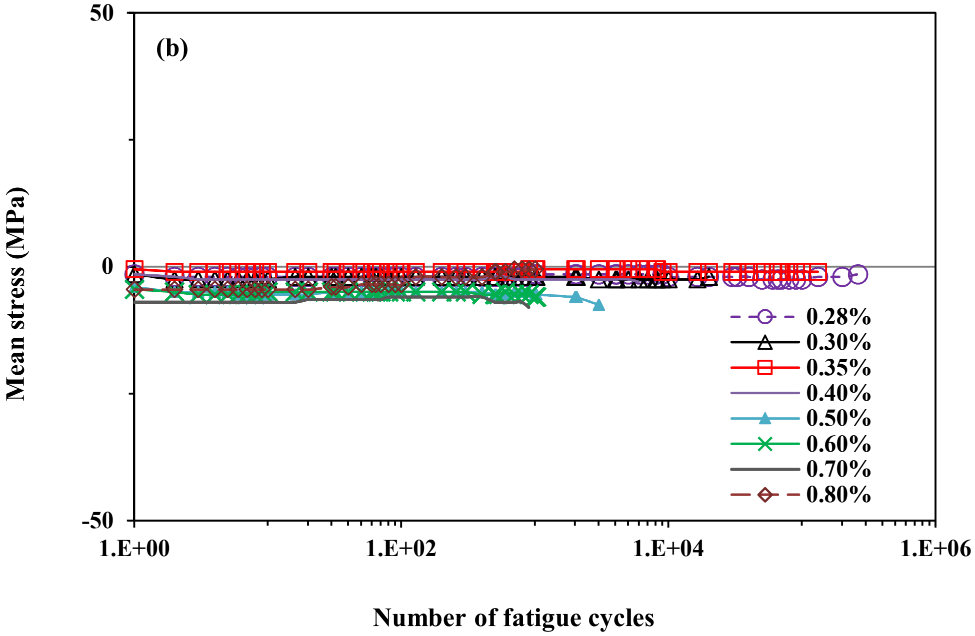
(b)
Mean stress (MPa)
50
0
-50
1.E+00
1.E+02
1.E+04
1.E+06
Number of fatigue cycles
0.28%
0.30%
0.35%
0.40%
0.50%
0.60%
0.70%
0.80%

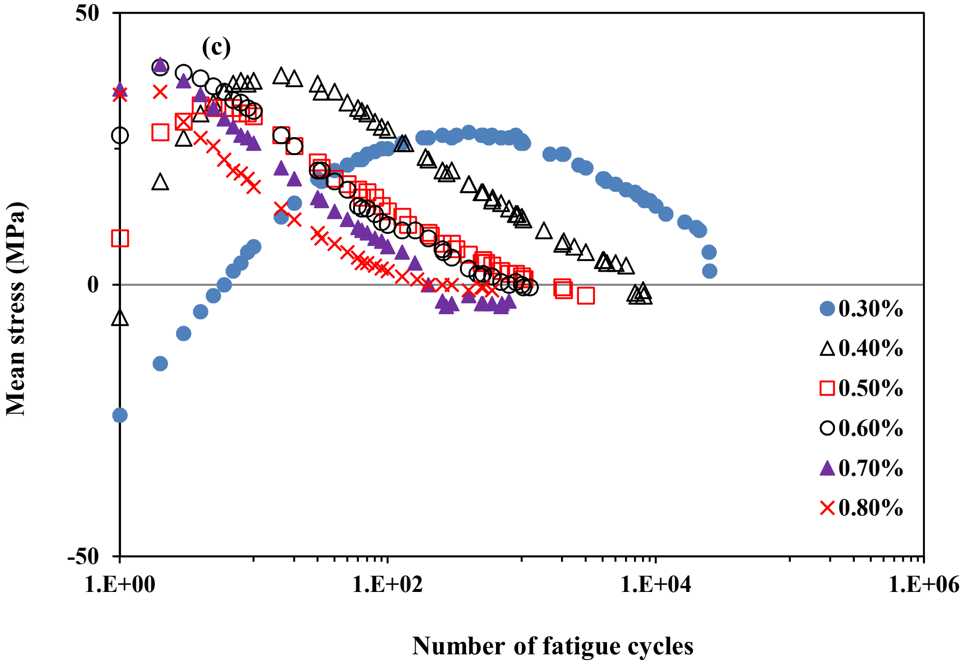

Figure 25: Mean stress evolution with number of cycles for the three alloys: (a) AW2099-T83, (b) ZK60A, and (c) AISI 410.

v. Axial Fatigue Life Correlation

The fatigue life is the number of cycles to failure for a given strain amplitude. Failure is defined here as the number of cycles at which the maximum load drops to 50% of its value during the fatigue cycle. Correlation between the strain amplitude and fatigue life in strain-controlled tests is given in a strain-life curve. By using Eq. (1.11) and (1.12), experimentally measured strain amplitudes and fatigue life for individual alloys is fitted to a linearized power curve to obtain the following fatigue properties: fatigue strength coefficient $(\sigma_f{}')$, fatigue strength exponent (b), fatigue ductility coefficient (ε_f') and fatigue ductility exponent (c). The resulting curves are given Fig. 26. It is worth mentioning that the regression fitting for AW20999-T83 is carried out for fatigue life less than 100,000 cycles while that for ZK60A is done for fatigue life ≤ 53000 cycles. Since, low cycle fatigue properties is the target, the data range selected helps to reduce scatter and improve accuracy [2,16]. The strain-controlled fatigue properties for the three alloy are presented in Table 13.

Low-cycle fatigue experimental data for the three alloy is scarce in published literature. Common aerospace grade alloy for which AW2099-T83 data can be compared are the 2xxx, 6xxx, and 7xxx series. The magnitude of |b| found in the current study is about twice the value reported for aluminum alloys 2024, 6082, 6060 and five times higher than that of AA6061 and AA7050 [132,134,135]. The fatigue strength coefficient is about three to eight times higher than those reported in the same work. The fatigue ductility parameters for ZK60A are about half the value reported for AZ31B [67,103] and AZ31[119] magnesium alloys. The fatigue parameters for AISI 410 stainless steel are lower than that reported for duplex steel by Chen et al [136].

The fatigue properties illustrated in Table 13 are employed to construct strain-life curves on a log-log scale in Fig. 27. The elastic and plastic strains correlations with fatigue life are also included in the figures. The characteristic strain-life curves show that life decreases with applied strain amplitude.

The curve fit for AW2099-T83, shown in Fig. 27(a) has the experimental fatigue data fairly distributed around it. Both the total and the elastic curve fits are superimposed since plastic strain is not observed for almost the entire range of strain amplitudes studied. Traditional aluminum alloys [132,134,135] have better Coffin-Manson fit than the investigated alloy. This attributable to the low plasticity behavior of AW2099-T83. Low cycle fatigue is associated with gross plastic deformation. Alloys with low plasticity usually exhibit high strength coefficient $(\sigma_f{}')$, but low ductility coefficient (ε_f'), causing the fatigue behavior to be dominated by elastic behavior, as was observed in the hysteresis loops in Fig. 20. Since the plastic strain data is insufficient to obtain a reliable curve fit for *c*, the equation for the curve fit in Fig. 27(a) for AW2099-T83 is just the Basquin equation. Therefore, the strain-life equation for AW2099-T83 is given in Eq. (4.3). Where ε_a is the applied strain amplitude and N_f is the fatigue life.

$$\varepsilon_a = \frac{1385.60}{80300}\left(2N_f\right)^{-0.131} \text{ ....(4.3)}$$

The strain-life curve for ZK60A shown in Fig. 27(b) exhibits a smooth curve profile while the plastic and elastic fittings are straight-line asymptotes. Fatigue life is within intermediate and high cycle fatigue. The developed Coffin-Manson curve fit for the alloy is given in Eq. 4.4.

$$\varepsilon_a = \frac{322.26}{44300}\left(2N_f\right)^{-0.088} + 1.5694\left(2N_f\right)^{-0.777} \text{ ....(4.4)}$$

The point of intersection of the elastic curve with the plastic curve defines the transition fatigue life, N_t. Transition fatigue life is where the elastic strain amplitude is equal the plastic strain amplitude. This strain is found to approximately 0.0038. Thus, by the applying Eq. (1.14), N_t is estimated to be about 1220 fatigue cycles. Prior to N_t the fatigue behavior is predominantly plastic.

Low cycle fatigue life of other magnesium alloys have been described by Coffin-Mason relation [67,119,137]. Correlation of uniaxial fatigue data of magnesium alloys with Coffin-Manson generally shows good fitting. Strain-life curve of magnesium alloys with kink have been correlated with three-parameter strain-life curves [47,67,118,120,138]. Considering the gap between the straight lines and the total strain-life curve, it is observed that at low strain amplitude the plastic strain effect is minimal as the curve is far from the total strain-life curve. However, at high strain amplitude, the plastic strain curve is closer to the total life-curve than the elastic strain-life line indicating that the former has the dominant effect.

The low cycle fatigue-life curve for AISI 410 is shown in Fig. 27(c). Good correlation is obtained with Coffin-Manson equation. Likewise, the elastic and plastic curves are straight lines, while the total strain-life plot shows a smooth curved profile. The transition life for the alloy is approximately 10,000 cycles. The Coffin-Manson equation for AISI 410 is given in Eq. (4.5):

$$\varepsilon_a = \frac{705.08}{208000}\left(2N_f\right)^{-0.058} + 0.1565\left(2N_f\right)^{-0.445} \text{............4.5}$$

The majority of the fatigue life is in the intermediate and low-cycle fatigue life region. Coffin-Manson relation is known to give a good correlation for uniaxial fatigue data of several low carbon and stainless steels [125–127,136,139].

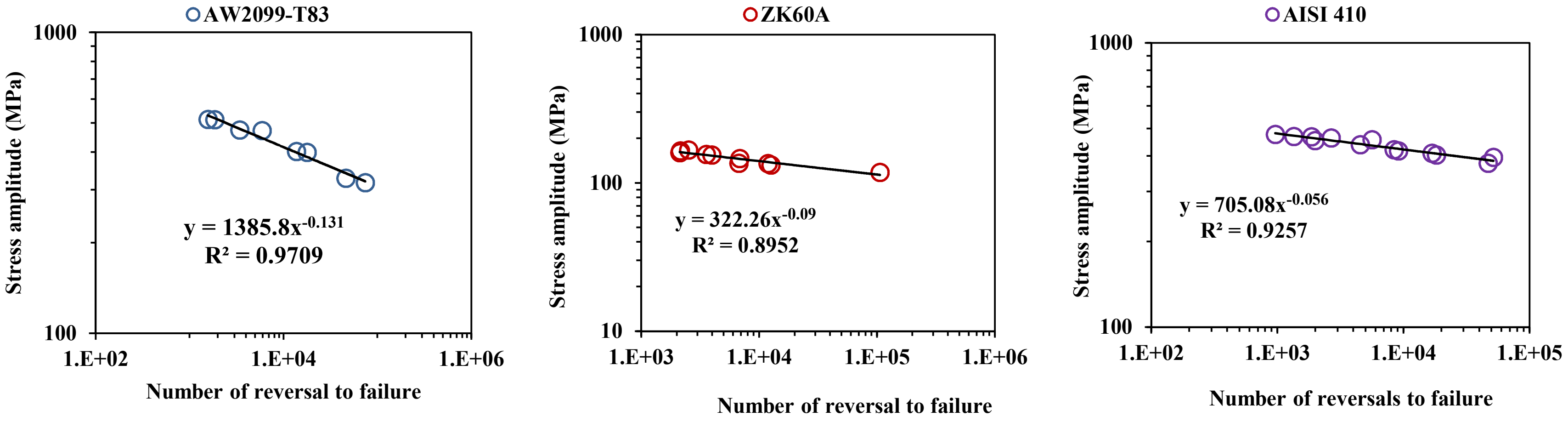

AW2099-T83
Stress amplitude (MPa)
1000
100
1.E+02
1.E+04
1.E+06
y = 1385.8x^-0.131
R² = 0.9709
Number of reversal to failure
ZK60A
Stress amplitude (MPa)
1000
100
10
1.E+03
1.E+04
1.E+05
1.E+06
y = 322.26x^-0.09
R² = 0.8952
Number of reversal to failure
AISI 410
Stress amplitude (MPa)
1000
100
1.E+02
1.E+03
1.E+04
1.E+05
y = 705.08x^-0.056
R² = 0.9257
Number of reversals to failure

(a)

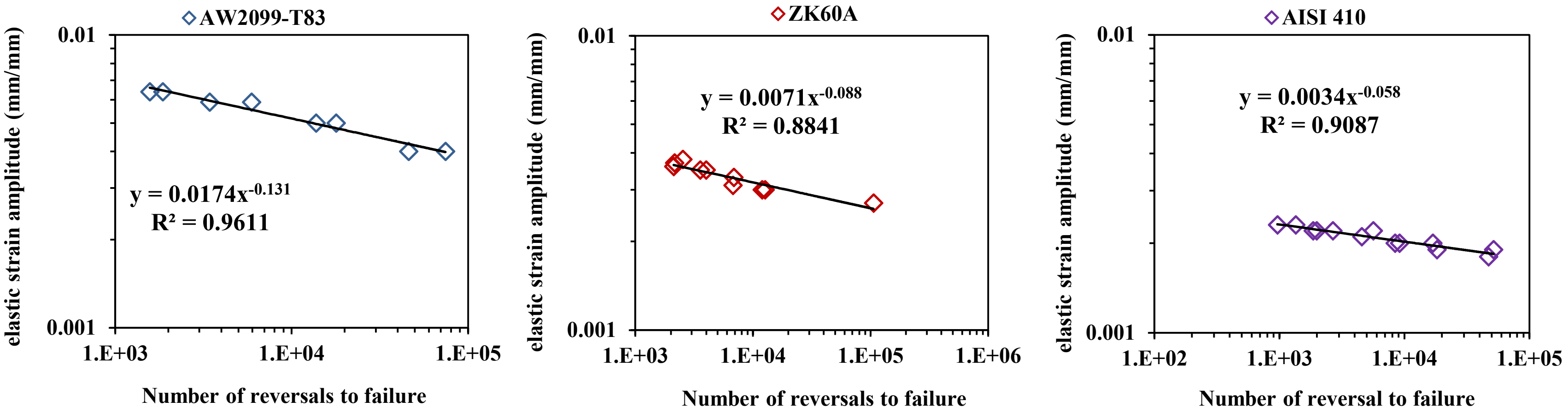

AW2099-T83
elastic strain amplitude (mm/mm)
0.01
0.001
1.E+03
1.E+04
1.E+05
y = 0.0174x^-0.131
R² = 0.9611
Number of reversals to failure
ZK60A
elastic strain amplitude (mm/mm)
0.01
0.001
1.E+03
1.E+04
1.E+05
1.E+06
y = 0.0071x^-0.088
R² = 0.8841
Number of reversals to failure
AISI 410
elastic strain amplitude (mm/mm)
0.01
0.001
1.E+02
1.E+03
1.E+04
1.E+05
y = 0.0034x^-0.058
R² = 0.9087
Number of reversal to failure

(b)

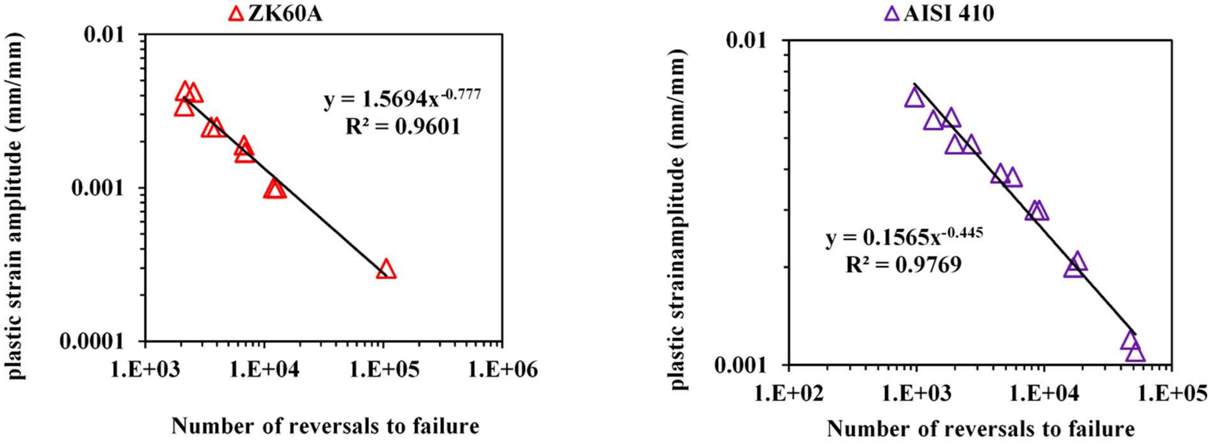

(c)

Figure 26: Regression curves to estimate the axial fatigue properties of the three alloys: (a) fatigue strength coefficient (b) fatigue strength exponent and (c) fatigue ductility coefficient and exponent.

Table 13: Axial fatigue properties of the three alloys.

Fatigue properties	AW2099-T83	ZK60A	AISI 410
σ_f' (MPa)	1385.6	322.26	705.08
b	-0.131	-0.088	-0.058
ε_f'	-	1.5694	0.1565
c	-	-0.777	-0.445
K' (MPa)	-	385.18	881.48
n'	-	0.1549	0.1238

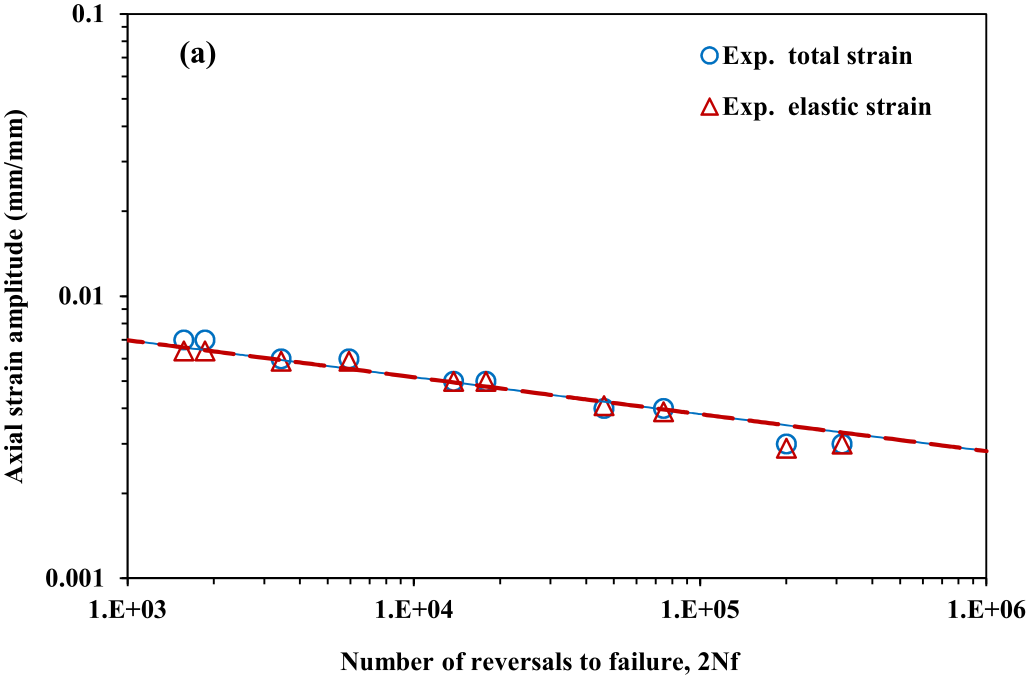

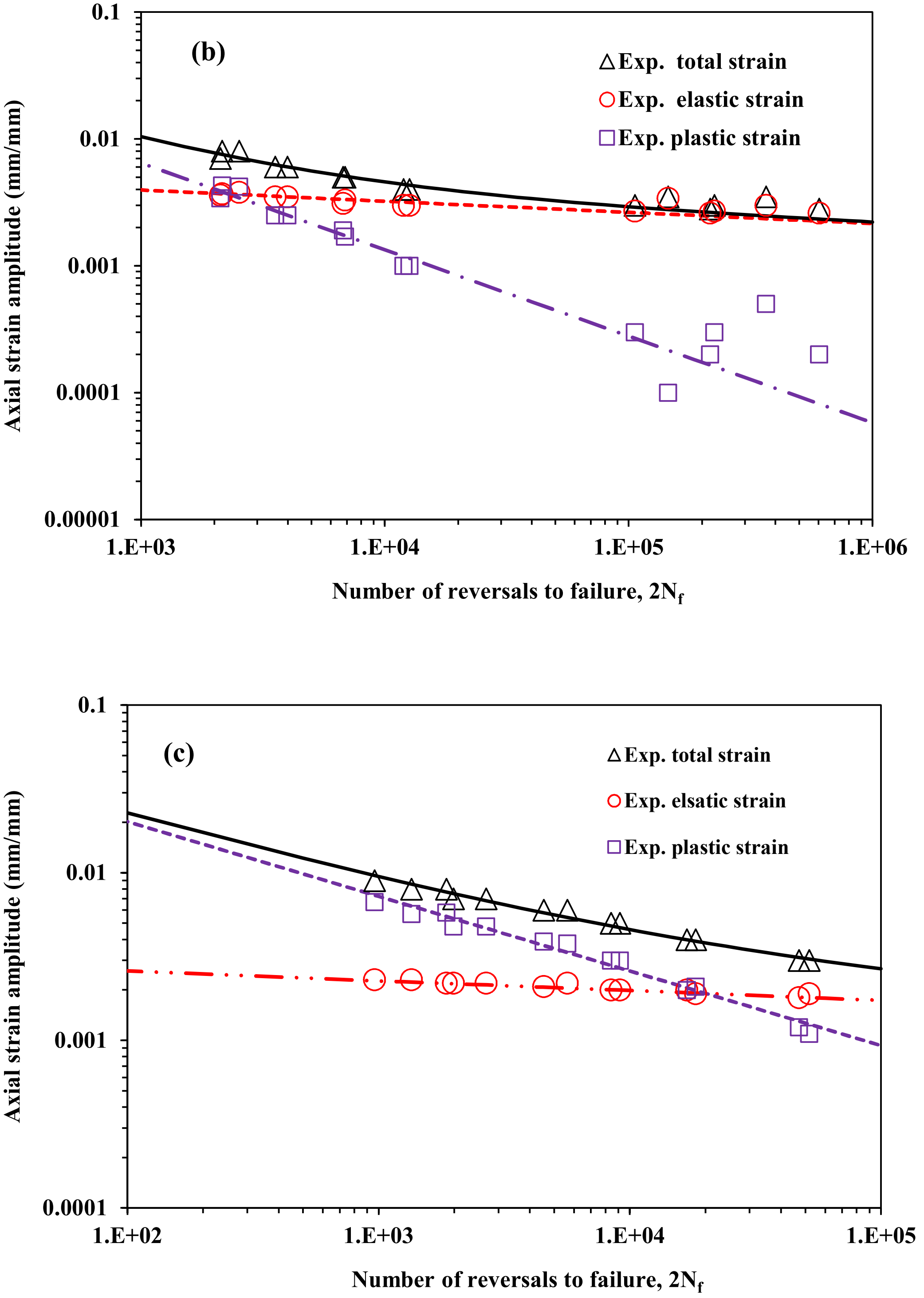

Figure 27: Axial strain-life curves for the three alloys: (a) AW2099-T83, (b) ZK60A, and (c) AISI 410.

4.4.2 Torsional Fatigue Behavior

i. Cyclic Shear Stress-Strain Curve

The results from the torsional cyclic tests for the three alloys are presented in Tables 14-16. These results have been obtained as follows: the shear stress amplitudes have been calculated using Eq. (1.16). Elastic strain amplitudes are estimated from Eq. (1.18), while plastic strain amplitudes are obtained by the application of Eq. (1.19). The fatigue life was recorded by the computer software of the testing machine. These results are used to estimate the shear fatigue parameters and shear-strain-life curves which are presented subsequently. Similar to the axial fatigue, life decreases with increasing shear strain amplitude due to rise in shear stress amplitude. The cyclic shear stress-strain curves are obtained in a similar manner as was described for axial fatigue tests in section 4.4.1. The shear plastic strain amplitudes for individual alloys in Table 14-16 are plotted against the shear stress amplitude to determine the shear strength coefficients, K_s' and exponents, n_s' as illustrated in Fig. 28 for the three alloys. K_s' is the slope of the curve while n_s' is the exponent in the equation of the line fit. These constants are then used to obtain the shear CSS given in Fig. 29 along with the Ramberg-Osgood fit.

Each curve in Fig. 29 shows a smooth deviation from the yield point. The data for AW2099-T83 does not fit well perhaps because of the few number of data points for plastic strain. The trend of the curves is precursor to the fact that stress evolution in AISI 410 will be higher, followed by that of AW2099-T83 and, lastly, ZK60A.

Table 14: Results and experimental parameters for cyclic torsion test for AW2099-T83 alloy.

Spec. ID	d_i (mm)	d_o (mm)	γ_a (%)	Freq. (Hz)	τ_{max} (MPa)	τ_{min} (MPa)	τ_a (MPa)	τ_m (MPa)	γ_e (%)	γ_p (%)	N_f (cycles)
PT5	7.95	9.95	0.5	0.35	122.74	-167.59	145.18	-22.43	0.5	0	30001
PT6	7.98	9.94	0.6	0.3	144.96	-204.96	184.96	-30	0.6	0	8115
PT7	7.96	9.96	0.6	0.3	142.43	-198.94	180.68	-28.26	0.6	0	5570
PT9	7.98	9.95	0.6	0.3	148.86	-196.67	182.77	-23.9	0.6	0	6482
PT3	7.97	9.96	0.7	0.25	185.14	-219.67	202.4	-18.26	0.7	0	2804
PT4	7.98	9.99	0.7	0.25	186.82	-220.33	203.58	-16.75	0.7	0	2255
PT11	7.95	9.95	0.75	0.2	198.91	-214.2	206.56	-7.64	0.75	0	844
PT12	7.97	9.95	0.75	0.2	193.2	-208.86	201.03	-7.83	0.75	0	959
PT1	7.97	9.97	1.0	0.1	208.27	-209.46	208.87	-0.59	0.77	0.23	316
PT2	7.94	9.97	1.0	0.1	208.98	-211.34	210.16	-1.18	0.78	0.22	340
PT8	7.97	9.97	1.5	0.06	246.05	-246.11	246.08	-0.03	0.9	0.6	55

Table 15: Results and experimental parameters for cyclic torsion test for ZK60A alloy.

Spec. ID	d_i (mm)	d_o (mm)	γ_a (%)	Freq. (Hz)	τ_{max} (MPa)	τ_{min} (MPa)	τ_a (MPa)	τ_m (MPa)	γ_e (%)	γ_p (%)	N_f (cycles)
ZK-PT13	7.96	9.98	0.4	0.5	54.96	-65.68	60.32	-5.36	0.35	0.05	1157265
ZK-PT10	7.97	9.97	0.6	0.4	71.94	-81.46	76.7	-4.76	0.45	0.15	82500
ZK-PT11	7.97	9.97	0.6	0.4	72.72	-83.97	78.35	-5.63	0.46	0.14	76161
ZK-PT1	7.96	9.95	0.8	0.2	86.99	-88.43	87.71	-0.72	0.52	0.28	13141
ZK-PT9	7.97	9.99	0.8	0.3	85.87	-91.83	88.85	-2.98	0.52	0.28	25936
ZK-PT12	7.99	9.99	0.8	0.3	87.27	-92.58	89.93	-2.66	0.53	0.27	18783
ZK-PT4	7.95	9.97	1	0.2	100.61	-101.88	101.25	-0.63	0.59	0.41	4203
ZK-PT8	7.98	9.99	1	0.3	99.95	-102.11	101.03	-1.08	0.59	0.41	4406
ZK-PT5	7.97	9.98	1.3	0.2	112.74	-115	113.87	-1.13	0.67	0.63	996
ZK-PT6	7.97	9.98	1.3	0.2	114.23	-114.44	114.34	-0.1	0.67	0.63	1165
ZK-PT2	7.98	9.96	1.5	0.1	114	-114.06	113.99	-0.07	0.67	0.83	628
ZK-PT3	7.98	9.96	1.5	0.1	118.35	-118.03	118.69	-0.34	0.69	0.81	506

Table 16: Results and experimental parameters for cyclic torsion test for AISI 410 alloy.

Spec ID	d_i (mm)	d_o (mm)	γ_a (%)	Freq. (Hz)	τ_{max} (MPa)	τ_{min} (MPa)	τ_a (MPa)	τ_m (MPa)	γ_e (%)	γ_p (%)	N_f (cycles)
SS-PT8	7.98	9.97	0.5	0.4	269.19	-271.01	270.1	-0.91	0.34	0.16	33055
SS-PT9	7.97	9.97	0.5	0.4	257.11	-260.8	258.96	-1.85	0.33	0.18	20965
SS-PT2	7.99	10.00	0.7	0.3	288.8	-288.75	288.78	0.02	0.36	0.34	8973
SS-PT3	7.97	9.97	0.7	0.3	283.62	-284.4	284.01	-0.39	0.36	0.34	9132
SS-PT6	7.98	9.93	1.5	0.1	335.14	-336.08	335.61	-0.47	0.42	1.08	483
SS-PT7	7.98	9.99	1.5	0.1	328.56	-328.39	328.48	0.09	0.41	1.09	541

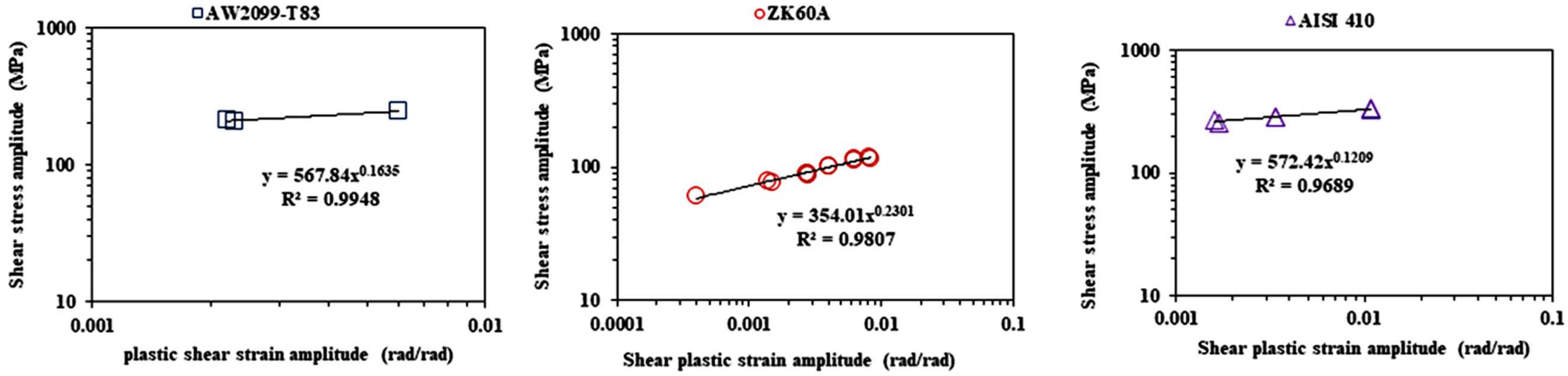

Figure 28: Regression curves to estimate shear strength coefficient K_s' and exponent, n_s' for the three alloys.

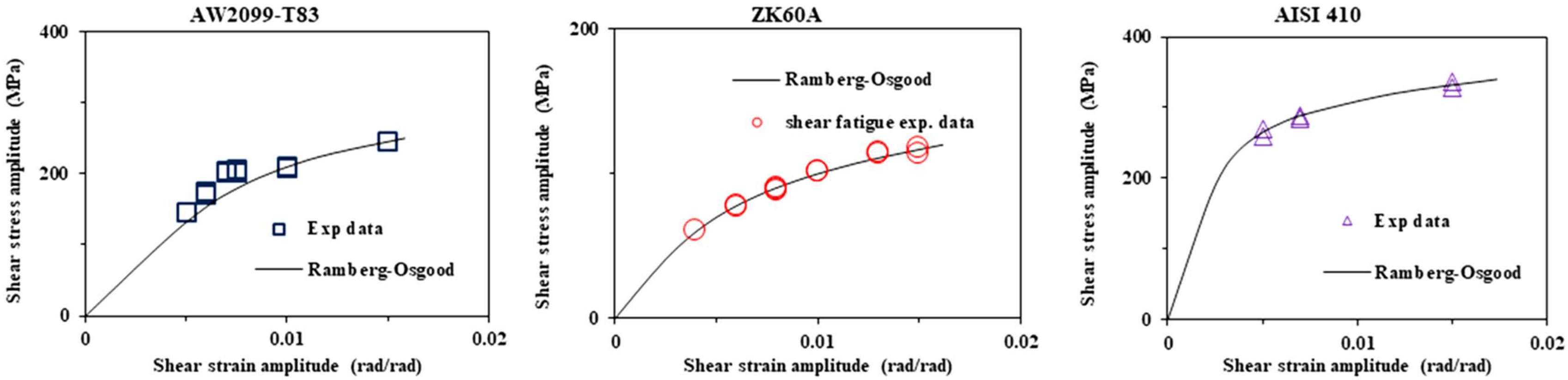

Figure 29: Cyclic shear stress-shear strain curves for the three alloys.

ii. Hysteresis Loop Evolution

The characteristic hysteresis loops at second and half-life cycles are shown in Figs. 30, 31 and 32, for AW2099-T83, ZK60A and AISI 410, respectively. As previously mentioned in section 4.4.1, the second cycle is chosen being the first complete loop, while at half-life, the fatigue cycle is considered to have stabilized. As can be seen from Table 14 and from Fig. 30, AW2099-T83 alloy shows no shear plastic strain until at applied shear strain amplitude of 0.75%. Measurable shear plastic strain for the alloy starts at an applied strain amplitude of 1.0%. It means that prior to a strain amplitude of 0.75% the shear deformation is elastic. This behavior can be attributed to alloy with high strength but low ductility. Strong alloys resist cyclic deformation in elastic mode [117]. It can be noticed that at applied strain amplitudes of 1.0 and 1.5%, plastic strain amplitude increases with the number of cycles. This is similar to the behavior earlier observed in axial hysteresis loop evolution at applied strain amplitudes where measurable plastic strain manifested. Therefore, similar to the axial fatigue, fatigue damage is increasing with the number of fatigue cycles at higher strain amplitudes.

Figure 31 illustrates the hysteresis loop evolution for ZK60A alloy. Plastic strain developed at all levels of applied strain amplitude. Likewise, plastic strain increases with increase in the applied strain amplitude. It can be seen that there is no change in plastic strain magnitude between the second and half-life cycle, meaning that fatigue damage is nearly completed in the first few cycles. This is similar to the hysteresis loop evolution in axial fatigue. However, no concavity is observed in the hysteresis loop for shear fatigue. This probably supports the inference drawn in section 4.4.1 that the concavity in the axial hysteresis loop is due to twinning effect. Twinning-detwinning phenomenon only occurs in axial loading mode for textured magnesium alloy under uniaxial loading [16,103,138].

The evolution of hysteresis loop with applied strain amplitudes for AISI 410 is illustrated in Fig. 32. Similar to the axial fatigue, the alloy exhibits wide hysteresis loops with substantial plastic strain especially at large applied strain amplitudes. It can be observed that plastic strain amplitudes increase with the number of cycle signifying the accumulation of fatigue damage with the number of cycles.

As a summary, the characteristic hysteresis loop from each of the alloy depends on the strength and ductility as was previously discussed for axial fatigue in section 4.4.1. For a strong, less ductile alloy like AW2099-T83, slim hysteresis loop evolves because the alloy possess the strength to resist the applied strain, resulting to high stress but low plastic deformation. However, for soft alloy, as is the case for ZK60A, the resistance to cyclic strain is weak. Therefore, a considerable amount of plastic strain is experienced. For tough alloy like AISI 410, the hysteresis loop is in-between that of a weak and strong alloys.

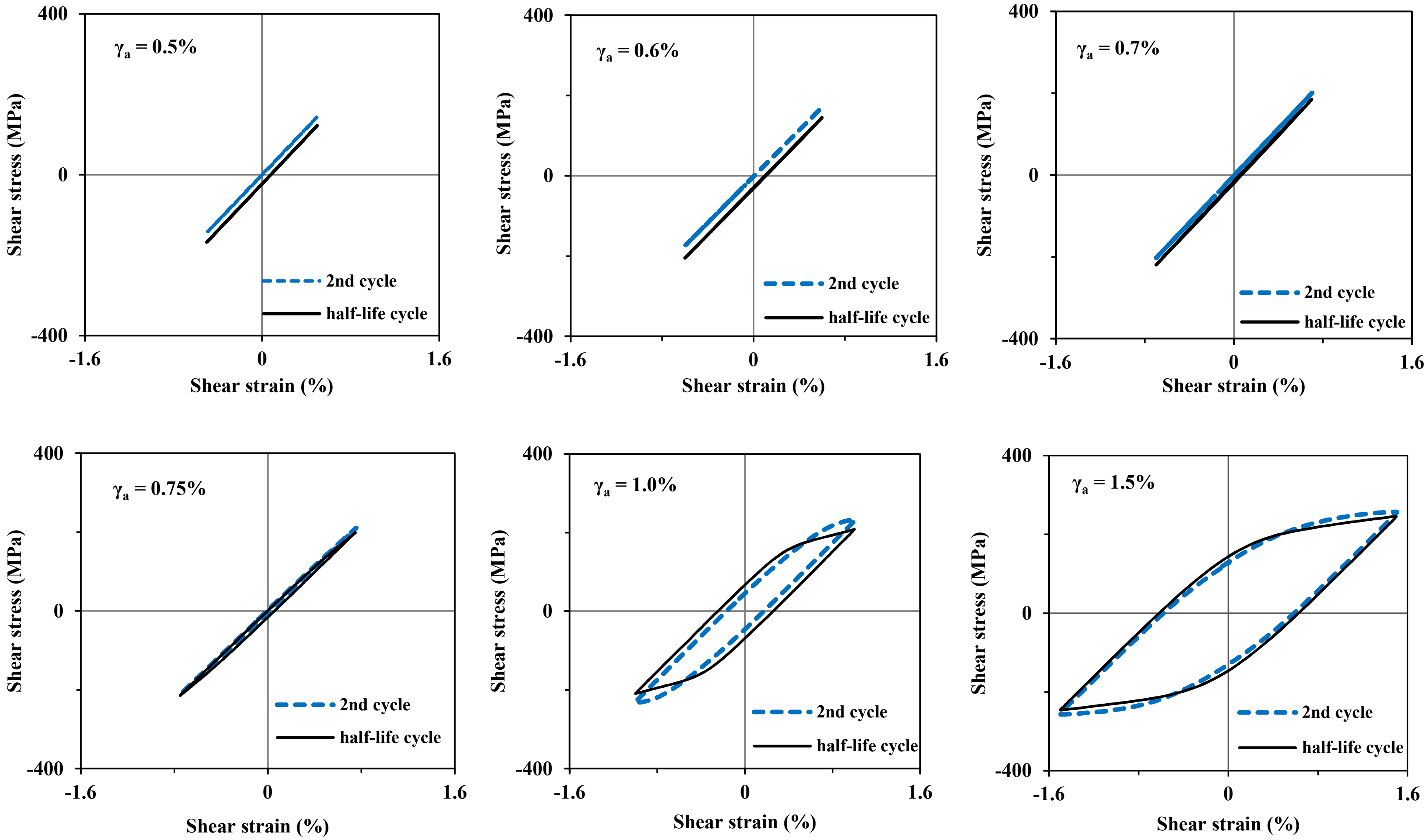

Figure 30: Shear hysteresis loop evolution for AW2099-T83 for all the shear strain amplitudes studied.

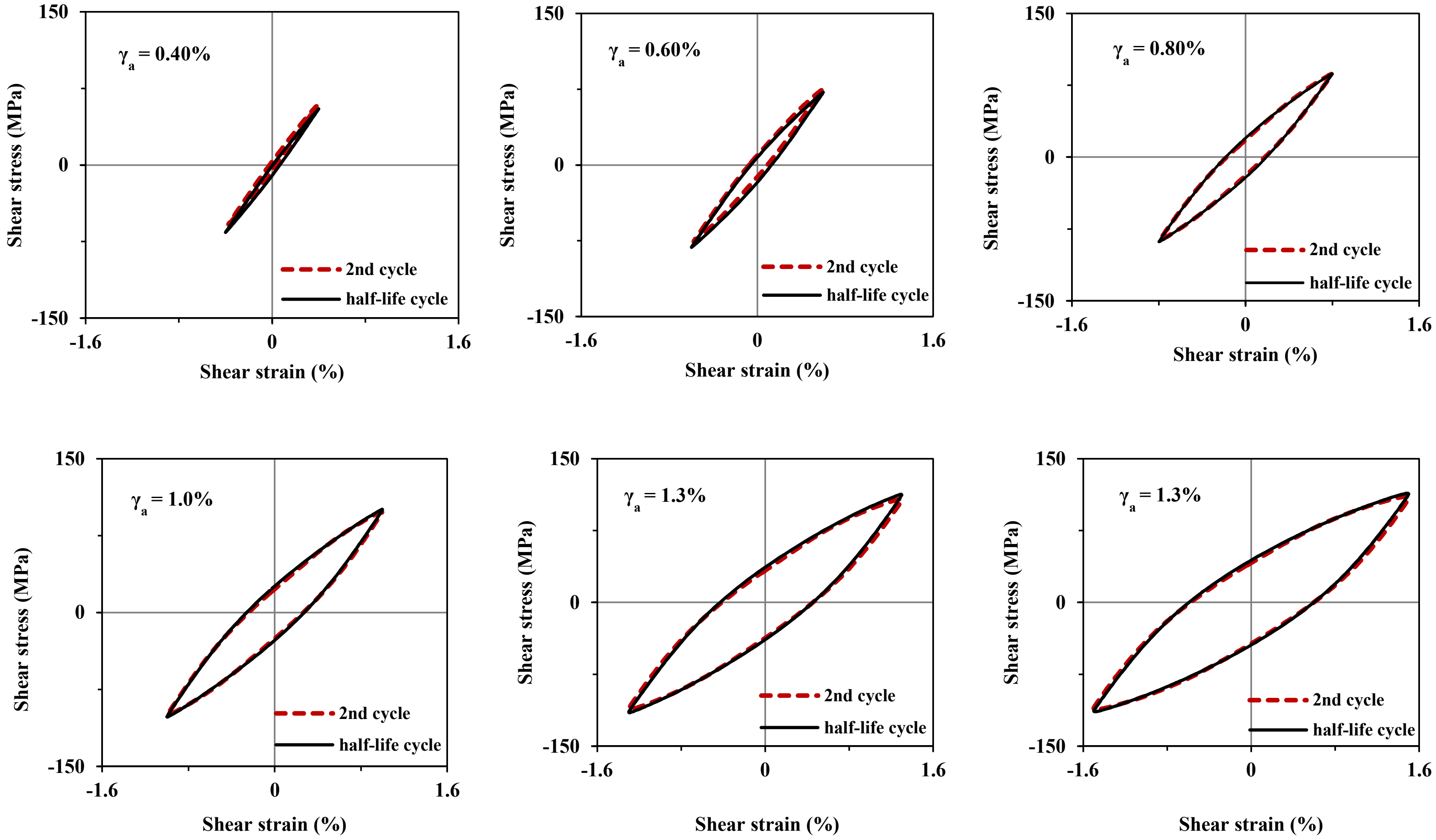

Figure 31: Shear hysteresis loop evolution for ZK60A for all the shear strain amplitudes studied.

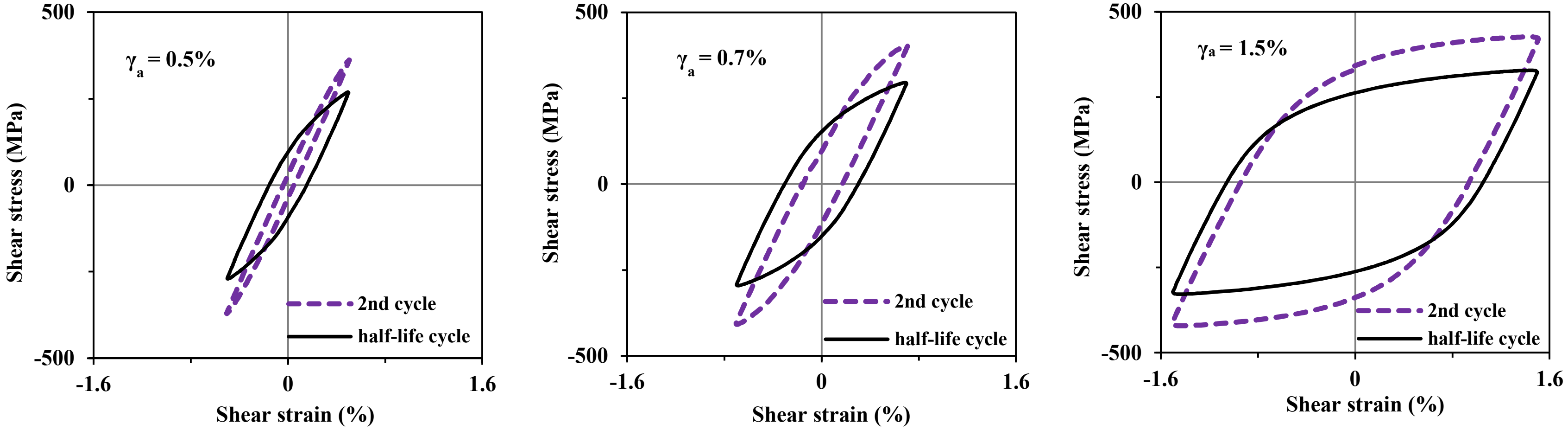

Figure 32: Shear hysteresis loop evolution for AISI 410 for all the shear strain amplitude studied.

iii. Cyclic Shear Stress Response

The cyclic shear stress evolutions with the number of cycles for the three alloys are presented in Figs. 33(a)-(c) on a semi-log scale. Figure 33(a) shows that the cyclic shear stress response of AW2099-T83 is that of a cyclic softening material. There are an initial stress stabilization and little cyclic hardening in the first-five circle at applied shear strain amplitudes greater than or equal to 1%. Plastic strain deformation is observed at these applied strain amplitudes. This behavior is similar to the observation in axial fatigue where cyclic hardening is observed in the early fatigue cycles for strain amplitudes where plastic strain becomes significant. From Fig. 33(a), it can be noticed that with increasing number of fatigue cycles, the curves further deviate downward. This indicates fatigue damage due to cracking. This will be confirmed by crack analysis in a later section.

Figure 33(b) is the cyclic shear stress curve for ZK60A. There is no substantial difference in the cyclic shear stress trend at all strain amplitudes investigated. Although, a discrete analysis of individual curve shows that cyclic softening occurs at the lowest applied strain amplitude of 0.28%. While at applied strain amplitude of 1.5%, slight cyclic hardening of about 1-2 MPa is noticed. Therefore, the trend of cyclic shear stress evolution for ZK60A is unchanged with the number of fatigue cycle and applied strain amplitude.

There is no ambiguity in the cyclic stress response of AISI 410 as shown in Fig. 33(c). The trend by which the cyclic stress varies with the number of cycles at each of the applied strain amplitude is constant. Cyclic stress softening occurred from the first cycle to failure at all strain amplitudes. The rate of softening, as can be measured from the slope of the curves, is independent of applied strain. The consistence in the stress behavior can be related to the microstructure of the alloy, the microstructure of AISI 410 alloy is the same in all orientations and locations as illustrated in Fig. 14 in section 4.2. Microstructural influence on the cyclic stress behavior of the alloys has been discussed earlier in section 4.4.1.

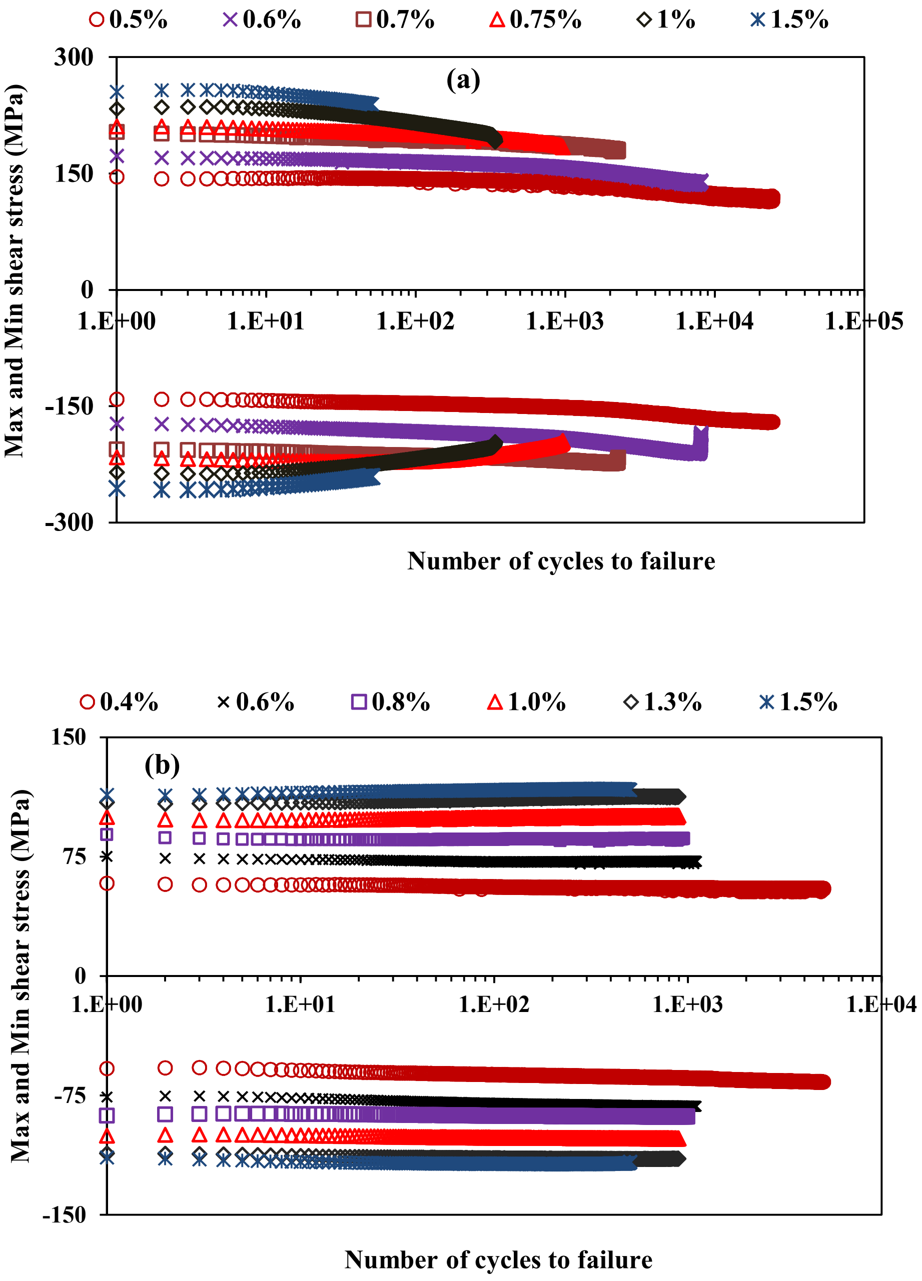

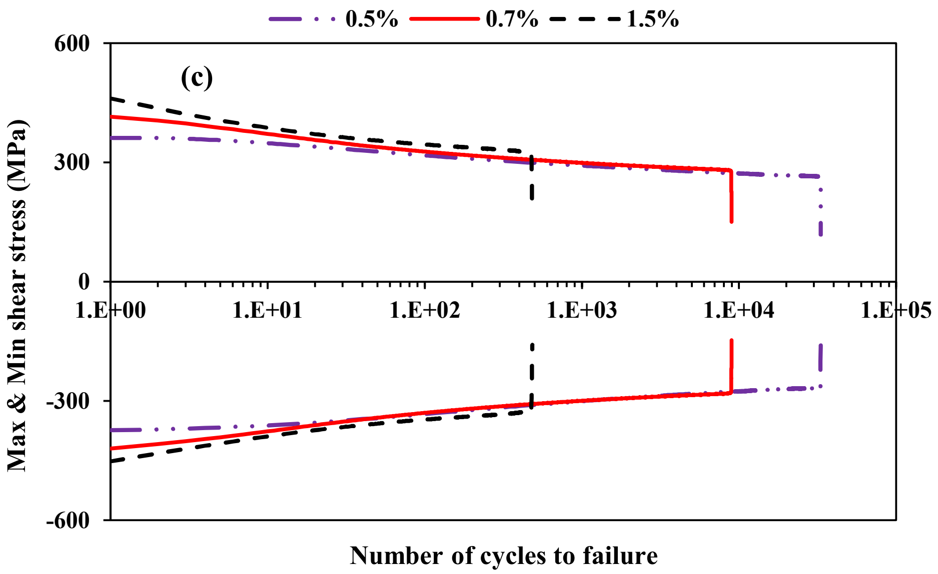

Figure 33: Shear stress evolution with the number of cycles for the three alloys: (a) AW2009-T83, (b) ZK60A and (c) AISI 410.

iv. Shear Mean Stress Evolution

Mean stress evolution as shown in Fig. 34(a) for AW2099-T83 indicates that negative mean stress evolves with the number of cycles especially at applied strain level where plastic strain is absent. With increase in applied strain amplitude, the mean stress value tends to become positive. A compressive mean stress of about -40 MPa is observed at the lowest strain amplitude of 0.5%. This increases toward positive value as applied strain amplitude is increased, becoming nearly zero at shear amplitude of 1 and 1.5%. The trend in the mean stress here differs from that observed in axial fatigue. While the axial mean stress rises with the number of fatigue cycle, the shear mean stress tends to become more compressive in nature as the number of fatigue increases for a given total strain amplitude.

Figure 34(b) shows the shear mean stress evolution with cycle for ZK60A. The overall shear mean stress is compressive but negligible. It indicates there is no variation between the tensile and compressive peak stresses. The maximum mean stress observed is about 10 MPa in compression, which is achieved at the maximum lowest applied strain amplitude of 0.4%.

The shear mean stress for AISI 410 as illustrated with Fig. 34(c) is in compressive mode. There is no significant variation with increase in applied strain amplitude and the number of cycles. Separate analysis of the curves would indicate that mean stress was initially positive for the largest applied strain amplitude of 1.5% before it assumes negative value after about five cycles. In addition, at applied strain amplitude 0.5%, fluctuation of the mean stress can be seen. However, these variations do not contribute any significant change to the general trend of the mean stress.

As already discussed in section 4.4.1, mean stress results due to peak stress asymmetry. The mean stress evolution for the alloys under shear loading show variation for the different structure. It can be concluded that mean stress is also plastic strain dependent. With increased plastic strain, the shear mean stress tends to become tensile.

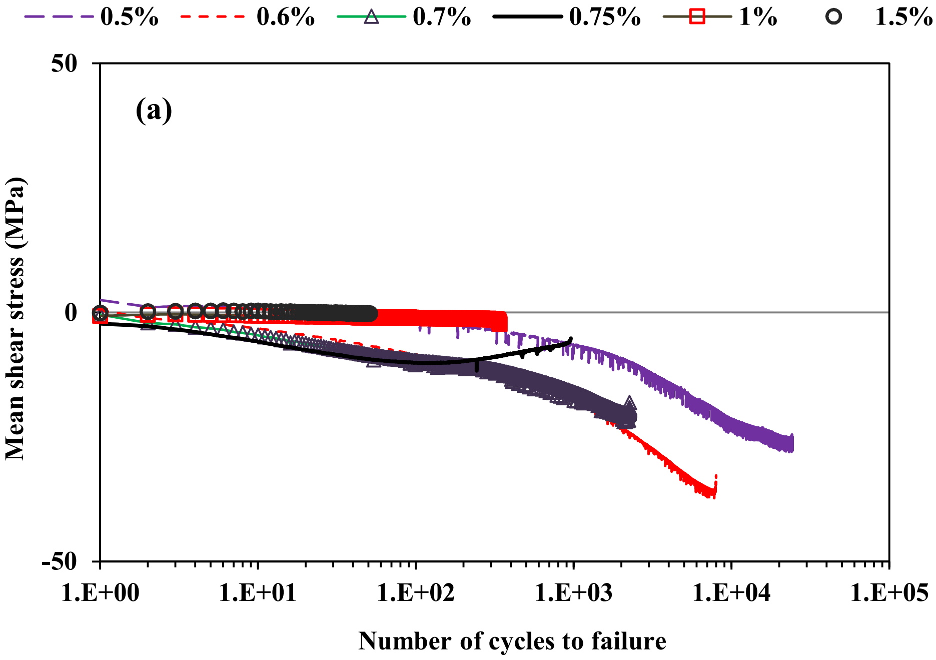
0.5%
0.6%
0.7%
0.75%
1%
1.5%
50
(a)
0
-50
Mean shear stress (MPa)
1.E+00
1.E+01
1.E+02
1.E+03
1.E+04
1.E+05
Number of cycles to failure

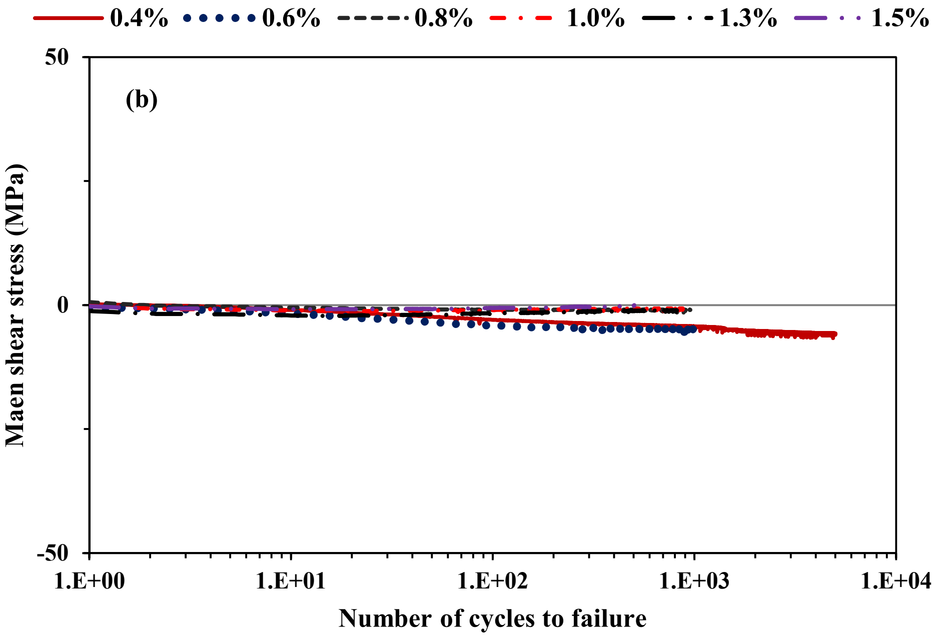
0.4%
0.6%
0.8%
1.0%
1.3%
1.5%
50
(b)
0
-50
Maen shear stress (MPa)
1.E+00
1.E+01
1.E+02
1.E+03
1.E+04
Number of cycles to failure

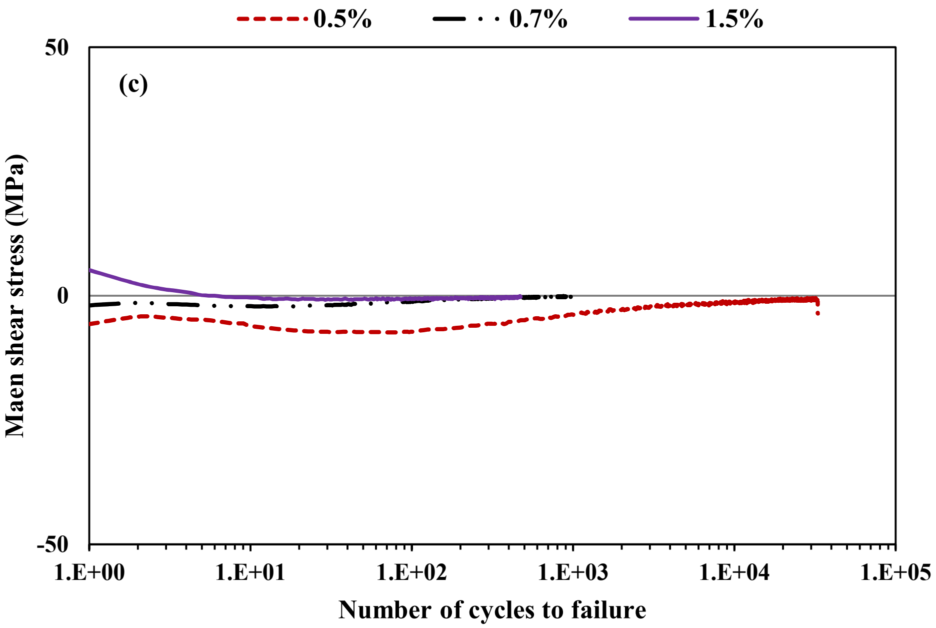

Figure 34: Means stress vs. the number of fatigue cycles for the three alloys: (a) AW2009-T83, (b) ZK60A and (c) AISI 410.

v. Shear Fatigue Life Correlation

The shear fatigue life here is defined as the number of cycle when the maximum torque achieved drops to 50% of its value. Torsional fatigue parameters are obtained from regression curves in Fig. 35 according to Eq. (1.22) and (1.23). These parameters, presented in Table 17, are the shear fatigue strength coefficient ($\tau_f{}'$), fatigue ductility coefficient (ε_f'), shear fatigue strength exponent (b_s) and shear fatigue ductility exponent(c_s). Torsional fatigue data are not as common as axial fatigue is. To make a comparison with the axial fatigue data, the torsional fatigue data are first converted to axial equivalent using the set of approximations in Eq. (4.6) [2]. Where $\tau_f'\ and\ \sigma_f'$ are the torsional and axial fatigue strength coefficients, $\gamma_f'\ and\ \varepsilon_f'$ are the torsional and axial fatigue ductility coefficients. Similarly, $b \, and \, b_s$ are the torsional and axial fatigue strength exponents, while $c \, and \, c_s$ are the torsional and axial fatigue ductility exponents.

$$\tau_f' \approx \frac{\sigma_f'}{\sqrt{3}} \text{……….(4.6a)} \qquad \gamma_f' \approx \varepsilon_f' \sqrt{3} \text{……….(4.6b)}$$

$$b \approx b_s \text{……….(4.6c)} \qquad c \approx c_s \text{……....(4.6d)}$$

Based on Eq. (4.5a)-(4.5d), it can be concluded that the shear fatigue parameters are lower than those of the alloys [132,134,135] with which axial fatigue parameters were compared in section 4.4.1. The fatigue parameters for individual alloys are used to develop shear strain-life curves illustrated in Fig. 36 on a log-log scale. The data for elastic and plastic strains have also been used to develop fitting lines on same scale. It can be seen that fatigue life decrease with increase in strain amplitude.

Figure 36(a) is the shear strain-life curve for AW2099-T83 and the corresponding curve equation is given in Eq. (4.7). A good fit is achieved for the fatigue data and developed curve. The strain-life curve generally approaches the elastic line compare to the plastic line. This is because majority of the strain amplitude applied produces no plastic strain as is evident in Fig. 30. The transition life is approximately 25 fatigue cycles. The position of the transition life signifies that no substantial plasticity occurred during the fatigue cycle.

$$\gamma_a = \frac{353.15}{27100}\left(2N_f\right)^{-0.089} + 0.0795\left(2N_f\right)^{-0.55} \dots\dots\dots\dots\dots (4.7)$$

In section 4.4.1, the axial fatigue data for AW2099-T83 was used to develop a fatigue curve that fitted the Basquin equation due to the absence of ductility parameters arising from low plasticity. Now, with the combination of the set of Eq. (4.6) and the shear fatigue constants, an equivalent axial Coffin-Manson equation can be derived. The derived equation is given in Eq. (4.8). It can be deduced from the equation that fatigue strength of the alloy expectedly decreases as the fatigue ductility rises.

$$\varepsilon_a = \frac{611}{80300}\left(2N_f\right)^{-0.089} + 0.046\left(2N_f\right)^{-0.55} \ldots\ldots\ldots\ldots..(4.8)$$

The shear strain curve for ZK60A is given in Fig. 36(b) and the corresponding Coffin-Manson strain-life equation is given in Eq. (4.9). The transition life is found to be approximately 1000 fatigue life. Good correlation is achieved between data and the curve. Similar curve has been reported for AZ31B by Albinmousa [103].

$$\gamma_a = \frac{218.10}{16900}\left(2N_f\right)^{-0.085} + 0.082\left(2N_f\right)^{-0.33} \ldots\ldots\ldots\ldots\ldots(4.9)$$

Similarly, the shear strain-life curve for AISI 410 is illustrated in Fig. 36(c) and the Coffin-Mason equation is similarly given in Eq. (4.10).

$$\gamma_a = \frac{488.44}{79400}\left(2N_f\right)^{-0.053} + 0.2716\left(2N_f\right)^{-0.46} \ldots\ldots\ldots\ldots\ldots(4.10)$$

Although, a narrow range of shear strain amplitude was studied for AISI 410, the trend for the fatigue life curve can be imagined. The close proximity that is maintained between the strain-life curve and the elastic fit line in an evidence of substantial plasticity. This agrees with the observation in the hysteresis loop evolution earlier discussed in this section. The transition life is estimated to be around 9000 fatigue cycles.

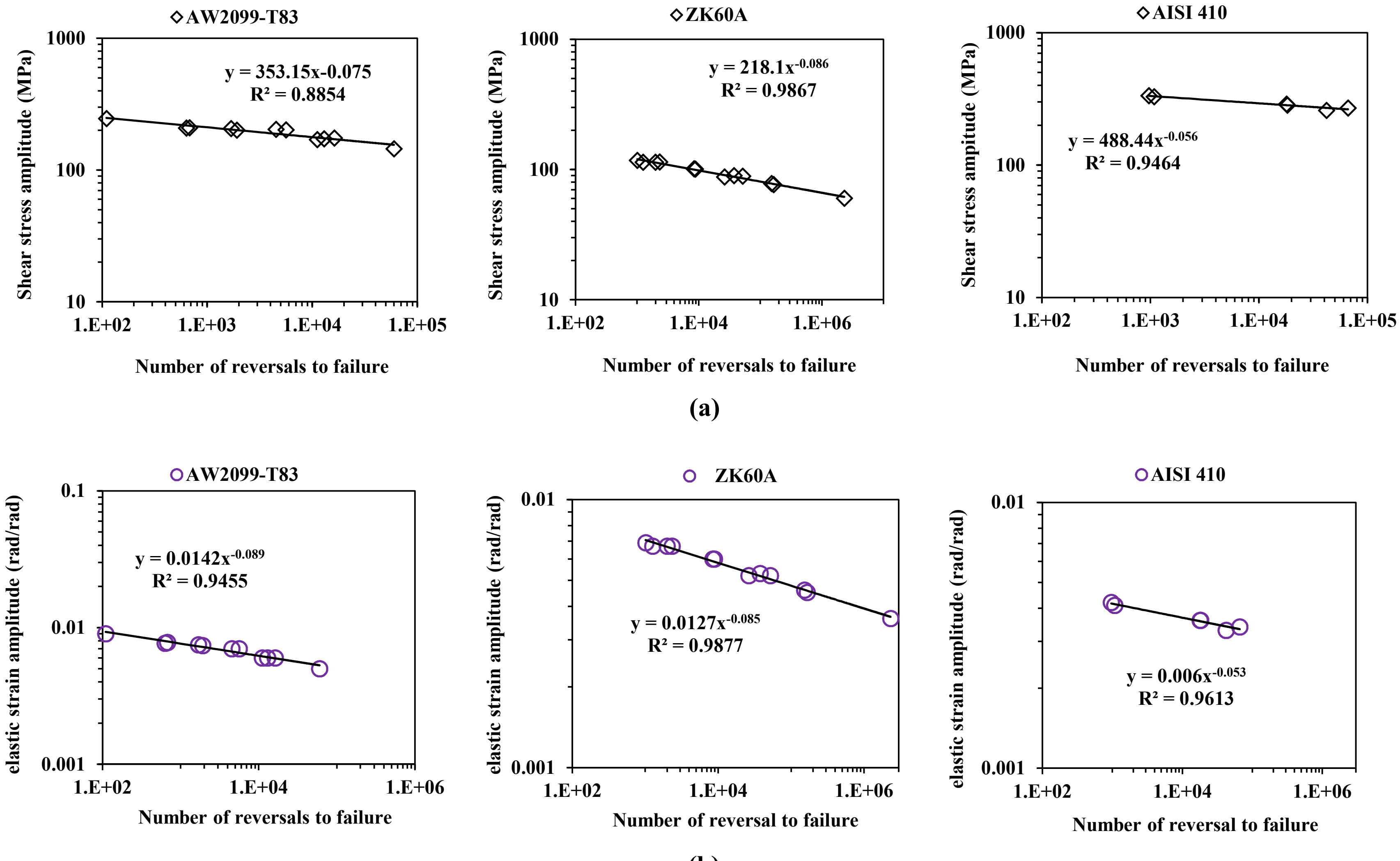
◇AW2099-T83
y = 353.15x-0.075
R² = 0.8854
Shear stress amplitude (MPa)
1000
100
10
1.E+02
1.E+03
1.E+04
1.E+05
Number of reversals to failure
◇ZK60A
y = 218.1x^-0.086
R² = 0.9867
Shear stress amplitude (MPa)
1000
100
10
1.E+02
1.E+04
1.E+06
Number of reversals to failure
◇AISI 410
y = 488.44x^-0.056
R² = 0.9464
Shear stress amplitude (MPa)
1000
100
10
1.E+02
1.E+03
1.E+04
1.E+05
Number of reversals to failure
○AW2099-T83
y = 0.0142x^-0.089
R² = 0.9455
elastic strain amplitude (rad/rad)
0.1
0.01
0.001
1.E+02
1.E+04
1.E+06
Number of reversals to failure
○ ZK60A
y = 0.0127x^-0.085
R² = 0.9877
elastic strain amplitude (rad/rad)
0.01
0.001
1.E+02
1.E+04
1.E+06
Number of reversal to failure
○AISI 410
y = 0.006x^-0.053
R² = 0.9613
elastic strain amplitude (rad/rad)
0.01
0.001
1.E+02
1.E+04
1.E+06
Number of reversal to failure

(a)

(b)

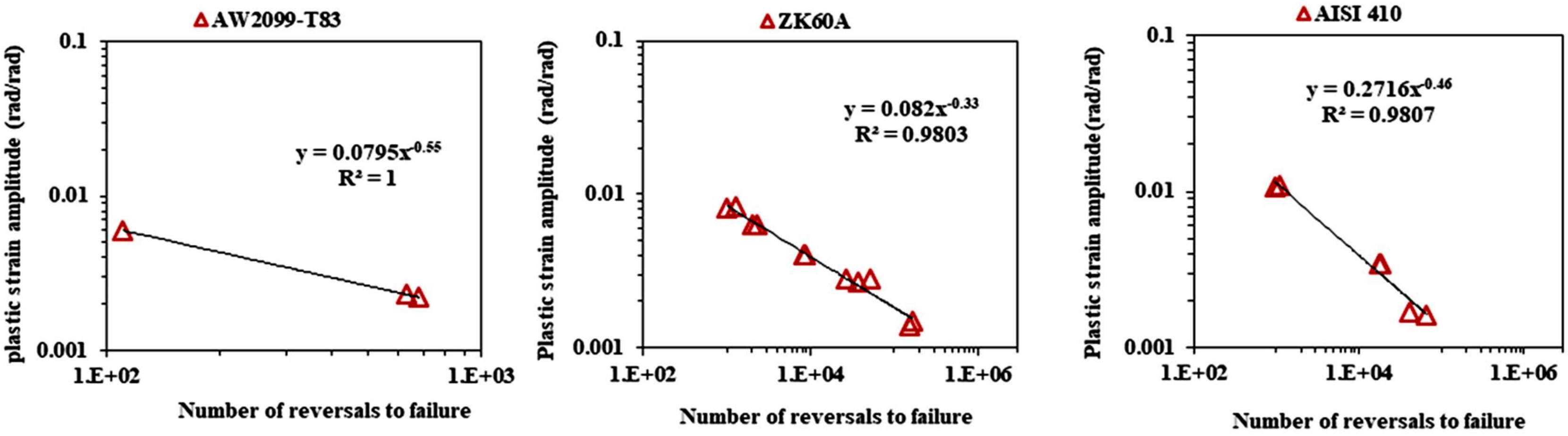

(c)

Figure 35: Regression curves to estimate the shear fatigue properties for the three alloys: (a) fatigue strength coefficient (b) fatigue strength exponent and (c) fatigue ductility coefficient and exponent.

Table 17: Strain-controlled shear fatigue properties for the three alloys.

Shear fatigue properties	AW2099-T83	ZK60A	AISI 410
τ_f' (MPa)	353.15	218.1	488.44
b_s	-0.089	-0.085	-0.053
γ_f'	0.0795	0.082	0.2716
c_s	-0.55	-0.33	-0.46
K'_s (MPa)	567.89	354.01	572.42
n'_s	0.1635	0.2301	0.1209

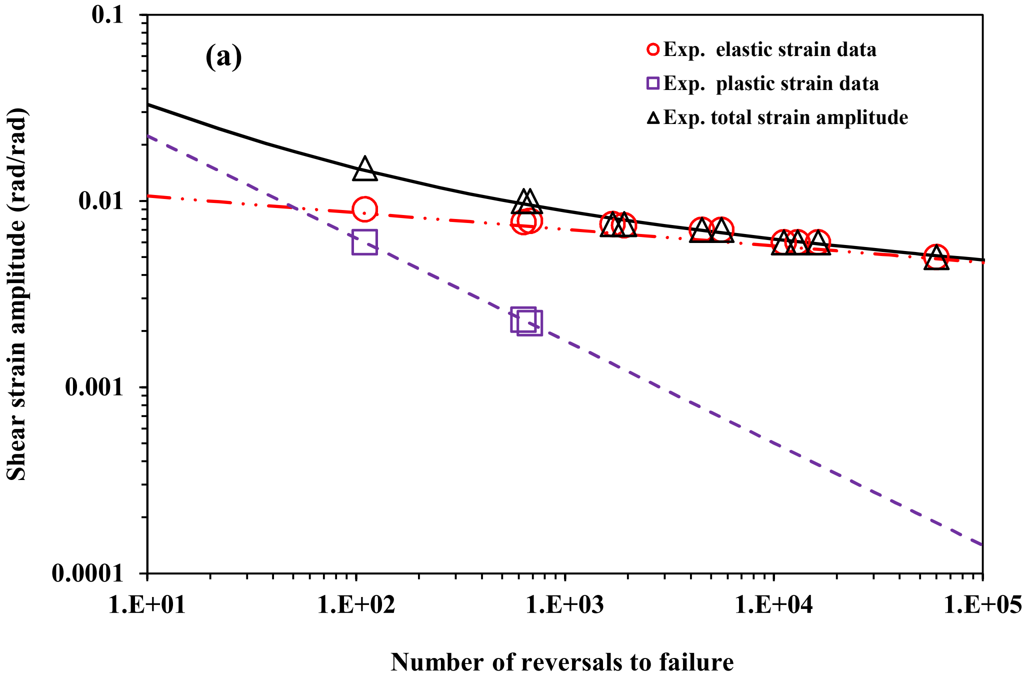

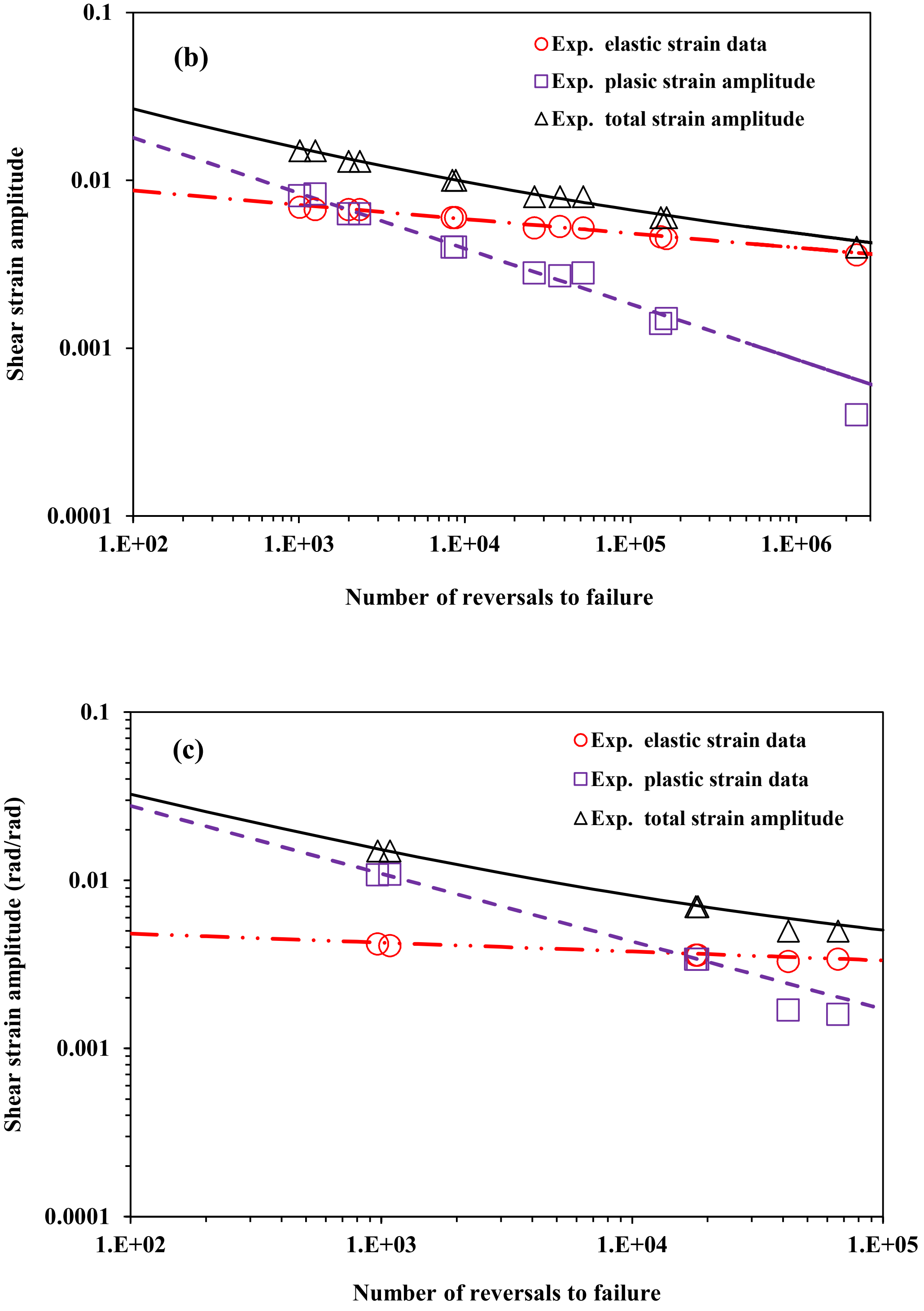

Figure 36: Shear strain-life curve for the three alloys: (a) AW2009-T83, (b) ZK60A, and (c) AISI 410.

4.5 Multiaxial Fatigue Behavior

The experimental results obtained from multiaxial fatigue tests described in section 3.5 for AW2099-T83, ZK60A and AISI 410 are presented in Table 18-20. These include axial stress amplitude (σ_a), shear stress amplitude (τ_a), axial elastic strain (ε_e), axial plastic strain (ε_p), shear elastic strain (γ_e) and shear plastic strain (γ_p). The stress amplitudes are estimated from Eq. (1.3) and (1.16) for the axial and shear stress, respectively. The elastic and plastic strains amplitudes for axial mode are found from Eq. (1.6) and (1.7). Correspondingly, elastic and plastic strain components for shear mode are calculated from (1.18) and (1.19). The normalization process used to select the applied biaxial strain amplitudes for each of the alloy after taking into account the monotonic behavior of the materials was previously discussed in section 3.5.

4.5.1 Effect of Strain Amplitudes and Phase Angle on Stress Evolution and Fatigue Cycles

As can be seen from Table 18 for AW2099-T83, both the fatigue life (N_f) and cyclic stress response vary with change in strain amplitudes and phase angle, θ. Increase in the applied shear strain amplitude from 0.66% to 0.76% for a constant axial strain of 0.53% causes a reduction in the cyclic axial stress in both proportional and nonproportional loading modes by 7% and 9%, respectively. The corresponding cyclic shear stresses, increase by 6% in the proportional loadings and 12% in nonproportional loadings. The effect of this is the drop in fatigue life by 28% in the proportional loading path and by 62% in the nonproportional loading mode. Correspondingly, the change in the phase angle from 0° to 90° at applied biaxial strain amplitudes of ε_a,γ_a = 0.53%, 0.66% results to a rise in the fatigue life by 39%. Conversely, for the same change in phase angle from 0° to 90°, at applied biaxial strain amplitudes of $\varepsilon_{a,}\gamma_a$ = 0.53%, 0.76%, the fatigue life decreases by 13%.

Table 19 presents the multiaxial fatigue data for ZK60A alloy. Under proportional loading, increase in shear strain amplitude from 0.4% to 0.46% with a constant axial strain amplitude of 0.32%, the axial stress rises by 30%, but the shear stress decreases by 12%. The fatigue life is reduced on the average by 55%. For similar shear strain variation at a fixed axial strain amplitude of 0.43%, the resulting change in axial stress amplitude is negligible while the shear strain amplitude increases by 9% and fatigue life is decreased marginally by 5%. However, with change in the phase angle from 0° to 90°, at applied strain amplitudes of $\varepsilon_{a,}\gamma_a$ = 0.32%, 0.4%, fatigue life increases by 140%, while axial stress amplitude increase by 7% and the shear stress amplitude by 11%. Likewise, at biaxial strain amplitudes of $\varepsilon_{a,}\gamma_a$ = 0.32%, 0.46%, the fatigue life is increased by about 90%, while the axial stress amplitude rises by 6%, the shear stress amplitude rises by 9.3%.

Varying the axial strain amplitude and phase angle while maintaining the same applied shear strain amplitudes, change in stress as well as fatigue life can also be observed. As an example, at a fixed shear strain amplitude of 0.4%, increasing the axial strain amplitude from 0.32% to 0.43% in proportional loading causes a drop in the fatigue life by as much as 70%. A reduction in the fatigue life by 62% in proportional loading is observed when axial strain amplitude is increased from 0.32% to 0.43% at constant shear strain amplitude of 0.46%. It is observed that the fatigue life under nonproportional loadings is higher than that in proportional loadings, suggesting that the effect of nonproportionality may be beneficial to the alloy. Similar finding has been reported by Albinmousa and Jahed for AZ31B [16].

From Table 20, for AISI 410, cyclic axial stress amplitude drops by 21% when the applied shear strain amplitude is increased from 0.42% to 0.48% at applied axial strain amplitude of 0.3% in proportional loading path. Meanwhile, the corresponding shear stress drops by 8%. The fatigue life decreases by 22% regardless of the decrease in the stresses. However, under nonproportional loading, no substantial change is seen in the stress evolution by increasing the shear strain amplitude from 0.42% to 0.48%. The stresses in both the axial and shear modes change by less than 2%. Nonetheless, fatigue life decreases by 7%. The change in the phase angle from 0° to 90° for the same applied strain amplitudes of $\varepsilon_{a,}\gamma_a$ = 0.30%, 0.42%, results in fatigue life reduction by 55% while the axial and shear stress amplitudes increase by 15% and 33%, respectively. Similar change in the phase angle for applied strain amplitudes of $\varepsilon_{a,}\gamma_a$ = 0.30%, 0.48% results to a decrement in fatigue life by 23%. It can be concluded that increase in the strain amplitude and phase angle results in decrement in fatigue life for AISI 410. Same observation has been reported for similar alloy by Itoh and Yang [43].

In summary, the fatigue life in multiaxial fatigue is not uniquely controlled by stress level as was seen in the uniaxial cases where a rise in the stress instantaneously translates to a decrease in fatigue life. The mechanism of multiaxial loading is therefore more complex and less understood than in uniaxial fatigue. A combination of phase angle, evolved plastic strain and stress as well as dislocation mode during fatigue cycle produces the net multiaxial fatigue effect. However, the level of interaction between these parameters is a complex fatigue mechanism that it is difficult to determine the amount of separate influence each of them has contributed. Therefore, a more involving tests and analysis is required to determine the separate effect of each of the parameters.

Table 18: Results and experimental parameters for multiaxial fatigue testing of AW2099-T83 alloy.

Spec. ID#	d_i (mm)	d_o (mm)	θ (°)	ε_a (%)	ε_e (%)	ε_p (%)	σ_a (MPa)	σ_m (MPa)	γ_a (%)	γ_e (%)	γ_p (%)	τ_a (MPa)	τ_m (MPa)	N_f (cycle)	ε_{eqv} (%)
AW2_0	7.98	9.97	0	0.53	0.43	0.10	348.73	12.91	0.66	0.53	0.13	143.94	-12.38	783	0.65
AW1_0	7.96	9.96	0	0.53	0.41	0.12	325.20	-4.19	0.76	0.56	0.20	152.59	-7.23	561	0.69
AW2_90	7.97	9.95	90	0.53	0.51	0.02	410.72	32.07	0.66	0.66	0	189.52	-27.39	1276	0.65
AW1_90	7.97	10.00	90	0.53	0.51	0.02	407.07	11.12	0.76	0.76	0	211.94	-11.10	486	0.69

Table 19: Results and experimental parameters for multiaxial fatigue testing of ZK60A alloy.

Spec. ID#	d_i (mm)	d_o (mm)	θ (°)	ε_a (%)	ε_e (%)	ε_p (%)	σ_a (MPa)	σ_m (MPa)	γ_a (%)	γ_e (%)	γ_p (%)	τ_a (MPa)	τ_m (MPa)	N_f (cycle)	ε_{eqv} (%)
ZK3_0	7.96	10	0	0.32	0.28	0.04	124.26	-5.25	0.40	0.31	0.09	51.96	-1.72	19885	0.39
ZK4_0	7.98	9.99	0	0.32	0.28	0.04	125.43	-0.21	0.46	0.35	0.11	58.83	-2.58	15032	0.42
ZK2_0	7.96	9.97	0	0.43	0.37	0.06	162.03	2.61	0.40	0.3	0.10	50.17	-0.05	5953	0.49
ZK1_0	7.96	9.98	0	0.43	0.37	0.06	163.39	11.07	0.46	0.32	0.14	54.47	-1.16	5677	0.51
ZK3_90	7.97	9.97	90	0.32	0.3	0.02	132.91	-9.04	0.40	0.34	0.06	57.47	-1.87	47484	0.39
ZK4_90	7.98	9.98	90	0.32	0.3	0.02	132.42	-8.06	0.46	0.38	0.08	64.23	-3.38	28491	0.42
ZK2_90	7.96	9.99	90	0.43	0.38	0.05	169.64	-1.50	0.40	0.33	0.07	55.16	-2.47	9508	0.49
ZK1_90	7.96	9.98	90	0.43	0.38	0.05	166.21	-2.19	0.46	0.36	0.10	60.37	-2.97	5818	0.51
ZK5_0	7.98	10	0	0.43	0.37	0.06	163.66	2.08	0.40	0.29	0.11	48.55	0.97	7817	0.49

Table 20: Results and experimental parameters for multiaxial fatigue testing of AISI 410 alloy.

Spec. ID#	d_i (mm)	d_o (mm)	θ (°)	ε_a (%)	ε_e (%)	ε_p (%)	σ_a (MPa)	σ_m (MPa)	γ_a (%)	γ_e (%)	γ_p (%)	τ_a (MPa)	τ_m (MPa)	N_f (cycle)	ε_{eqv} (%)
AISI2_0	7.99	10	0	0.3	0.19	0.11	398.69	14.24	0.42	0.26	0.16	203.80	-3.58	3619	0.39
AISI1_0	7.97	9.98	0	0.3	0.15	0.15	315.47	3.90	0.48	0.24	0.24	186.89	-2.50	2827	0.41
AISI2_90	7.98	9.94	90	0.3	0.22	0.08	456.95	1.27	0.42	0.34	0.08	271.30	0.15	2340	0.39
AISI1_90	7.96	9.97	90	0.3	0.22	0.08	451.24	0.25	0.48	0.35	0.13	275.83	0.12	2185	0.41

4.5.2 Effect of Phase Angle and Loading Paths on the Hysteresis Loops

Figures 37-41 illustrate the half-life hysteresis loops in both axial and shear modes for proportional and nonproportional loadings. The effect of phase angle on the hysteresis loop for each of the three alloys is discussed next.

Figure 37(a) shows the hysteresis loop for AW2099-T83, in proportional loadings. Plastic strains evolved both in the axial and shear modes. However, in the hysteresis loop for nonproportional loadings (Fig. 37(b)), no quantifiable plastic strain is present even though the evolved axial and shear stress amplitudes are higher (Table 18). Thus, plastic strain energy is measurable in the proportional loading only. There is no indication of nonproportional cyclic hardening, as both the strain and stress maximum values are coincident at tip of the loop. Nonproportional cyclic hardening is identifiable by rounding of the tip of the hysteresis loop. Nonproportional cyclic hardening for Aluminum alloys is usually not observed or is negligible [43,140].

Axial and shear modes hysteresis loops for ZK60A alloy are shown in Figs. 38 and 39, for applied axial strain amplitudes of 0.43% and 0.32%, respectively. At all strain amplitudes, plastic deformation is evident regardless of phase angle. The axial plastic strains are higher in the proportional modes (Figs. 38(a) and 39(a)) than those at equivalent strain amplitudes in the non-proportional loading (Figs. 38(b) and 39(b)). The value for the strain amplitudes are recorded in Table 19. There is a rounding of the tip of the hysteresis loop in the shear mode in non-proportional loading, which indicates additional cyclic hardening due to nonproportional loading. However, the cyclic hardening is mild, resulting in stress difference of less than 10 MPa between the proportional and non-proportional phase.

Nonproportional cyclic hardening is due to the activation of multiple slip plane in metallic alloys. Such multiple planes activation causes dislocation interactions resulting in rise in the evolved stress. Albinmousa and Jahed [16,46] and Xiong et al [47] have reported nonproportional hardening for AZ31B.

The hysteresis loops for AISI 410 are illustrated in Fig. 40. Significant plastic deformation occurs at all applied strain amplitude both in the axial and shear mode. At the same equivalent strain, the plastic deformation in the proportional loading is higher. The values of plastic strain are already presented in Table 20. Nonproportional cyclic hardening is obvious, as there is significant rounding of the tips of hysteresis loops tips both in the shear and in axial modes. The additional hardening causes an increase in the average axial stress amplitude by 100 MPa and the shear stress amplitude by 80 MPa. Nonproportional cyclic hardening have been reported for various types of steel in the literature [20,24,37,40,70]. More fatigue damage in nonproportional loading is attributed to additional cyclic hardening [43,141]. Nonproportional cyclic hardening, as previously discussed is due to simultaneous activation of multiple slip planes. The rotation of the principal planes with loading planes cause the interaction of slips resulting to an increase in stress that is observed as additional hardening. Nonproportional hardening in alloy steel is attributed to the microstructure and crystal structure [37,43]. Fatigue life in the nonproportional loading is lower which can be attributed to the nonproportional cyclic hardening.

The effect of loading path on the hysteresis loop at similar strain amplitudes is illustrated for the three alloys in Fig. 41. Figure 41(a) is the hysteresis loop for AW2099-T83 at applied axial strain amplitude of nearly 0.5% and shear strain amplitude of about 0.75%.

The shape of the hysteresis loop in pure cyclic axial and torsion are similar with those at nonproportional loading. The stress level and strain amplitude are nearly same for both the cyclic axial and proportional paths. Stress level is least in proportional loading, but with greater plastic strain amplitude.

The hysteresis loops for ZK60A under different loading paths are compared in Fig. 41(b) at applied strain amplitude of approximately 0.32% in axial and 0.40% in torsion. In both the axial and shear modes, there is no appreciable difference in the hysteresis loops in shape, stress level and plastic strain amplitude.

Figure 41(c) is used to compare the hysteresis loops of AISI 410 under different loading paths. At applied axial strain amplitude of 0.3% and shear strain amplitude of nearly 0.5%, the shapes of the hysteresis loop in pure modes are preserved in the proportional loading path. However, stress level in the pure mode is higher than that in the proportional mode. The effect of additional cyclic hardening is evident in the hysteresis loop for nonproportional loading. Thus, the shape of hysteresis loop in nonproportional loading differs from those of the pure mode and proportional path. The stress level in the nonproportional path is highest due to the effect of additional cyclic hardening.

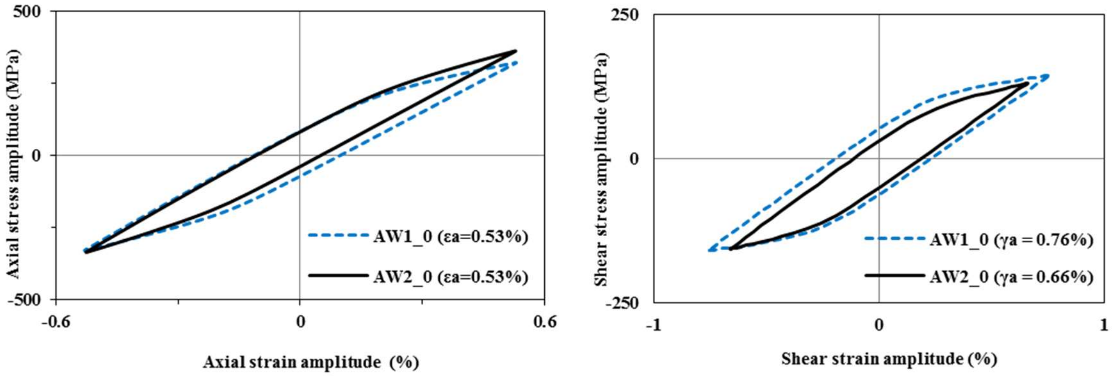

(a) proportional loading

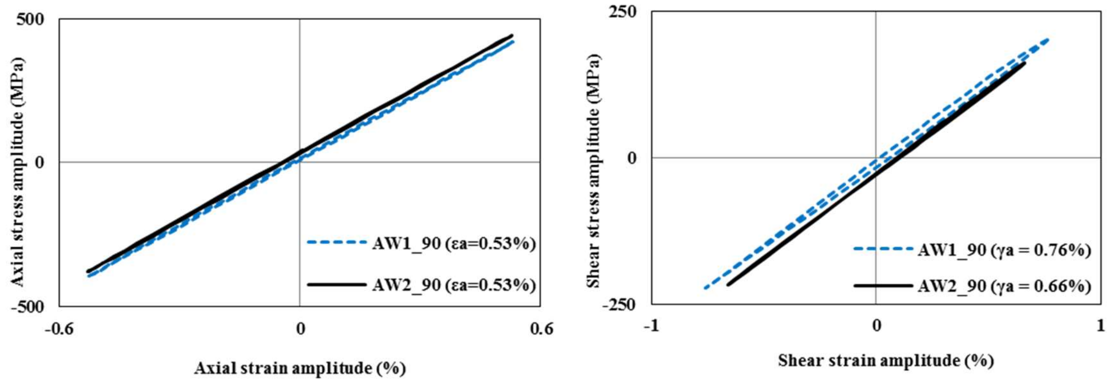

(b) nonproportional loading

Figure 37: Axial and shear modes half-life hysteresis loops for AW2099-T83 at biaxial strain amplitudes of ε_a, γ_a = 0.53%, 0.76% (AW1) and ε_a, γ_a = 0.53%, 0.66% (AW2).

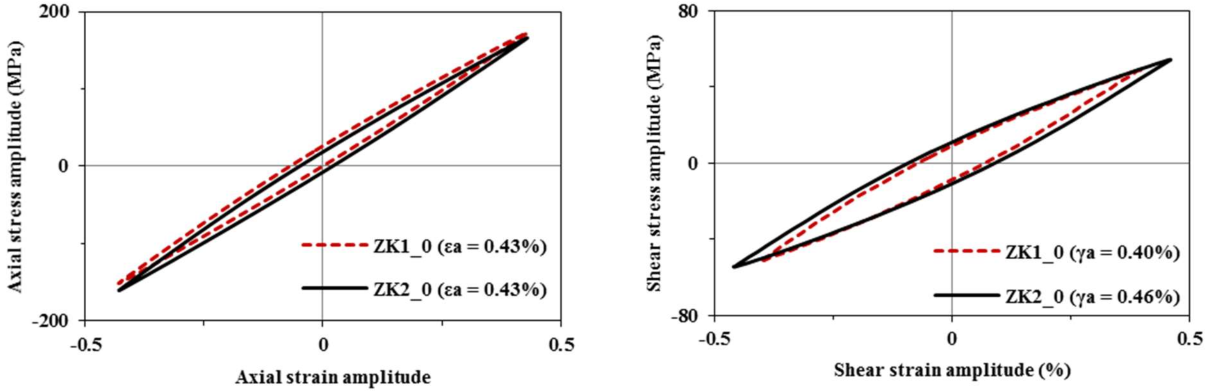

(a) proportional loading

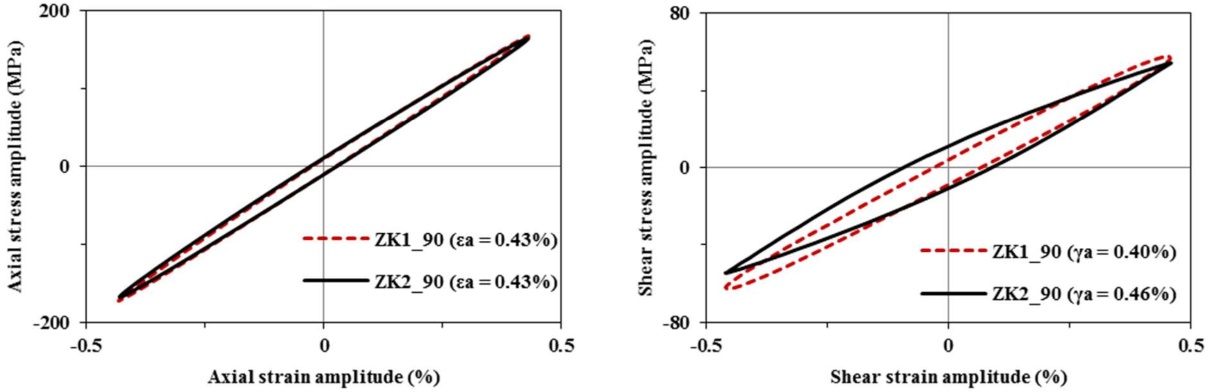

(b) nonproportional loading

Figure 38: Axial and shear modes half-life hysteresis loops for ZK60A at biaxial strain amplitudes of ε_a, γ_a = 0.43%, 0.40% (ZK1) and ε_a, γ_a = 0.43%, 0.46% (ZK2).

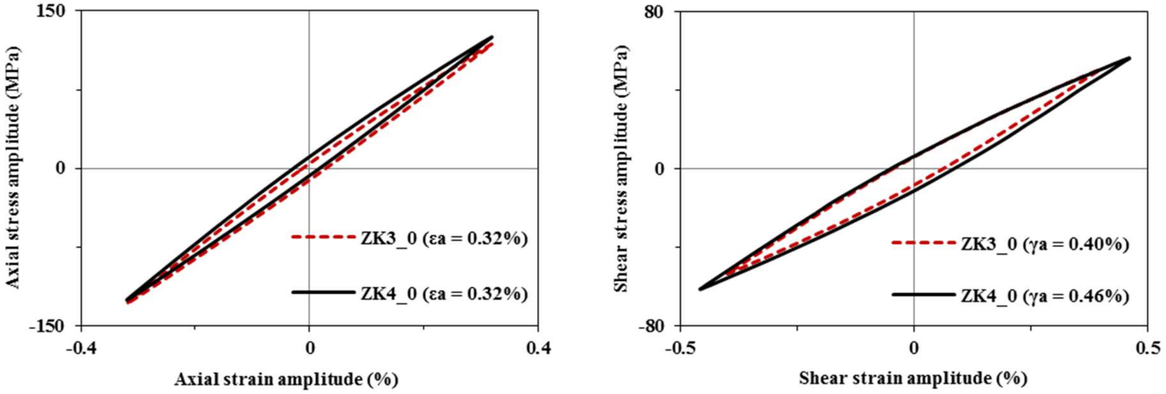

(a) proportional loading

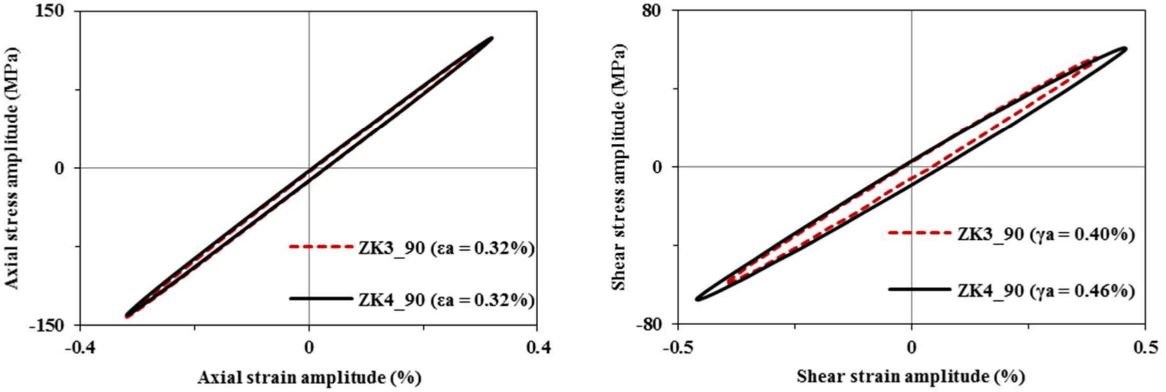

(b) nonproportional loading

Figure 39: Axial and shear modes half-life hysteresis loops for ZK60A at biaxial strain amplitudes of ε_a, $\gamma_a = 0.32\%, 0.40\%$ (ZK3) and ε_a, $\gamma_a = 0.32\%, 0.46\%$ (ZK4).

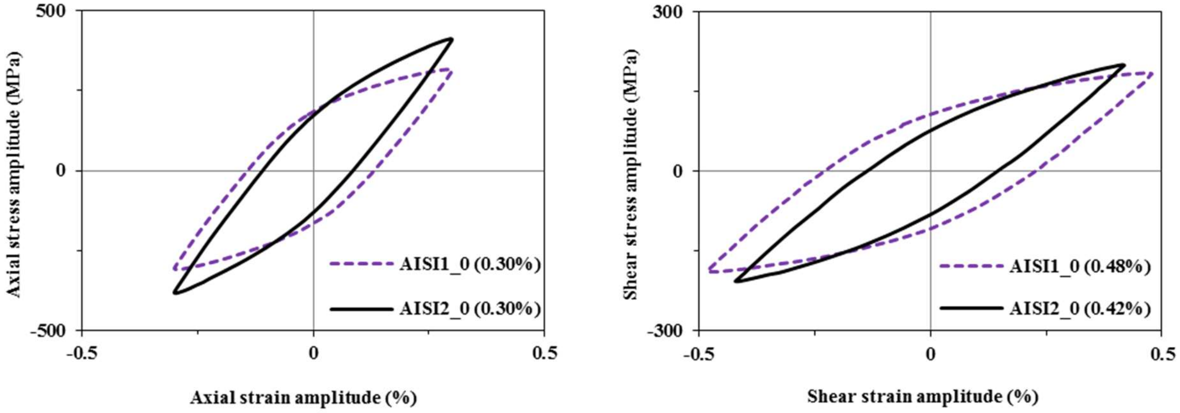

(a) proportional loading

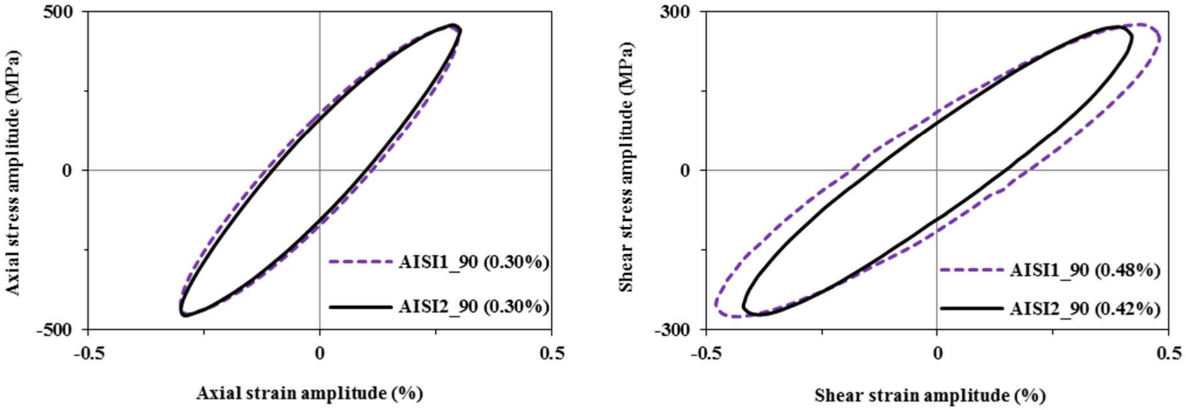

(b) nonproportional loading

Figure 40: Axial and shear modes half-life hysteresis loops for AISI 410 at biaxial strain amplitudes of ε_a, γ_a = 0.30%, 0.48% (AISI1) and ε_a, γ_a = 0.3%, 0.42% (AISI2).

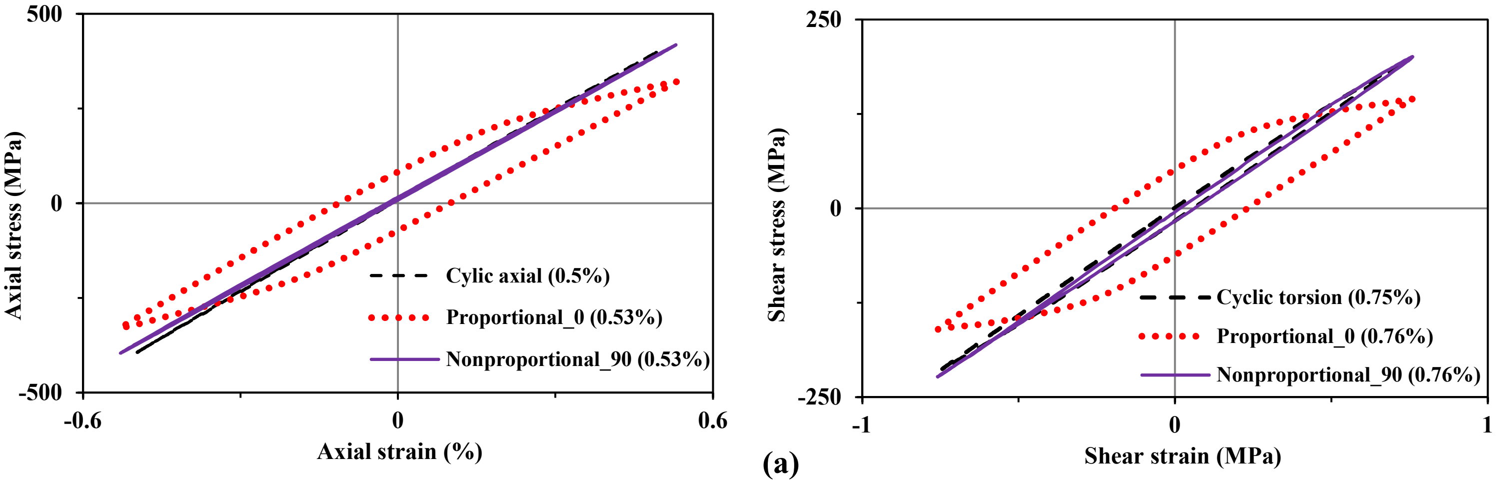
500
0
-500
-0.6
0
0.6
Axial stress (MPa)
Axial strain (%)
Cylic axial (0.5%)
Proportional_0 (0.53%)
Nonproportional_90 (0.53%)
250
0
-250
-1
0
1
Shear stress (MPa)
Shear strain (MPa)
Cyclic torsion (0.75%)
Proportional_0 (0.76%)
Nonproportional_90 (0.76%)

(a)

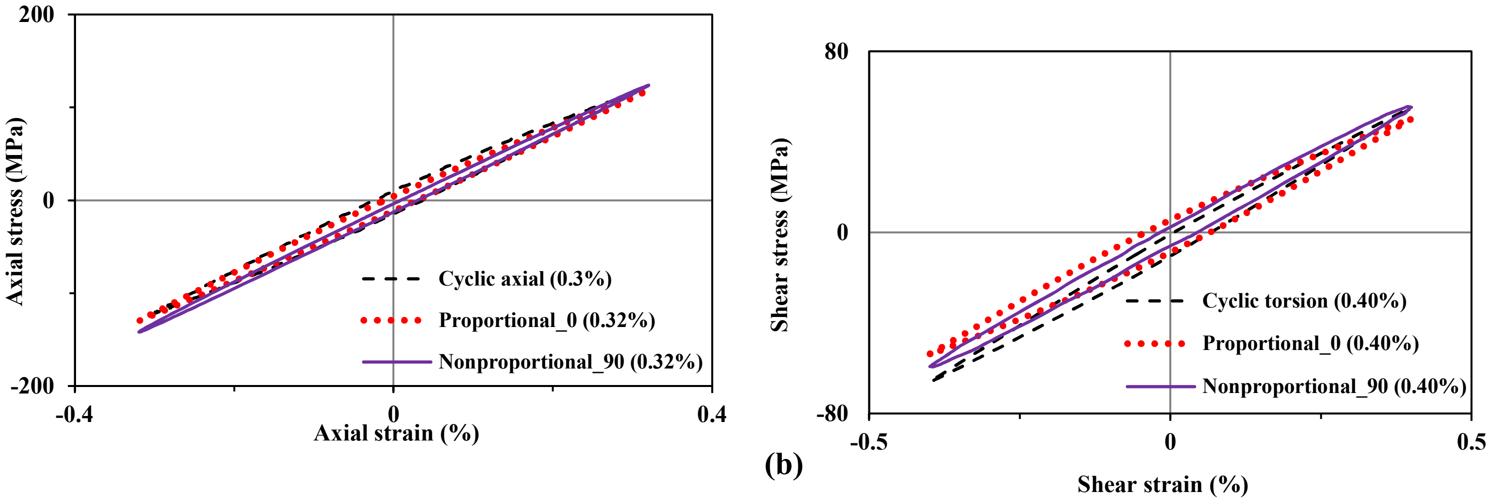
200
0
-200
-0.4
0
0.4
Axial stress (MPa)
Axial strain (%)
Cyclic axial (0.3%)
Proportional_0 (0.32%)
Nonproportional_90 (0.32%)
80
0
-80
-0.5
0
0.5
Shear stress (MPa)
Shear strain (%)
Cyclic torsion (0.40%)
Proportional_0 (0.40%)
Nonproportional_90 (0.40%)

(b)

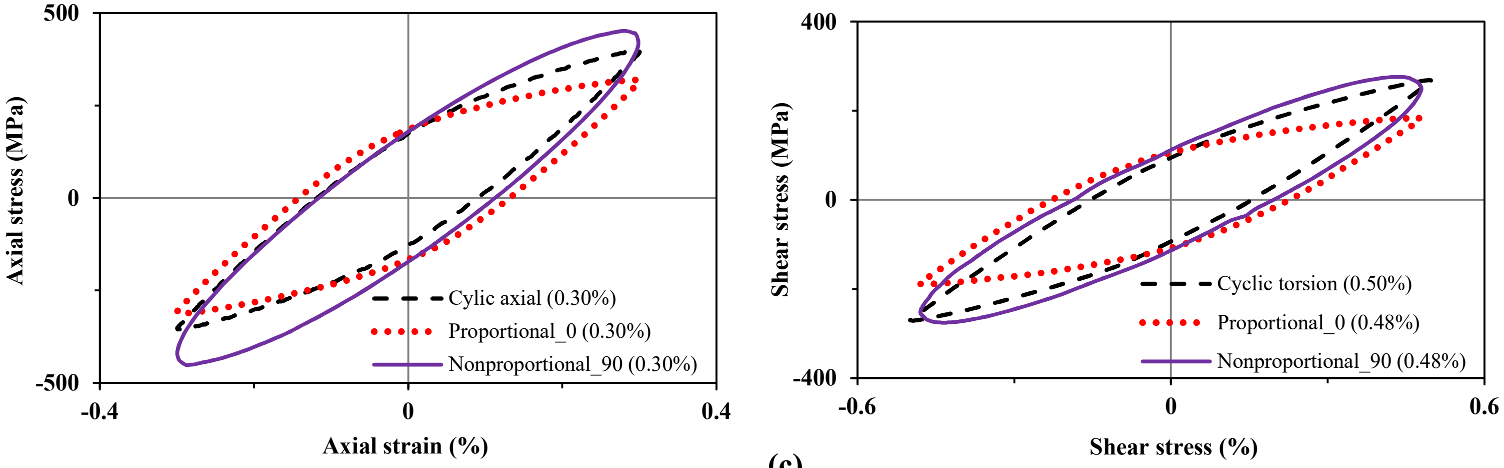

(c)

Figure 41: Effect of loading path on hysteresis loop: (a) AW2099-T83, (b) ZK60A and (c) AISI 410.

4.5.3 Effect of Loading Path on Fatigue Life

The fatigue life of the three alloys in cyclic axial, cyclic torsion, proportional and nonproportional loading paths are compared using von Mises equivalent strain amplitude. The von Mises relation is given in Eq. (4.11). ε_{eqv} is the equivalent von Mises strain amplitude, ε_a is the axial strain amplitude and γ_a is the shear strain amplitude.

$$\varepsilon_{eqv} = \sqrt{\varepsilon_a^2 + \frac{\gamma_a^2}{3}} \text{ ………………..(4.11)}$$

Figure 42(a) is the strain-fatigue life relation for all the loading modes for AW2099-T83 under von Mises equivalent strain. At equivalent von Mises strain, the lowest fatigue life is produced in the shear mode, while the cyclic axial mode produces the highest fatigue life, meaning that the shear load mode is more destructive than the other loading modes. The fatigue life curves from the in-phase and out-of-phase loadings are between the axial and shear modes, with the fatigue life curve in the nonproportional mode fairly higher than the proportional loading mode. Zhao and Jiang [140] have shown that nonproportional loading path is more damaging than proportional loading mode for Al alloy 7075-T651.

Figure 42(b) shows that the highest fatigue life resulted from cyclic torsion in ZK60A alloy under the same von Mises equivalent strain. The lowest fatigue life is obtained in the cyclic axial loading. The fatigue life in nonproportional mode is higher than the proportional loading. In fact, the fatigue life trend in nonproportional loading is similar to that of the cyclic axial loading. Anes et al [18] have reported that fatigue life trend for AZ31, an HCP alloy, under stress-controlled loading, is similar in cyclic axial, cyclic torsion and proportional loading modes when correlated with von Misses stress relation.

The authors concluded that von Misses is a good correlation method for these loading modes exception of nonproportional loading. Similar trend is observed in the present investigation as illustrated in Fig. 42(b) for ZK60A alloy where the trends for the aforementioned loading modes are almost parallel. However, it has been shown by Xiong [47] that the torsional and nonproportional loadings are the more damaging loading paths to AZ31B.

Fatigue life for AISI 410 as illustrated in Fig. 42(c) is generally the same in torsion and axial loading modes. The two loading modes produced similar fatigue life at same von Mises strain amplitudes. The lowest fatigue life occurred at nonproportional loading. Anes et al. [18] showed that for a martensitic steel 42CrMo4, pure shear mode was less damaging while the nonproportional loading produced the most damaging effect. This is also in close agreement with the observation in the current investigation where the out-of-phase loading exhibits the lowest life while the pure torsion gives the highest fatigue life at same equivalent strain amplitude.

The fatigue life resulting from different loading modes can be attributed to several factors, which include the deformation mode, evolution of stress and plastic strain amplitudes. Higher stress is likely to introduce low life. So is the amount of plastic strain. The slip characteristic is directly related to the microstructure of the alloy and may be the most important factors, as other factors are dependent on it.

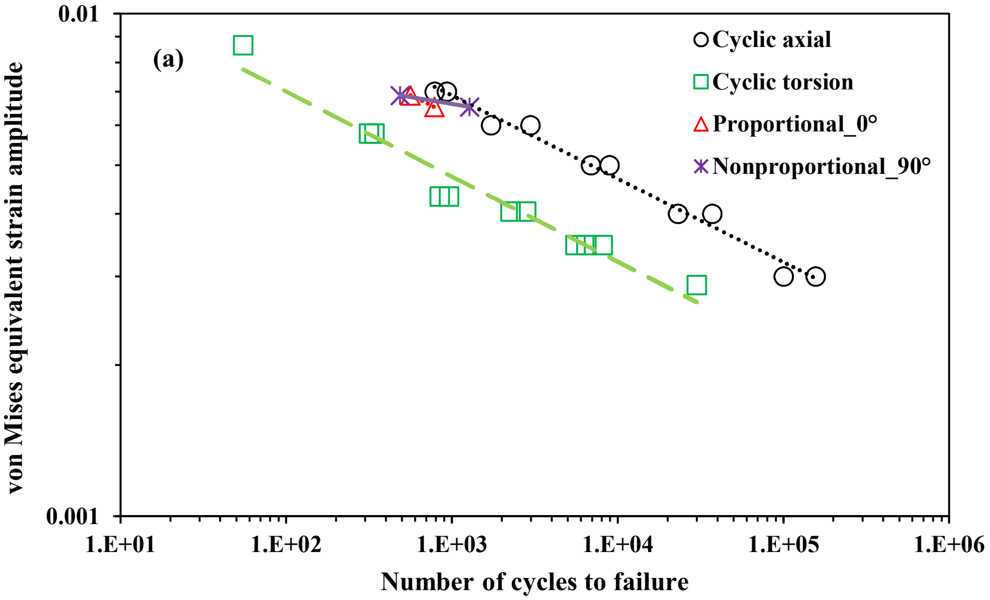
(a)
Cyclic axial
Cyclic torsion
Proportional_0°
Nonproportional_90°
0.01
0.001
1.E+01
1.E+02
1.E+03
1.E+04
1.E+05
1.E+06
von Mises equivalent strain amplitude
Number of cycles to failure

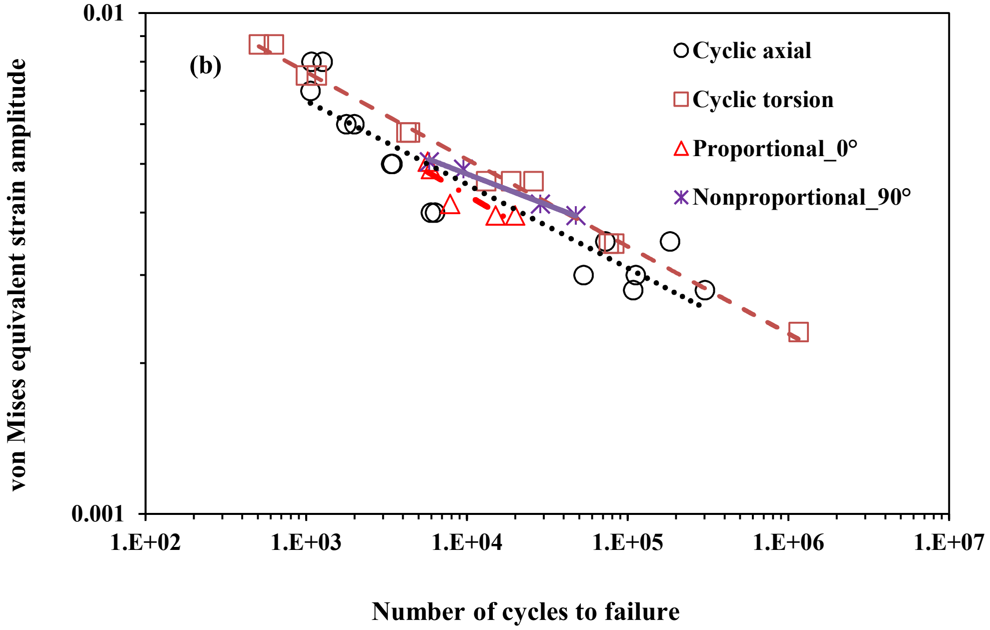
(b)
Cyclic axial
Cyclic torsion
Proportional_0°
Nonproportional_90°
0.01
0.001
1.E+02
1.E+03
1.E+04
1.E+05
1.E+06
1.E+07
von Mises equivalent strain amplitude
Number of cycles to failure

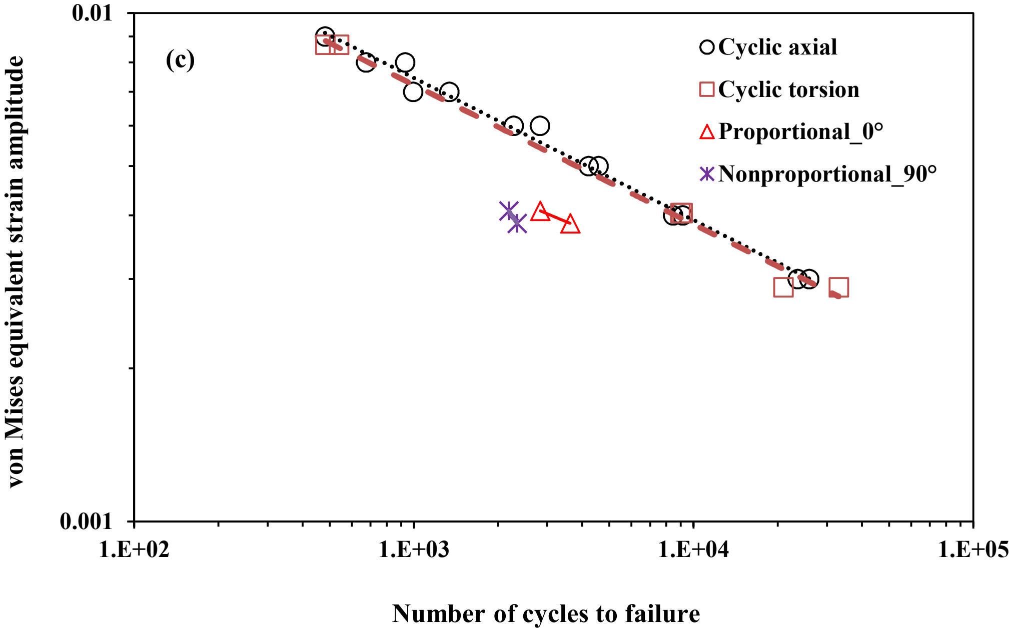

Figure 42: Equivalent strain amplitude vs. fatigue life for the three alloys (a) AW2099-T83, (b) ZK60A and (c) AISI 410.

4.5.4 Fatigue Life Prediction Using Smith-Watson-Topper (SWT) and Fatemi-Socie (FS) Critical Plane Models

Multiaxial fatigue models are used to correlate multiaxial fatigue data by employing uniaxial fatigue parameters in order to predict same life as would be in uniaxial loading mode. Two fatigue life prediction models, namely, the Smith-Watson-Topper (SWT) [47,140,142] and Fatemi-Socie (FS) [2,141] models are tested on the multiaxial fatigue results obtained in the present work. Both the SWT and FS models are critical plane models. Critical plane models are based on the observation that fatigue damage is initiated on a specific plane during cycling due to maximum strain or stress in that plane. The FS damage model recognizes the critical plane as the loading plane with maximum shear strain amplitude, while the SWT model identifies the critical plane as the loading plane of maximum normal strain. The formulations for both models have been given in section 1.7.2 as Eq. (1.28) and (1.29) for the FS and SWT models, respectively.

The application of FS is preceded by finding a material constant *k*, which requires fitting fatigue data for axial and torsional fatigue tests to a single line. This procedure is illustrated in Fig. 43 for the three alloys. The best line fit for AW2099-T83 is when $k = 0.01$. Similarly, 1.7 and 0.03 are found for ZK60A and AISI 410, respectively, as the values for *k*. It is observed that the tests data for AW2099-T83 hardly converge to a single line compare to ZK60A and AISI 410. This might be due to the low plasticity behavior of the alloy. The best convergence of the axial and torsional fatigue tests data is shown by AISI 410, which also exhibits the highest plasticity.

The fatigue life predictions from both criteria are shown in Figs. 44-46. The solid line represents a perfect prediction while the broken lines are band factors, which give allowance for the kind of fatigue life variation in fatigue experiment from sample to sample under same applied load. The fatigue life predicted by the FS and SWT criteria are compared with the experimental fatigue life for AW2099-T83 in Fig. 44. As can be seen from Fig. 44(a), SWT model performs well for the cyclic axial mode but shows poor correlation for the cyclic torsional. The data for the proportional and nonproportional loading modes also lie outside the factor-of-two scatter band in the non-conservative region. The fatigue life prediction by FS criterion (Fig. 44(b)) for AW2099-T83 is not much better than SWT. Although all the data points lie outside the factor-of-two boundaries, the majority are in the conservative (safe) region, meaning that fatigue life is predicted far below the experimental fatigue life. This can lead to ‘over-design’ where components are withdrawn from service even though they would still have useful service life. With a factor-of-five scatter band, the FS criterion looks promising for the cyclic torsion and as well as for the high cycle life in cyclic axial.

For ZK60A, Figs. 45(a) and 45(b) illustrate the predicted fatigue life with experimental life by the SWT and FS model, respectively. The SWT gives a fairly good fatigue life prediction for all the loading modes except the cyclic torsion which are mostly non-conservatively predicted. The FS criterion predicts fatigue life in which the cyclic axial and cyclic torsion are within the factor-of-two scatter band. The proportional and nonproportional lives are predicted in the conservative region. It can therefore be said that the FS performs better for ZK60A than it is for AW2099-T83.

The fatigue life prediction for AISI 410 by SWT is shown in Fig. 46(a). The prediction is similar to what is obtained for AW2099-T83, where only the cyclic axial data are within the factor-of-two scatter band. The predictions for all other loading modes are majorly in the non-conservative region. However, its prediction for the cyclic torsion looks better when compared to that for same loading mode for ZK60A and AW2099-T83. The life prediction has moved closer to the factor-of-two boundaries. The FS prediction has only the 90^{o} out-of-phase data in the unconservative, while the proportional load is at boundary. However, the cyclic axial and torsion fatigue lives for AISI 410 are fairly well predicted.

It can be concluded generally that none of the model works perfectly for all the three alloys for the different loading paths. The SWT perform poorly for all the alloys in pure cyclic torsion. The best data correlation by SWT is for the cyclic axial loading. Fatigue life estimation by FS is generally good for ZK60A and AISI 410 except for the 90° out-of-phase loading in AISI 410. The ability of some criteria to work for some loading mode and alloy, while failing in others can be attributed to the failure mode of the alloys. Model developed for tensile cracking, like the SWT, may not be able to represent the damage for an alloy which fails in share. The FS model is based on a shear-cracking mode and thus it may not be surprising if it fails to make good fatigue life prediction reasonably for shear cracking mode. Except for torsional loading, the fatigue life is well predicted for all the three alloys within a factor-of-five.

The general trend of the predictions in the present study agrees with results available in literature for majority of metallic alloys [16,24,78,120,140,141,143–145]. Torsional prediction were found mostly to lie outside a factor-of-2 boundary in the non-conservative region by a number of researchers [140,143,144]. Multiaxial fatigue data for 7075-T651 aluminum alloy were well correlated by SWT within a scatter band of five [140]. The SWT model well correlated torsion data for 16MnR steel while the low cycle multiaxial fatigue prediction lies on the factor-of-two band [24]. Xiong et al. [120] have shown that SWT parameter well correlates the uniaxial data of ZK60. These results are in agreement with the results obtained in the present investigation.

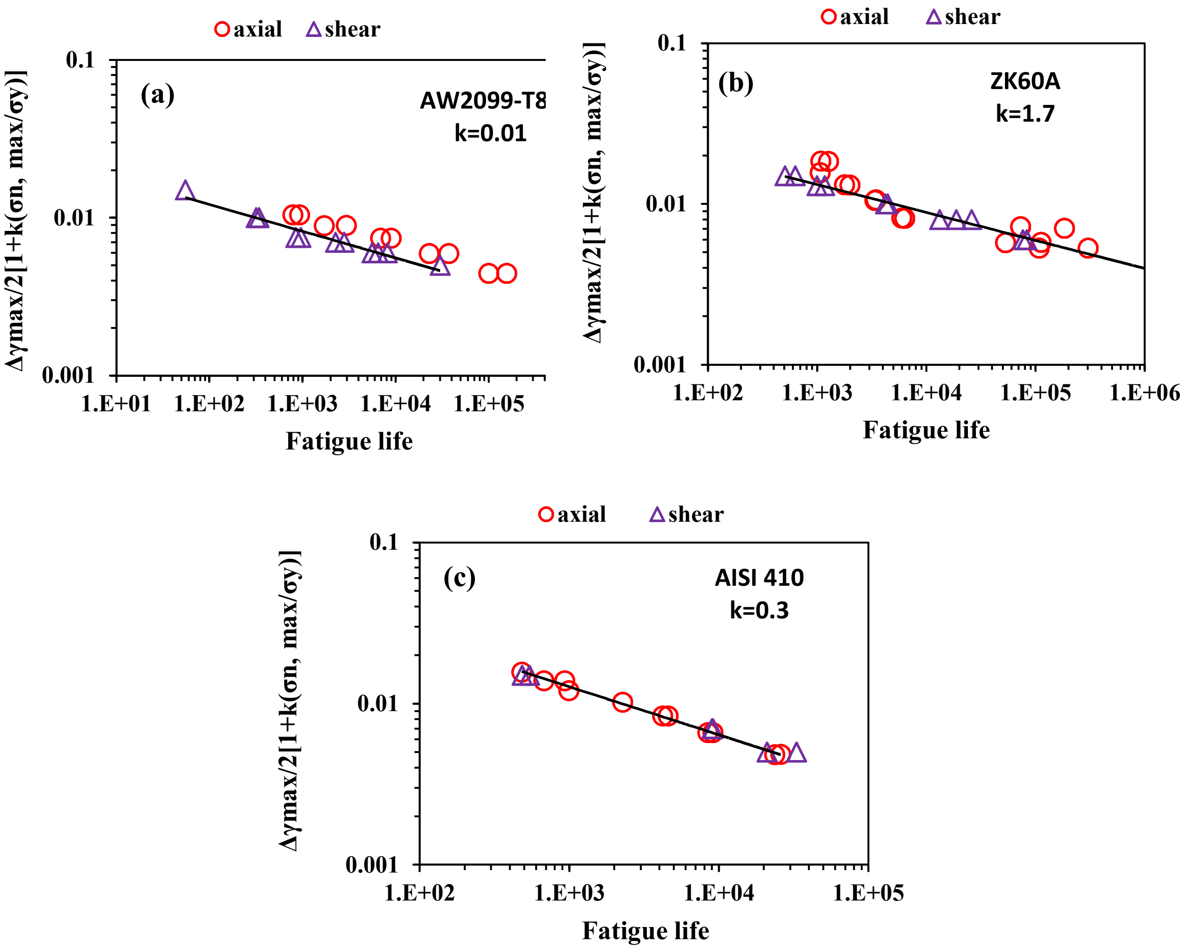

Figure 43: Determination of k for FS criterion for (a) AW2099-T83, (b) ZK60A and (c) AISI 410.

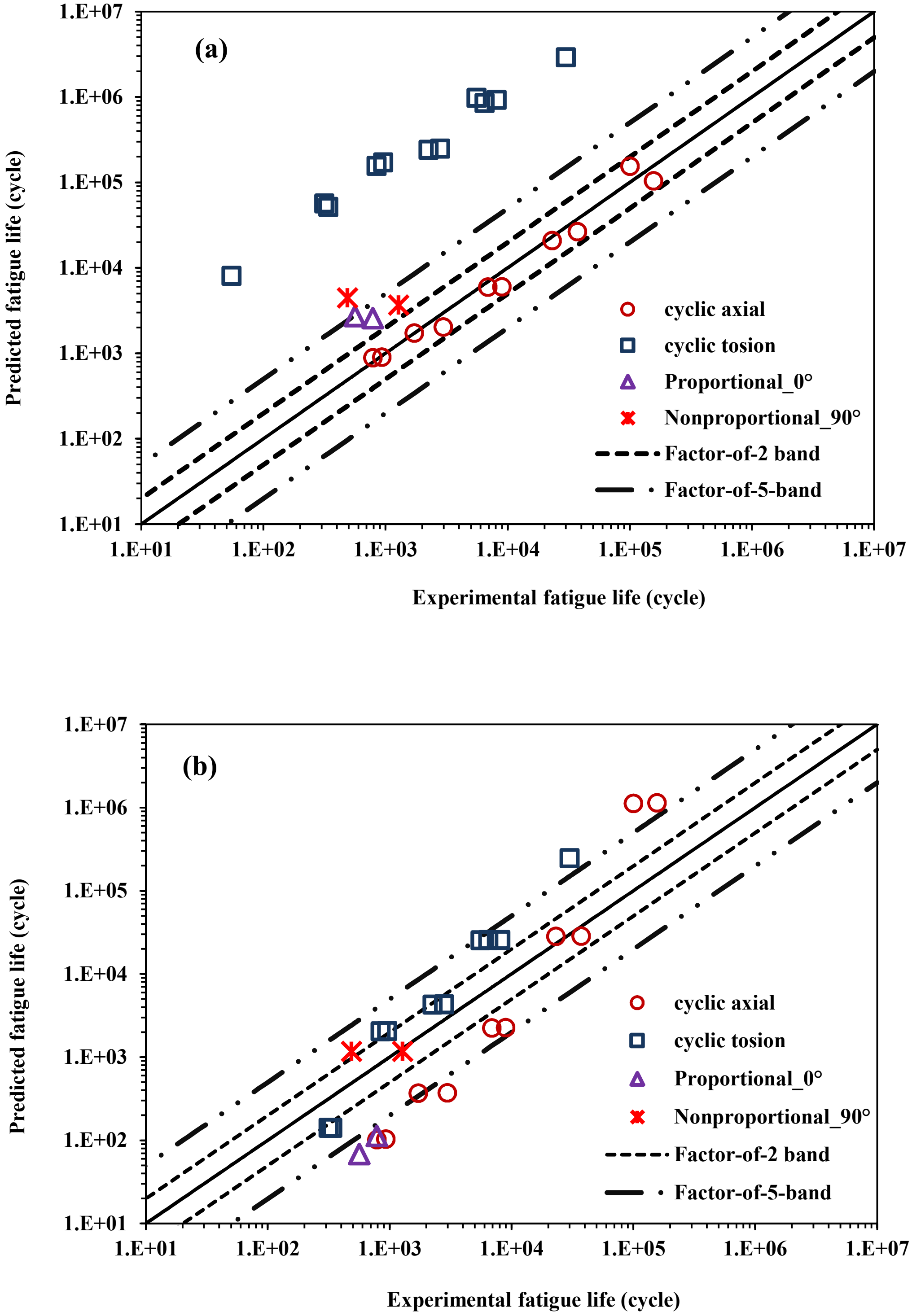

Figure 44: Fatigue life prediction vs. observed life for AW2099-T83 using: (a) SWT and (b) FS.

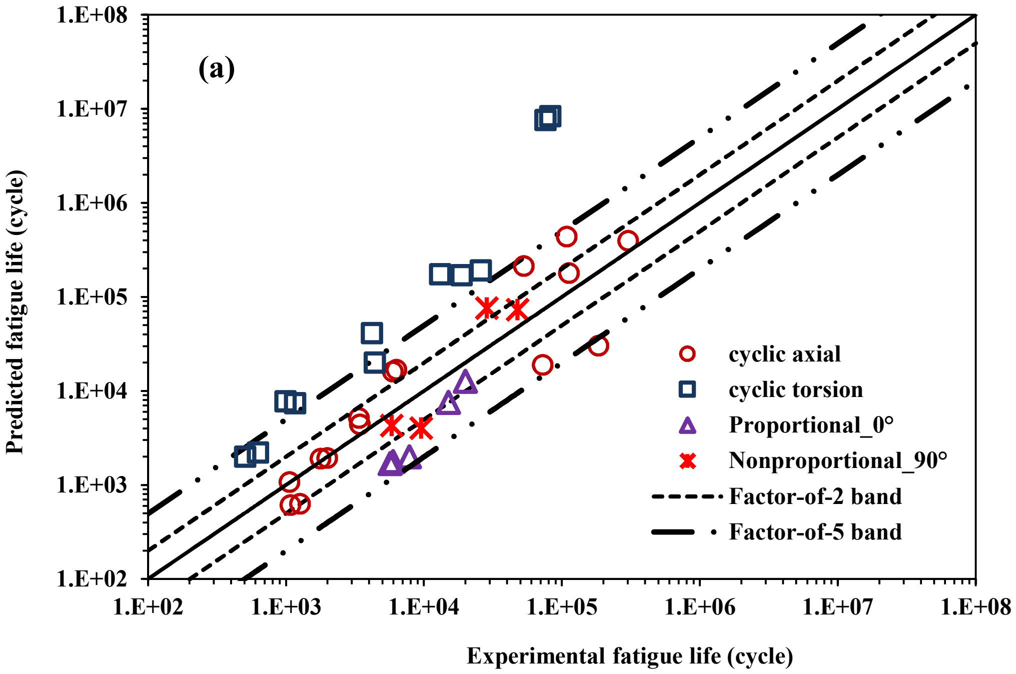

Figure 45: Fatigue life prediction vs. observed life for ZK60A using: (a) SWT and (b) FS.

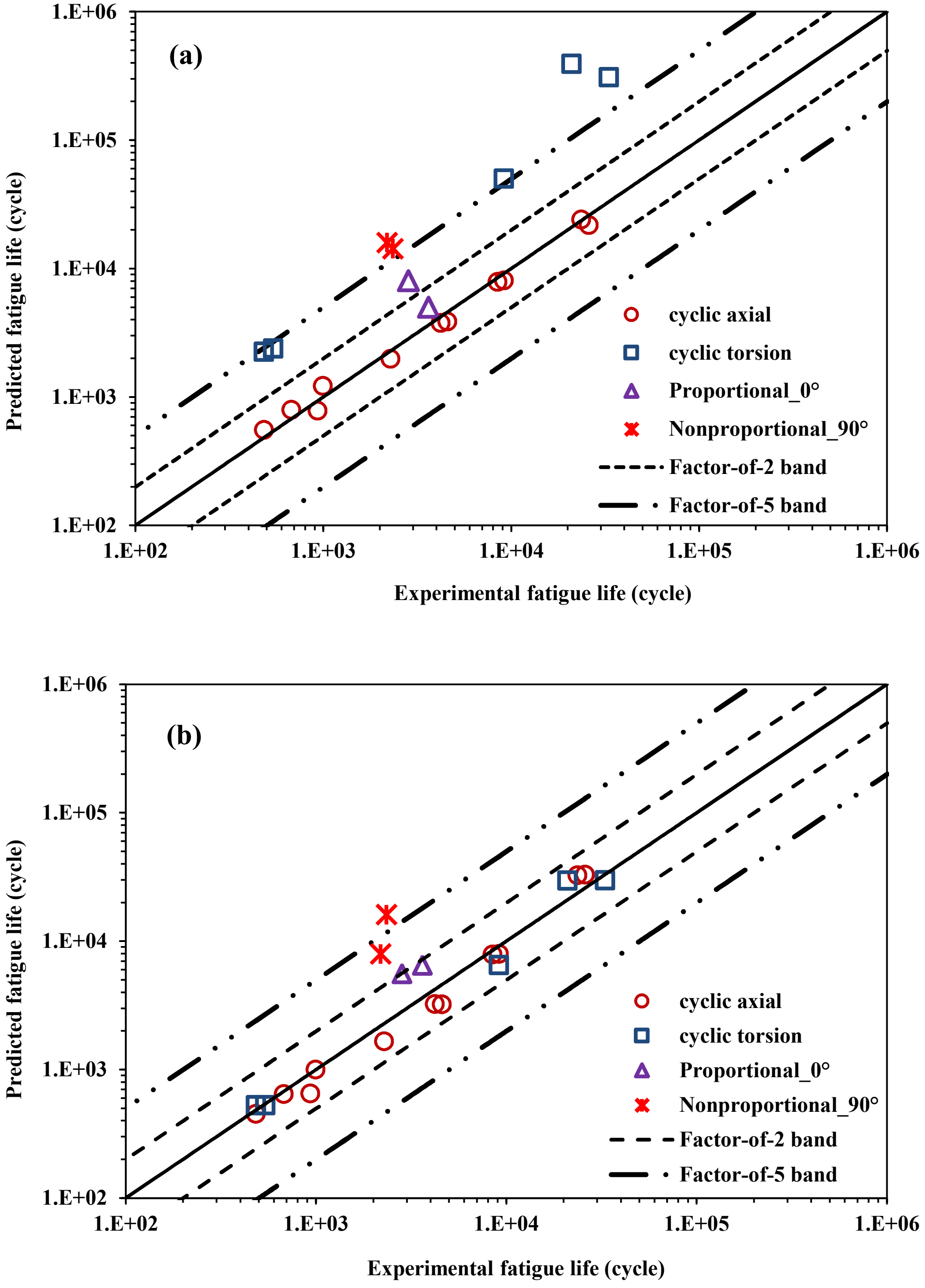

Figure 46: Fatigue life prediction vs. observed life for AISI 410 using: (a) SWT and (b) FS.

4.6 Crack Profile and Fractography

Crack formation and propagation is the driving phenomenon for fatigue damage. Thus, the characterization of cracks in fatigue can give insight into the entire process that lead to fatigue failure. Crack characteristic in the three alloys have been studied with digital camera, optical microscope and scanning electron microscope (SEM) both at microscopic and macroscopic levels. The crack features for AW2099-T83 in axial and torsion path are presented, followed by those in multiaxial fatigue for the three alloys. Then, fractography for selected loadings in axial and torsional loading path are subsequently presented.

4.6.1 Crack Profile

i. Cyclic Axial

Figure 47 is optical micrographs of fatigue cracks observed on the fractured surface of AW2099-T83 specimen tested at axial strain amplitude of 0.6%. The surfaces were etched in solution of sodium hydroxide. In the micrograph on left side of Fig. 47(a), two adjacent secondary cracks are observed to have propagated on the fractured surface of the specimen. The thinner crack advanced faster than the bigger one. Both cracks appear to have initiated from the surface of the specimen and propagated toward the radius. A close-up look on a section of the thinner, but longer crack is shown on the right side micrograph of Fig. 47(a). It can be observed that the crack meander through several grain boundaries and sometimes through the grains. Therefore the cracking is mainly intergranular and partially transgranular. Zhong et al [146] have shown that fatigue crack moves across several grain in a 2A97 Al-Li sample tested under stress control fatigue. The pattern of the crack propagation suggests that the grains can act as crack stopper restricting crack to grain boundaries. However, as the stress became higher and the crack driving energy is increased, the grain resistance to crack propagation is overcome resulting to a transgranular cleavage. By comparing with the microstructure presented in Fig. 14, it can be inferred that crack growth happened on the location T1 in the transverse orientation. The transverse orientation is the plane of loading in the cyclic axial fatigue. This location possesses the large, unrecrystallized grain which have been reported to reduce Al-Li resistance to crack growth [99,104]. The susceptibility of large and elongated grains of A356 Aluminum alloys to cracking have been reported by Mo et al [49].

Figure 47(b) shows cracks observed under the microscope on the outer surfaces close to the specimen fracture point. It can be seen that cracks propagated along the grain boundaries, whether in the region of the elongated grains or the smaller subgrains. By comparing the observed structure to Fig. 14 in section 4.2, it can be observed that the grain boundaries in the tested specimen have become wider signifying grain boundary separation. Elongated grains in the alloy are hence weak region for fatigue crack to exploit.

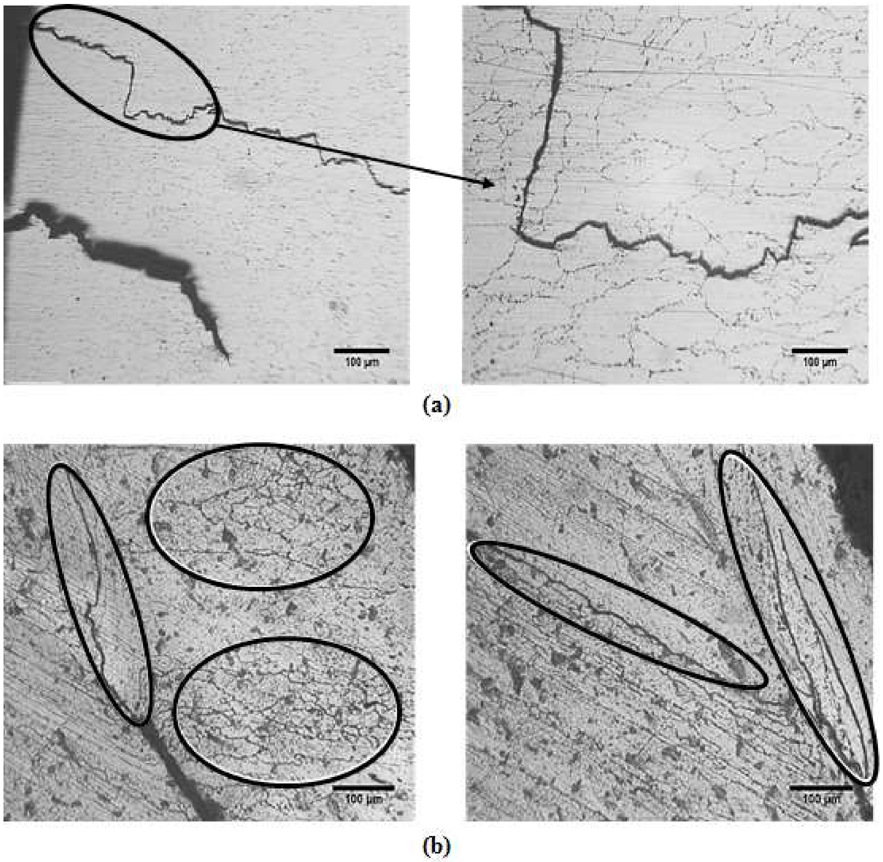

Figure 47: Optical micrographs of cracks on the fractured sample of AW2099-T83.

ii. Cyclic Torsion

A schematic representation of the cracks profiles observed at different strain amplitudes for AW2099-T83 in cyclic torsion are annotated in Fig. 48. Most of the cracking occurred in the longitudinal (L) axis, along the extrusion direction, at approximately 90º to the transverse (T) stress axis. Stepped cracks (L-T) (Fig. 48A) were observed for specimens tested in the strain amplitude ranging between 0.5-0.7%, while straight longitudinal (L) crack profiles (Fig. 48B), which grew along the entire gage section, were observed for specimens tested at strain amplitudes of 1.0% and 1.5%. A view of the section of the step on the cross-section of the tubular specimen is sketched in Fig. 48A(ii)(shaded portion).

Figure 49 shows the microscopic images for sections of the cracks for applied strain amplitudes of 0.6% and 1.0, which are respective representation for crack at the strain amplitude ranges of 0.5-0.7% and 1-1.5%. Since a nearly straight crack was observed for applied strain amplitudes of 1.0% and 1.5%, a non-specific location was analyzed using replica method [147]. However, different sections of the representative crack for applied strain amplitudes of 0.5% -0.7% were analyzed by direct imaging of tested specimen under optical microscope.

It can be seen that the crack at higher strain amplitudes (1.0% and 1.5%), as shown in Fig. 4.9(a), is generally straight with smooth edges, but with occasional branching. However, crack at strain amplitudes below 1.0%, Fig. 49(b), is coarse with frequent bifurcation in a 'staircase-like' pattern along the direction of the specimen axis, while it is generally smooth in the circumferential direction. It is not uncommon to report crack growing in both transverse and longitudinal directions under cyclic torsion loading [147]. However, no such perpendicular branching has been reported elsewhere. Crack branching in both traditional aluminum and Al-Li alloys has been reported in the literature for axial fatigue [104,146,148,149]. Crack turning in Al-li is linked to anisotropy due to crystallographic texture, slip planarity and inhomogeneity of the alloy [83,88]. Al-Li alloy is known for high anisotropy and inhomogeneity [87,96–99,150]. Zhong et al. [146] explained that the bifurcation of crack in 2A97 Al-Li was due to high angle grain boundary hindering the movement of persistent slip bands (PSBs).

Sharp crack tips were observed for cracks represented in Fig. 49(a) suggesting that cracks propagated in directions nearly parallel to the specimen axis. In Fig. 49(b), it can be noticed that the physical damage to the specimen is higher at low strain amplitude. This might help to explain the excessive deflection of the cyclic shear stress curve and the mean shear stress curve observed in Figs. 33(a) and 34(a). With much damage in the specimen, its fatigue strength is reduced resulting to a drop in the stress it can withstand.

The difference in crack behavior in the alloy can be linked to its microstructure, previously shown in Fig. 14(a), which contains both recrystallized grain and aligned structure. Recrystallized grains in Al-Li degrade its mechanical property, particularly the resistance to fatigue crack growth [99,104]. The structure along the extrusion direction is elongated like bundles of fibre. Thus, there is a possibility of cracks to propagate along the boundary of the microstructure. Furthermore, crack driving energy can be the cause for different crack observation at different stain amplitudes. Crack energy at higher strain amplitude is greater than at low strain amplitude. Such crack of higher energy moves faster thereby cutting through grains with minimal crack arrest, resulting in straight crack. On the contrary, crack at low strain amplitude is driven slowly and there is the chance of it being deflected by the strengthening precipitates in Al-Li due to low driving energy of the crack.

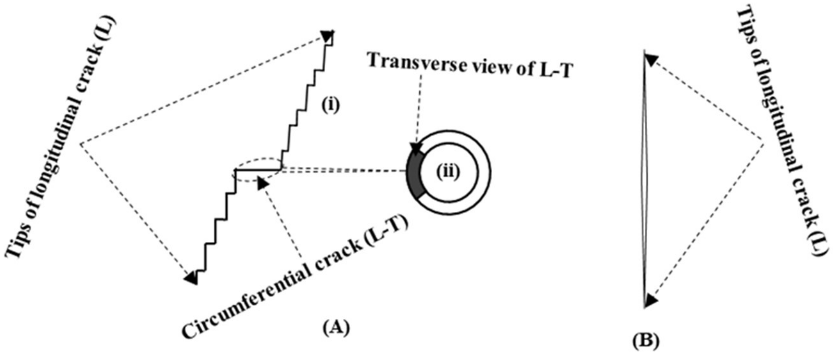

Figure 48: Schematics of crack profiles in the test specimen: (A) (i) longitudinal, (ii) transverse profile (shaded) representative for γ_a=0.5%, 0.6% and 0.7%, (B) representative crack profile for γ_a= 1.0% and 1.5%.

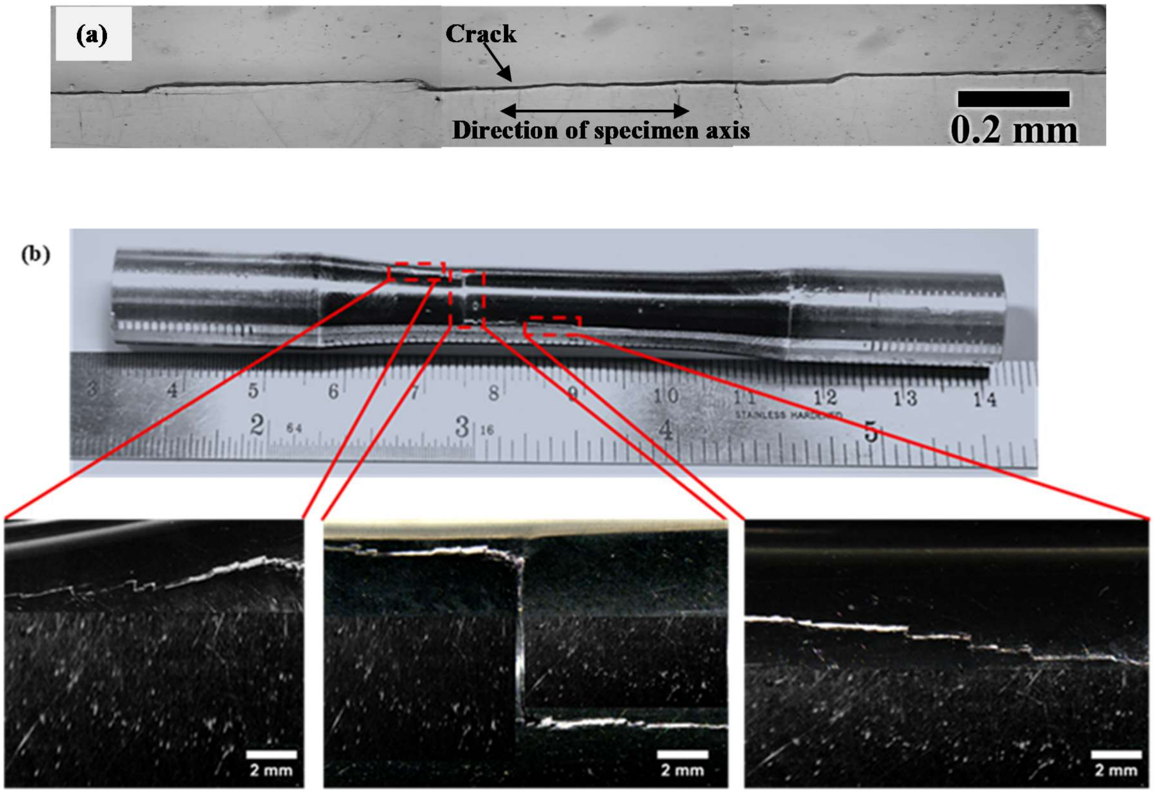

Figure 49: Microscopic images of cracks in in AW2099-T83 specimens tested at (a) 1.0% and (b) 0.6%.

iii. Crack Profile for Multiaxial Test Specimens

Representative crack profiles for proportional (0°) and nonproportional (90°) loadings for selected load for each of the alloys are shown in Fig. 50. AW2099-T83 specimen cracked in 0°-in-phase loading in longitudinal shear mode. The direction of growth was almost parallel to the axial loading mode direction. The 90° out-of-phase loading developed crack on a plane both parallel and perpendicular to specimen axis. The vertical crack grow was probably along the grain boundary considering the microstructure in Fig. 14(a). The predicted critical planes angles by Fatemi-Socie (FS) for the proportional (0°) and nonproportional (90°) loadings are 23-24° and 41°, respectively. The Smith-Watson-Topper (SWT) model predicted the critical plane angles for the 0° in-phase and 90° out-of-phase loadings are 69° and 89°, respectively. Hence, the SWT crack angles prediction are closer to the observed crack angle.

ZK60A and AISI 410 have their cracks almost in the plane of maximum normal. However, the angle of cracking for AISI 410, especially in proportional loading is almost entirely in the plane of maximum normal. The crack in the out-of-phase loading occurs in the 45° plane. The FS model predicted critical plane angle of 26° for in-phase loading and about 40° for out-of-phase loading for ZK60A, while SWT predictions are 71° and 87° for proportional and nonproportional loadings, respectively. For AISI 410, critical plane angles of 21° and 35° are predicted for proportional and nonproportional loadings. Critical plane angles by SWT for AISI 410 are 66° and 87° for in-phase and 90° out-of-phase loading, respectively.

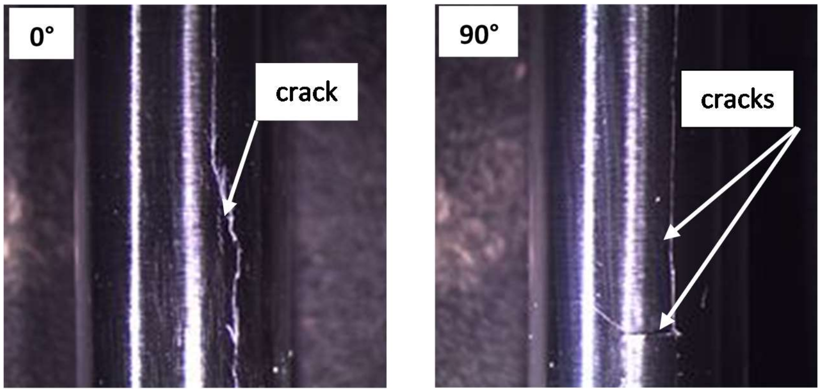

(a) AW2099-T83

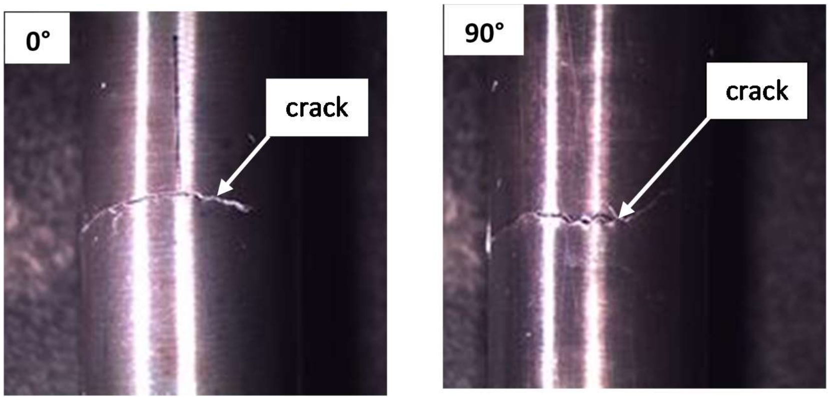

(b) ZK60A

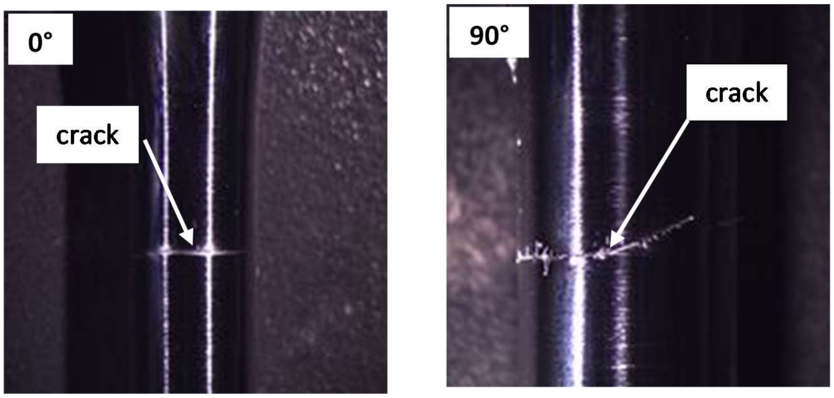

(c) AISI 410

Figure 50: Crack profiles for multiaxial fatigue specimens at in-phase 0° and 90°-out-of-phase loading paths.

4.6.2 Fractography

i. AW2099-T83 Alloy under Cyclic Axial Load

The fractured specimens for AW2099-T83 generally present a somewhat difficult fracture geometry, which made imaging to be challenging. SEM micrographs for AW2099-T83 tested at an applied strain amplitude of 0.3% are presented in Fig. 51(a). The overall fracture happened on a plane of maximum shear suggesting that the load causing the fracture is shear in nature. As can be seen in Fig. 51a(i), the fatigue fracture surface exhibits two separate areas: a fibrous section and a fairly smooth area with ridges. Close-up looks on the different sections of fractured surface are illustrated in Fig. 51a(ii-v). The fibrous area provides the clue that crack started from the edge of the smooth area (Fig. 51a(iv)). Final fracture zones usually show fibrous appearance [2,147]. There exist a transition zone from slow crack propagation to rapid crack growth area (Fig. 51a(iii)) which signifies that a shear deformation occurred during the transition from slow to fast fracture. The ridges on the smooth surface are perhaps beach marks indicating crack arrest. Figure 51a(v) is a higher magnification showing cleavage fracture.

SEM micrographs for AW2099-T83 specimen tested at axial strain amplitude of 0.5% are shown in Fig. 51(b). The fracture specimen appears like a wedge or bevel. A slow crack propagation region and crack initiation areas can be seen (Figs. 51b(i) and 51b(ii)). The presence of secondary crack in this region can be seen as illustrated in Fig. 51(b)(iii). The secondary crack appears to follow a grain boundary. The final fracture area, shown in Fig. 51b(iv), presents a texture that is characteristics of a semi-ductile fracture.

Figure 51(c) illustrates SEM micrographs of fractured surface of AW2099-T83 specimen tested at strain amplitude of 0.7%. The surface consists of a flat region (marked A) and a slant final fractured surface (marked B) at an angle to the loading axis as illustrated in Figs. 51(c)(i) and (c)(ii) for two different magnifications. Similar fracture has been reported by Alexopoulos et al. [90] for 2198 Al-Li. The multiplication of secondary cracks due to higher strain is clearly visible in Fig. 51(c)(iii). Evidence of crack branching can also be observed on same illustration. The fracture region, Fig. 51(c)(iv), is similar to that obtained at lower strain amplitude.

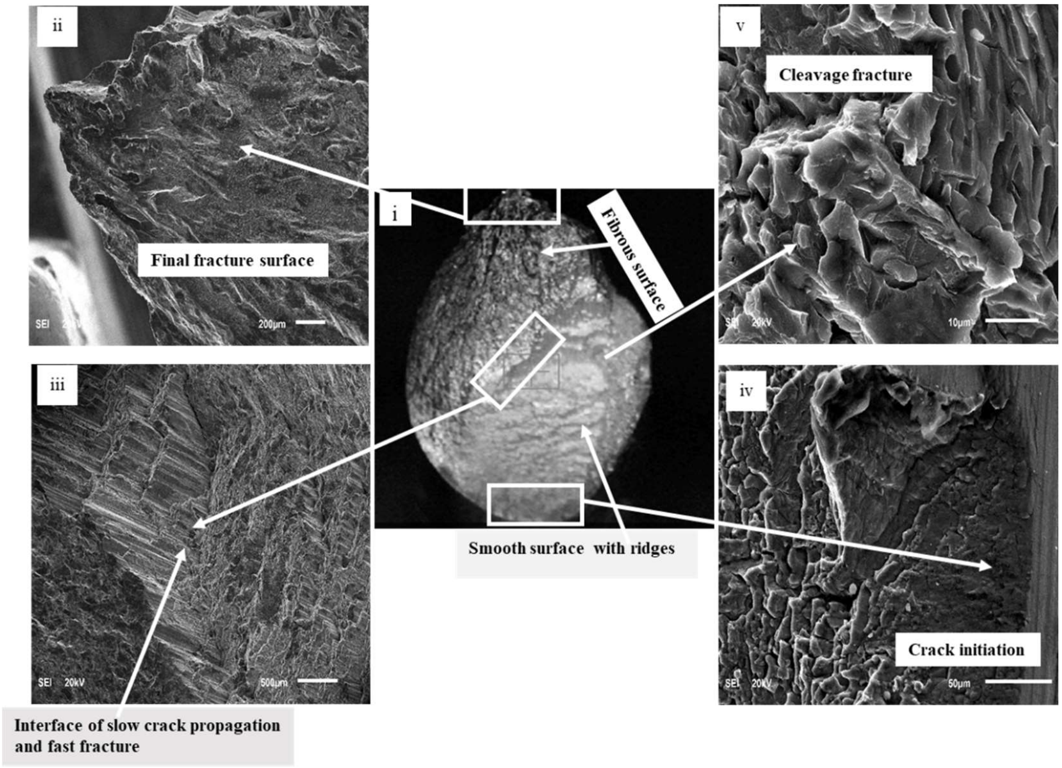

(a) Fractured surface of AW2099-T83 specimen tested at axial strain amplitude of 0.3%.

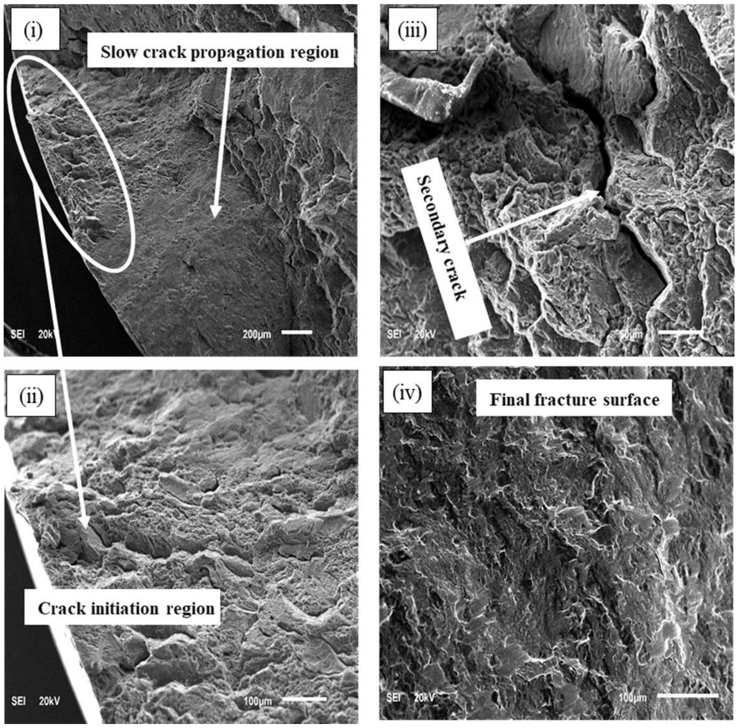

(b) Fractured surface of AW2099-T83 specimen tested at axial strain amplitude of 0.5%.

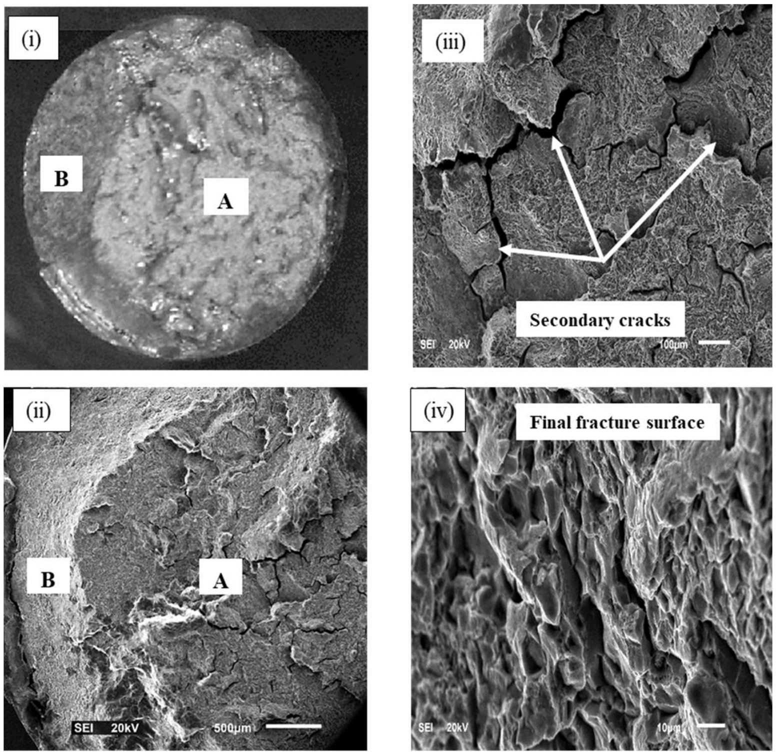

(c) Fractured surface of AW2099-T83 specimen tested at axial strain amplitude of 0.7%.

Figure 51: SEM micrograph of fractured surfaces of AW2099-T83 specimens under cyclic axial loading.

ii. ZK60A Alloy under Cyclic Axial Load

Figure 52 shows the fractured surface of ZK60A for different strain amplitudes. Distinct areas of crack initiation, propagation and final fracture are identifiable in Figs. 52(a)-(c), as illustrated for strain amplitude of 0.3%, 0.5% and 0.7%, respectively. The region of the crack advancement gradually decreases with increase in applied strain amplitude. The crack propagation stage dominates at lower applied strain amplitude, while fast fracture is prominent at higher applied strain amplitude. Shear lips are observed on the edge of the final fracture for the selected specimens (sharp edge of a section of the edges of the fracture region). Shear lip develops because of the change in state of stress during fracture. It provides information on where cracks started and also indicative of brittle fracture[147].

The height of the observed shear lips decreases with applied strain amplitudes indicating the extent of shear rupture. It may also be suggestive of hardening with higher applied strain amplitude for the present alloy. As was observed in section 4.4.1, cyclic hardening increases with increase in applied strain amplitude. From Fig. 52, a clear difference in surface texture between the crack region and the fracture area can be observed. Secondary cracks are multiplied with increase in applied strain amplitude. This is an indication of more damage due to higher strain.

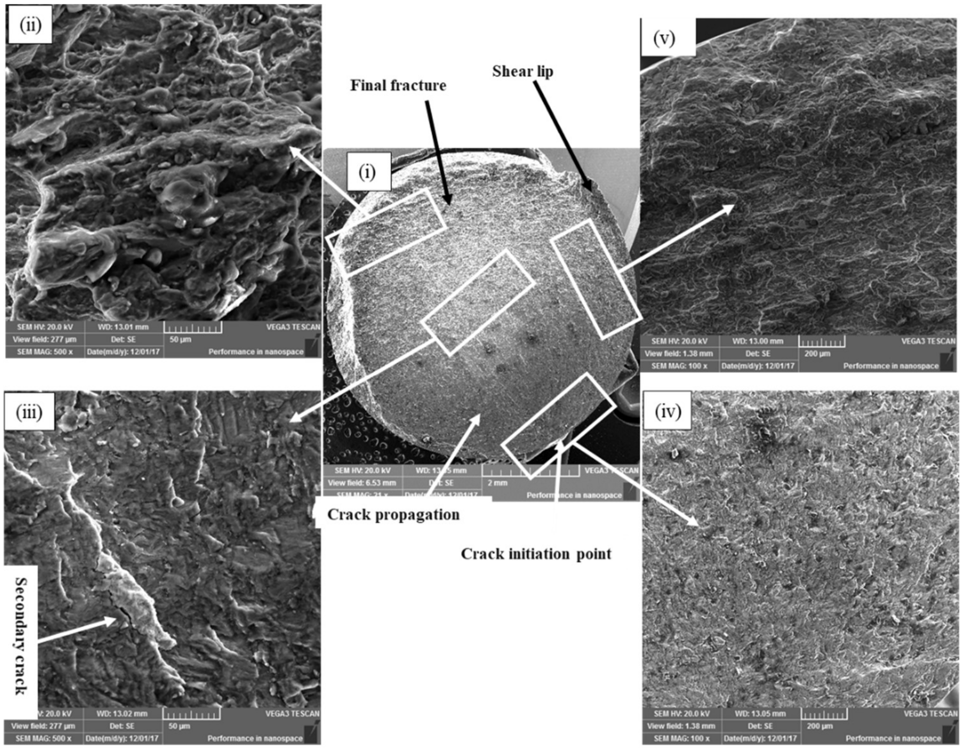

(a) Fractured surface of ZK60A specimen tested at axial strain amplitude of 0.3%.

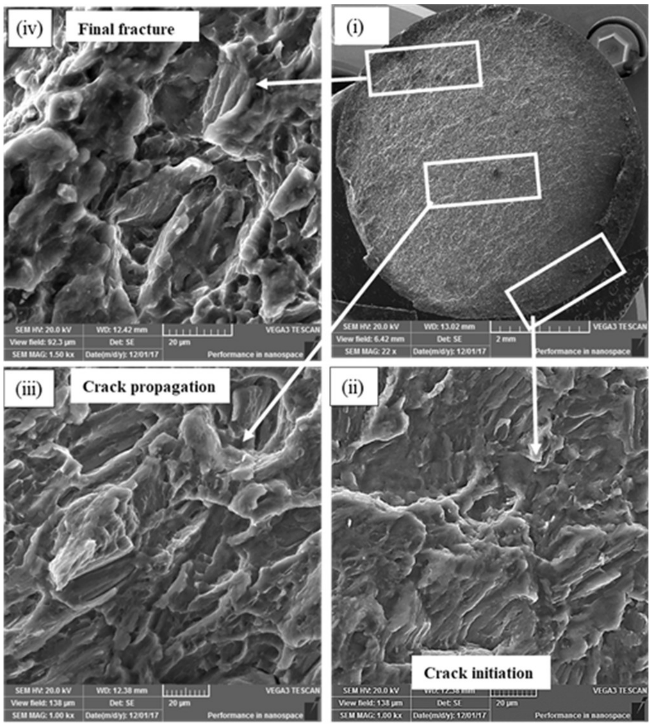

(b) Fractured surface of ZK60A specimen tested at axial strain amplitude of 0.5%.

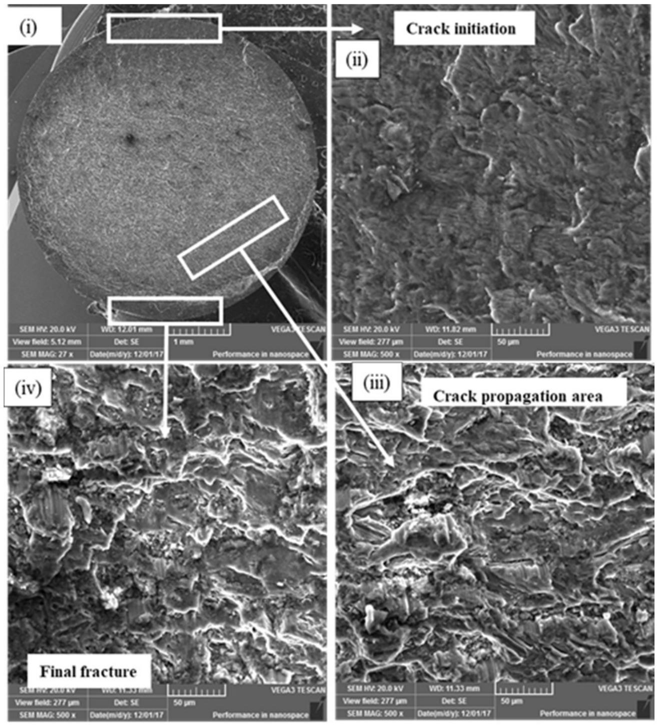

(c) Fractured surface of ZK60A specimen tested at axial strain amplitude of 0.7%.

Figure 52: SEM micrograph of fractured surfaces of ZK60A specimens under cyclic axial load.

iii. AISI 410 Alloy under Cyclic Axial Load

Fractures surfaces of AISI 410 specimens, illustrated in Fig. 53, consist of shiny regions of slow crack growth and dark and dull areas of fast fracture. The crack growth area in the specimen tested at 0.3% strain amplitude can be clearly seen in Fig. 53a(ii). An elliptical crack appears to have coalesced from several cracks which nucleated from microvoids as illustrated in Fig. 53a(ii). Regions of fast fracture and final fracture are shown in Figs. 53a(iii) and 53a(iv). Rivers-like markings are visible in fast fracture region.

Fig. 53(b) illustrates the fracture for specimen tested at strain amplitude of 0.5%. A smooth area of crack initiation is shown in Fig. 53b(ii). Crack propagation region is dominated by several secondary cracks. More secondary crack traces can be seen in Figs. 53b(iii) and 53b(iv). The increase in secondary cracks is because of higher damage due to increase in strain amplitude. Fractured sample for specimen tested at strain amplitude of 0.8% is shown in Fig. 53(c). The crack propagation zone (A) and final fracture area (B) are visible, as shown in Fig. 53(c)(i). Multiplication of secondary cracks are also visible due to increase in applied strain amplitude as can be observed in Fig. 53(c)(ii). Shear lips are present on the edge of fracture surface.

A brief summary on the fracture behavior under axial load is given. It can be observed that features of crack initiation, propagation and final fracture are present. However, the topographical feature for each alloy is different. The transition in the fractured surface of AW2099-T83 specimen from shear mode at low strain amplitude to almost completely tensile as applied strain amplitude becomes higher is indicative of the influence of strain amplitude on the cracking which lead to fracture. This correlates with the observation in the cyclic stress evolution presented in section 4.4.1 where cyclic softening and hardening depend on the number of applied cycles and strain amplitude. The varying fracture behavior might also be because of the dissimilar grain structure in different orientations shown in Fig. 14.

For ZK60A alloy, there is the consistence in its fracture mode; it is always tensile in nature. Such consistency can also be seen in the cyclic stress evolution. The decrease in the shear lip with increasing strain amplitude suggests increased cyclic hardening. This is in agreement with the observation in the cyclic stress evolution also.

Physical inspection of the fracture specimen of AISI 410 shows gross plastic deformation and increase in the shear lip area especially at higher applied strain amplitude. The multiplication of secondary cracks on the fracture specimen for AISI 410 indicates a greater fatigue damage. This might explains the low life for AISI 410 at equal strain amplitude applied across the alloys. Plastic strain for AISI 410 was higher at equivalent strain across the three alloys.

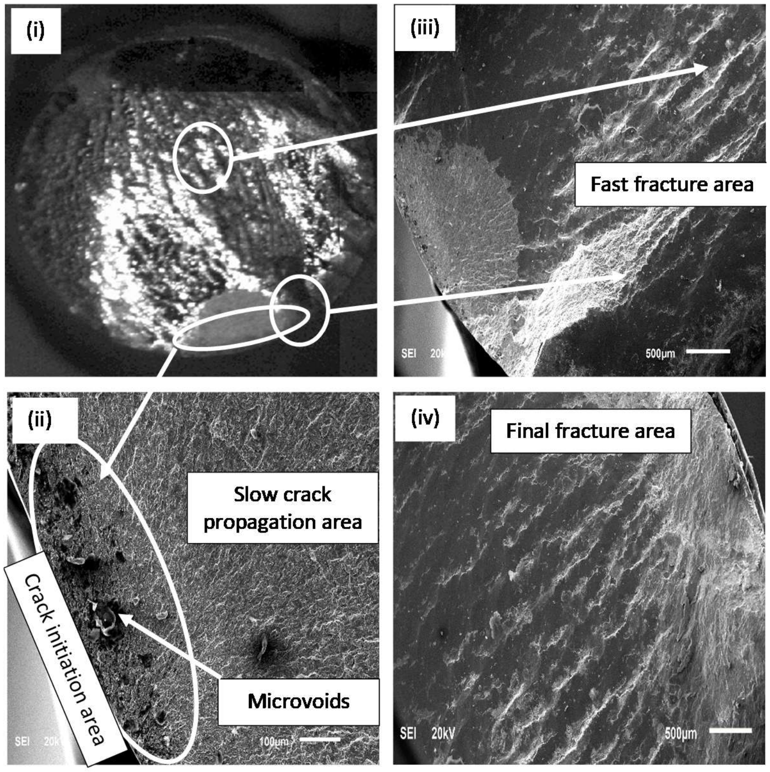

(a) Fractured surface of AISI 410 specimen tested at axial strain amplitude of 0.3%.

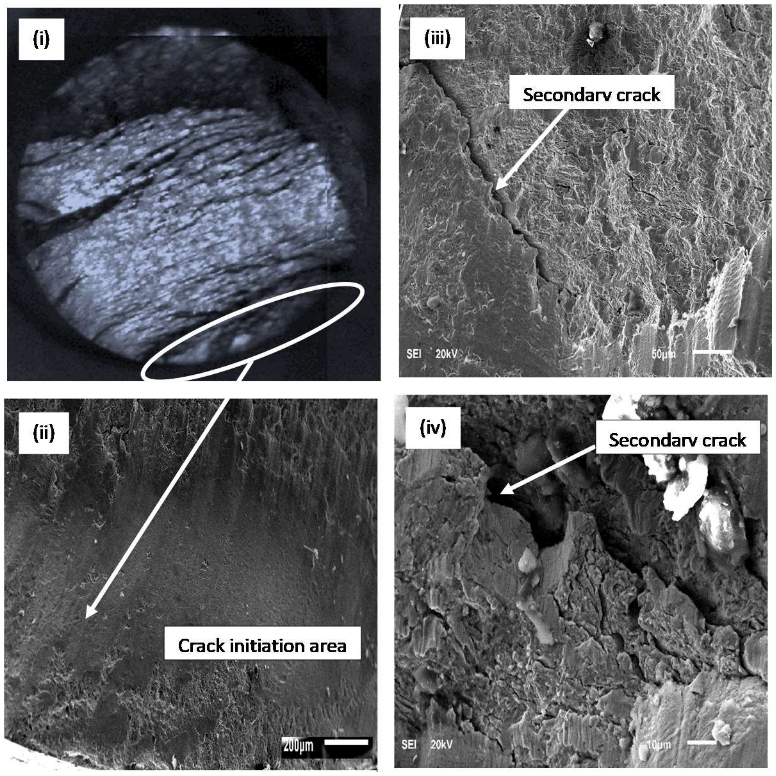

(b) Fractured surface of AISI 410 specimen tested at axial strain amplitude of 0.5%.

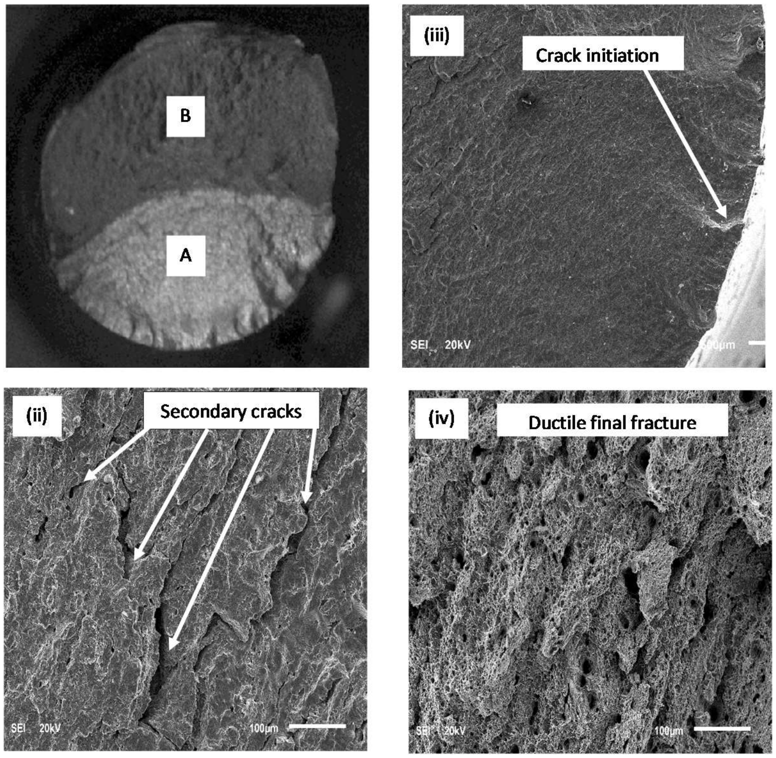

(c) Fractured surface of AISI 410 specimen tested at axial strain amplitude of 0.8%.

Figure 53: SEM micrograph of fractured surfaces of AISI 410 specimens under cyclic axial load.

iv. AW2099-T83 Alloy under Cyclic Torsion Load

Figure 54(a) is the morphology of the crack surface in the cross section (Fig. 48A(ii)) for an applied shear strain amplitude of 0.6%. Figure 54a(i) is the overall view of the transverse crack surface which is generally flat with little facets. Further magnification in Fig. 54a(ii) shows traces which are most likely striation-like mark. The striation-like markings are not present in the longitudinal section of the crack indicating that primary crack progression occurred in the cross section of the tubular test specimen. Multiple secondary cracks can be seen in Fig 54a(iii). This is indicative that cracks might have initiated from this orientation.

The crack morphology parallel to specimen axis is illustrated in Fig. 54(b). The generalized feature reveals a highly fibrous crack surface. Intense amount of secondary cracking occurs in this direction as can be seen from Fig. 54b(ii). At higher magnification in Fig. 54b(iii), cleavage structure with dimples can be observed.

Figure 54(c) is the SEM fractograph for specimen tested at shear strain amplitude of 1.0%. The generalized features of the crack are shown in Fig. 54c(i). Crack growth traces in the portion closer to the exterior of the specimen can be seen, suggesting that crack initiated at the specimen surface where highest stress are expected. Smoother crack surface is observed in the interior of the crack (Fig. 54c(ii)). Higher magnification in Fig. 54c(iii) shows crack progresses parallel to the direction of the alloy fibrous microstructure.

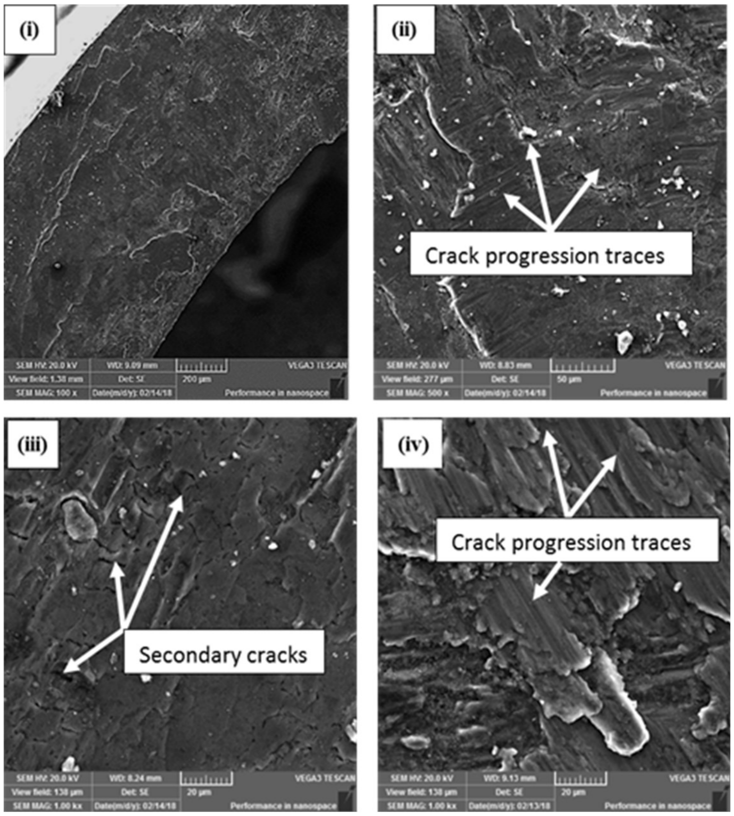

(a) Circumferential section of crack surface for sample tested at shear strain of 0.6%.

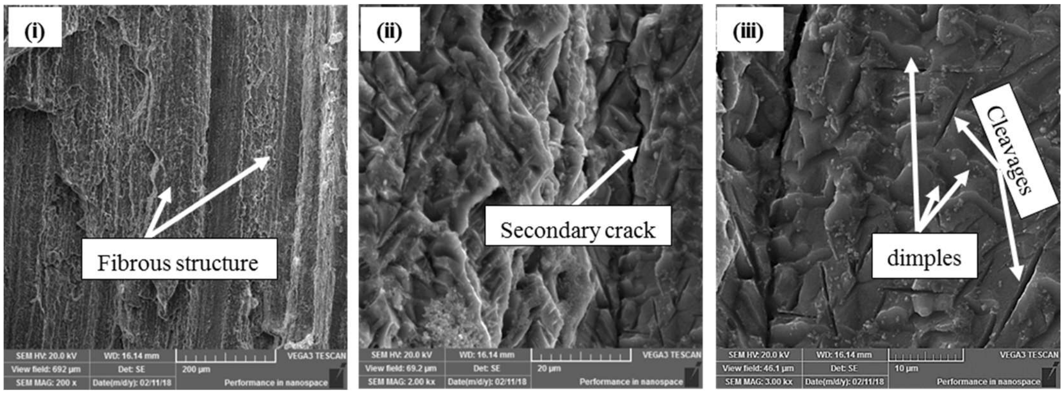

(b) Longitudinal section of crack surface for sample tested at shear strain of 0.6%.

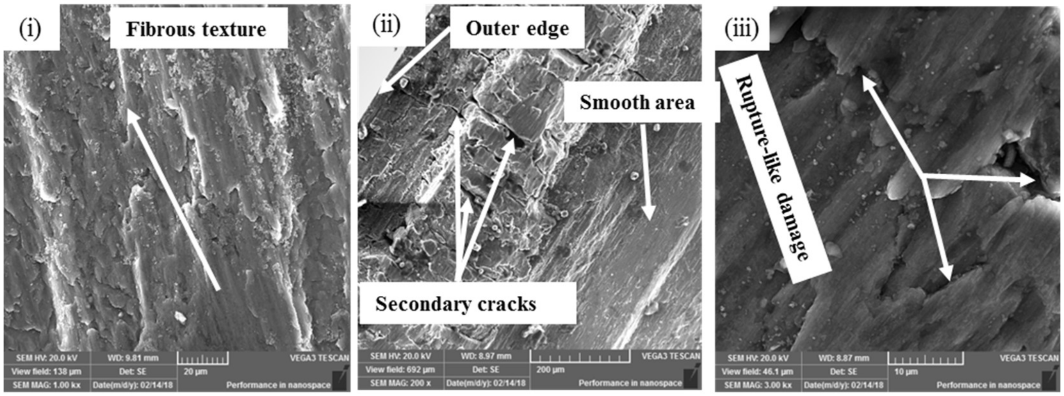

(c) Morphology of crack surface for sample tested at shear strain of 1%

Figure 54: SEM micrographs of specimen tested at shear strain amplitude of: (a), (b) 0.6 % and (c) 1.0%.

CHAPTER 5

CONCLUSIONS AND RECOMENDATIONS

5.1 Summary and Conclusions

A systematic experimental program, which consisted of metallography, monotonic tensile testing, monotonic torsion testing, strain-controlled cyclic axial, cyclic torsion and multiaxial proportional and nonproportional fatigue testing has been implemented on three metallic alloys, namely, AW2099-T83 aluminum-lithium, ZK60A magnesium alloy and AISI 410 stainless steel. The main findings of this work are summarized in this section.

1. Microstructure

The grains present in the transverse orientation for AW2099-T83 aluminum-lithium alloy are a combination of small and large grains, while elongated grains are present in the extrusion direction. Grain sizes at the core are smaller than those at the periphery in both transverse and extrusion directions. The grain sizes vary between 8 and 40 microns. ZK60A alloy has a coarse structure in the transverse direction while the extrusion direction contains both equiaxial and elongated structures. Twin grains were observed in the as-received alloy. The grains sizes vary between 11 to 140 microns. AISI 410 stainless steel exhibits a tempered martensitic structure which is similar in size and distribution in all the orientations studied. The average size for the grains is 5 microns.

2. Monotonic tensile behavior

The tensile properties of all the three alloys were investigated wherein the engineering stress-strain curves were generated. While ZK60A alloy hardened considerably before failure, AISI 410 showed the characteristic of a tough alloy with a weak strain-work hardening behavior. AW2099-T83 alloy exhibited the least hardening behavior with a curve profile that resembles a perfectly elastic-plastic material. ZK60A alloy has an average tensile strength of approximately 290 MPa, which is 50% the tensile strengths of AW2099-T83 and AISI 410 alloys. The tensile strength of AISI 410 alloy is only 4% higher than that of AW2099-T83 alloy. The least ductile of the three alloys is AW2099-T83 alloy. It has a fracture strain of 7%, which is 33% and 39% the fracture strain of ZK60A and AISI 410 alloys, respectively. The amount of necking in the fractured specimens is highest in AISI 410 alloy and is a further evidence of the plastic deformation behavior of the alloys. The strength coefficients, K and strain-hardening exponents, n, were determined from the strain curve. These two parameters were hardly available in literature for the alloys.

3. Monotonic torsional behavior

Likewise, the engineering shear stress-strain curves for the three alloys were generated. All the alloys exhibited hardening behavior post yielding. Strain-work hardening was higher in torsion than in tensile for AW2099-T83 and ZK60A alloys, while it was lower in tensile than in torsion for AISI 410 alloy. The average shear strength for ZK60A alloy is 182 MPa which is 38% and 61% of those of AISI 410 and ZK60A alloys, respectively. The strength coefficients K_s, and the strain-hardening exponents, n_s, which were hardly found in literature, were equally estimated from the stress-strain curve. Based on the monotonic behavior, it can be concluded that AW2099-T83 is a high strength alloy with little ductility, while ZK60A is a weak alloy and AISI 410 is a tough alloy.

4. Cyclic axial behavior

Strain-controlled cyclic axial behaviour of the three alloys has been investigated. Measureable plastic deformation for AW2099-T83 alloy was only present at applied strain amplitude of 0.7% and above. Below strain amplitude of 0.7%, the deformation was mainly elastic. However, plastic strain evolved at all the strain amplitudes investigated for ZK60A and AISI 410 alloys. Plastic strain increased with the number of cycle for AISI 410 alloy while it was unchanged for ZK60A alloy. At the same applied strain amplitude, AISI 410 alloy exhibited the largest plastic strain. The shapes of the hysteresis loops for the three alloys were generally symmetrical which can be attributed to slip deformation mode. With regard to peak stresses, slight asymmetry was observed resulting in minor mean stresses.

Cyclic axial stress evolution for AW2099-T83 alloy was dependent both on the applied strain amplitude and on the number of cycles. Cyclic hardening was observed in the early cycles at high strain amplitude, but was only observed at later cycles in low and intermediate strain amplitudes. Cyclic axial stress evolution for ZK60A alloy was mainly stable with minor cyclic hardening. AISI 410 alloy generally softened to failure at all applied strain amplitudes. Compressive mean stresses, which were mostly negligible, evolved for the three alloys. Fatigue life for the alloys expectedly decreased with increase in the applied strain amplitude due to rise in cyclic stress amplitude. Through regression analysis, curve fittings were constructed to model strain-life curves for the alloys. Axial fatigue properties, which include fatigue strength coefficient (σ_f'), fatigue strength exponent ($\boldsymbol{b}$), fatigue ductility coefficient $\left(\boldsymbol{\varepsilon}'_{\boldsymbol{f}}\right)$ and fatigue ductility exponent ($\boldsymbol{c}$) were determined and used to develop Coffin-Manson type strain-life equations for the three alloys. These equations can be used to estimate fatigue life for the alloys.

5. Cyclic torsional behavior

Under cyclic torsion, plastic strain evolved for ZK60A and AISI 410 alloys at all tested strain amplitudes, while it was only measurable for AW2099-T83 alloy at shear strain amplitude equal or higher than 1.0%. At same applied strain amplitude, plastic deformation in AISI 410 alloy was highest. The shapes of the hysteresis loops were mainly symmetrical. From the cyclic shear stress evolution trend, AW2099-T83 alloy softened to failure while ZK60A alloy was mainly stable with the number of cycles to failure. AISI 410 alloy continuously softened to failure. The cyclic softening behavior of AISI 410 alloy was more rapid than AW2099-T83 alloy. The trends in the strain and stress evolutions under cyclic torsion generally conform to those of the cyclic axial. Similarly, through curve fittings, strain-controlled shear fatigue parameters were determined and the shear Coffin-Manson equations, which can be used to estimate fatigue life, were developed for the three alloys.

6. Biaxial fatigue behavior

Multiaxial fatigue experiments under proportional and nonproportional loading paths were conducted on the three alloys. Contrary to expectation, it was found that fatigue life under nonproportional loadings was mainly higher than the fatigue life under proportional loadings for AW2099-T83 and ZK60A alloys. It was only in AISI 410 alloy that the fatigue life in nonproportional loading path was found to be consistently lower than that of the proportional loading path. This is attributable to the additional cyclic hardening, which was significantly present in the hysteresis loop of AISI 410 alloy. For similar applied strain amplitudes in AW2099-T83 alloy under different loading modes, the shape of the hysteresis loop and stress level in uniaxial fatigue and nonproportional loading path were similar. Proportional loading mode consistently exhibited lower stress level but higher plastic strain amplitude under same applied strain amplitude. The hysteresis loops for ZK60A alloy under equal strain amplitude for the different loading paths were similar except that plastic strain was higher in proportional loading path than in nonproportional loading path. The hysteresis loop for AISI 410 alloy in nonproportional loading path showed significant nonproportional cyclic hardening. This was the reason for the higher stress evolution and lower fatigue life under this loading path. Therefore, it can be concluded that multiple slip activation due to nonproportional loading only occurred in AISI 410 alloy. By means of von Misses equivalent strain method, it was found that cyclic torsional loading path was more damaging for AW2099-T83 alloy, while cyclic axial loading was the least destructive. For ZK60A alloy, the most damaging loading path was the cyclic axial loading, while the cyclic torsion produced the highest fatigue life. The multiaxial loading paths were more detrimental to AISI 410 alloy. Fatemi-Socie (FS) critical plane criterion made better prediction of fatigue life than Smith-Watson-Topper (SWT) critical plane criterion for majority of the loading paths studied.

7. Cracking and fracture behavior

In AW2099-T83 alloy, straight crack that was generally smooth resulted for shear strain amplitudes of 1.0% and greater. Shear strain amplitudes less than 1.0% produced rough crack profile in a ‘staircase-like’ pattern that caused higher physical damage to tested specimens. The observed perpendicular crack bifurcations under low shear strain amplitudes had not been reported elsewhere. Cleavage was the dominant mode of fracture under cyclic shear test. Crack profile in the multiaxial fatigue tested specimens for AW2099-T83 alloy was mainly in shear mode under proportional loading while it was almost tensile in nonproportional loading path. Cracking occurred for ZK60A and AISI 410 alloys mainly in tensile manner regardless of loading path. Under cyclic axial, secondary cracks in AW2099-T83 were found mainly along the grain boundary. AW2099-T83 alloy specimen under cyclic axial loading failed by shear mode at low applied strain amplitudes, but by tensile mode at higher applied strain amplitudes. ZK60A alloy consistently failed in tensile manner regardless of applied strain amplitude. AISI 410 alloy mainly failed in shear mode with gross plastic deformation at higher strain amplitudes.

In conclusion, the differences observed in the fatigue behavior of the three alloys can be explained by the different microstructures and dislocation behavior. The microstructure of AW2099-T83 alloy was strengthened by aging precipitates that interacted with dislocations, causing cyclic hardening. However, when precipitates were sheared due to higher stress, their resistance to dislocation movement was weakened and cyclic softening resulted. The ZK60A alloy hardened due to fewer slip planes present in its structure and due to twining mode of dislocation. With increase in the number of cycles, dislocation was increased but there was insufficient plane for dislocation mobility to occur. The overall softening observed in AISI 410 alloy was because of its tempered martensite which did not restrict dislocation mobility. In addition, cycle-dependent and strain-dependent fatigue behavior as were seen in AW2099-T83 and ZK60A could be linked to their microstructures both of which exhibit strong texture. However, such behavior was not seen in AISI 410 alloy which maintained the same grain structures and sizes in all the orientations. Based on the analysis that has been carried out in the present work, it can be concluded that the fatigue performance of each of the three alloys depend on their microstructures.

5.2 Recommendations for Future Work

A possible future work can include

- Study on the fracture mechanism of AW2099-T83 alloy. Crack profile seems to suggest an unstable crack propagation mechanism in the alloy especially in torsional loading.
- Study on the fatigue behavior in high cycle regime for ZK60A alloy. Fatigue life appears within a narrow band resulting to a bad fit using Coffin-Manson strain-life curve.
- A study on the plasticity of AISI 410 alloy, because the alloy exhibits low plastic work hardening in monotonic behavior, yet it shows large plastic deformation in fatigue.
- Testing in different orientations for AW2099-T83 and ZK60A alloys, both in monotonic and cyclic tests, for comparison study because of the dissimilar grains distributions and sizes in different orientations.
- Additional testing for AISI 410 alloy under cyclic torsion to increase the size of the data so that shear fatigue parameters are more reliable.
- More testing under biaxial loading paths, especially for AW2099-T83 and AISI 410 alloys are required.
- SEM and TEM studies of as received microstructure and post fracture microstructure.
- Study on the heat treatment effect on the fatigue behavior of the three alloys.

References

[1] Suresh S. Fatigue of Materials. 2nd ed. Cambridge: Cambridge University Press; 1998.

[2] Stephens, Ralph I, Fatemi A, Stephens, Robert R, Fuchs, Henry O. Metal Fatigue in Engineering. vol. 3. 2nd ed. John Wiley & Sons; 2001.

[3] Callister WD, Rethwisch DG. Materials Science and Engineering. 8th ed. John Wiley and Sons, Inc; 2011.

[4] ASTM. Case Histories Involving Fatigue and Fracture Mechanics: A Symposium, 918. Philadelphia: 1986.

[5] Brown MW, Miller KJ, editors. Biaxial and Multiaxial Fatigue (EGF 3). Wiley; 1989.

[6] Rie KT, Portella PD, editors. Low Cycle Fatigue and Elasto-Plastic Behaviour of Mataerials. Elsevier; 1998.

[7] Dowling NE. Mechanical Behavior of Materials, Engineering Methods for Deformation, Fracture, and Fatigue. 3rd ed. Pearson Prentice Hall, New Jersey; 2007.

[8] Mazzini D, Santus C. Static strength and High and Low-Cycle Fatigue at room temperature 2 / 2 2015.

[9] Itoh T, Sakane M. Evaluation of Multiaxial Low Cycle Fatigue Life under Non-proportional Loading. 10th Int Conf Multiaxial Fatigue Fract 2013.

[10] Nakamura H, Takanashi M, Itoh T, Wu M, Shimizu Y. Fatigue crack initiation and growth behavior of Ti-6Al-4V under non-proportional multiaxial loading. Int J Fatigue 2011;33:842–8. doi:10.1016/j.ijfatigue.2010.12.013.

[11] ASTM International. Strain-Controlled Axial-Torsional Fatigue Testing with Thin-Walled Tubular Specimens 2008:1–8. doi:10.1520/E2207-08.2.

[12] ASTM International. Standard Practice for Strain-Controlled Fatigue Testing, E 606 -99, West Conshohocken, PA. 2004. 24. 1999.

[13] www.sv.vt.edu/classes/ MSE2094_NoteBook/97ClassProj/exper/meyer/www/meyer.html n.d.

[14] Brown MW, Miller KJ. A theory for fatigue failure under multiaxial stress–strain conditions. Arch Proc Inst Mech Eng 1847-1982 (Vols 1-196) 2006;187:745–55.

[15] Fatemi A, Socie DF. Critical Plane Approach To Multiaxial Fatigue Damage Including Out-of-Phase Loading. Fatigue Fract Eng Mater Struct 1988;11:149–65. doi:10.1111/j.1460-2695.1988.tb01169.x.

[16] Albinmousa J, Jahed H. Multiaxial effects on LCF behaviour and fatigue failure of AZ31B magnesium extrusion. Int J Fatigue 2014;67:103–16.

[17] Smith K, Topper TH, Watson P. A stress-strain function for the fatigue of metals(Stress-strain function for metal fatigue including mean stress effect). J Mater 1970;5:767–78.

[18] Anes V, Reis L, Li B, Freitas M. Crack path evaluation on HC and BCC microstructures under multiaxial cyclic loading. Int J Fatigue 2014;58:102–13. doi:10.1016/j.ijfatigue.2013.03.014.

[19] Liu KC. A method based on virtual strain-energy parameters for multiaxial fatigue life prediction. Adv Multiaxial Fatigue 1993.

[20] Facheris G, Janssens KGF, Foletti S. Multiaxial fatigue behavior of AISI 316L subjected to strain-controlled and ratcheting paths. Int J Fatigue 2014;68:195–208. doi:10.1016/j.ijfatigue.2014.05.003.

[21] Mohammadpour M, Kalajahi MH, Oskouei RH, Shakouri M. Fatigue life estimation of coach peel riveted joints using multi-axial fatigue criteria. Mater Des 2014;62:327–33. doi:10.1016/j.matdes.2014.05.033.

[22] Shamsaei N, McKelvey SA. Multiaxial life predictions in absence of any fatigue properties. Int J Fatigue 2014;67:62–72. doi:10.1016/j.ijfatigue.2014.02.020.

[23] Shamsaei N, Gladskyi M, Panasovskyi K, Shukaev S, Fatemi A. Multiaxial fatigue of titanium including step loading and load path alteration and sequence effects. Int J Fatigue 2010;32:1862–74. doi:10.1016/j.ijfatigue.2010.05.006.

[24] Gao Z, Zhao T, Wang X, Jiang Y. Multiaxial Fatigue of 16MnR Steel. J Press Vessel Technol 2009;131:021403. doi:10.1115/1.3008041.

[25] Hirsch J, Al-Samman T. Superior light metals by texture engineering: Optimized aluminum and magnesium alloys for automotive applications. Acta Mater 2013;61:818–43. doi:10.1016/j.actamat.2012.10.044.

[26] Eswara Prasad N, Gokhale AA, Wanhill RJH, editors. Aluminum-Lithium Alloys: Processing, Properties, and Applications. 1st ed. Butterworth Heinemann; 2014.

[27] Wanhill RJH. Aerospace Applications of Aluminum-Lithium Alloys. Elsevier Inc.; 2013. doi:10.1016/B978-0-12-401698-9.00015-X.

[28] Jata K V., Singh AK. Texture and its effects on properties in aluminum-lithium alloys. Elsevier Inc.; 2013. doi:10.1016/B978-0-12-401698-9.00005-7.

[29] Kulekci MK. Magnesium and its alloys applications in automotive industry. Int J Adv Manuf Technol 2008;39:851–65. doi:10.1007/s00170-007-1279-2.

[30] crystal | physics | Britannica.com n.d. https://www.britannica.com/science/crystal (accessed November 23, 2017).

[31] Zhou Y, Rao GB, Wang JQ, Zhang B, Yu ZM, Ke W, et al. Influence of Ti/TiN bilayered and multilayered films on the axial fatigue performance of Ti46Al8Nb alloy. Thin Solid Films 2011;519:2207–12. doi:10.1016/j.tsf.2010.10.025.

[32] Castelluccio GM, McDowell DL. Microstructure-sensitive small fatigue crack growth assessment: Effect of strain ratio, multiaxial strain state, and geometric discontinuities. Int J Fatigue 2015;82:521–9. doi:10.1016/j.ijfatigue.2015.09.007.

[33] Tan C, Li X, Sun Q, Xiao L, Zhao Y, Sun J. Effect of α-phase morphology on low-cycle fatigue behavior of TC21 alloy. Int J Fatigue 2015;75:1–9.

[34] Verdhan N, Bhende DD, Kapoor R, Chakravartty JK. Effect of microstructure on the fatigue crack growth behaviour of a near-α Ti alloy. Int J Fatigue 2015;74:46–54. doi:10.1016/j.ijfatigue.2014.12.013.

[35] Jiang R, Everitt S, Lewandowski M, Gao N, Reed PAS. Grain size effects in a Ni-based turbine disc alloy in the time and cycle dependent crack growth regimes. Int J Fatigue 2014;62:217–27. doi:10.1016/j.ijfatigue.2013.07.014.

[36] Jiang R, Karpasitis N, Gao N, Reed PAS. Effects of microstructures on fatigue crack initiation and short crack propagation at room temperature in an advanced disc superalloy. Mater Sci Eng A 2015;641:148–59. doi:10.1016/j.msea.2015.05.065.

[37] Shamsaei N, Fatemi A. Effect of microstructure and hardness on non-proportional cyclic hardening coefficient and predictions. Mater Sci Eng A 2010;527:3015–24. doi:10.1016/j.msea.2010.01.056.

[38] Lin YC, Chen X-M, Liu Z-H, Chen J. Investigation of uniaxial low-cycle fatigue failure behavior of hot-rolled AZ91 magnesium alloy. Int J Fatigue 2013;48:122–32.

[39] Fintová S, Kunz L. Fatigue properties of magnesium alloy AZ91 processed by severe plastic deformation. J Mech Behav Biomed Mater 2015;42:219–28.

[40] Shamsaei N, Fatemi A. Deformation and fatigue behaviors of case-hardened steels in torsion: Experiments and predictions. Int J Fatigue 2009;31:1386–96.

[41] Lee EU, Vasudevan AK, Glinka G. Environmental effects on low cycle fatigue of 2024-T351 and 7075-T651 aluminum alloys. Int J Fatigue 2009;31:1938–42.

[42] Li J, Li CW, Qiao YJ, Zhang ZP. Fatigue life prediction for some metallic materials under constant amplitude multiaxial loading. Int J Fatigue 2014;68:10–23.

[43] Itoh T, Yang T. Material dependence of multiaxial low cycle fatigue lives under non-proportional loading. Int J Fatigue 2011;33:1025–31.

[44] Lv F, Yang F, Duan QQ, Yang YS, Wu SD, Li SX, et al. Fatigue properties of rolled magnesium alloy (AZ31) sheet: Influence of specimen orientation. Int J Fatigue 2011;33:672–82. doi:10.1016/j.ijfatigue.2010.10.013.

[45] Fouad Y. Fatigue behaviour of a rolled AZ31 magnesium alloys prepared by EP and BB conditions. Iran J Mater Sci Eng 2010;7:30–4. doi:10.1016/j.aej.2011.01.004.

[46] Jahed H, Albinmousa J. Multiaxial behaviour of wrought magnesium alloys - A review and suitability of energy-based fatigue life model. Theor Appl Fract Mech 2014;73:97–108. doi:10.1016/j.tafmec.2014.08.004.

[47] Xiong Y, Yu Q, Jiang Y. Multiaxial fatigue of extruded AZ31B magnesium alloy. Mater Sci Eng A 2012;546:119–28. doi:10.1016/j.msea.2012.03.039.

[48] Koike J, Fujiyama N, Ando D, Sutou Y. Roles of deformation twinning and dislocation slip in the fatigue failure mechanism of AZ31 Mg alloys. Scr Mater 2010;63:747–50. doi:10.1016/j.scriptamat.2010.03.021.

[49] De-Feng M, Guo-Qiu H, Zheng-Fei H, Zheng-Yu Z, Cheng-Shu C, Wei-Hua Z. Crack initiation and propagation of cast A356 aluminum alloy under multi-axial cyclic loadings. Int J Fatigue 2008;30:1843–50.

[50] Le V-D, Morel F, Bellett D, Saintier N, Osmond P. Multiaxial high cycle fatigue damage mechanisms associated with the different microstructural heterogeneities of cast aluminium alloys. Mater Sci Eng A 2016;649:426–40.

[51] Deng C, Wang H, Gong B, Li X, Lei Z. Effects of microstructural heterogeneity on very high cycle fatigue properties of 7050-T7451 aluminum alloy friction stir butt welds. Int J Fatigue 2016;83:100–8. doi:10.1016/j.ijfatigue.2015.10.001.

[52] Huter P, Renhart P, Oberfrank S, Schwab M, Grün F, Stauder B, et al. High- and Low- cycle fatigue influence of silicon, copper, strontium and iron on hypo-eutectic Al-Si-Cu and Al-Si-Mg cast alloys used in cylinder heads. Int J Fatigue 2015;82:1–23.

[53] Hornqvist M, Karlsson B. Dynamic strain ageing and dynamic precipitation in AA7030 during cyclic deformation. Procedia Eng 2010;2:265–73.

[54] Shankar V, Kumar A, Mariappan K, Sandhya R, Laha K, Bhaduri AK, et al. Occurrence of dynamic strain aging in Alloy 617M under low cycle fatigue loading. Int J Fatigue 2017;100:12–20. doi:10.1016/j.ijfatigue.2017.03.001.

[55] Verma P, Rao GS, Chellapandi P, Mahobia GS, Chattopadhyay K, Srinivas NCS, et al. Dynamic strain ageing, deformation, and fracture behavior of modified 9Cr – 1Mo steel. Mater Sci Eng A 2015;621:39–51. doi:10.1016/j.msea.2014.10.011.

[56] Keller C, Margulies MM, Guillot I. Experimental analysis of the dynamic strain ageing for a modified T91 martensitic steel. Mater Sci Eng A 2012;536:273–5.

[57] Valdes-Tabernero MA, Sancho-Cadenas R, Sabirov I, Murashkin MY, Ovid'ko IA, Galvez F. Effect of SPD processing on mechanical behavior and dynamic strain aging of an Al-Mg alloy in various deformation modes and wide strain rate range. Mater Sci Eng A 2017;696:348–59.

[58] Peng G, Gan X, Jiang Y, Li Z, Zhou K. Effect of dynamic strain aging on the deformation behavior and microstructure of Cu-15Ni-8Sn alloy. J Alloys Compd 2017;718:182–7.

[59] Lan P, Zhang J. Twinning and dynamic strain aging behavior during tensile deformation of FE-Mn-C TWIP steel. Mater Sci Eng A 2017;700:250–8.

[60] Srinivas NCS, Verma P, Singh V. Dynamic Strain Ageing Behaviour of Modified 9Cr-1Mo Steel under Monotonic and Cyclic Loading. Procedia Eng 2017;184:765–72. doi:10.1016/j.proeng.2017.04.155.

[61] Chen C, Lv B, Wang F, Zhang F. Low-cycle fatigue behaviors of pre-hardening Hadfield steel. Mater Sci Eng A 2017;695:144–53.

[62] Huang Z, Wagner D, Bathias C. Some metallurgical aspects of Dynamic Strain Aging effect on the Low Cycle Fatigue behavior of C – Mn steels. Int J Fatigue 2015;80:113–20. doi:10.1016/j.ijfatigue.2015.04.008.

[63] Huang ZY, Wagner D, Wang QY, Khan MK, Chaboche JL. A low cycle fatigue model for low carbon manganese steel including the effect of dynamic strain aging. Mater Sci Eng A 2016;654:77–84. doi:10.1016/j.msea.2015.12.022.

[64] Aritra Sarkar, A. Nagesha, P. Parameswaran, R. Sandhya, M. Okazaki. Implications of dynamic strain aging under LCF-HCF interactions in a type 316LN stainless steel. Mater Sci Eng A 2017;708:91–103. doi:10.1016/j.msea.2017.09.057.

[65] Varvani-Farahani A. New energy-critical plane parameter for fatigue life assessment of various metallic materials subjected to in-phase and out-of-phase multiaxial fatigue loading conditions. Int J Fatigue 2000;22:295–305. doi:10.1016/S0142-1123(00)00002-5.

[66] Wu ZR, Hu XT, Song YD. Multiaxial fatigue life prediction for titanium alloy TC4 under proportional and nonproportional loading. Int J Fatigue 2014;59:170–5.

[67] Lin XZ, Chen DL. Strain controlled cyclic deformation behavior of an extruded magnesium alloy. Mater Sci Eng A 2008;496:106–13.

[68] Samaei M, Zehsaz M, Chakherlou TN. Experimental and numerical study of fatigue crack growth of aluminum alloy 2024-T3 single lap simple bolted and hybrid (adhesive/bolted) joints. Eng Fail Anal 2015;59:253–68.

[69] Lei, B-M., Tran, V-X., Taheri, S., Le Roux, J-C., Curtit, F., He, M., Wan, L., Zhou Y. Towards consistent fatigue crack initiation criteria for 304L austenitic stainless steel under multi-axial loads. Int J Fatigue 2014;15:39.

[70] Sun GQ, Shang DG, Bao M. Multiaxial fatigue damage parameter and life prediction under low cycle loading for GH4169 alloy and other structural materials. Int J Fatigue 2010;32:1108–15. doi:10.1016/j.ijfatigue.2009.12.007.

[71] Anes V, Reis L, Li B, Fonte M, de Freitas M. New approach for analysis of complex multiaxial loading paths. Int J Fatigue 2014;62:21–33.

[72] Mamiya EN, Castro FC, Araújo JA. Recent developments on multiaxial fatigue: The contribution of the University of Brasília. Theor Appl Fract Mech 2014;73:48–59. doi:10.1016/j.tafmec.2014.06.007.

[73] Madrigal C, Chaves V, Navarro A. Numerical implementation of a multiaxial cyclic plasticity model for the Local Strain Method in low cycle fatigue. Frat Ed Integrità Strutt 2014;30:153–61. doi:10.3221/IGF-ESIS.30.20.

[74] Esmaeili F, Rahmani A, Barzegar S, Afkar A. Prediction of fatigue life for multi-spot welded joints with different arrangements using different multiaxial fatigue criteria. Mater Des 2015;72:21–30. doi:10.1016/j.matdes.2015.02.008.

[75] Heyes PJ, Milsted M., Dakin J. multiaxial fatigue assessment of Automotive Chassis Components on the basis of finite element analysis. Multiaxial Fatigue Des 1996:461–75.

[76] Ince A, Glinka G. Innovative computational modeling of multiaxial fatigue analysis for notched components. Int J Fatigue 2016;82:134–45.

[77] Wan X, Shan Y, Liu X, Wang H, Wang J. Simulation of biaxial wheel test and fatigue life estimation considering the influence of tire and wheel camber. Adv Eng Softw 2016;92:57–64. doi:10.1016/j.advengsoft.2015.11.005.

[78] Filippini M, Foletti S, Pasquero G. Assessment of multiaxial fatigue life prediction methodologies for Inconel 718. Procedia Eng 2010;2:2347–56.

[79] Sakane M, Itoh T, Kida S, Ohnami M, Socie D. Dislocation structure and non-proportional hardening of type 304 stainless steel. Fatigue Fract Eng Mater Struct 1997;20:1375–86.

[80] Rao HM, Jordon JB, Barkey ME, Guo YB, Su X, Badarinarayan H. Influence of structural integrity on fatigue behavior of friction stir spot welded AZ31 Mg alloy. Mater Sci Eng A 2013;564:369–80.

[81] Luo T, Shi B, Duan Q, Fu J, Yang Y. Fatigue behavior of friction stir spot welded AZ31 Mg alloy sheet joints. Trans Nonferrous Met Soc China 2013;23:1949–56. doi:10.1016/S1003-6326(13)62682-5.

[82] Mikheevskiy S, Bogdanov S, Glinka G. Analysis of fatigue crack growth under spectrum loading - The UniGrow fatigue crack growth model. Theor Appl Fract Mech 2015;79:25–33. doi:10.1016/j.tafmec.2015.06.010.

[83] Rioja RJ, Liu J. The evolution of Al-Li base products for aerospace and space applications. Metall Mater Trans A Phys Metall Mater Sci 2012;43A:3325–37. doi:10.1007/s11661-012-1155-z.

[84] Ashby M, Johnson K. Materials and Design 2002;56:862–71.

[85] Wanhill RJH. Status and prospects for aluminium-lithium alloys in aircraft structures. Fatigue 1994;16:3–20. doi:0142-1123/94/01/0003-18.

[86] Wanhill RJH, Bray GH. Aerostructural Design and Its Application to Aluminum-Lithium Alloys. Elsevier Inc.; 2013. doi:10.1016/B978-0-12-401698-9.00002-1.

[87] Bois-Brochu A, Blais C, Tchitembo Goma FA, Larouche D. Modelling of anisotropy for Al-Li 2099 T83 extrusions and effect of precipitate density. Mater Sci Eng A 2016;673:581–6. doi:10.1016/j.msea.2016.07.081.

[88] Dursun T, Soutis C. Recent developments in advanced aircraft aluminium alloys. Mater Des 2014;56:862–71.

[89] Li J-F, Liu P, Chen Y, Zhang X, Zheng Z. Microstructure and mechanical properties of Mg, Ag and Zn multi-microalloyed Al-(3.2-3.8)Cu-(1.0-1.4)Li alloys. Trans Nonferrous Met Soc China 2015;25:2103–12.

[90] Alexopoulos ND, Migklis E, Stylianos A, Myriounis DP. Fatigue behavior of the aeronautical Al – Li (2198) aluminum alloy under constant amplitude loading. Int J Fatigue 2013;56:95–105.

[91] Srivatsan TS, Coyne EJ. Cyclic stress response and deformation behaviour of precipitation-hardened aluminium-lithium alloys. Int J Fatigue 1986;4:201–8.

[92] Jata K V, Starke EA. Fatigue Crack Growth and Fracture Toughness Behavior of an Al-Li-Cu Alloy. Metall Trans A 1986;17A:1011–26.

[93] Yang JR, Tsai MC, Du JS, Lin YJ. Phase transformations in AISI 410 stainless steel. Japan Inst Met Proceedings, Vol 12, (Jimic-3), Pts 1 2 1999;332:1605–8.

[94] Hejripour F, Aidun DK. Consumable selection for arc welding between Stainless Steel 410 and Inconel 718. J Mater Process Technol 2017;245:287–99.

[95] Vamsi Krishna B, Bandyopadhyay A. Surface modification of AISI 410 stainless steel using laser engineered net shaping (LENSTM). Mater Des 2009;30:1490–6. doi:10.1016/j.matdes.2008.08.003.

[96] Lin Y, Zheng ZQ, Li SC. Effect of solution treatment on microstructures and mechanical properties of 2099 Al–Li alloy. Arch Civ Mech Eng 2014;14:61–71. doi:10.1016/j.acme.2013.07.005.

[97] Lin Y, Zheng Z, Li S, Kong X, Han Y. Microstructures and properties of 2099 Al-Li alloy. Mater Charact 2013;84:88–99. doi:10.1016/j.matchar.2013.07.015.

[98] Bois-Brochu A, Blais C, Goma FAT, Larouche D, Boselli J, Brochu M. Characterization of Al–Li 2099 extrusions and the influence of fiber texture on the anisotropy of static mechanical properties. Mater Sci Eng A 2014;597:62–9. doi:10.1016/j.msea.2013.12.060.

[99] Goma FAT, Larouche D, Bois-Brochu A, Blais C, Boselli J, Brochu M. Effect of extrusion aspect ratio and test temperatures on fatigue crack growth behavior of a 2099-T83 Al-Li alloy. Int J Fatigue 2014;59:244–53.

[100] Wu L, Jain A, Brown DW, Stoica GM, Agnew SR, Clausen B, et al. Twinning-detwinning behavior during the strain-controlled low-cycle fatigue testing of a wrought magnesium alloy, ZK60A. Acta Mater 2008;56:688–95.

[101] Qiao H, Agnew SR, Wu PD. Modeling twinning and detwinning behavior of Mg alloy ZK60A during monotonic and cyclic loading. Int J Plast 2015;65:61–84.

[102] ASTM E8 / E8M-08, Standard Test Methods for Tension Testing of Metallic Materials, ASTM International, West Conshohocken, PA, 2008., n.d.

[103] Albinmousa J, Jahed H, Lambert S. Cyclic behaviour of wrought magnesium alloy under multiaxial load. Int J Fatigue 2011;33:1127–39.

[104] Jata K V, Starke EA. Fatigue Crack Growth and Fracture Toughness Behavior of an AI-Li-Cu Alloy. Metall Trans A 1986;17A:1011–26.

[105] Satya Prasad K, Eswara Prasad N, Gokhale AA. Microstructure and Precipitate Characteristics of Aluminum-Lithium Alloys. In: Eswara Prasad N, Gokhale AA, Wanhill RJH, editors. Aluminum-Lithium Alloy. Process. Prop. Appl. 1st ed., Elsevier Inc.; 2014, p. 99–137.

[106] Li H, Huang D, Kang W, Liu J, Ou Y, Li D. Effect of Different Aging Processes on the Microstructure and Mechanical Properties of a Novel Al – Cu – Li Alloy. J Mater Sci Technol 2016;32:1049–53.

[107] Zhang F, Shen J, Yan XD, Sun JL, Sun XL, Yang Y. Homogenization heat treatment of 2099 Al-Li alloy. Rare Met 2014;33:28–36. doi:10.1007/s12598-013-0099-9.

[108] Jenabali Jahromi SA, Khajeh A, Mahmoudi B. Effect of different pre-heat treatment processes on the hardness of AISI 410 martensitic stainless steels surface-treated using pulsed neodymium-doped yttrium aluminum garnet laser. Mater Des 2012;34:857–62. doi:10.1016/j.matdes.2011.08.020.

[109] Xiong Y, Yu Q, Jiang Y. An experimental study of cyclic plastic deformation of extruded ZK60 magnesium alloy under uniaxial loading at room temperature. Int J Plast 2014;53:107–24. doi:10.1016/j.ijplas.2013.07.008.

[110] Jabra J, Romios M, Lai J, Lee E, Setiawan M, Lee EW, et al. The Effect of Thermal Exposure on the Mechanical Properties of 2099-T6 Die Forgings, 2099-T83 Extrusions, 7075-T7651 Plate, 7085-T7452 Die Forgings, 7085-T7651 Plate, and 2397-T87 Plate Aluminum Alloys. J Mater Eng Perform 2006;15:601–7.

[111] Sun Z, Huang M. Fatigue crack propagation of new aluminum lithium alloy bonded with titanium alloy strap. Chinese J Aeronaut 2013;26:601–5.

[112] Fu B, Qin G, Meng X, Ji Y, Zou Y, Lei Z. Microstructure and mechanical properties of newly developed aluminum – lithium alloy 2A97 welded by fiber laser. Mater Sci Eng A 2014;617:1–11.

[113] Li JF, Liu PL, Chen YL, Zhang XH, Zheng ZQ. Microstructure and mechanical properties of Mg, Ag and Zn multi-microalloyed Al-(3.2-3.8)Cu-(1.0-1.4)Li alloys. Trans Nonferrous Met Soc China (English Ed 2015;25:2103–12.

[114] Paramsothy M, Chan J, Kwok R, Gupta M. Addition of CNTs to enhance tensile/compressive response of magnesium alloy ZK60A. Compos Part A Appl Sci Manuf 2011;42:180–8. doi:10.1016/j.compositesa.2010.11.001.

[115] Dallmeier J, Huber O, Saage H, Eigenfeld K. Uniaxial cyclic deformation and fatigue behavior of AM50 magnesium alloy sheet metals under symmetric and asymmetric loadings. Mater Des 2015;70:10–30.

[116] Shamsaei N. Multiaxial Fatigue and Deformation Including Non-proportional Hardening and Variable Amplitude Loading Effects. University of Toledo, 2010.

[117] Mughrabi H. Fatigue Life and Cyclic Stress-Strain Behavior. Encycl Mater 2001:2917–31.

[118] Xiong Y, Jiang Y. Cyclic deformation and fatigue of rolled AZ80 magnesium alloy along different material orientations. Mater Sci Eng A 2016;677:58–67. doi:10.1016/j.msea.2016.09.031.

[119] Begum S, Chen DL, Xu S, Luo AA. Low cycle fatigue properties of an extruded AZ31 magnesium alloy. Int J Fatigue 2009;31:726–35.

[120] Xiong Y, Jiang Y. Fatigue of ZK60 magnesium alloy under uniaxial loading. Int J Fatigue 2014;64:74–83. doi:10.1016/j.ijfatigue.2014.02.019.

[121] Yu Q, Zhang J, Jiang Y, Li Q. An experimental study on cyclic deformation and fatigue of extruded ZK60 magnesium alloy. Int J Fatigue 2012;36:47–58. doi:10.1016/j.ijfatigue.2011.08.016.

[122] Vasilev E, Linderov M, Nugmanov D, Sitdikov O, Markushev M, Vinogradov A. Fatigue Performance of Mg-Zn-Zr Alloy Processed by Hot Severe Plastic Deformation. Metals (Basel) 2015;5:2316–27. doi:10.3390/met5042316.

[123] Branco R, Costa JD, Antunes F V. Low-cycle fatigue behaviour of 34CrNiMo6 high strength steel. Theor Appl Fract Mech 2012;58:28–34.

[124] Hormozi R, Biglari F, Nikbin K. Experimental study of Type 316 Stainless Steel Failure under LCF / TMF Loading Conditions. Int J Fatigue 2015;75:153–69.

[125] Zhang Q, Zhang J, Zhao P, Huang Y, Yu Z, Fang X. Low-cycle fatigue behaviors of a new type of 10% Cr martensitic steel and welded joint with Ni-based weld metal. Int J Fatigue 2016;88:78–87. doi:dx.doi.org/10.1016/j.ijfatigue.2016.03.003.

[126] Hu X, Huang L, Wang W, Yang Z, Sha W, Wang W, et al. Low cycle fatigue properties of CLAM steel at room temperature 2013;88:3050–9.

[127] Zhang J, Yu D, Zhao Z, Zhang Z, Chen G, Chen X. Low cycle fatigue of 2.25Cr1Mo steel with tensile and compressed hold loading at elevated temperature. Mater Sci Eng A 2016;667:251–60. doi:10.1016/j.msea.2016.04.064.

[128] Zhang S-L, Xuan F-Z. Interaction of cyclic softening and stress relaxation of 9–12% Cr steel under strain-controlled fatigue-creep condition: Experimental and modeling. Int J Plast 2017:1–20. doi:10.1016/j.ijplas.2017.06.007.

[129] Mishnev R, Dudova N, Kaibyshev R. Effect of the strain rate on the low cycle fatigue behavior of a 10Cr-2W-Mo-3Co-NbV steel at 650 °C. Int J Fatigue 2017;100:113–25. doi:10.1016/j.ijfatigue.2017.03.025.

[130] Zhou J, Sun Z, Kanouté P, Retraint D. Effect of surface mechanical attrition treatment on low cycle fatigue properties of an austenitic stainless steel. Int J Fatigue 2017;103:309–17. doi:10.1016/j.ijfatigue.2017.06.011.

[131] Begum S, Chen DL, Xu S, Luo AA. Effect of strain ratio and strain rate on low cycle fatigue behavior of AZ31 wrought magnesium alloy. Mater Sci Eng A 2009;517:334–43. doi:10.1016/j.msea.2009.04.051.

[132] Borrego LP, Abreu LM, Costa JM, Ferreira JM. Analysis of low cycle fatigue in AlMgSi aluminium alloys. Eng Fail Anal 2004;11:715–25.

[133] Mazánová V, Škorík V, Kruml T, Polák J. Cyclic response and early damage evolution in multiaxial cyclic loading of 316L austenitic steel. Int J Fatigue 2017;100:466–76. doi:10.1016/j.ijfatigue.2016.11.018.

[134] Szusta J, Seweryn A. Experimental study of the low-cycle fatigue life under multiaxial loading of aluminum alloy EN AW-2024-T3 at elevated temperatures. Int J Fatigue 2017;96:28–42. doi:10.1016/j.ijfatigue.2016.11.009.

[135] Rodriguez RI, Jordon JB, Allison PG, Rushing T, Garcia L. Low-cycle fatigue of dissimilar friction stir welded aluminum alloys. Mater Sci Eng A 2016;654:236–48.

[136] Chen W, Fei X, Tian Y, Yu D, Yu W, Chen X. Effect of thermal aging on the low cycle fatigue behavior of Z3CN20.09M cast duplex stainless steel. Mater Sci Eng A 2015;646:263--271.

[137] Wu Y, Zhu R, Cai X, Liu L. Fatigue behavior of variable-plane-rolled AZ31 magnesium alloy. Mater Sci Eng A 2016;650:273–80.

[138] Yu Q, Zhang J, Jiang Y, Li Q. Multiaxial fatigue of extruded AZ61A magnesium alloy. Int J Fatigue 2011;33:437–47. doi:10.1016/j.ijfatigue.2010.09.020.

[139] Yuan X, Yu W, Fu S, Yu D, Chen X. Effect of mean stress and ratcheting strain on

the low cycle fatigue behavior of a wrought 316LN stainless steel. Mater Sci Eng A 2016;677:193–202. doi:10.1016/j.msea.2016.09.053.

[140] Zhao T, Jiang Y. Fatigue of 7075-T651 aluminum alloy. Int J Fatigue 2008;30:834–49. doi:10.1016/j.ijfatigue.2007.07.005.

[141] Fatemi A, Socie DF. a Critical Plane Approach To Multiaxial Fatigue Damage Including Out of Phase Loading. Fatigue Fract Eng Mater Struct 1988;11:149–65.

[142] Esmaeili F, Chakherlou TN, Zehsaz M. Prediction of fatigue life in aircraft double lap bolted joints using several multiaxial fatigue criteria. Mater Des 2014;59:430–8.

[143] Zhong B, Wang Y, Wei D, Wang J. A new life prediction model for multiaxial fatigue under proportional and non-proportional loading paths based on the pi-plane projection. Int J Fatigue 2017;102:241–51.

[144] Gates NR, Fatemi A. On the consideration of normal and shear stress interaction in multiaxial fatigue damage analysis. Int J Fatigue 2017;100:322–36.

[145] Jahed H, Varvani-Farahani A. Upper and lower fatigue life limits model using energy-based fatigue properties. Int J Fatigue 2006;28:467–73.

[146] Zhong J, Zhong S, Zheng ZQ, Zhang HF, Luo XF. Fatigue crack initiation and early propagation behavior of 2A97 Al-Li alloy. Trans Nonferrous Met Soc China (English Ed 2014;24:303–9. doi:10.1016/S1003-6326(14)63061-2.

[147] Metal Handbook: Failure Analysis and Prevention. 9th ed. Ohio: American Society for Metals; 1986.

[148] Pandey V, Chattopadhyay K, Srinivas NCS, Singh V. Role of ultrasonic shot peening on low cycle fatigue behavior of 7075 aluminium alloy. Int J Fatigue 2017;103:426–35.

[149] Schubbe JJ. Evaluation of fatigue life and crack growth rates in 7050-T7451 aluminum plate for T-L and L-S oriented failure under truncated spectra loading. Eng Fail Anal 2009;16:340–9. doi:10.1016/j.engfailanal.2008.05.009.

[150] Zhu Z, Han J, Gao C, Liu M, Song J, Wang Z, et al. Microstructures and mechanical properties of Al-Li 2198-T8 alloys processed by two different severe plastic deformation methods: A comparative study. Mater Sci Eng A 2017;681:65–73.

Vitae

Name:	Muhammed Jamiu Suleiman Adinoyi
Nationality:	Nigeria
Date of Birth	13th June 1980
Email	mjadinoyi@gmail.com
Academic Background	B. Eng. (Mechanical Engineering), Bayero University, Kano State, Nigeria, Dec. 2005. M.Sc. (Mechanical Engineering), King Fahd University of Petroleum and Minerals, Dhahran, Saudi Arabia, June 2010. Ph.D. (Mechanical Engineering), King Fahd University of Petroleum and Minerals, Dhahran, Saudi Arabia, Dec. 2017.

PUBLICATIONS

1. **Muhammed J. Adinoyi,** N. Merah and J. Albinmousa, “Shear Fatigue Behavior of AW2099-T83 Aluminum-Lithium Alloy” **Accepted**, International Journal of Fatigue, 2018.
2. **Muhammed J. Adinoyi** and Syed A.M. Said, “Effect of Dust Accumulation on the Power Outputs of Solar PV Modules” Journal of Renewable Energy Vol. 60 (2013) pp 633-636.
3. **M. J. Adinoyi**, N. Merah, Z. Gasem and N. Al-Aqeeli, “Variation of Mechanical Properties of Epoxy-Clay Nanocomposite with Sonication Time and Clay Loading”, Key Engineering Materials Vols. 471-472 (2011) pp 496-501.
4. **M. J. Adinoyi**, N. Merah, Z. Gasem and N. Al-Aqeeli, “Effect of Sonication Time and Clay Loading on Nanoclay Dispersion and Thermal Property of Epoxy-Clay Nanocomposite”, Key Engineering Materials, Vol. 471-472 (2011), pp 490-495.

5. Shafique M. A. Khan, Nesar Merah and **Muhammad. J. Adinoyi** "3D effects on crack front core regions, stress intensity factors and crack initiation angles" International Journal of Solids and Structure Vol. 50 (2013) pp 1449–1459.
6. Z. M. Gasem, N. Merah, **M. J. Adinoyi** and Z. Khan, "The Effects of Clay Content and Sonication Time on Water Uptake in Epoxy-Organoclay Nanocomposites", Advanced Materials Research, Vol. 445 (2012), pp 509-513.
7. M. Al-Qadhi, N. Merah, Z. Khan, K. Mezghani, Z. Gasem and **M. J. Adinoyi**, "Effect of Sonication and High Shear Mixing Parameters on Nanoclay Dispersion in Epoxy", 15th European Conference on Composite Materials (ECCM15), Venice, Italy, 24-28 June 2012.